



Altti Torkkeli

Droplet microfluidics on a planar surface

VTT PUBLICATIONS 504

Droplet microfluidics on a planar surface

Altti Torkkeli

VTT Information Technology

Dissertation for the degree of Doctor of Science in Technology to be presented with due permission of the Department of Electrical Engineering, for public examination and debate in Auditorium S4 at Helsinki University of Technology (Espoo, Finland) on the 3rd of October, 2003, at 12 noon.



ISBN 951-38-6237-2 (soft back ed.)

ISSN 1235-0621 (soft back ed.)

ISBN 951-38-6238-0 (URL: <http://www.vtt.fi/inf/pdf/>)

ISSN 1455-0849 (URL: <http://www.vtt.fi/inf/pdf/>)

Copyright © VTT Technical Research Centre of Finland 2003

JULKAISIJA – UTGIVARE – PUBLISHER

VTT, Vuorimiehentie 5, PL 2000, 02044 VTT

puh. vaihde (09) 4561, faksi (09) 456 4374

VTT, Bergsmansvägen 5, PB 2000, 02044 VTT

tel. växel (09) 4561, fax (09) 456 4374

VTT Technical Research Centre of Finland, Vuorimiehentie 5, P.O.Box 2000, FIN-02044 VTT, Finland

phone internat. + 358 9 4561, fax + 358 9 456 4374

VTT Tietotekniikka, Tietotie 3, PL 1208, 02044 VTT

puh. vaihde (09) 4561, faksi (09) 456 7012

VTT Informationsteknik, Tietotie 3, PB 1208, 02044 VTT

tel. växel (09) 4561, fax (09) 456 7012

VTT Information Technology, Tietotie 3, P.O.Box 1208, FIN-02044 VTT, Finland

phone internat. + 358 9 4561, fax + 358 9 456 7012

The author's present contact address:

VTI Technologies

Myllykivenkuja 6, P.O.Box 27,

FIN-01621 VANTAA, Finland

Tel +358 9 8791 81

Direct +358 9 8791 8381

Fax +358 9 8791 8793

Technical editing Leena Ukoski

Otamedia Oy, Espoo 2003

Torkkeli, Altti Droplet microfluidics on a planar surface. Espoo 2003. VTT Publications 504. 194 p. + app. 19 p.

Keywords microfluidics, lab-on-a-chip, electrostatic droplet actuation, electrowetting, superhydrophobic surfaces, MEMS

Abstract

This work reports on the modelling of, and experiments on, a method in which liquid is transported as droplets on a planar hydrophobic surface with no moving parts, merely through electrostatic forces generated by the underlying electrodes. Two-directional transportation along a straight electrode path and across a junction, fusion of two droplets and methods for importing, exporting and filtering of water droplets were demonstrated, and can be used as basic functions of a lab-on-a-chip type microfluidic system.

In this work, the electrostatic droplet actuation is for the first time demonstrated on superhydrophobic surfaces. Such surfaces are composed of air-filled pores and exhibit a very low droplet sliding resistance due to reduced contact angle hysteresis and a high water contact angle (usually $> 150^\circ$). This work shows that superhydrophobic surfaces can be used to reduce the minimum voltage and to increase the maximum speed under certain conditions, but there are some harmful side-effects. First of all, the electrostatic pressure can push water into the surface pores, which hinders actuation. The phenomenon can also be treated as a vertical electrowetting effect. Another drawback is that the use of superhydrophobic surfaces makes actuation more critical to the properties of the liquid. For example, actuation of biological buffer solutions was not successful. For these reasons, it is concluded that it is more beneficial to use a smooth surface with low hysteresis than a superhydrophobic surface in droplet actuation.

Electrostatic droplet actuation is a potential method for manipulating liquid on a microscopic scale, but there is still work to do. This work contains a detailed examination of the droplet actuation mechanism, and trapping of charges in the solid-liquid interface is found to be the most severe problem that needs to be solved.

Preface

This dissertation is the result of work carried out at VTT Information Technology in Microelectronics research field. The experimental work was performed mainly during 1997–2000 in a project funded by Wallac Oy (currently PerkinElmer Life Sciences) and Tekes, the National Technology Agency of Finland. The theoretical work and writing of the thesis, carried out during 2000–2003, was funded by VTT and the Academy of Finland through the author's position at the Graduate School of Electronics Manufacturing at Helsinki University of Technology.

First of all, I would like to thank the working group of the droplet project. This included Prof. Ari Lehto, Dr. Jaakko Saarilahti and Mr. Ari Häärä at the VTT Microelectronics; Dr. Harri Härmä and Dr. Tero Soukka at the University of Turku; and M.Sc. Hannu Kojola and M.Sc. Pertti Tolonen at Wallac. This subject was originally proposed for me by Prof. Lehto, but without the support of Prof. Hannu Kattelus, Prof. Pekka Kuivalainen, Prof. Matti Leppihalme, Prof. Jouni Heleskivi and research manager M.Sc. Ilkka Suni I would not have been able to develop the project results into a thesis. I would also like to thank all members of VTT Microelectronics, especially in the micromechanics group, for the excellent work atmosphere. Special thanks for their help belong to the clean-room operators Ms. Kirsi Järvi, Mrs. Riitta Lindman and Mrs. Merja Markkanen, and research scientists M.Sc. Tomi Haatainen, M.Sc. Jani Karttunen, Lic.Tech. Jyrki Kiihamäki, Lic.Ph. Tapio Mäkelä, Dr. Panu Pekko, M.Sc. Nina Pirilä and M.Sc. Ingmar Stuns. I would also like to thank Prof. Kari Laajalehto at the University of Turku, Mr. Kaius Ruokonen at the Helsinki University of Technology, and M.Sc. Terho Kololuoma at VTT Electronics for their contribution. The discussions and comments obtained from my colleagues at the 3rd Electrowetting Workshop in Grenoble, especially those from Dr. Terry Blake in Kodak, were also very useful.

I would like to thank Prof. Thomas B. Jones at the University of Rochester for acting as the opponent and Prof. Göran Stemme at the Royal Institute of Technology and Prof. Heikki Koivo at the Helsinki University of Technology for the pre-examination of the thesis. Many thanks to Mrs Adelaide Lonnberg for checking of the language.

Many warm thanks to my wife Sirpa and to our small children Aino and Sandra for their patience during the process.

Finally, I really thank God that this work has now reached this final phase.

Espoo, August 2003

Altti Torkkeli

Contents

Abstract.....	3
Preface	4
List of symbols and abbreviations	10
1. Introduction.....	15
1.1 Background.....	15
1.1.1 Micropumps and valves	15
1.1.2 Valveless pumping	17
1.2 Droplet reactor concept	18
1.2.1 Review of other droplet-based microfluidic systems	20
1.3 Objectives and organisation of the thesis	22
1.4 Contribution of the thesis	22
1.5 Authors contribution.....	24
2. Hydrophobic surfaces	26
2.1 Contact angle	26
2.2 Contact angle hysteresis	27
2.3 Superhydrophobic surfaces.....	29
2.3.1 Equilibrium contact angle	32
2.3.2 Hysteresis	33
2.3.3 Critical pressure	35
2.3.4 Fabrication of superhydrophobic surfaces	40
2.3.5 Droplet motion on superhydrophobic surfaces	41
2.3.6 Superhydrophobic surfaces in droplet actuation	42
3. Theory and modelling of droplet actuation.....	44
3.1 Bulk water – electric field interactions.....	44
3.1.1 Electrical properties of liquid water	44
3.1.2 Dielectrophoresis.....	46
3.1.3 Electrostatic force.....	48
3.2 Electrical aspects of the liquid-vapour interface	51
3.2.1 Electrostatic pressure in the droplet surface.....	51
3.2.2 Electrohydrodynamic instability	52

3.3	Electrical aspects of the solid-liquid interface.....	53
3.3.1	Electrical double layer.....	53
3.3.2	Electrowetting.....	55
3.3.3	Electrowetting on superhydrophobic surfaces.....	58
3.3.4	Alternative solution for the electrowetting equation.....	67
3.3.5	Liquid contact charging.....	68
3.3.6	Charging effects and electrowetting.....	72
3.4	Model for droplet actuation.....	81
3.4.1	Electrostatic energy and force.....	83
3.4.2	Contact angle and electrowetting force.....	87
3.4.3	Actuation criterion.....	91
3.4.4	Electrostatic pressure.....	93
3.4.5	Charging effects.....	95
3.4.6	Summary and limitations of the model.....	99
3.5	FE simulations.....	102
3.5.1	3-dimensional simulation.....	102
3.5.2	2-dimensional simulations.....	105
4.	Experimental results and discussion.....	108
4.1	Setup and methods.....	108
4.2	Hydrophobic surfaces.....	110
4.2.1	Spin-coated Teflon [®] AF.....	110
4.2.2	ICP fluoropolymer.....	111
4.2.3	Sprayed AKD.....	113
4.2.4	Evaporated AKD.....	116
4.2.5	Sprayed Teflon [®] AF.....	118
4.2.6	Plasma-etched Teflon [®] AF.....	119
4.2.7	Lithographic patterning of Teflon [®] AF.....	121
4.2.8	Structured silicon surfaces with ICP fluoropolymer.....	123
4.2.9	Structured silicon surfaces with FAS coating.....	127
4.2.10	Structured silicon with nanoporous Al ₂ O ₃ and FAS.....	130
4.2.11	Surfaces with sloped side walls.....	133
4.2.12	Compatibility of superhydrophobic surfaces with biological solutions.....	136
4.3	Droplet transport experiments.....	138
4.3.1	1 st generation transport devices.....	138
4.3.2	Polymer ball actuation.....	142

4.3.3	2 nd generation transport devices	143
4.3.4	Droplet branching and fusion.....	149
4.3.5	Double-sided control.....	151
4.3.6	3 rd generation transport devices.....	152
4.3.7	Droplet vibrations with AC voltage	160
4.3.8	Droplet motion analysis	164
4.3.9	Long term stability problems	165
4.3.10	Actuation of biological solutions	167
4.3.11	Downscaling of droplet volumes.....	169
4.4	Droplet reactor functions.....	170
4.4.1	Droplet import.....	170
4.4.2	Droplet export and filtering.....	173
4.4.3	Evaporation control.....	175
4.4.4	Integration of droplet functions.....	176
5.	Conclusions.....	181
	References.....	184

Appendices

Appendix A: Analysis of model surfaces with different patterns

Appendix B: Capacitance between a spherical droplet and a conducting plane

Appendix C: Auxiliary equations for a spherical droplet and an equivalent capacitor

List of figures which are available as a movie file in <http://www.vtt.fi/tte/research/tte6/micromechanics/activities/microfluidics/droplet.htm>

	File name
Figure 65	Critical pressure exceeding.m1v
Figure 66	Sliding droplet.m1v
Figure 76	Polymer ball actuation.m1v
Figure 80a	Droplet moving on PWB-AKDspray.m1v
Figure 80b	Droplet moving fast.m1v
Figure 82	Droplet in a junction (2x speed).m1v
Figure 83	Droplet fusion.m1v

Figure 84	Two-sided control.m1v
Figure 87	Droplet moving on Si-AKDevap 124V.m1v
Figure 89ab	Sticking droplet.m1v
Figure 89cd	Stuck droplet.m1v
Figure 90	Droplet moving on thin insulator.m1v
Figure 92a	Droplet vibrations A.m1v
Figure 92b	Droplet vibrations B.m1v
Figure 92c	Oval droplet.m1v
Figure 95	Droplet bottom enlarged.m1v
Figure 99	Droplet generation.m1v
Figure 102 & Figure 103	Droplet export and filtering (2x speed).m1v
Figure 106	Droplet moving on sprayed Teflon.m1v

List of symbols and abbreviations

a	Capillary length
A	Area
A_c	Contact area between droplet and surface
A_{cp}	Cross-sectional area of a capillary
A_{eq}	Area of the equivalent plate capacitor
A_{lv}	Liquid-vapour interface area
A_{sl}	Solid-liquid interface area
A'_{sl}	Effective solid-liquid interface area
A_x	Auxiliary variable for the area of a circular segment
c_{dl}	Capacitance density of the electrical double layer
C_{cp}	Capacitance of the elementary capillary
C_d	Capacitance between droplet and electrode
C_e	Capacitance between two electrodes
d	Thickness of a dielectric layer
D	Electric flux density
d_{diff}	Diffuse layer thickness
D_s	Characteristic surface dimension of a model surface
d_{Stern}	Stern layer thickness
E	Electric field intensity
E_b	Breakdown field
F	Force
f	Fractional area of a composite surface
F_{DEP}	Dielectrophoretic force
F_e	Electrostatic force
F_{EW}	Electrowetting force
F_q	Coulomb force

f_r	Resonance frequency
g	Gravitational acceleration
J	Electric flux
K	Boltzmann's constant
k	Charge transfer factor
l	Length
L_{cp}	Perimeter of a capillary
M	Molecular weight
n	Concentration of ions in liquid
n_M	Mole number of liquid molecules
\mathbf{n}	Unit normal vector
P	Pressure
P_c	Critical pressure
P_{cp}	Capillary pressure
P_e	Electrostatic pressure
q	Elementary charge
Q	Electric charge
R	Radius of a droplet
r	Rounding radius
R_b	Radius of a ball having the same volume as the droplet
R_c	Radius of the droplet-surface contact area
R_{eq}	Radius of the equivalent plate capacitor
R_M	Molar gas constant
S	Surface
s_p	Preferentially adsorbed surface charge density
s_t	Trapped surface charge density
T	Temperature
U	Voltage

U_0	Potential induced by preferentially adsorbed surface charge
U_c	Charge induced voltage
U_d	Voltage of charged droplet
U_t	Threshold voltage of charge trapping
V	Volume
w	Width of the droplet bottom
W	Energy
W_e	Electrostatic energy
W_s	Characteristic surface dimension of a model surface
x	Droplet displacement
y	Auxiliary variable for distance
α	Auxiliary variable for angle
α_r	Rotation angle
α_s	Slope of the structure side walls of a rough surface
β	Auxiliary variable for angle
δ	Auxiliary variable for angle
ε	Absolute permittivity
ε_0	Permittivity of a vacuum
ε_{diff}	Diffuse layer permittivity
ε_{Stern}	Stern layer permittivity
ε_r	Relative permittivity
ϕ	Auxiliary variable for angle
γ	Surface tension
γ_e	Electric-field induced surface tension
γ_{elv}	Electric-field induced surface tension in the liquid-vapour
γ'_{esl}	Electric-field induced surface tension in the effective solid-liquid
γ_{lv}	Surface tension between liquid and vapour
γ_{sl}	Surface tension between solid and liquid

γ_{sv}	Surface tension between solid and vapour
κ	Inverse of the Debye length
Λ_M	Eigenmode of droplet vibration
π	Pi
ρ_c	Volume charge density
ρ_l	Liquid density
θ	Contact angle between solid and liquid
θ_0	Young contact angle
θ_a	Advancing contact angle
θ_c	Contact angle of a composite surface
θ_e	Contact angle in the presence of electric field
θ_r	Receding contact angle
σ	Conductivity
τ	Time constant
μ TAS	Micro Total Analysis System
AKD	Alkylketene Dimer
BSA	Bovine Serum Albumin
CVD	Chemical Vapour Deposition
DI	Deionized
DIL	Dual In Line
DNA	DeoxyriboNucleic Acid
EDTA	EthyleneDiamine Tetra-acetic Acid
EDX	Energy Dispersive X-ray
EHD	ElectroHydroDynamic
FAS	Fluoro Alkyne Silane
FE	Finite Element
FEP	PolyfluoroEthylene-Propylene
HEPA	High Efficiency Particulate Absorber

ICP	Inductively Coupled Plasma
IPA	IsoPropyl Alcohol
MEMS	Micro Electro Mechanical System
MOS	Metal Oxide Semiconductor
PDMS	PolyDiMethyl Siloxane
PE	PolyEthylene
PECVD	Plasma Enhanced Chemical Vapour Deposition
PEG	PolyEthyleneGlycol
PET	PolyEthylene Terephthalate
PFA	PerFluoroAlkoxy
PP	PolyPropylene
PSG	PhosphoSilicate Glass
PTFE	PolyTetraFluoroEthylene
PWB	Printed Wiring Board
RF	Radio Frequency
SAW	Surface Acoustic Wave
SEM	Scanning Electron Microscope
TEOS	TetraEthyl OrthoSilicate
TMAH	TetraMethyl Ammonium Hydroxide
TRIAC	Triode AC switch
TSA	Tyramide Signal Amplification
UV	Ultraviolet
XPS	X-ray Photoelectron Spectroscopy
YAG	Yttrium Aluminium Garnet

1. Introduction

1.1 Background

Miniaturisation is a current trend in chemical and biochemical laboratory technology [1, 2, 3]. The advantages are reduced reagent consumption, increased reaction speeds, parallelisation of the analysis, and portability. Chips with miniaturised arrayed biosensors, referred to as biochips or microarrays, are already used routinely in biochemistry and are at present manufactured commercially by 49 companies world-wide [4]. Currently the leading application is optical detection of DNA hybridisation, but similar approaches for proteins and living cells are being developed. Functionality is also increased so that in addition to detection, also other parts of the assay are combined with the same device. The ultimate goal is to perform the entire analysis on the chip scale. Such devices are called as bioMEMS (micro-electromechanical systems), lab-on-a-chips or μ TAS (micro total analysis systems). In practice, the analysis requires multiple manipulation steps of liquid samples. An example is given in Figure 1. At present, liquid manipulation still relies more or less on pumping and pipetting, which requires a large mechanical apparatus. Thus there is a strong demand to develop techniques for manipulating fluids on a microscopic scale. This field of technology is referred as microfluidics.

1.1.1 Micropumps and valves

The most straightforward strategy in the development of microfluidic systems is miniaturisation and integration of traditional fluidic components, such as liquid channels, reservoirs, pumps, valves, mixers, reaction vessels and detectors. However, downscaling leads to some problems. For example, the flow resistance of a channel is increased, while the pump performance decreases. The problems with micromechanical pumps are dead volumes, low flow rate, priming, blocking due to air bubbles, and sticking. A large stroke helps with these problems, but it is difficult to achieve with electrostatic force, which is otherwise the most convenient source of mechanical energy with the MEMS. Piezoactuators [5, 6, 7] and electromagnets [8] have been used instead, but they lead to large devices which are difficult to integrate on the chip scale. As a partial solution, modular systems with separated actuators and fluidic

components have been proposed [9]. Micromechanical valves suffer from similar problems to those of pumps.

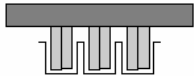
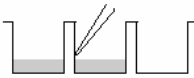
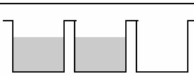
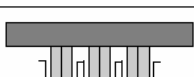

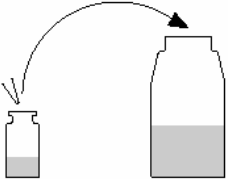
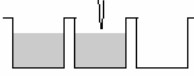
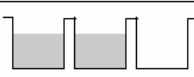

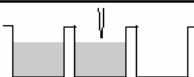
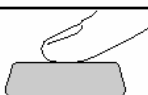
Wash.		Prewash the streptavidin coated plates (C122-105)
Add buffer containing biotinylated protein.		100 μ l of Assay Buffer (1244-106) containing eg. 100 ng/ml of biotinylated protein
Incubate.		Slow shaking 1-2 hours RT
Wash.		Wash gently once
Add standards and samples		10 μ l
Dilute tracer.		25-500 ng/ml Eu-labelled protein in Assay Buffer
Add tracer.		100 μ l
Incubate		Slow shaking 60 min. RT
Wash.		4-6 washes (1244-114)
Enhance.		200 μ l, slow shaking 5 min
Count.		Create counting protocol and count with VICTOR ²

Figure 1. A protocol for protein binding assay. Reprinted with permission from Advice for setting up robust DELFIA[®] binding assays, PerkinElmer Life Sciences, Application Notes, 2001 [10]. Copyright © 2001 PerkinElmer, Inc.

1.1.2 Valveless pumping

Due to problems in miniaturisation of pumps and valves, various valveless liquid actuation methods have been developed. The commonest method used with μ TAS is referred to as electrokinetic or electro-osmotic pumping [11, 12, 13, 14]. It is based on the motion of ions in the electrical double layer of the capillary wall when a longitudinal electric field is applied. It has no moving parts and can be easily combined with an electrophoretic separation. Such a system can be very simple, and disposable moulded plastic devices are already being manufactured commercially [15]. However, electrical contacts with the liquid and rather high voltages (80–300 V/cm) are needed. Transport properties are also dependent on the pH of the solution. Less popular methods are electro- and magnetohydrodynamics [16, 17], which are based on electric (Coulomb) or magnetic (Lorentz) forces acting on ionic charges in the bulk of the liquid. With these methods the transport efficiency is also strongly dependent on the fluid properties such as conductivity and viscosity. For example, electrohydrodynamic (EHD) pumping works only with non-aqueous solutions, which limits its use in biochemistry. Some non-electrical valveless pumping methods have been also proposed. One unique idea, which is already commercialised, is to use inertial force to pump the liquid [18]. In such a system, the channels are made on circular discs and liquid is moved radially by rotating the disc at various speeds. The advantage is that the liquid properties do not have a significant influence and the technology for low-cost disc manufacture and controlled spinning and optical detection can be adapted directly from CDs and CD players. However, such a system is not really chip size. Thermal energy has also been used. Transport of liquid plugs in channels by thermal control of vapour bubbles has been demonstrated [19], but suffers from heating and slow operation.

It appears, however, that valveless pumping in channels raises a new problem. If there are no valves, the liquid cannot be controlled freely. Liquid motion in some part of the channel induces motion everywhere else. Thus, in the existing valveless pumping methods, the degree of freedom in liquid manipulation is severely restricted so that they can be only used in limited applications.

1.2 Droplet reactor concept

Manipulating small liquid volumes as droplets instead of continuous flow can solve part of the miniaturisation problem. In the droplet reactor concept, the droplets are transported on a planar hydrophobic surface using electric fields generated by underlying electrodes (Figure 2). When the electrodes are arranged as suitable paths, samples and reagents can be manipulated individually or mixed with each other in a controlled manner. Sorting and optical detection can be also easily arranged. In this concept, liquid import and export are arranged as small holes through the surface. There is no need for integrated pumps, valves, channels or any other moving parts. With the droplet reactor, versatile functions can be performed with an extremely simple device.

Evaporation of the droplets may be a problem if very long analyses are performed. This can be solved by arranging a controlled saturated vapour atmosphere around the system. Although this requires encapsulation it is not a major disadvantage, as some kind of protecting cover is usually needed anyway with very sensitive systems.

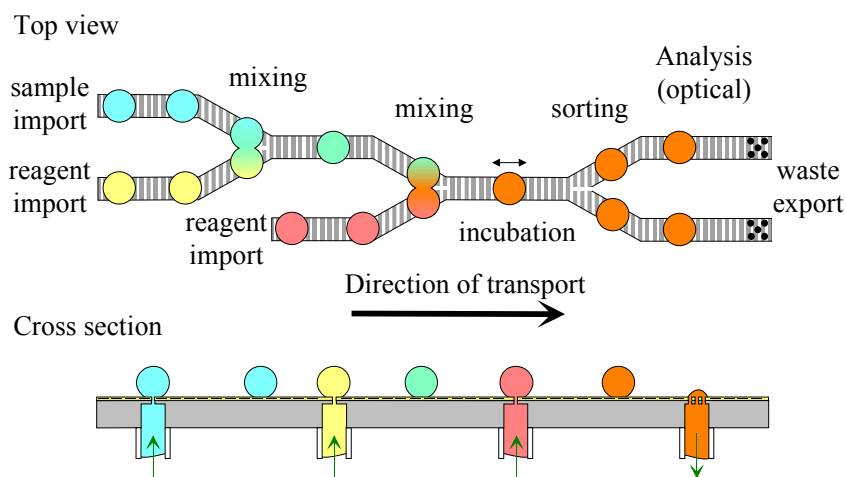


Figure 2. Droplet reactor concept.

The principle of electrostatic droplet actuation is shown in Figure 3. A set of shaped electrodes, separated by an insulator, is placed beneath the surface. When one or several of the electrodes is connected to a voltage source and the others

are grounded, an electric field will be generated which induces charges in the solid-liquid and liquid-vapour interfaces of the droplet. If the voltage between the electrodes is sufficiently high and the surface is hydrophobic enough, the droplet moves towards the powered electrodes due to the electrostatic force originating from the attraction between induced charges and charged electrodes. By switching the electrodes sequentially either to the voltage source or to the ground, the droplet can be transported along the electrode path. In principle, the mechanism is very suitable for miniaturisation, since it is dominated by surface effects that overcome the body forces as the dimensions decrease. As a matter of fact, most of the problems with micropumps and valves are related to this scaling law.

It appears that successful actuation is very critical to the characteristics of the hydrophobic surface. In order to improve actuation, superhydrophobic surfaces were used in this work. These are based on a special surface structure and they combine a large apparent contact angle with small contact angle hysteresis, which are the key parameters of sliding resistance.

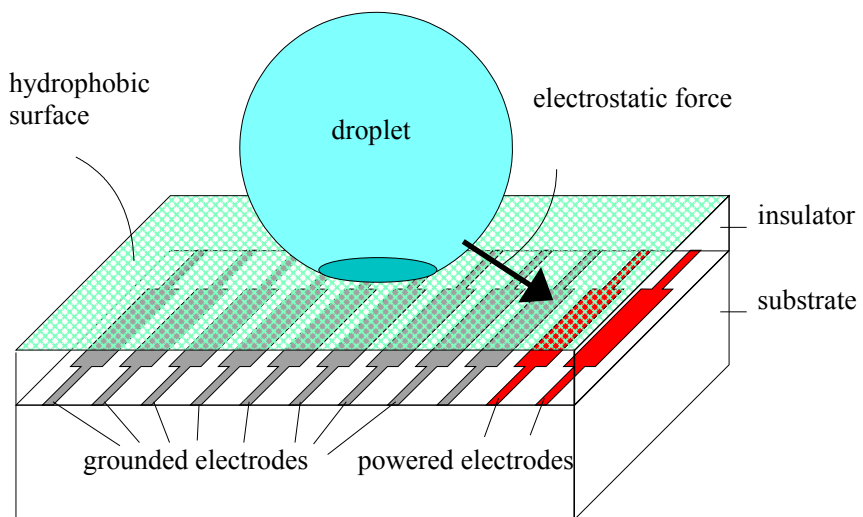


Figure 3. Principle of electrostatic droplet actuation.

1.2.1 Review of other droplet-based microfluidic systems

The droplet reactor concept was originally presented in 1997 by M. Washizu [20, 21]. It is close to the concept of this work in that the droplets are being manipulated on an open surface, but instead of electrode shaping, Washizu used grooves to guide the droplets along the surface. Furthermore, no methods for importing or exporting droplets, which are essential features for a fully operational system, were presented. The most significant difference is that Washizu used a smooth hydrophobic surface (Teflon[®]AF), whereas superhydrophobic surfaces are used here. Physical modification of the hydrophobic surface in order to reduce the actuation voltage was already proposed by Washizu, but poor results were achieved. The minimum actuation voltage was 300 V rms and the maximum droplet speed 0.4 mm/s.

Actually, the idea of electrical actuation of droplets is much older. Already in 1982, six years before the term μ TAS was even introduced, J.S. Batchelder [22] demonstrated that water droplets can be transported with planar electrodes in a narrow gap filled with insulating fluid, and proposed the method to be used in chemical applications. Eighteen years later, a very similar technique was published by Pollack, Fair and Shenderov [23] (Figure 4) and then given the term digital microfluidics by Pollack [24]. Droplet actuation was demonstrated in both silicone oil and air filled cavities using Teflon[®]AF as the hydrophobic surface. The minimum voltage was 40 V and the maximum speed 30 mm/s. Droplet generation, mixing and splitting were also demonstrated. The improvement of characteristics is due largely to a thinner insulator, which increases the electrostatic force, and the use of silicone oil which reduces the droplet sliding resistance. The work was soon followed by a very similar system by Lee, Cho, and their co-workers [25, 26, 27]. They were able to reduce the minimum actuation voltage down to 15 V with the use of a high permittivity insulator (barium strontium titanate) in combination with Teflon[®]AF. Both of these groups claim that the droplet actuation is based on electrowetting, since the electric field modifies the apparent wetting condition between the droplet and the surface. Batchelder [22] explained the actuation in terms of dielectrophoresis.

It should be noted that the closed system [23, 26] (Figure 4) does not have all the advantages of the droplet reactor concept. First of all, the fabrication complexity

is comparable to a system with closed channels, or even beyond that if filler fluid is used. Fabrication of the open-air system is much simpler; for example there is no need for transparent top electrodes or a 3-dimensional assembly. Secondly, the open-air system is more flexible to modifications. For example, implementation of some kind of detection of the liquid is a demanding task with the closed system. Furthermore, electrostatic actuation of solid spheres can be integrated more easily with the open-air device. Such particles are used as a solid phase in biochemistry, for example in miniaturised immunoassays [28]. A possible advantage of the closed systems is that the droplets may evaporate somewhat more slowly than with the open-air system.

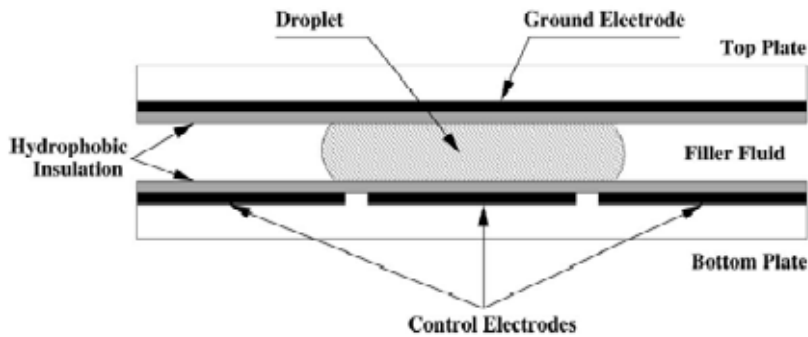


Figure 4. Principle of a closed droplet actuator system. Reprinted with permission from Pollack, Fair and Shenderov, *App. Phys. Lett.* 77 (11), 2000, 1725–1726 [23]. Copyright © 2000 American Institute of Physics.

Also other methods for droplet-based microfluidics have been proposed. The use of RF electric fields to form small droplets from larger ones on a hydrophobic surface has been reported by Jones, Gunji, Washizu and Feldman [29]. Although the droplets could not otherwise be moved, the results are interesting and are referred to in greater detail later in this work. O. Sandre et al. [30] demonstrated lateral droplet motion using vertical shaking on an asymmetrically structured surface. The disadvantage is that actuation is only possible in one direction. S. Nilsson et al. [31] used ultrasound to levitate droplets, but the method requires a large apparatus, and is not suitable for miniaturisation. A more promising method that uses acoustic energy to move the droplets has been reported by Strobl et al. [32, 33]. Droplet actuation was achieved on a surface acoustic wave (SAW) device covered with a hydrophobic layer. Recently, droplet actuation

based on thermal (Marangoni effect) [34] and optoelectronic [35] modification of contact angle have been reported.

1.3 Objectives and organisation of the thesis

The main goal of the work that is reported in this thesis was to realise the droplet reactor concept shown in Figure 2. The use of superhydrophobic surfaces was introduced in an early phase of the project, as soon as it was noticed that a reduced sliding resistance is needed even to achieve some kind of actuation.

The principles of superhydrophobic surfaces are presented using some calculations of model surfaces in section 2. The theory and modelling of droplet actuation is presented in section 3. The goal was to investigate the physics behind the actuation and build a model that could be used for further optimisation of the actuator device. Another goal was to explain the mechanisms that hinder actuation. Charge trapping in solid-liquid interfaces, which is of utmost importance in this context, is reviewed and included in the model. The electrowetting effect, which is in close relation to the electrostatic force, is analysed in general and in superhydrophobic surfaces in particular, and is also included in the model.

The experimental work is reported and discussed in section 4, and includes the development of superhydrophobic surfaces, droplet actuation devices, methods for importing and exporting droplets, and a trial to combine all functions on the same substrate. Finally, conclusions and suggestions for future work are given.

Some experiments are also available as movie files from the internet. The web site, figure numbers and file names are listed in the table of contents.

1.4 Contribution of the thesis

Droplet actuation using electrical forces is an emerging microfluidic technique. This work contributes to advancing the field in the following way:

- This thesis demonstrates for the first time droplet actuation on superhydrophobic surfaces. Higher droplet speeds and, under certain conditions, lower actuation voltages can be achieved using such surfaces, but the properties of the liquid must not differ too much from pure water and the vertical electrostatic pressure must not exceed the critical pressure of the surface. The latter effect can be reduced by making the dimensions of the surface structures as small as possible. This may also help in downscaling liquid volumes.
- New combinations of materials and methods for producing superhydrophobic surfaces are demonstrated. These include evaporated AKD, sprayed AKD, sprayed Teflon[®] AF and lithographically structured silicon coated with ICP fluoropolymer or Sol-Gel FAS.
- This thesis demonstrates new features of the open surface droplet reactor concept. These are the guiding of droplets by electrode shaping instead of grooves, and methods for importing, exporting and filtering.
- The physical mechanisms behind droplet actuation are considered in detail and the role of electrostatic force is stressed. Explanations of droplet actuation mechanisms have been not congruent in earlier papers on electrostatic droplet actuation.
- The electrowetting effect is still under discussion in the scientific community. In this thesis electrowetting is considered both in general and for the first time in the special case of superhydrophobic surfaces. A new vertical electrowetting effect has been found in this thesis which can be treated equally as electrostatic pressure. The difference between electrowetting and electrostatic force as the droplet driving force is discussed.
- Existing knowledge of charging effects in the three-phase contact line is reviewed and applied to droplet actuation. Although the charging effects are of utmost importance they are not truly discussed in existing droplet actuation papers. Threshold-type charging is confirmed and the threshold voltage is seen to be somehow connected to the electrowetting effect. The

charging properties of various hydrophobic materials found in the literature are compared and their usability in droplet actuation is considered.

- A model for electrostatic droplet actuation is given which can be used to calculate the actuation forces and voltages. The model can be applied in the open-surface actuator device design with both normal and superhydrophobic surfaces. The model includes all relevant physical phenomena such as electrowetting and charging effects. A force calculation in a closed droplet actuator having filler fluid and different geometry has been published recently [36] but a somewhat different formulation was obtained, since the droplet-fluid interface was neglected. With superhydrophobic surfaces this simplification cannot be done.

Part of the results were presented at the MEMS2001 conference in Interlaken, Switzerland [37], at the Transducers '01 – Eurosensors XV conference in Munich, Germany [38] and in the 3rd Electrowetting Workshop in Grenoble, France [39].

1.5 Authors contribution

Writing of the thesis, including theoretical considerations and interpretations of the experimental results, was done solely by the author. The experimental work was carried out in co-operation with several other persons. The device structures and their fabrication processes were designed by the author, but part of the mask layouts were designed by Dr. Jaakko Saarilahti, who also performed a major part of the 2-dimensional simulations jointly with the author. Three-dimensional simulations were performed by Mr. Kaius Ruokonen at Helsinki University of Technology. Wafer level fabrication of the devices was carried out by the clean room operators at VTT Microelectronics, and the assembly was made by the author and Mr. Ari Häärä, who designed and fabricated the control electronics. The building of the test setup and the device testing were performed by the author and Mr. Ari Häärä.

The development and characterisation of superhydrophobic surfaces was carried out jointly by the author, Dr. Harri Härmä and Dr. Tero Soukka at the University of Turku. Dr. Härmä developed the spraying and evaporation processes for

AKD. Dr. Härmä and Mr. Häärä fabricated the surfaces for the actuator devices. Prof. Kari Laajalehto at the University of Turku performed the XPS analysis and M.Sc. Terho Kololuoma from VTT Electronics fabricated the Sol-Gel coatings. The mask for the pillar surfaces was obtained from Lic.Tech. Jyrki Kiihamäki, and ICP etching and ICP fluoropolymer coatings were made by M.Sc. Jani Karttunen and Dr. Panu Pekko. Prof. Hannu Kattelus performed the parallel plate plasma etching of silicon, while O₂ plasma etching of Teflon[®] AF was performed by the author with the help of M.Sc. Tomi Haatainen. In addition, useful assistance was given by M.Sc. Ingmar Stuns, Lic.Ph. Tapio Mäkelä and M.Sc. Nina Pirilä.

2. Hydrophobic surfaces

2.1 Contact angle

When a small amount of liquid is placed on a hydrophobic surface, it forms a droplet whose shape is determined by the liquid volume and the equilibrium contact angle between the liquid and the surface. With the equilibrium contact angle the energy of the system reaches a local minimum. If the volume of the droplet is of the order of μl , or less, the gravitational effects have little effect, and droplet shape is very close to a cap of a sphere. The equilibrium contact angle depends on the surface condition. If the surface is ideal (smooth, planar, rigid and homogeneous) the equilibrium contact angle is equal to Young's angle, which can be determined from the force balance between the interfacial tensions at the three-phase contact line formed by solid, liquid and vapour (Figure 5). The force balance leads to the well-known Young equation:

$$\gamma_{lv} \cos \theta_0 = \gamma_{sv} - \gamma_{sl}, \quad (1)$$

where θ_0 is the Young contact angle and γ_{sl} , γ_{sv} and γ_{lv} are surface tensions at solid-liquid, solid-vapour (air) and liquid-vapour interfaces.

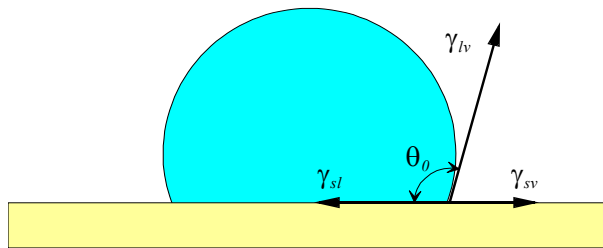


Figure 5. Droplet on an ideal hydrophobic surface.

The contact angle is a measure of wetting characteristics of the surface, so that a surface with a contact angle of less than 90° is called wetting or hydrophilic and a surface with a contact angle of over 90° is non-wetting or hydrophobic. Hydrophobic materials are sometimes referred to as water-repellent. This may be misleading, because hydrophobic materials actually attract water, but the

attraction between the water and the surface molecules is weaker than between water molecules. Surface tension is a manifestation of the intermolecular forces at a surface (or interface) and is defined as the energy needed to increase the surface area per increase in surface area:

$$\gamma = \frac{dW}{dA}. \quad (2)$$

The surface tension value in N/m is equal to the surface free energy in J/m². According to the Young equation, the smaller the surface tension (or free energy) of the surface, the larger is the contact angle. The lowest free energy of all surfaces is obtained with the closest hexagonal packing of $-\text{CF}_3$ groups, and a water contact angle of 119° has been measured for such a surface [40]. This can be considered to be practically the highest Young's angle of all materials known to date.

2.2 Contact angle hysteresis

In real surfaces, the equilibrium contact angle is not exactly the Young value, but varies within a certain range around it. The contact angle reaches its maximum value for an advancing liquid edge and the minimum value for a receding liquid edge. Therefore the maximum and minimum values are called advancing and receding contact angles respectively, and their difference is termed contact angle hysteresis. Contact angle hysteresis is related to non-idealities such as non-homogeneity and roughness, but the origin of the phenomenon has not been fully explored. Static advancing and receding angles can be easily observed from a tilted sessile droplet as shown in Figure 6. In a dynamic case, the contact angles change from the static values so that the advancing angle increases and the receding angle decreases as a function of the speed of the three-phase contact line.

Contact angle hysteresis is a very important parameter when droplet motion is being considered. This can be seen from equation (3), which gives the force needed to move a droplet on the surface. The equation, derived simply by equating the energy of wetting on the advancing edge and the energy released by

dewetting of the receding edge, was originally presented by Furmidge [41] and later confirmed without approximations by Dussan and Chow [42].

$$F_s = \gamma_{lv} w (\cos \theta_r - \cos \theta_a), \quad (3)$$

where w is width of the droplet bottom perpendicular to the direct of the motion and θ_a and θ_r are advancing and receding contact angles of the surface. The width of the droplet bottom can be calculated from the average of the advancing and receding angles:

$$F_s = 2R\gamma_{lv} \sin\left(\frac{\theta_a + \theta_r}{2}\right) (\cos \theta_r - \cos \theta_a), \quad (4)$$

where R is the radius of the droplet. The moving force can be measured easily by tilting the surface with a droplet of known volume and recording the angle when the droplet starts to move. The equation (4) shows that the sliding force is a strong function of the contact angle hysteresis, but also the average of the advancing and receding angles matters. This means that the mobility of droplets on a surface can be improved in two ways: The first is to minimise the contact angle hysteresis only. This means getting the surface as smooth and homogeneous as possible. Another way is to accept some hysteresis, but increase both advancing and receding contact angles so that the hysteresis stays small enough. This can be achieved with proper surface roughness.

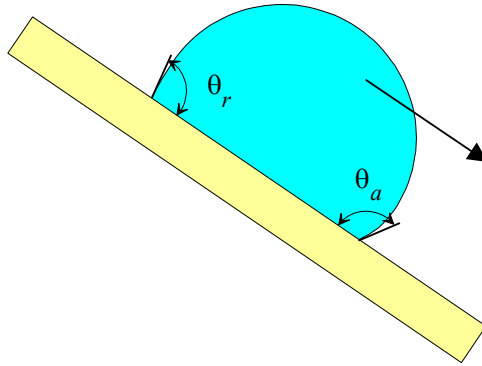
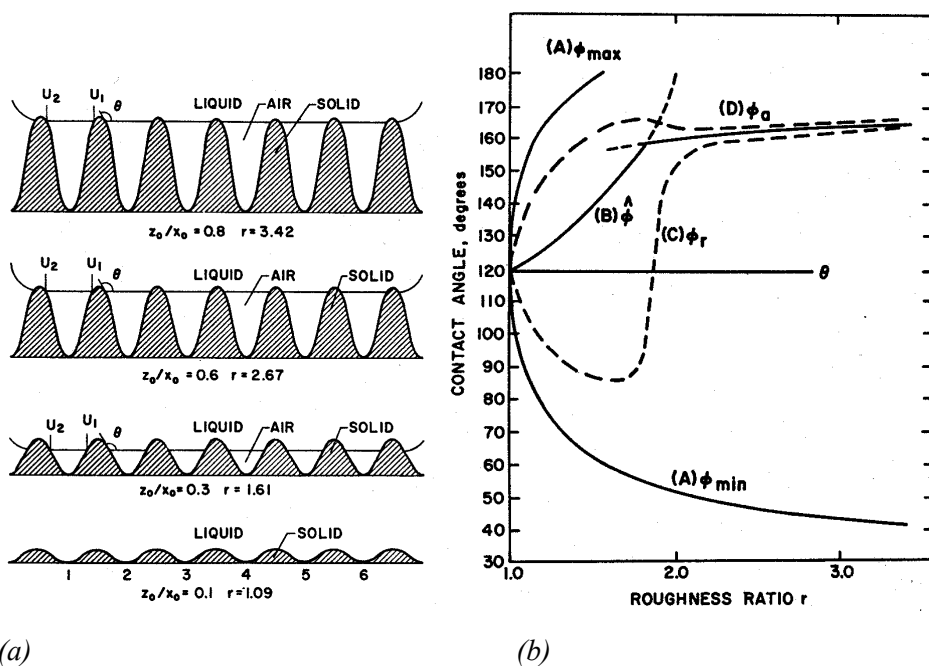


Figure 6. Contact angle hysteresis.

2.3 Superhydrophobic surfaces

Numerous papers have been published recently on superhydrophobic surfaces, as shown in a review by Nakajima et al. [43]. The terms ultra- and -repellent have also emerged in this context. However, the condition of a surface being superhydrophobic is not very well defined. The prefix “super-” suggests that such a surface attracts water far less than a "normal" hydrophobic surface. This begs the question, what is a good measure of water attraction? In this work we deal with moving droplets, and for us it is obvious to take the force needed to move droplets on the surface as the criterion. Being related to the energy needed to remove water from the surface, the droplet moving force is also a good measure of practical hydrophobicity. As shown in equation (4), this is related to contact angle hysteresis. However, this is often forgotten, even in scientific journal papers on super- or ultrahydrophobic surfaces. This reveals that the elementary studies on the subject, published already in the 1960s, have been forgotten. This was pointed out in two papers by Chen, Öner and their co-workers [44, 45]. In many papers, the hydrophobic quality of the surface is judged only according to one stationary (advancing) contact angle, and if the value is high enough, typically over 150° , the surface is called superhydrophobic. However, such a surface may have large contact angle hysteresis, when it is actually less hydrophobic than a normal surface. Thus in order to say something about the water-repellent properties of a surface, both advancing and receding contact angles should be given. Alternatively, the droplet moving force or tilt angle should be given, as was done by Miwa et al. [46].

The papers of Johnson and Dettre [47, 48] can be considered among the elementary studies on superhydrophobic surfaces. Although the term superhydrophobic was not used, the principles of the phenomenon were discovered. The basis of the consideration is that contact angle hysteresis due to surface roughness is determined by a balance between the macroscopic vibrational energy and the heights of the energy barriers between metastable states of the droplet. Using a sinusoidal model surface (Figure 7a) and numerical calculations of free energy, they were able to analyse contact angle hysteresis with respect to variable surface roughness. Figure 7b shows calculated advancing and receding angles with a variable surface roughness factor.



(a) Water droplet on an idealised sinusoidal surface with different roughness ratios. (b) Calculated advancing and receding contact angles (dashed lines) as a function of roughness. Reprinted with permission from Johnson and Dettre, *Adv. Chem. series* 43, 1964, 112–135 [47]. Copyright © 1964 American Chemical Society.

The definition of the roughness factor is not presented here, but some examples of the correlation between the roughness factor and the surface profile are given in Figure 7a. When the roughness is gradually increased, first the advancing angle increases and the receding angle decreases. Thus a surface with low roughness has a high advancing angle and large contact angle hysteresis, and the surface is actually less water-repellent than the original smooth surface. This reveals why only one stationary (advancing) contact angle tells nothing about the water-repellent properties of the surface. When the roughness becomes steep enough, also the receding angle begins to increase and finally both angles become much higher than Young's angle and the hysteresis is small. Droplets roll away from such a surface with a very small tilt, and the surface can be called superhydrophobic. This kind of surface can be also found in the nature, for example on plant leaves [49].

As shown in Figure 7, after a certain roughness ratio the receding angle (curve C) increases very rapidly. This happens when it is both geometrically and energetically favourable for the droplet to come into contact with only the tips of the surface structures, so that small air volumes remain between the droplet and the surface. Figure 8 illustrates the geometric criterion. Because the contact angle between liquid and solid is Young's angle everywhere, liquid tries to form concave menisci between the surface structures if the slope angle is too low. This results in capillary action, which wets the surface completely. With high slope angle roughness, liquid tries to form convex menisci between the surface structures. This results in negative capillary action that drives liquid from the surface, resulting in an air layer between the surface and the liquid. The droplet mass is supported by the negative capillary pressure of these small liquid membranes. Such a surface can be considered as a composite or heterogeneous surface consisting of small portions of solid material and air. From Figure 8 we can derive the geometric criterion for a composite surface. The surface must consist of structures having slope angles

$$\alpha_s \geq 180^\circ - \theta_0. \quad (5)$$

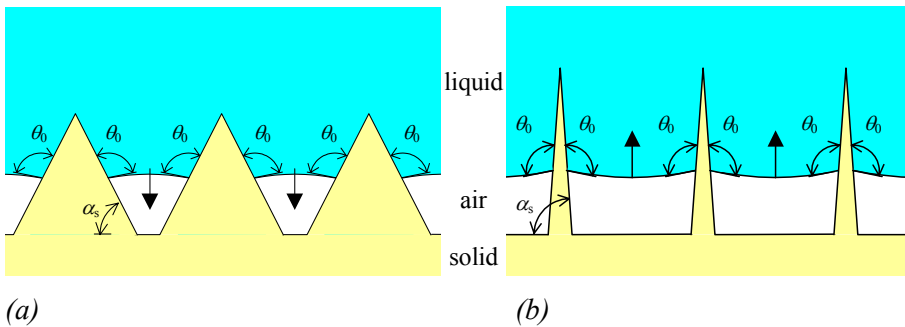


Figure 8. Water and rough hydrophobic surface with (a) low and (b) high slope angle structures.

Johnson and Dettre [47] point out that the geometrical criterion is not fully adequate, because in some cases the geometrical criterion may be slightly fulfilled, but it is energetically favourable for the liquid to fill the gaps between the surface structures. For this reason it is reasonable to have as high slope

angles as possible. A composite condition can be also achieved with a randomly rough surface, provided the criterion of (5) is fulfilled. In that case, the droplet is supported by randomly shaped menisci with different areas and capillary pressures, as shown in Figure 9.

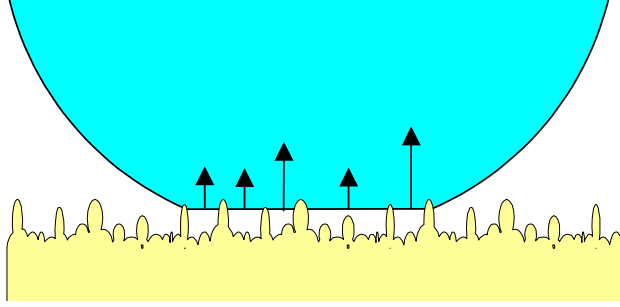


Figure 9. Droplet on a randomly rough superhydrophobic surface.

2.3.1 Equilibrium contact angle

The macroscopic interface between a droplet and a superhydrophobic surface can be considered as a mixture of small areas of solid and air. The macroscopic equilibrium contact angle can then be calculated by averaging water-solid and water-air interfacial tensions, and the resulting equation is known as the Cassie and Baxter equation [50]:

$$\cos \theta_c = f_1 \cos \theta_0 - f_2, \quad (6)$$

where f_1 and f_2 are the fractional areas of solid and air. Because $f_1 + f_2 = 1$, we can write the Cassie and Baxter equation as:

$$\cos \theta_c = f(\cos \theta_0 + 1) - 1, \quad (7)$$

where f is fraction of the original solid material. f can be approximated to be equal to the projected area of the solid-liquid contacts divided by the total projected area of the droplet bottom. Figure 10 shows contact angles calculated from the Cassie and Baxter equation with variable f and θ_0 . It is worth noting that, in order to achieve very high contact angle values such as $> 170^\circ$, the

fractional area of the original material must be less than 2%. Also, with small fractional areas the influence of the Young angle is very small. This means that the choice of hydrophobic material is not very critical. However, because of the critical angle of surface slopes, a material with a high Young angle is favoured.

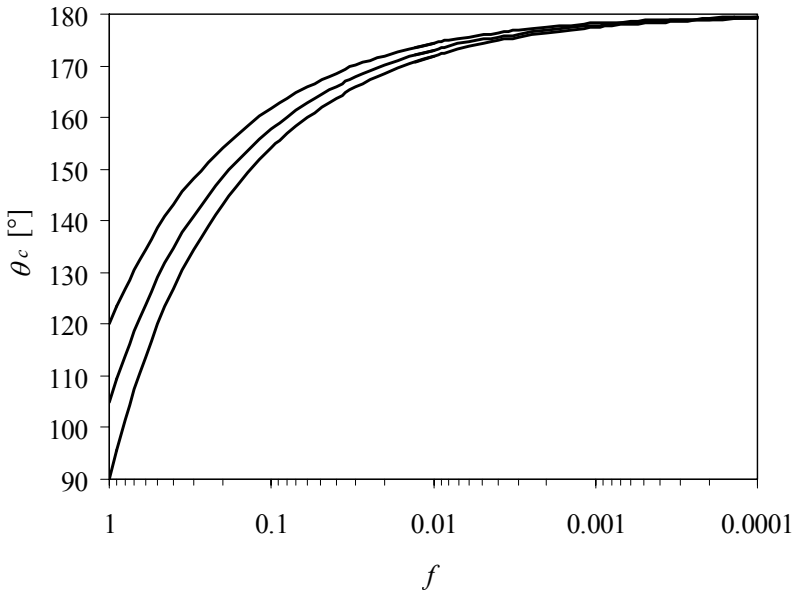


Figure 10. Equilibrium contact angle of a composite surface calculated from the Cassie and Baxter equation (7) with Young contact angles 90° , 105° and 120° .

2.3.2 Hysteresis

Unfortunately, the Cassie and Baxter equation (7) does not give any information on the contact angle hysteresis of a composite surface, which is of utmost importance for droplet mobility. Johnson and Dettre [47] state that the Cassie and Baxter equation gives the contact angle with the lowest possible free energy. Thus the advancing angle may be higher and the receding angle lower than the Cassie and Baxter angle. Johnson and Dettre [47] were able to show only qualitatively that a composite surface has a low hysteresis. Calculation of numerical values is very difficult, because axial symmetry of the geometry is lost, and the vibrational energy of the droplet must be known very accurately.

Despite the large number of papers published recently on superhydrophobic surfaces, theoretical understanding of the hysteresis of composite surfaces has not been developed since the days of Johnson and Dettre. The scientific novelty in most of the papers is only a new fabrication method for producing a suitable roughness.

Some new experimental information on hysteresis can be found in the studies of Bico, Marzolin and Quéré [51] and Öner and McCarthy [45]. They studied composite surfaces with vertical sidewalls and lithographically defined regular patterns. With most of the surfaces, the advancing angle was higher than the value predicted by the Cassie and Baxter equation (7). An important point to note is that contact angle hysteresis is dependent on the geometry of the surface pattern, so that surfaces having the same proportional area but a different pattern showed different hysteresis values. This is understandable, as the energy barriers between metastable states of the droplet contact line are strongly dependent on the microscopic geometry of the contact line. Interestingly, Öner and McCarthy [45] showed that the length scale of the structures (varied between 2 and 32 μm) does not have any effect on hysteresis, as long as the composite condition is maintained, so that water does not penetrate between the structures. When considering model surfaces with grid and pillar patterns (Figure 11), Chen and McCarthy et al. [44] speculate that the grid configuration has much larger hysteresis than the pillars, so that the receding angle of the grid equals that of a smooth surface. However, they do not report any experiments to confirm their theory. Our experiments, which are discussed later in this work, show that the hysteresis of a grid surface is not that bad.

In another paper, Chen, McCarthy et al. [44] showed that a composite surface with random roughness made of submicrometre variable-diameter spherical particles of polytetrafluoroethylene (PTFE) can show high a contact angle (177°) and zero (non-measurable) hysteresis. This is probably the most hydrophobic surface ever reported. Water droplets do not come to rest on a horizontal surface, but "dance around", which indicates that the energy barrier between metastable states of the contact line is lower than the vibration energy of the droplet. In other words, the contact line cannot be stabilised in one position but moves constantly. It is worth mentioning that the same group [44] also demonstrated a smooth surface with nearly zero hysteresis, consisting of a flexible, liquid-like

covalently attached monolayer with rotating groups that prevent the contact line from being stabilised.

2.3.3 Critical pressure

In practice, the equilibrium contact angle of a superhydrophobic composite surface cannot be made equal to 180° . As originally noticed by Dettre, Jackson and Johnson [52], there is a practical limitation to diminishing the fractional area. When the free space between the surface structures is increased, the pressure needed to push the liquid into the hydrophobic capillaries formed by the surface decreases. Simultaneously, the droplet bottom area decreases and the pressure induced on the surface by the droplet mass increases. If the liquid pressure overcomes the capillary pressure, the capillaries will be filled with liquid and the water repellence of the surface will be destroyed.

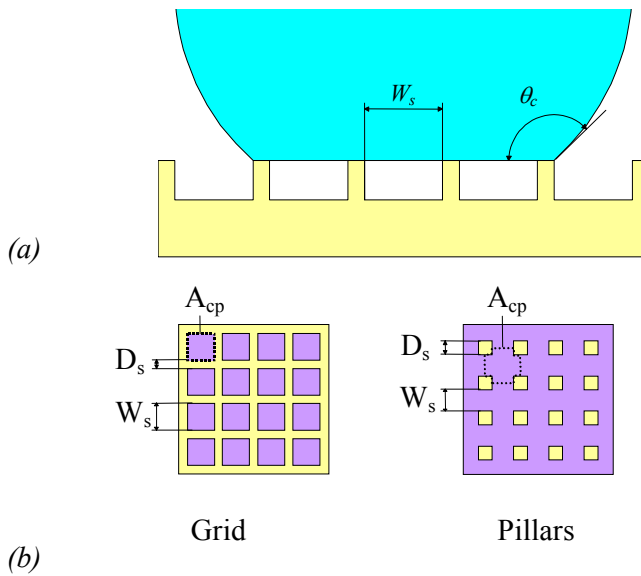


Figure 11. Model surfaces a) cross-section, b) top views.

Let us term the pressure required to wet the superhydrophobic surface the *critical pressure*. In order to consider how the surface dimensions relate to the critical pressure, we use two different model surfaces, shown in Figure 11. Both surfaces are regularly patterned vertically-sloped structures made of

hydrophobic material with an initial contact angle θ_0 . The grid surface consists of a net of square holes of diameter W_s , and spacing D_s . The pillar surface consists of rectangular shaped pillars placed in a rectangular matrix. Theoretical equilibrium contact angles of the model surfaces can be calculated using the Cassie and Baxter equation (7). Figure 12 shows the plot of contact angles as a function of surface dimensions W_s and D_s . The equations are given in Appendix A. One can see that it is easier to obtain high contact angles with a pillar surface than with a grid surface.

The rise of liquid into a *hydrophilic capillary* can be treated by considering a column of liquid to be hanging from the capillary walls so that the weight of the column equals the vertical component of the surface tension multiplied by the circumference of the capillary cross-section [53]. The pressure that drives liquid into the capillary is then

$$P_{cp} = \lambda_{lv} \cos \theta_0 \frac{L_{cp}}{A_{cp}}, \quad (8)$$

where L_{cp} is the perimeter and A_{cp} the cross-sectional area of the capillary. If the capillary is made of hydrophobic material, with $\theta_0 > 90^\circ$, the capillary pressure assumes a negative value. This means that in a *hydrophobic capillary* the capillary pressure drives the liquid in the opposite direction, out of the capillary. Respectively, this force must be exceeded to push liquid into the hydrophobic capillary. The model surfaces consist of a large amounts of small identical elementary hydrophobic capillaries. The *critical pressure* of the surface is then given as the negative value of the capillary pressure of an elementary capillary:

$$P_c = -\lambda_{lv} \cos \theta_0 \frac{L_{cp}}{A_{cp}}. \quad (9)$$

As shown in Appendix A, for the grid surface the critical pressure can be written as follows:

$$P_{c,grid} = \lambda_{lv} \cos \theta_0 \frac{4}{D_s} \left(1 - \frac{1}{\sqrt{1-f}} \right). \quad (10)$$

Appendix A also shows that the result is the same for a hexagonal grid (honeycomb). A net of circular holes results in a lower critical pressure if the equilibrium contact angle is the same. It is probable that for all regularly shaped nets consisting of lines with constant width D_s , the critical pressure can be written as in equation (10). For the pillar surface the critical pressure is (Appendix A):

$$P_{c,pillars} = \lambda_{lv} \cos \theta_0 \frac{4}{D_s \left(1 - \frac{1}{f} \right)}. \quad (11)$$

Appendix A shows that the result is identical also for circular pillars in a rectangular and a hexagonal matrix. The pillar pattern results in a higher critical pressure than does the grid. With a given value of f , the critical pressure of the pillar surface is slightly more than twice the critical pressure of the grid surface. Also a combination of grid and pillar surfaces is analysed in Appendix A. It has a critical pressure which is exactly half of the value of the pillar surface. Figure 13 is a graphical presentation of equations (10) and (11).

The minimum requirement for a superhydrophobic surface is that the critical pressure must be larger than the pressure induced by the droplet mass. This is, however, difficult to calculate exactly, as the droplet contact area is widened due to gravity with large contact angles. Some estimates can still be made. Let us take a surface that has $\theta_0 = 100^\circ$ and $f = 0.01$, which equals a contact angle of around 173° . A droplet with a diameter of 2 mm then causes maximally around 900 Pa pressure on the surface. According to equations (10) and (11), the grid surface must have $D_s < 0.3 \mu\text{m}$, and the pillar surface $D_s < 0.6 \mu\text{m}$. Fabrication of such surfaces is possible, but a demanding task using standard UV lithography.

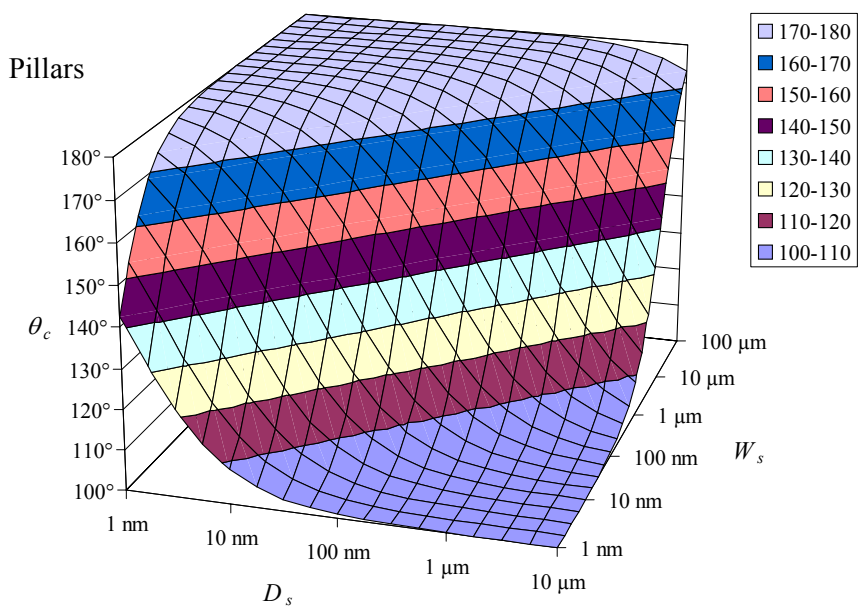
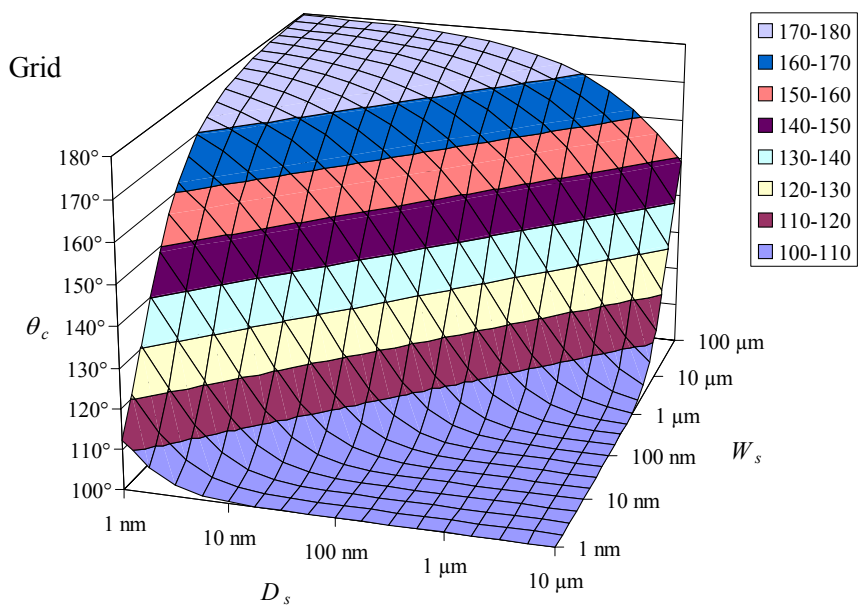
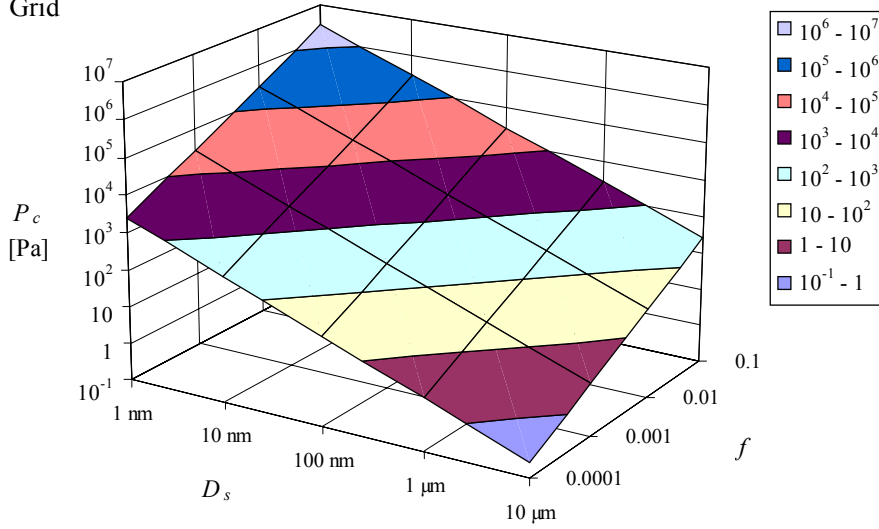


Figure 12. Theoretical contact angles of grid and square pillars in a rectangular matrix as a function of surface pattern dimensions. Initial contact angle of the surface material is 100°.

Grid



Pillars

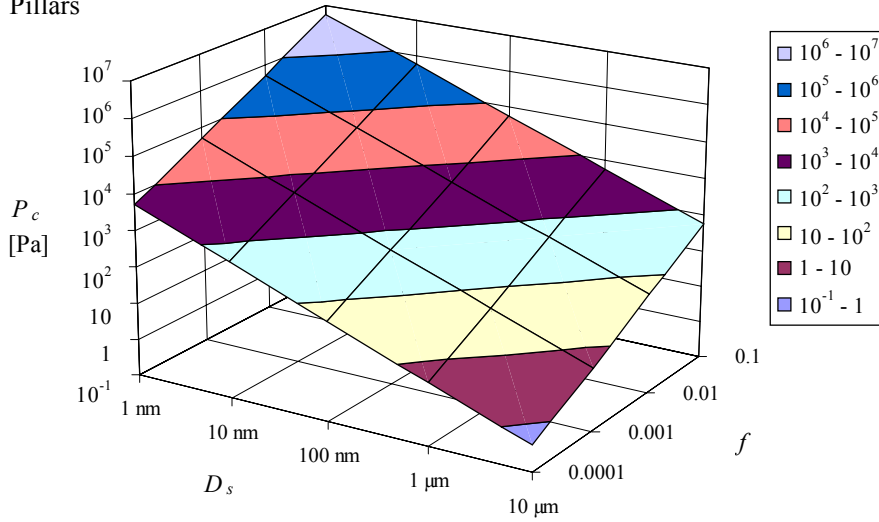


Figure 13. Calculated critical pressures of model surfaces with initial contact angle of 100° .

With randomly rough composite surfaces, the exact value for a critical pressure cannot be given. As shown in Figure 9, the droplet-surface interface on a randomly rough surface consists of small liquid membranes with different sizes and different critical pressures. When the external pressure is increased, the larger air cavities fill with water before the smaller ones. This means that the superhydrophobic properties of a randomly rough surface collapse gradually, in contrast to the sudden collapse of regularly patterned surfaces. If it is assumed that randomly rough surfaces are composed of a large number of randomly-shaped and -sized pillars and grids, the surface shows some distribution of critical pressures. Then the critical pressure of the randomly rough surface could be defined as the average of the distribution. However, this kind of mathematical approach is not very convenient, since the distribution cannot easily be measured. It is more reasonable to take the critical pressure of a randomly rough surface as a pressure that leads to severe degradation of hydrophobic properties of the surface. What is severe depends on the application. In droplet actuation it can be defined as the sliding resistance increasing so much that actuation is no longer possible. Whatever the exact definition, it can be expected that the critical pressure is inversely proportional to the characteristic surface dimensions, also in the case of randomly rough surfaces.

2.3.4 Fabrication of superhydrophobic surfaces

Fabrication of a superhydrophobic surface is in principle very simple. It consists merely of a low energy surface with suitable roughness. The roughness must fulfil the slope criteria, which is related to the Young contact angle of the low energy surface according to equation (5). In practice, there are many possibilities to fabricate such a surface. A review of the subject [43] reveals a wide variety of methods for producing roughness. They include the addition of fillers (silica particles, PTFE particles, glass beads), etching (randomly or using a lithographically defined pattern), sputtering, plasma polymerisation, simultaneous plating with fluoride particles, wax solidification, anode oxidation of metal, solution-precipitation reaction in hot water, chemical vapour deposition (CVD), addition of sublimation material, phase separation, and moulding. It should be stressed, however, that it is not clear from all papers whether the roughness really fulfils the criterion of equation (5), as the contact angle hysteresis or slide angle data is missing. Also the low energy surface can be

produced with various methods such as coating, mixing or polymerising of various materials, such as fluoroalkylsilanes, fluoropolymers, organic polymers, wax, and other fluorine compounds. The references to individual experiments can be found elsewhere [43].

2.3.5 Droplet motion on superhydrophobic surfaces

An interesting question regarding droplet actuation is how the droplets move along the surface. This has been of physical interest, and it has been shown that instead of sliding, droplets move by rolling along a superhydrophobic surface [54]. The maximum speed of the droplet is then limited by viscous forces, which leads to the paradoxical behaviour of small droplets moving faster than larger ones [54, 55].

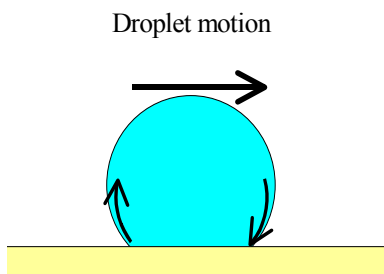


Figure 14. Internal flows of a droplet sliding along a surface.

However, it is risky to describe liquid motion in the same mechanical terms as for solid objects. The question arises as to what is really meant by droplets moving by ‘sliding’ or ‘rolling’. Pure sliding reminds a condition in which all liquid molecules on the solid-liquid interface are able to move in the direction of movement. However, it is commonly known that a laminar flow has zero speed at the solid-liquid interface, and a lot of energy is needed to overcome this so called non-slip condition. This means that pure sliding does not occur in normal conditions, but the droplet moves like a caterpillar tread, with a new interface being formed at the advancing edge while the old interface is dissembled at the receding edge. This kind of motion means that there are circulating liquid flows inside the droplet, as shown in Figure 14. Anderson et al. [56] showed with dyed water that similar internal circulating flows are generated also in a liquid plug

which moves in a tube. Thus there seem to be no fundamental differences between so-called sliding and rolling motions of a droplet. We can assume that the sliding force given in equation (3) also governs droplet motion on superhydrophobic surfaces. We also performed experimental analyses of the droplet motion during actuation; this is discussed in the experimental section of this work.

2.3.6 Superhydrophobic surfaces in droplet actuation

In the case of droplet actuation on superhydrophobic surfaces, the surface structures must withstand both gravity-induced pressure and vertical electrostatic pressure. Assuming that the electric field below the droplet is uniform, we can write the electrostatic pressure acting on the liquid membranes as

$$P_e = \frac{1}{2} \frac{\varepsilon_0 \varepsilon_r U^2}{d^2}. \quad (12)$$

where ε_0 is permittivity of the vacuum, U is voltage between the droplet and the electrode, and d and ε_r are the thickness and effective permittivity of the layer between the droplet and the electrode. P_e is strongly dependent on d and U . For order of magnitude calculations, it can be assumed that droplet actuation requires 250 V, which was a typical value in our experiments. If $\varepsilon_r = 3$, and $d = 5 \mu\text{m}$, one gets $P_e = 3 \times 10^4 \text{ Pa}$, and in order to endure such a pressure, a composite surface with $f = 0.01$ (contact angle $> 170^\circ$) must have characteristic dimensions of the order of nanometres. On the other hand, it was noticed in the experiments that droplet actuation is possible on surfaces which have $d = 70 \mu\text{m}$, and f of the order of 0.1 (contact angle of the order of $150\text{--}160^\circ$). With these values $P_e = 170 \text{ Pa}$ and the minimum critical dimension is of the order of several tens of micrometres. Thus it should be possible to use lithographic patterning to produce surfaces which can be used for droplet actuation in suitable conditions.

It can be concluded that when superhydrophobic surfaces are applied for droplet actuation, the critical pressure is of utmost importance because it limits the electric field which can be applied. When comparing the model surface geometries in Figure 11, one could conclude that a pillar surface is a better configuration in droplet actuation, because it has twice the critical pressure. On

the other hand, the grid surface is interesting in that air presumably cannot escape from the droplet-surface interface as easily as with a pillar surface, because the grid surface forms closed cavities. The cavities can be considered as gas springs that give rise to the critical pressure. Another thing that matters is of course the contact angle hysteresis, which depends on the surface pattern. Unfortunately there is no simple theory that could be used to predict the contact angle hysteresis for a given surface pattern, or to optimise the surface pattern to minimise the hysteresis. Since there is no theory that is good enough, the selection of a good superhydrophobic surface for droplet actuation must be done experimentally. On the other hand, there are some guidelines that should be followed. As mentioned in the previous section, the characteristic surface dimension should be small enough to ensure a high critical pressure. Another boundary condition is that the fabrication must include deposition of a uniform and relatively thin layer on top of the electrode and insulator layers. We tested several methods to produce a superhydrophobic layer suitable for droplet actuation. The experiments and results are reported later in this work.

In the literature two examples were found of superhydrophobic-type surfaces being combined with droplet actuation. Washizu [20] tried unsuccessfully to reduce the droplet sliding force and actuation voltage with vertically patterned surfaces. He speculates that the covering of the surface patterns with a hydrophobic layer was not good enough. The author of this work also considers it possible that the critical pressure was in fact exceeded. Recently, W. Shen J. and C.-J. Kim [57] used a line-patterned composite surface in another type of droplet actuation, and showed that the droplet sliding force and actuation voltages can be reduced considerably compared with the original smooth surface. The system of this experiment was used for electrical switching, and consisted of a mercury droplet that was actuated using side or top electrodes. Thus there is no electrostatic pressure against the surface. It should be noted that this system cannot be used for lab-on-a-chip purposes, as the electrode configuration does not allow long journeys of the droplet.

3. Theory and modelling of droplet actuation

Existing papers on electrostatic droplet actuation concentrate mainly on experimental results and give very little analysis of the physical mechanisms of actuation. Washizu [20] simulated 2-dimensionally the Maxwell stress (electrostatic pressure) at the droplet surface, but did not make any force calculations or detailed analysis. Recently, Ren et al. [36] published an analysis of dissipation mechanisms of droplet actuation in silicone oil, but the results are not directly applicable in this work due to different actuator structure. Batchelder [22] explained the actuation in terms of *dielectrophoresis*, which means motion of neutral matter caused by polarisation effects in a non-uniform electric field. Also Washizu states in his conference paper on electrostatic droplet actuation [20] that the droplets are actuated dielectrophoretically, but he later no longer uses the term in a journal article [21]. Pollack et al. [23, 24] and C.-J. Kim and his co-workers [25, 26, 27] explain the actuation in terms of *electrowetting*, which means charge-induced modification of the surface tension. The variety of terms reveals that current physical understanding of the actuation mechanism is poor. The aim of this section is to study the physics behind the droplet actuation and to determine which phenomena are relevant and which are not. The interactions between the electric field and a water droplet are discussed separately in three domains: liquid bulk, liquid-vapour interface and solid-liquid interface. Based on this knowledge a model that can be used to calculate the actuation force is presented.

3.1 Bulk water – electric field interactions

3.1.1 Electrical properties of liquid water

Water molecules are dipoles, and when an electric field is applied, they become aligned with the field as shown schematically in Figure 15. Thus water is a dielectric material. The basic electrical properties of water are listed elsewhere [58]. At room temperature the relative permittivity of water is around 80 and the time constant for molecular orientation is around 8 ps. When the temperature is varied between 0 and 50°C the permittivity changes from 87.9 to 69.88 and the

time constant from 17.67 to 4.75 ps, respectively. As a function of frequency, the permittivity stays real and constant up to 10 MHz, when the imaginary part of the permittivity begins gradually to increase. The real and imaginary components are equal around 20 GHz frequency. In real water there are also ions and dissolved molecules. However, it can be assumed that small amounts of dissolved molecules do not have a significant influence on the bulk electrical properties of water, and they can be neglected. Because water molecules are dipoles, they are electrically attracted to ions, with the result that ions become surrounded by water molecules. This process is termed *hydration* of ions. Hydration has an important contribution to surface effects, which are considered later in this work. Ionic charges are able to move, and they try to position themselves so as to minimise the electric field inside the water. Thus real water is not a good insulator but is more or less conductive. The relaxation time, meaning the time needed to stabilise the field inside the water, can be calculated from the water conductivity as [59]:

$$\tau = \frac{\epsilon_0 \epsilon_r}{\sigma} . \quad (13)$$

where ϵ_0 is the permittivity of a vacuum, ϵ_r the relative permittivity of water, and σ is the water conductivity. The theoretical limit of ultra pure water at 23°C is 5.48 $\mu\text{S/m}$ (18.2 $\text{M}\Omega\text{cm}$) [60], which gives the relaxation time of 1.3×10^{-4} s. For normal tap water with a conductivity of around 10 mS/m , the time constant is 7×10^{-8} s. It can be concluded that all the electrical time constants are so short that when using DC or low frequency AC fields, the time-dependent effects can be neglected.

It was found that practical liquid water can be considered as lossy dielectric material. However, this definition leads to complicated calculations requiring treatment of complex permittivity. It is therefore useful to treat the water droplet either as a dielectric volume or as a conductive shell. Which one is the better approximation? When considering this question it should be remembered that the relative permittivity of water is very high compared to air or any usual insulator. Thus when a water droplet is placed in an electrostatic field with flux density \mathbf{D} , the electric field intensity inside the water is

$$\mathbf{E} = \frac{\mathbf{D}}{\epsilon_0 \epsilon_r} . \quad (14)$$

This means that the electric field intensity in water is only 1/80 of the value in air, or less than 1/10 of the value in most insulators. On the other hand, inside a perfect conductor the electric field intensity is zero. It can be concluded that when water is in contact with air or low permittivity dielectrics, the difference between treating water as an insulator or a conductor is quite small. Thus either approximation is possible and the best choice between them depends on the situation.

3.1.2 Dielectrophoresis

A bulk effect called *dielectrophoresis* is one of the proposed driving mechanisms in droplet actuation. Figure 15 shows a sketch of a dielectric sphere, like a small water droplet, which has no net charge, placed in a non-uniform electric field. The electrostatic forces acting on oppositely charged sides of the droplet are unequal and there is a net force which moves the droplet towards the field gradient. This phenomenon has been defined by H. A. Pohl as *dielectrophoresis* [61]. The dielectrophoretic force does not depend on the polarity; i.e. if the polarity of the electrodes is changed, the polarity of the droplet is changed respectively, but the net force stays towards the field gradient.

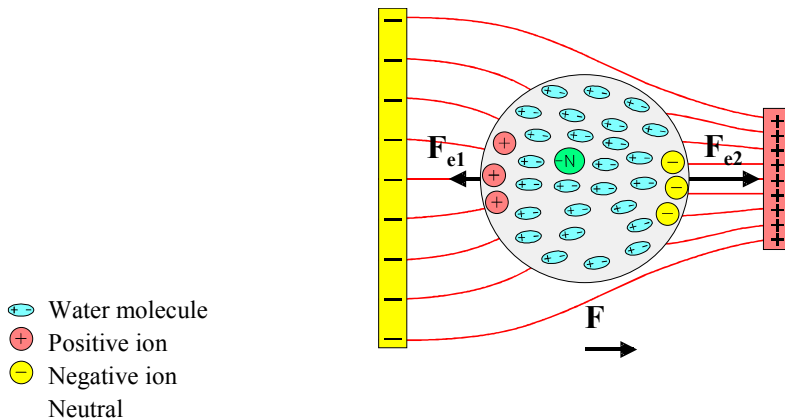


Figure 15. Sketch of a water droplet in a non-uniform electric field. \mathbf{F}_{DEP} is the dielectrophoretic force. Ion hydration is not shown.

However, dielectrophoresis usually deals with small dielectric particles surrounded by fluidic media. Thus severe problems arise if macroscopic droplets on solid surfaces are assumed to be moving according to the same laws. The formulations of the dielectrophoretic force, originally presented by H. A. Pohl [61], are based on the assumption that the moving objects are so small that the gradient of the electric field does not change significantly at the length scale of the particle diameter. Under this condition, the whole particle can be described with a single dipole moment vector. However, the geometry in the case of droplet actuation is very different. The droplets are so large that several electrodes can be located underneath the droplet. The electric field between the energised and grounded electrodes penetrates the droplet in a complex way so that it is wrong to treat the whole droplet with a single dipole moment vector. Thus the basic formulations of dielectrophoretic force cannot be used in droplet actuation. Consequently, without making any force calculations, one may be misled in electrode transport device design if dielectrophoresis is considered as the actuation mechanism, because dielectrophoresis stresses the importance of the electric field gradient as the driving force. For example, we tried to improve the droplet actuation force by making the electrodes as small as possible to increase the electric field gradient. This is, however, completely wrong, as was learned later.

If dielectrophoretic force acting on macroscopic droplets is unreasonable, how about dielectrophoretic force acting on water molecules inside the droplet? Could it be considered to be the driving mechanism for the whole droplet? Some information can be gleaned from the publication of T. B. Jones et al. [29]. They reported dielectrophoretic modification of the water droplet shape and formation of liquid microstructures on a solid hydrophobic surface. Because the cross-sectional geometry of the liquid and the electrodes is quite similar to those used in electrostatic actuation of droplets, some conclusions can be drawn. Figure 16 shows a cross-section of a dielectrophoretically generated water stripe and the equivalent circuit model that takes into account the dielectric nature of water as a capacitor and the conductive nature of water as a resistor. It was found that the presented shape of the water profile is generated only if the electric field intensity in the water is high enough. This depends on the water conductivity and on the frequency of the high voltage fed into the electrodes. With high resistivity ($\sim 1 \text{ M}\Omega$) water, no electric field induced modification on the original droplet shape was noticed below 10 kHz. Using the equivalent circuit model, it

was concluded that for a frequency of less than 30 kHz, virtually the entire voltage drop occurs across the dielectric layer and the water becomes practically an equipotential body with zero field inside. We can assume that this is also the case when DC or low frequency (~ 50 Hz) AC voltages are used for droplet actuation. Without significant electric field in the water there is no significant dielectrophoretic force acting on the water molecules either.

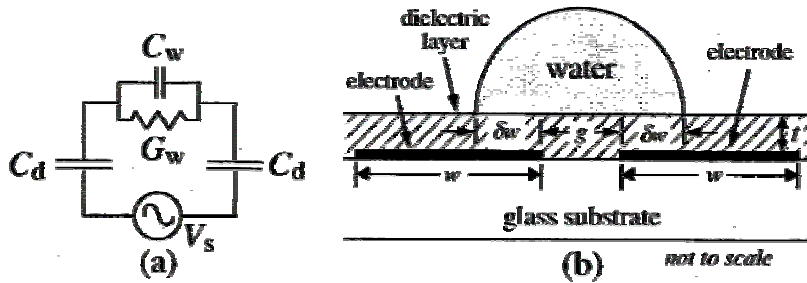


Figure 16. Circuit model (a) and cross-section (b) of a dielectrophoretically generated water stripe. Reprinted with permission from Jones et al. *J. App. Phys.* 89 (2), 2001, 1441–1448 [29]. Copyright © 2001 American Institute of Physics.

We can conclude that the phenomenon called dielectrophoresis concerns only special cases of electromagnetics, and with droplet actuation these special requirements are not fulfilled. Thus dielectrophoresis should not be considered as the driving force in electrostatic droplet actuation. In order to explain the droplet actuation, classical electrostatic theory must be used instead.

3.1.3 Electrostatic force

Generally speaking, there is always a force acting on a body located in an electric field. Physically the electrostatic force originates from Coulomb interaction between charges. Formally, the mechanical forces in electrostatic fields can be considered in two different ways. The first method is based on the law coupling electromagnetic fields to mechanical ones, known as the *Lorentz force law*. In a stationary electrostatic field, the Lorentz force law is

$$\mathbf{f} = \rho_c \mathbf{E}, \quad (15)$$

where \mathbf{f} is the force density (per unit volume), ρ_c is the charge density (per unit volume) and \mathbf{E} is the electric field intensity. A force acting on a body in the electric field can be calculated by integrating the force density over the body volume V . The volume integration can be changed into a surface integral over the body surface S , and after a series of manipulations the electrostatic force is given by [62]

$$\mathbf{F}_e = \int_V \rho_c \mathbf{E} dV = \oint_S \left[\epsilon \mathbf{E} (\mathbf{E} \cdot \mathbf{n}) - \frac{\epsilon}{2} E^2 \mathbf{n} \right] dS, \quad (16)$$

where E is the magnitude of the electric field intensity, ϵ is the permittivity of the media surrounded by the droplet, and \mathbf{n} is the unit vector normal to the surface. The integrand represents the electrostatic pressure on the body surface. It is termed frequently the *Maxwell stress*, and equation (16) has also been referred to as the *Maxwell stress equation*. Because the electrostatic pressure is proportional to the electric field intensity on the surface of the body, there is a force towards where the electric field intensity is greatest. This is actually the definition of dielectrophoresis. Thus, the dielectrophoretic force is only a special case of electrostatic body force which can be considered using the Maxwell stress equation.

The second method to formulate electrostatic force is based on *Thomson's theorem* which says that the energy of the resulting electrostatic field is always a minimum. In order to minimise its energy the electric field tries to modify the geometry of the system, which induces mechanical force. An elementary example of electrostatic force solved in this way is the motion of a dielectric slab partially inserted between the plates of a parallel-plate capacitor, which is discussed in most textbooks on electromagnetics, for example in the works by Cheng and Paris & Kurd [59, 62]. The droplet motion can be explained analogously to this. However, the physical origin of the motion is somewhat different than with the classical example [63], because the droplet is a lossy dielectric body, and as discussed in the previous sections there is no significant electric field inside the droplet. The general definition of the force is a negative

gradient of the work done. In the system of electrodes and a droplet, the work done equals the change in electrostatic energy:

$$\mathbf{F}_e = -\nabla W_e . \quad (17)$$

In electromechanics, this method is also called the *principle of virtual work*. The electrostatic energy can in most cases be expressed using capacitances between the conductors in the system.

In this work we have calculated the electrostatic force acting on the droplet using both of the above methods. In both methods, the electric field around the body must be solved at least once. In the case of droplet actuation, the field is difficult to solve analytically, even in a simplified case, because the geometry contains a mixture of spherical and Cartesian co-ordinates. However, numerical methods such as finite-element (FE) modelling can be used. We have used both 3-dimensional ANSYS® and 2-dimensional Quick Field™ software for the electric field calculations. The same software can be used to calculate the electrostatic force using the Maxwell stress equation. The results of FE analysis are discussed later.

The benefit of the Maxwell stress method is that it gives information on the spatial distribution of the electrostatic pressure on the surface of the droplet. The drawback is that FE calculation has to be used, and it is not possible to take fully into account the surface effects, which are very important. In the method based on Thomson's theorem the spatial information on the electrostatic pressure is lost. However, a significant benefit is that it is possible to build a model for droplet actuation, where the most important surface effects can be taken into account. If the electrostatic energy can be expressed using capacitances that are simple functions of geometrical parameters of the system, the geometrical parameters can be changed and force can be calculated without performing any electric field calculation. Using the above approach, a model was developed where the contact angle of the droplet is free to change due to the so-called electrowetting effect.

3.2 Electrical aspects of the liquid-vapour interface

The electrical properties of the water-vapour interface are not very well known, but some aspects can be found from an article by B. E. Conway [64]. It assumed that there is a small potential drop between bulk and surface because water molecules may have a preferential orientation in the surface. A second reason is that the hydrated ions are surrounded by water molecules and therefore do not want to be located in the surface itself. However, the depth scale of these processes is in angstroms, making them negligible on the droplet scale. The voltage drop at the surface is also very small; in some case a value of about 0.13 V has been derived. This is negligible compared to the voltages used for droplet actuation. We can conclude that sophisticated molecular and ionic phenomena at the liquid-vapour interface can be neglected. Thus the water surface can be assumed to be electrically an ideal conductor with mechanical properties characterised by water surface tension.

3.2.1 Electrostatic pressure in the droplet surface

The electric field can modify the shape of the water surface due to outward electrostatic pressure. Taking the electrostatic pressure-effect into account in droplet actuation would require simultaneous electrical and mechanical field calculation. This is a difficult, although a common problem with MEMS. Nowadays there are commercial MEMS design tools capable of performing coupled electromechanical analysis, at least in some general geometrical cases. However, some estimates of the effect can be made using simple calculations. If we assume that the droplet is conductive, the electric field is perpendicular to the liquid surface. Then, from the Maxwell stress equation (16), the electrostatic pressure at the liquid surface equals $\frac{1}{2}\epsilon E^2$. Surface tension causes inward pressure across a curved liquid surface; this is termed the Laplace pressure [53]. Setting the outward electrostatic pressure equal to the Laplace pressure we get:

$$\frac{1}{2}\epsilon E^2 = \frac{2\gamma_{lv}}{r}, \quad (18)$$

where r is the radius of curvature of the liquid surface. We can solve the threshold field intensity as:

$$E = \sqrt{\frac{4\gamma_{lv}}{\epsilon r}}. \quad (19)$$

Only if the electric field is above the value given in equation (19) can the electric field modify the shape of the droplet surface. In our experiments, the smallest r values were of the order of 0.5 mm, while the upper limit can be assumed to be equal to the capillary length a , which gives the ratio of surface tension and gravitational forces. Capillary length is given by [53]

$$a = \sqrt{\frac{\gamma_{lv}}{\rho_l g}}, \quad (20)$$

where ρ_l is the liquid density and g is the gravitational acceleration, and it equals 2.7 mm for water. Droplets with radius $R > a$ can be considered to be flattened due to gravity [54]. With these values, the threshold electric field is varied between 8.1×10^6 and 3.5×10^6 V/m. It should be noted that these values are of the same order of magnitude as the breakdown field in air, which depends inversely on the air layer thickness, according to Paschen's law. Based on the Paschen curve of air [65], for a droplet with $R = 0.5$ mm the breakdown field is larger than the threshold field of electrostatic pressure effects with air layers thinner than ~ 0.2 mm. With a droplet with $R = a$, the critical thickness is of the order of 3 mm. Thus in our experiments some electrostatic pressure effects can occur before breakdown in air.

3.2.2 Electrohydrodynamic instability

Eventually, if the electric field is increased, the electrostatic pressure overcomes the surface tension and the surface of the liquid becomes unstable with the development of conical protrusions and the ejection of charged drops and ions. This phenomenon, referred to also as electrohydrodynamic (EHD) instability, has found industrial use in electrostatic spraying of liquids [66]. It should be noted that if the threshold field given in equation (19) is exceeded, this does not mean that EHD instabilities begin to occur immediately. As soon as the droplet surface is bent outwards, the radius of curvature is increased, and a larger field is needed for further bending. Only if the surface modification gives a high enough rise to the electrostatic pressure do instabilities become possible. Thus EHD

instabilities are comparable to the pull-in effect in capacitive micromechanical components. EHD instabilities have been analysed in a special case, and the protrusions are referred to as Taylor cones [67] according to the author of the first comprehensive studies on the subject. However, theoretical analysis of EHD instabilities in the case of droplet actuation is very complicated due to complex geometry and is outside the scope of this work.

3.3 Electrical aspects of the solid-liquid interface

3.3.1 Electrical double layer

Electrical properties of the solid-liquid interface are crucial in droplet actuation and therefore we must start the consideration from the molecular level. When a liquid containing free ions is placed in contact with a solid surface, adsorption of ions and water molecules occurs at the solid surface due to the action of short-range van der Waals forces. If a particular ion species is preferentially adsorbed, an *electrical double layer* is formed which consists of a net surface charge bound to the solid together with a region of diffuse counter-charge extending into the liquid, as shown in Figure 17.

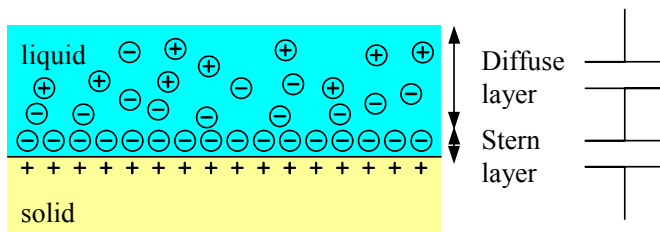


Figure 17. Electrical double layer at solid-liquid interface formed due to adsorption of negative ions.

On electrically charged solid surfaces the double layer is formed because ions of opposite charge are electrically attracted at the surface, while ions having the same sign are repelled away from the surface. The double layer may be formed in water-solid interfaces without any initial charge, too, if ions of another polarity are preferentially adsorbed at the surface. It has been reported that positive ions are usually more hydrated than negative ions and so have a greater

tendency to reside in the bulk aqueous medium [68]. Adsorption of water molecules does not introduce a net surface charge, but may make a significant contribution to the nature of the double layer.

Electrically, the double layer can be presented as a series combination of two parallel-plate capacitors as shown in Figure 17. The lower capacitor represents the so-called Stern layer, which is formed by a single layer of specifically adsorbed ions and water molecules. The thickness of the Stern layer is comparable to the size of the ions at the surface, and values between one [69] and five [68] angstroms have been given in the literature. The relative permittivity of the Stern layer is lower than in the bulk liquid due to the orientation of water molecules; values between 5 and 10 have been estimated [68]. The potential of the diffuse layer decays as a function of thickness at a rate dependent on the ionic concentration of the liquid. The effective thickness of the diffuse layer is defined as the Debye length, $1/\kappa$, where [68]

$$\kappa = \sqrt{\frac{2q^2n}{\epsilon KT}} . \quad (21)$$

q is the elementary charge, n is the concentration of (positive or negative) ions in the liquid, ϵ is the permittivity of the liquid, K is Boltzmann's constant and T is temperature. We notice that the Debye length decreases as a function of ion concentration. Thus we can estimate the maximum thickness of the diffuse layer to be found in deionised water, which contains only H^+ and OH^- ions. At room temperature the ion product of water is of the order of 10^{-14} mol/kg [58], which equals an ionic concentration of $n = 6 \times 10^{19}$ 1/m³. Substituting this into equation (21) gives the Debye length of 0.97 μm . The total capacitance density of the double layer is:

$$c_{dl} = \frac{1}{\frac{d_{Stern}}{\epsilon_{Stern}} + \frac{d_{diff}}{\epsilon_{diff}}} , \quad (22)$$

where d_{Stern} , ϵ_{Stern} , d_{diff} and ϵ_{diff} are thicknesses and permittivities of the Stern and diffuse layer, respectively. Substituting 5 Å for d_{Stern} , 5 for ϵ_{Stern} , 0.97 μm for d_{diff}

and 80 for ϵ_{diff} , we get $c_{dl} = 7.24 \times 10^{-4} \text{ F/m}^2$. The values for d_{Stern} and ϵ_{Stern} were selected to give the minimum estimate for the double layer capacitance density.

The contribution of double layer capacitance in droplet actuation is assumed to be largest when a smooth hydrophobic surface is used. With superhydrophobic surfaces, the proportional area of the water-solid interface is much smaller because of the large portion of air between the droplet and the surface. In the case of a smooth hydrophobic surface, the double layer and the insulator capacitance are in a serial combination. Thus the double layer has maximal contribution to electric fields when the capacitance of the double layer is smallest and the insulator capacitance is greatest. The thinnest electrode insulator used in our experiments was $2 \mu\text{m}$ silicon dioxide with a permittivity of 3.9. This gives a capacitance density of $1.72 \times 10^{-5} \text{ F/m}^2$, which is 2% of the minimum value of the double layer capacitance. Thus the voltage drop across the double layer is very small and can be neglected, at least in model calculations. It should be noted, however, that if up to 2% of the voltages used in droplet actuation appear across the double layer, the so-called Debye-Hückel approximation for the diffuse layer is no longer valid and the effective thickness of the double layer cannot be expressed using equation (21). On the other hand, the potential decay is then predicted to decrease at a greater than exponential rate [68], which leads to larger diffuse layer capacitance and smaller contribution of the double layer.

3.3.2 Electrowetting

As electric field is applied between droplet and electrode, the electrostatic forces acting on the ions in the liquid can be observed as a reduction of the contact angle between solid and liquid as shown in Figure 18. The phenomenon is termed *electrowetting* and it is treated as the charge-induced change in the interfacial energy between the solid and liquid. Electrowetting has a contribution in droplet actuation and has even been proposed as the actual driving mechanism by Pollack et al. [23, 24] and Lee et al. [25]. In this section, we introduce the phenomenon and, because it is somewhat unknown, some literature and applications of the phenomenon as well. In the next section we consider the electrowetting equation with a superhydrophobic surface and later, in the section on charging effects, we discuss the role of surface charging in electrowetting.

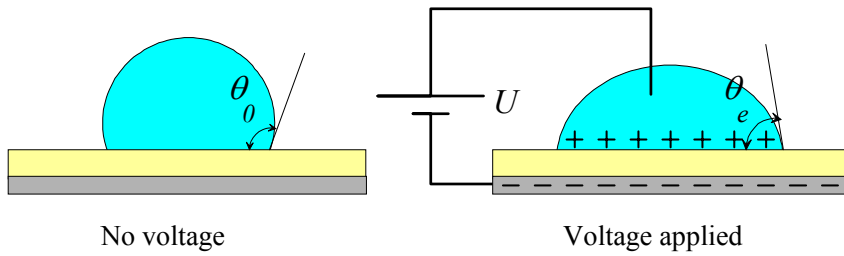


Figure 18. The electrowetting effect.

It is well known that electrical phenomena have an effect on interfacial tensions [53]. The first comprehensive investigations were made by G. Lippman in 1875. He studied liquid mercury-electrolyte interfaces and found that the external voltage changes the charge of the double layer and thus the interfacial tension. In Lippmann's apparatus the interfacial tension was observed by capillary rise, and the phenomenon was therefore referred to as electrocapillarity. Later, the electrical modulation of the contact angle was observed on insulating polymer surfaces, for example by Gludleigh in 1976 [94] and by Minnema et al. in 1980 [70], and on solid metal by Geni and Hackwood in 1981 [71, 72], who first termed the phenomenon as electrowetting. The pioneer of the current research on electrowetting is B. Berge, who published his first experiments and analysis of the phenomenon in 1993 [73]. The change in surface tension was observed by a change in the contact angle of a sessile water droplet (Figure 18). Because of the larger charge separation (smaller capacitance density), the required voltages are orders of magnitude larger than with the classical electrocapillarity. Berge's analysis was based on Lippmann's theory, except that the capacitance of the solid-liquid double layer was replaced by the insulator-separated capacitance between droplet and electrode. This is reasonable because the insulator is much thicker than the double layer and major part of the voltage drop appears across the insulator. The liquid-air interface was neglected by assuming that the capacitance is a parallel-plate capacitor with an area equal to the solid-liquid area. As a result, the equation governing the apparent contact angle θ_e under applied voltage U can be written as:

$$\cos\theta_e = \cos\theta_0 + \frac{1}{2} \frac{\varepsilon_0 \varepsilon_r}{d\gamma_{lv}} U^2, \quad (23)$$

where θ_e is the initial (Young) contact angle, d is the insulator thickness and ε_0 and ε_r are the permittivities of the vacuum and insulator, respectively. It can be seen that the electrowetting decreases the contact angle irrespectively of the voltage polarity.

The work of Berge has generated increasing interest on the electrowetting phenomenon and many papers have recently been published; a current review is given by Quillet and Berge [74]. Many applications have been proposed and demonstrated such as display [71, 72], variable focal lens [75, 76], micromotor [77], micropump [78, 79, 80] and droplet-based micro-liquid handling [23, 24, 25]. It is important to note at this point that the works of Pollack [23, 24], J. Lee et al. [25] and especially Kwon and L. Lee [76] give evidence that electrowetting works also without galvanic contact into the liquid. This is why the electrowetting must be considered in electrostatic droplet transport as well.

Regardless of the increased interest in the field, many doubts and questions still surround the phenomenon. Ideally, the contact angle could be reduced down to zero with a high enough voltage. In practice, the contact angle always saturates at some level. The saturation has been attributed to air ionisation [81] and trapping of charge in the surface [82, 83]. Possibly, for the same reasons, the electrowetting effect clearly degrades on some hydrophobic materials. Janocha et al. [82] have studied competitive electrowetting of water and decane and found that the strength of the effect varied greatly with different polymer materials. Also the basic formulation has raised questions. T. Blake et al. [84] have calculated thermodynamically and shown experimentally that the constant of the voltage term in equation (23) should be $1/4$ instead of $1/2$. Digilov [85] has proposed theoretically that the change in contact angle is due to a change in line tension. He also states that the electrowetting effect in a capillary reported by Prins et al. [86] is due to electrostatic force [87]. Also T. Blake has raised the question whether the observed phenomena are generated by a body force rather than a surface effect [88]. The most recent contribution to the discussion, a model that includes the phenomenon, is soon to be proposed by B. Saphiro [89]. In conclusion, there seems to be plenty of room for further research on electrowetting.

3.3.3 Electrowetting on superhydrophobic surfaces

Superhydrophobic surfaces have two special properties that have to be considered with the electrowetting phenomenon. First, due to the large contact angle, the solid-liquid area of a droplet is large. Thus, it cannot be just neglected, like done by Berge in the derivation of the electrowetting equation (23). Secondly, the droplet bottom is not equal to the solid-liquid interface, but it is composed of a large number of small liquid-air and liquid-solid interfaces, which may be irregularly shaped. In this analysis, both of these special properties are taken into account.

Let us start from the Lippmann equation written in a form which states that the reversible work dW associated with changes in area dA and charge dQ is given by [53]:

$$dW = \gamma dA + UdQ, \quad (24)$$

where γ is the surface tension and U is the voltage. The term UdQ equals the change in electrical energy dW_e . After substituting it we can write the surface tension of the charged interface as:

$$\gamma = \frac{dW}{dA} - \frac{dW_e}{dA}. \quad (25)$$

Here the first term is, by definition, equal to the surface tension without an applied field. The second term could be termed electric-field- or charge-induced change in the interfacial tension, as in most papers on electrowetting. However, in this paper the second term is referred to as electric-field induced surface tension. A similar notation has also been used by Verheijen and Prins [83]. From the author's point of view this is logical, as the formulation is equal to normal surface tension except that the mechanical energy is replaced by electrical. Electric-field induced surface tension is also easy to visualise with a vector similar to normal surface tension. Thus the external electric field introduces a new surface tension component which is defined as:

$$\gamma_e = \frac{dW_e}{dA}. \quad (26)$$

Because of the minus sign in equation (25), the electric-field induced surface tension is directed oppositely to the original interfacial tension between solid and liquid.

Let us then consider a conductive droplet on an insulating superhydrophobic surface which has a metal electrode underneath (Figure 19). We neglect the gravitational effects and assume the shape of the droplet to be like the cap of a sphere. The electric field is arranged between the droplet and the electrode so that the water surface and electrode are oppositely charged. The charge can be generated by applying a metal contact into the droplet or using non-contact electrodes so that the droplet becomes capacitively charged. Because superhydrophobic surfaces exhibit very large contact angles, the liquid-air area has to be taken into account. We do not yet take into account the special surface structure of the surface, but consider the droplet bottom to be an effective solid-liquid interface A'_{sl} , which consists of a large number of small liquid-air and liquid-solid interfaces. In the contact line of the droplet there are two electric-field induced surface tensions. γ'_{esl} is associated with the effective solid-liquid interface and γ_{elv} with the liquid-vapour (air) interface. They can be calculated according to the definition given in equation (26) as

$$\gamma'_{esl} = \frac{dW_e}{dA'_{sl}} \quad (27)$$

$$\gamma_{elv} = \frac{dW_e}{dA_{lv}}. \quad (28)$$

where A'_{sl} and A_{lv} are the areas of effective solid-liquid and real liquid-vapour interfaces. The electrostatic energy W_e is stored in the capacitance C_d between the droplet and the electrode.

$$W_e = \frac{1}{2} C_d U_d^2, \quad (29)$$

where U_d is the voltage between the droplet and the electrode. We get:

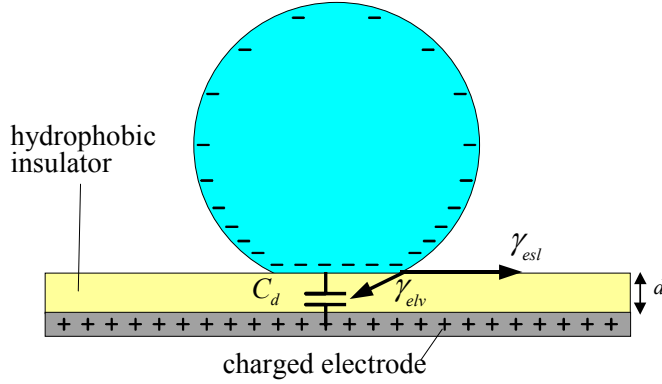


Figure 19. Electric field induced surface tensions acting on the contact line between a droplet and a superhydrophobic surface.

$$\gamma'_{esl} = \frac{U_d^2}{2} \frac{dC_d}{dA'_{sl}} \quad (30)$$

$$\gamma_{elv} = \frac{U_d^2}{2} \frac{dC_d}{dA_{lv}}. \quad (31)$$

We cannot estimate the capacitance C_d equal to the parallel plate capacitance with an area equal to the effective solid-liquid area. Therefore a more precise approximative formula for C_d is derived in Appendix B:

$$C_d \approx \frac{\varepsilon_0 \varepsilon_r \pi}{d} \left[R_c^2 + \frac{3.7}{\varepsilon_r^{0.57}} R_b^2 \left(\frac{d}{R_b} \right)^{0.734 \varepsilon_r^{0.085}} \right]. \quad (32)$$

where R_c is the radius of the solid-liquid contact area, R_b is the radius of a ball which has the same volume as the droplet, ε_r and d are the permittivity and thickness of the insulator. The effect of trapped air of superhydrophobic surfaces can be taken into account by considering ε_r as an effective value that depends on the surface structure and air content. On the other hand, the trapped air layer is usually much thinner than the insulator, thus its effect is very small. After rearranging and substituting $\pi R_c^2 = A'_{sl}$ we get:

$$C_d \approx \frac{\varepsilon_0 \varepsilon_r A'_{sl}}{d} + \frac{3.7\pi \varepsilon_0 \varepsilon_r^{0.43}}{d} R_b^2 \left(\frac{d}{R_b} \right)^{0.734 \varepsilon_r^{0.085}}. \quad (33)$$

Now it is important to note that the first part of the expression of C_d is equal to the parallel-plate capacitance between the effective solid-liquid contact area and the electrode. Thus the second part is the capacitance between the liquid-vapour area and the electrode. The second part depends only on the droplet volume but not on the contact angle. Thus, the derivative of the right part with respect to A_{lv} is zero. We get:

$$\gamma'_{est} = \frac{1}{2} \frac{\varepsilon_0 \varepsilon_r U_d^2}{d} \quad (34)$$

$$\gamma_{elv} = 0. \quad (35)$$

Surprisingly, the result is that the liquid-vapour interface can be ignored also with high contact angles. Not because it would be insignificant but because its contribution is (approximately) zero. Verheijen and Prins [90] have drawn the same conclusion for droplets with lower contact angles. They report that the contribution of the liquid-vapour interface to the capacitance between the droplet and electrode varies between 1% and 3% when the contact angle is between 90 and 120°. In another paper [83], the same authors have derived the electrowetting equation using differential free energy of the system and concluded that the liquid-vapour interface can be neglected because it makes a constant contribution to the free energy.

Next we take the trapped air into account by treating the superhydrophobic surface as a heterogeneous surface, which consists of solid and air. The proportional areas of solid and air are f and $1-f$, respectively. The surface tensions in the contact line between droplet and the surface are presented in Figure 20. The change in the apparent contact angle can be calculated by introducing the electric-field induced surface tension into the force balance equation of the droplet bottom perimeter line. Because the electric-field induced surface tension is effective only in the solid-liquid interface, γ'_{est} must be multiplied by f .

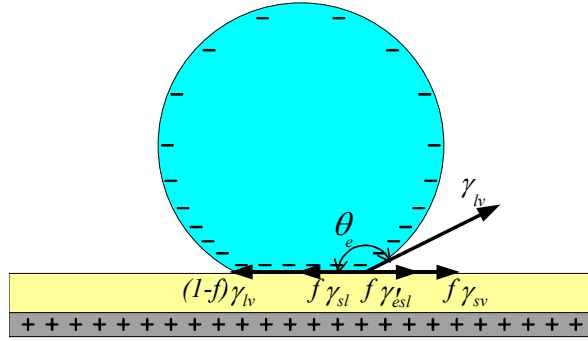


Figure 20. Interfacial tensions at the bottom of a droplet placed on a heterogeneous surface under an electric field.

From Figure 20 we obtain the following force balance equation:

$$\gamma_{lv} \cos \theta_e + (1-f)\gamma_{lv} + f\gamma_{sl} = f\gamma_{sv} + f\gamma'_{esl}, \quad (36)$$

where θ_e is the electric-field induced contact angle. After rearrangement we get:

$$\cos \theta_e = f \frac{\gamma_{sv} - \gamma_{sl}}{\gamma_{lv}} + f - 1 + \frac{f\gamma'_{esl}}{\gamma_{lv}}. \quad (37)$$

Substituting the Young equation (1) we get:

$$\cos \theta_e = f \cos \theta_0 + f - 1 + \frac{f\gamma'_{esl}}{\gamma_{lv}}. \quad (38)$$

Substituting the Cassie and Baxter equation (7) and γ'_{esl} from equation (34) we can write the contact angle as

$$\cos \theta_e = \cos \theta_c + \frac{1}{2} f \frac{\epsilon_0 \epsilon_r U_d^2}{d\gamma_{lv}}. \quad (39)$$

It can be seen that equation (39) is otherwise identical to equation (23) derived by Berge, but that the Young angle has been replaced by the initial contact angle of the superhydrophobic surface, and there is the fractional area f in the voltage

term. Because $f \ll 1$, the electrowetting effect is much weaker on superhydrophobic surfaces than on normal surfaces.

Equation (39) governs only the horizontal motion of the droplet contact line, but with superhydrophobic surfaces the vertical motion of the three-phase contact lines in the surface fine structures should also be considered. Figure 21 shows a cross-section of a single elementary capillary on a superhydrophobic surface, magnified enough to show the microscopic radius of curvature, which is always present on the structure corners. It is assumed that the dimensions of the capillary are much smaller than the droplet diameter, and that the effect of hydrostatic pressure is negligible, so that the liquid membrane formed by the capillary is planar. With no applied electric field, the contact angle between water and capillary walls can be assumed to be equal to the Young angle, and the position of the liquid membrane depends on the radius of curvature of the surface structures, as shown in Figure 21.

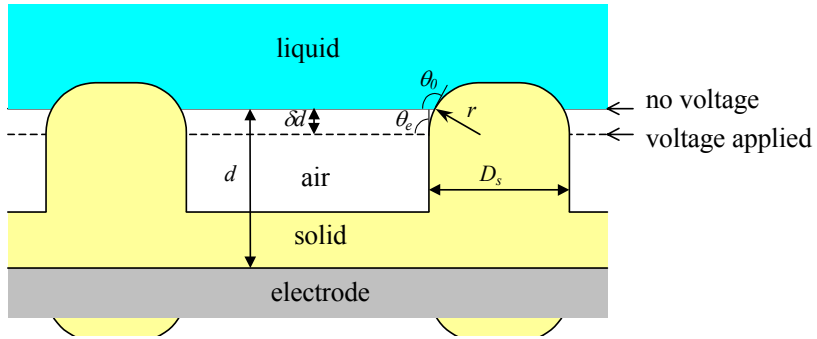


Figure 21. The vertical electrowetting effect in hydrophobic surface structures.

When voltage is applied between the droplet and the electrode, the electrowetting effect reduces the contact angle, and because of the surface structure curvature, the liquid membrane must move vertically by an amount δd to find a new equilibrium position. This changes the solid-liquid area approximately by

$$\delta A_{sl} = -L_{cp} \delta d , \quad (40)$$

where L_{cp} is the perimeter of the elementary capillary. The elementary capillary forms a capacitor C_{cp} between the electrode and the liquid membrane, which can be approximated as a parallel plate capacitor:

$$C_{cp} = \frac{\varepsilon_0 \varepsilon_r A_{cp}}{d}, \quad (41)$$

where A_{cp} is the area of the elementary capillary and ε_r is the (effective) permittivity between electrode and insulator. When the position of the liquid membrane changes, the capacitance changes by

$$\delta C_{cp} = -\frac{\varepsilon_0 \varepsilon_r A_{cp}}{d^2} \delta d, \quad (42)$$

and the electrostatic energy stored in the capacitance C_{cp} changes by

$$\delta W_e = -\frac{1}{2} \frac{\varepsilon_0 \varepsilon_r A_{cp} U^2}{d^2} \delta d. \quad (43)$$

The electric-field induced surface tension in the three-phase contact line between the liquid membrane and capillary wall can be calculated from equation (27), and after inserting equations (43) and (40) we get

$$\gamma_e = \frac{\delta W_e}{\delta A_{sl}} = \frac{1}{2} \frac{\varepsilon_0 \varepsilon_r U^2 A_{cp}}{d^2 L_{cp}}. \quad (44)$$

The electric-field induced contact angle in the liquid membrane is then

$$\cos \theta_e = \cos \theta_0 + \frac{1}{2} \frac{\varepsilon_0 \varepsilon_r U^2 A_{cp}}{d^2 \gamma_{lv} L_{cp}}. \quad (45)$$

Using equations (10) and (11), we can write equation (45) for the model surfaces of Figure 11. In the case of the pillar surface, we get:

$$\cos \theta_e = \cos \theta_0 + \frac{1}{2} \frac{\varepsilon_0 \varepsilon_r U^2}{d^2 \gamma_{lv}} \frac{D_s}{4} \left(\frac{1}{f} - 1 \right), \quad (46)$$

and in the case of the grid surface:

$$\cos \theta_e = \cos \theta_0 + \frac{1}{2} \frac{\varepsilon_0 \varepsilon_r U^2}{d^2 \gamma_{lv}} \frac{D_s}{4} \left(\frac{1}{\frac{1}{\sqrt{1-f}} - 1} \right). \quad (47)$$

If the contact angle between the liquid membrane and capillary walls falls below 90° , the capillaries will be filled with liquid due to capillary force and the superhydrophobic surface is wetted. The critical condition is achieved with

$$\cos \theta_0 + \frac{1}{2} \frac{\varepsilon_0 \varepsilon_r U^2 A_{cp}}{d^2 \gamma_{lv} L_{cp}} = 0. \quad (48)$$

This can be rearranged to give

$$\frac{1}{2} \frac{\varepsilon_0 \varepsilon_r U^2}{d^2} = -\gamma_{lv} \cos \theta_0 \frac{L_{cp}}{A_{cp}}. \quad (49)$$

As can be seen, the left side of equation is equal to the vertical electrostatic pressure acting on the liquid membrane, and the right side is equal to the critical pressure of the elementary capillary, given in equation (9). This means that the electric-field induced modification of liquid membranes equals the motion of liquid due to electrostatic pressure.

Now we have calculated the contact angle change as a function of voltage both with liquid membranes and with the whole droplet. Next, we estimate the ratio of the effects. A superhydrophobic surface with Young angle 105° , and apparent contact angle 170° has a proportional area f of around 0.02. Using the value $1 \mu\text{m}$ for the characteristic surface dimension D_s , we can calculate from equations (39), (46) and (47) that with the pillar surface the contact angle at the liquid membranes changes more than the apparent contact angle of the droplet, if the

insulator thickness $d < 0.6$ mm with the pillar surface, or if $d < 1.2$ mm with the grid surface. Thus the vertical electrowetting effect (electrostatic pressure) is more effective in droplet actuation than the apparent contact angle change.

The vertical motion also slightly changes the liquid-vapour area of the liquid membrane, which changes the apparent contact angle of the droplet according to the Cassie and Baxter equation (7). Next we estimate this effect. For simplicity, we assume that the surface structures are circular pillars in a rectangular matrix. The area change is largest when the profile of the surface tips is hemispherical, which means that $r = D_s/2$ in Figure 21. Then, the proportional area f changes by

$$\Delta f = \frac{\pi \left(\frac{D_s}{2} \right)^2 - \pi \left[\frac{D_s}{2} \cos(\theta_0 - \theta_e) \right]^2}{\pi \left(\frac{D_s}{2} \right)^2} = 1 - \cos^2(\theta_0 - \theta_e), \quad (50)$$

when the contact angle between the liquid membrane and surface structures changes from θ_0 to θ_e . Because the largest reported Young angle is 119° [40], the maximum possible change in the contact angle is around 30° . Substituting this for $\theta_0 - \theta_e$ in equation (50) we get $\Delta f = 25\%$. From the Cassie and Baxter equation (7) we can calculate that for a superhydrophobic surface with Young angle 105° and apparent contact angle 170° an increase of proportional area by 25% (from 0.02 to 0.025) reduces the contact angle by only 1° . Thus, depending on the surface geometry, the apparent contact angle changes somewhat more than predicted in equation (39).

As a conclusion, the electrowetting effect on superhydrophobic surfaces is much smaller than with normal hydrophobic surfaces. The maximum contact angle change is also limited by the critical pressure of the surface. Until that limit is reached, the apparent contact angle as a function of voltage is given approximately by equation (39).

3.3.4 Alternative solution for the electrowetting equation

It was noticed that in the case of liquid membranes between surface structures, the electrowetting effect is equal to the electrostatic force (pressure). As pointed out by R. Digilov [87], the same holds true for electric-field induced liquid rise in a capillary. As a matter of fact, it is rather simple to show that also in the classical electrowetting experiment, the motion of the three-phase contact line is due to electrostatic force. Let us consider a portion of the line with length l , shown in Figure 22.

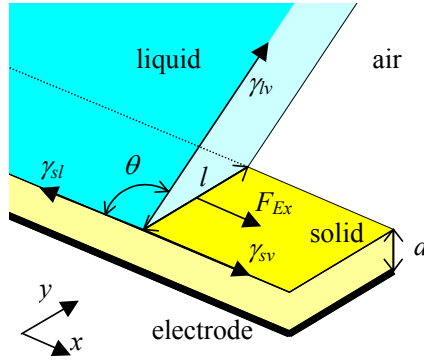


Figure 22. Electrostatic force induced motion of a three-phase contact line.

If there is voltage U between the liquid and the electrode, the absolute value of the horizontal electrostatic force acting on the liquid front is

$$F_{Ex} = |-\nabla W_e| = \frac{d}{dx} \left(\frac{1}{2} C U^2 \right) = \frac{d}{dx} \left(\frac{1}{2} \frac{\epsilon x l}{d} U^2 \right) = \frac{1}{2} \frac{\epsilon l}{d} U^2, \quad (51)$$

Where W_e , C , ϵ and d are the electrostatic energy, capacitance, permittivity and vertical distance between liquid and electrode. As explained in section 3.3.3 the capacitance between liquid and electrode can be assumed to be equal to a parallel plate capacitor, because the fringe field in air makes a constant contribution to the electrostatic energy. The force balance for the portion of the contact line equals:

$$l\gamma_{lv} \cos\theta = l\gamma_{sv} - l\gamma_{sl} + F_{Ex}, \quad (52)$$

By inserting equation (51) into (52), we can eliminate l . Then after some rearrangements and using the Young equation (1), we get:

$$\cos \theta = \frac{\gamma_{sv} - \gamma_{sl}}{\gamma_{lv}} + \frac{1}{2} \frac{\varepsilon}{d\gamma_{lv}} U^2 = \cos \theta_0 + \frac{1}{2} \frac{\varepsilon}{d\gamma_{lv}} U^2, \quad (53)$$

which is the well-known electrowetting equation (23).

3.3.5 Liquid contact charging

It is known from various experiments that when an electric field is applied across a solid-liquid interface, the solid surface may become permanently charged. The effect is apparently closely related to the double layer properties, but the physical mechanisms have not been fully explored. Surface charging is very harmful for electrostatic droplet actuation, which means that the charging properties of the hydrophobic surface are equally as important as the hydrophobic properties. Thus it is important to consider the charging phenomenon in detail. Since there is no well-established theory on the phenomenon, we review the most important studies and experiments on the subject.

Unlike particle charging in colloidal suspensions, the charging phenomenon in a three-phase system, such as a droplet and solid, is a little-studied subject. In the early 1970s the phenomenon was studied for use in electrostatic recording and electret production [91, 92, 93, 94]. The work was motivated by observations that the stability of the resulting charge can be surprisingly good. Englebrecht [93] found that the traces recorded with electrified water contact on PET (polyethylene terephthalate, Mylar™) surfaces were stored with no apparent degradation for more than 500 h. In another study by Chudleigh [92], decay time constants over 20 years were measured in the laboratory atmosphere for FEP (polyfluoroethylene-propylene) foils initially charged to 500V with ethyl alcohol contacts. Liquid contact charging has also been studied in the petroleum industry. The low conductivity of fuels enables considerable charging, which, together with high flammability, leads to risk of sparking and explosions. For example, in 1969 three supertankers exploded during washing operations [95]. Later, surface charging due to deionised water was studied because of the risk of

charge-induced device failure of MOS devices in the semiconductor industry [60, 96]. Recently, the liquid-surface charging phenomenon has been considered in the context of the electrowetting phenomenon [82, 83].

The charging aspects are poorly discussed in existing articles on droplet actuation. It has been reported in the dissertation by Pollack [24] that insulator degradation is a serious stability problem, and one symptom was referred to as surface energy variations of the hydrophobic surface, which caused unwanted droplet motion towards preferred locations. Electrode voltages between 10 and 15 V were needed to cancel the drift. Pollack considered whether the phenomenon is due to charge injection in the insulator or chemical rearrangement of the polymer. Lee et al. [27] also noticed surface degradation in droplet actuation, and proposed charge trapping as a reason for surface degradation. Interestingly, a similar phenomenon to that noticed by Pollack was reported much earlier in a quite similar setup and explained in terms of charge adsorption at the solid-liquid interface by Englebrecht [93]. His purpose was to study electrostatic recording of insulators, rather than droplet actuation, but he performed one experiment with a water droplet in a gap formed by two insulated oil-coated electrodes. He noticed that if the droplet was moved along the surface under applied field, it moved spontaneously back to the original position. When the polarity of the electrode voltage was changed, the droplet could be moved in the opposite direction, and by changing the voltage at a suitable rate, a steady back-and-forth movement was achieved. The droplet motion was observed with electrode voltages down to 30 V.

The best available theory on charging effects between liquid and a hydrophobic polymer surface is presented by Chudleigh [94]. According to Chudleigh, the charge transfer is controlled by the interaction of electrostatic and molecular forces acting on ionic charges in the double layer. The balance of these forces determines whether a charge remains on the liquid or becomes trapped on the surface. Chudleigh also performed charging experiments with 25 μm thick FEP films. The charging voltage was connected between a wet cotton pad in contact with the surface and the metallised backside of the FEP film. He tested four different liquids, an acid (0.01M HCl), a base (0.01M NaOH), deionised water (resistivity 2 M Ωcm) and ethanol. The contact times were varied between 2 sec and 1 h and the charging voltages between -2000 and +2000 V (DC). After removing the liquid contact, a qualitatively similar surface charging

characteristic was observed with all liquids. The charge behaviour was explained using three adsorption mechanisms: preferential adsorption of negative ions, electrostatic adsorption of counter-ions, and adsorption of solvent molecules. A sketch of theoretical and measured surface potential U_c as a function of charging voltage U is shown in Figure 23.

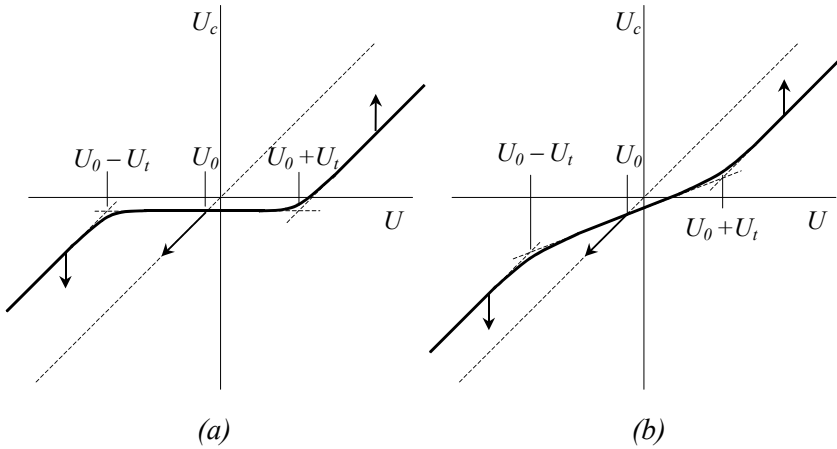


Figure 23. Charging behaviour of FEP surfaces (a) theoretical (b) measured. Sketched (not in scale) from the data reported by Chudleigh [94].

According to Chudleigh, if the externally applied electric field across the solid-liquid interface is low enough, cohesive molecular forces between solvent molecules in the liquid and solvent molecules around hydrated ions are stronger than the electrostatic force acting on ions, and only preferential adsorption occurs. Ideally, this would be seen in the characteristic curve in Figure 23a as an area $\pm U_t$ around voltage U_0 , where the residual surface potential U_c does not depend on the applied voltage U . The preferentially adsorbed surface charge density is proportional to U_0 as

$$s_p = \frac{U_0 \epsilon_0 \epsilon_r}{d}, \quad (54)$$

where ϵ_r and d are the permittivity and thickness of the polymer foil, respectively. If the magnitude of the voltage U is increased below $U_0 - U_t$ or above $U_0 + U_t$, the electrostatic forces overcome the intermolecular forces, and the separation occurs in the diffuse part of the double layer. Then, electrostatic

adsorption of either positive or negative ions occurs, depending on the polarity of the field. This is shown in the characteristic curve as a linear dependence of U_c on U with unity slope. The arrows indicate the direction of movement with increasing contact time and it can be seen that U_c approaches U . This is attributed to the time-dependent adsorption of solvent molecules at the interface. The cohesive force between adsorbed water molecules and water molecules in the hydration shells of the ions makes electrostatic adsorption of ions easier. The measured curves showed nearly predicted characteristics, including the preferential adsorption of negative ions (U_0 negative). Also a time-dependent trend towards the relation $U_c = U$ was observed. The model predicted the slope around the voltage U_0 to remain zero and U_t to decrease as a function of time. However, with measured curves U_t was nearly constant, while the slope increased as a function of time. Even with the shortest contact time, the slope was much closer to unity than to zero. This deviation from the theory is not satisfactorily explained by Chudleigh [94].

The experiments of Chudleigh [94] give direct information only on stationary liquid contacts. Some other experiments have been performed with moving liquid contacts or droplets, and these are reviewed next. Englebrecht [93] has reported electrostatic charging of PET (Mylar™) foils using a setup quite similar to Chudleigh [94], except that the water contact was a moistened ink recorder pen tip moving on the surface with speeds of up to 200 cm/sec. The adsorbed negative charge, detected with a positive toner, was varied linearly with the recording field intensity, as the foil thickness was varied between 3 and 500 μm . A threshold voltage of -20 V for the charge transfer process was observed at all charging field intensities, but the reason for the threshold was not discussed. Charge patterns of alternating polarity were also generated using the same setup but AC charging voltage with up to 1 kHz frequency and rms voltage between 20 and 100 V. Using the earlier discussed droplet-between-plates experiment, it was proven that no thin residual water film was left behind the water probe, so that the charge transfer through that mechanism was excluded. Otherwise, Englebrecht gives so little detail that it is impossible to draw any good conclusions. The results suggest only that if the applied voltage is high enough, electrostatic adsorption of counter-charge can occur with liquid contact speeds of up to 200 mm/sec and with time constant ≤ 1 ms.

Yatsuzuka et al. [60] studied the charging effects of water droplets dripping and sliding on tilted (PTFE) polytetrafluoroethylene plates with a grounded back side. The charge of the collected droplets and the charge distribution of the sliding path were measured as a function of several parameters, including path length, tilt angle, polymer thickness, number of droplets, liquid conductivity and initial charge of the droplets. The charge distribution of the surface was highly negative at the dripping point, but turned positive further along the path. The peak charge at the dripping point was increased as a function of droplet number, but was saturated after six droplets. In most cases, the charge of the droplet after sliding was positive, irrespective of the precharge of the droplet. Only if the slide path was short enough did the droplets with initial negative charge have a residual negative charge. It was found that the excess charge is left on the surface at the very beginning of the sliding path. Increase of the droplet charge as a function of sliding speed was also found. Another observation made by Yatsuzuka et al. [60] is that the charge of the collected droplets as well as the surface potential of the dripping point depends on the thickness of the PTFE plate, varied between 3.2 and 13.4 mm. The water conductivity had a clear negative effect on the residual droplet charge.

The results of Yatsuzuka et al. [60] emphasise that charge adsorption occurs also with free-running droplets, which is of concern for droplet actuation. The preferential adsorption of negative ions occurs immediately when the droplet touches the surface. When sliding further, adsorption of negative ions continues and the droplet gains an excess of positive ions, which eventually become adsorbed on the surface. According to the charge model of Chudleigh [94], this subsequent positive ion adsorption can be considered to be originating from the electrostatic attraction between the surface and positively charged droplet. The dependence between saturated surface charge and insulator thickness is considered in the next section.

3.3.6 Charging effects and electrowetting

Recently, liquid-surface charging aspects have been considered alongside the electrowetting effect. It will be seen later that the threshold voltage for charging is for some unknown reason closely related to the electrowetting effect. Thus it is useful to consider first the surface charging effects with electrowetting, then

apply the results in droplet actuation. Let us consider a droplet on a surface with electric-field induced charges on the electrode and droplet (Figure 24). If part of the charges become trapped, they are no longer electrically effective on the liquid side of the solid-liquid interface. Then the electrostatic energy stored in the capacitor between the droplet and the electrode is reduced to the value

$$W_e = \frac{1}{2} C_d (U - U_c)^2, \quad (55)$$

where U is the applied voltage between the droplet and the electrode and U_c is the voltage shift, which depends on the trapped surface charge density s_t as follows:

$$U_c = \frac{ds_t}{\epsilon_0 \epsilon_r}. \quad (56)$$

If the droplet is removed, the trapped charge induces a surface potential equal to U_c .

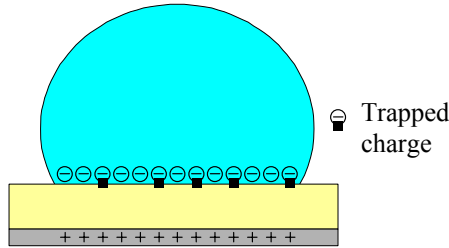


Figure 24. Droplet and electrode with trapped charges in the solid-liquid interface.

According to Chudleigh [94], the surface potential due to adsorbed charge is a function of applied voltage with the characteristics shown in Figure 23. There was some deviation between theory and measurements which was not fully explained by Chudleigh, but we can circumvent this problem by taking the slope around U_0 into account as parameter k , which then represents a kind of charge transfer factor. If $k = 0$, there is no charge adsorption and if $k = 1$ all induced charges are adsorbed. According to the results of Chudleigh [94], both values for

k and U_0 increase as a function of contact time. From Figure 23b we can approximate the partially linear relation between U and U_c , with:

$$U_c = \begin{cases} U + (1-k)U_t & \text{when } U < U_0 - U_t \\ kU + (1-k)U_0 & \text{when } U_0 - U_t \leq U \leq U_0 + U_t \\ U - (1-k)U_t & \text{when } U > U_0 + U_t \end{cases} \quad (57)$$

The electric-field induced surface tension γ_e is equal to electrostatic energy between the droplet and electrode derived by the solid-liquid interface area. Because the contribution of the liquid-vapour area to the droplet capacitance can be neglected, we get from equation (55):

$$\gamma_e = \frac{1}{2} \frac{\epsilon_0 \epsilon_r}{d} (U - U_c)^2. \quad (58)$$

Referring to the section of the electrowetting phenomenon, and using equation (58) we can write the modified electrowetting equation as:

$$\cos \theta_e = \cos \theta_0 + \frac{\epsilon_0 \epsilon_r}{2d\gamma_{lv}} (U - U_c)^2, \quad (59)$$

and if we use the partially linear approximation for U_c , given in equation (57), we can write $(U - U_c)^2$ as:

$$(U - U_c)^2 = \begin{cases} (1-k)^2 (U - U_0)^2 & \text{when } U_0 - U_t \leq U \leq U_0 + U_t \\ (1-k)^2 U_t^2 & \text{elsewhere} \end{cases}. \quad (60)$$

From equations (59) and (60) we can see how the surface charging affects electrowetting. If the applied voltage is between $U_0 - U_t$ and $U_0 + U_t$, the electrowetting effect is reduced by a factor $(1-k)^2$ and there is a voltage shift equal to U_0 . In other words, between $U_0 - U_t$ and $U_0 + U_t$ the characteristic curve between the voltage and cosine of the contact angle has the shape of a parabola, like in the ideal case, but it is shifted and broadened, depending on the values of U_0 and k . With applied voltages $U = U_0 - U_t$ and $U = U_0 + U_t$, the contact angle reaches a minimum value. With higher or lower voltages, the contact angle no longer depends on the applied voltage, but is saturated to the minimum value.

Saturation is observed in various electrowetting experiments. It is also possible that contact angle hysteresis in electrowetting is linked to charge trapping. If there is trapped charge, which is released with hysteretic behaviour during voltage rampdown, then the number of electrically effective charges at the solid-liquid interface increases, which means that k is negative. From equations (59) and (60) we can see that this results in parabolic behaviour which is narrower than the ideal curve. On the other hand, all surfaces also have a contact angle hysteresis without an applied field, which may be visible in electrowetting curves. Next, we review some literature experiments and check how the charging behaviour presented by Chudleigh [94] can be used to explain the observed non-idealities of electrowetting.

Chudleigh [94] measured DI water contact angles of 105° and 87° on FEP surfaces with charging voltages of 0 V and -1000 V, respectively. If the electrowetting effect is ideally present and equation (23) holds true, contact angle reduction from 105° to 87° could be achieved with an applied voltage of -252 V. Thus the electrowetting is clearly degraded in Chudleigh's experiment and can be attributed to charge trapping. From the data of Chudleigh [94] we can estimate that $U_i \approx 500$ V with aqueous solutions, which means that with the applied voltage of -1000 V, the contact angle is saturated. Using equations (59) and (60) we get $k \approx 0.6$ in the contact angle measurement. From the DI water data of Chudleigh [94] we can approximate $k \approx 0.7$ and $k \approx 0.9$ for stationary contact times of 2 sec and 30 min, respectively. Thus the contact angle measurement suggests somewhat smaller charge transfer than the surface potential measurement. This is reasonable, because charge transfer increases as a function of time, while the response time of electrowetting is of the order of ms [90], which is much shorter than the shortest contact time in the surface potential measurements of Chudleigh [94].

B. Berge and his co-workers have been studying the electrowetting effect with PTFE [73, 81] and PET [97] films using AC voltage. With all experiments, saturation of the contact angle was recorded at high voltages. The saturation was reversible, except with PET. Interestingly, the saturation voltage U_i was found to be proportional to the square root of the insulator thickness d , so that with PTFE samples of thickness between 53 and 267 μm , the saturation voltage was varied between 700 V and 1550 V, respectively. With 12 μm thick PET, the saturation voltage was around 170 V. The saturation was attributed to air ionisation,

because luminescence was observed at or above the saturation voltage. On the other hand, it is not clear whether air ionisation and luminescence are reasons or consequences of the saturation. If charge trapping is the origin of the saturation, then the experiments of Berge's group suggest that it also occurs with AC voltages up to a few kilohertz. This is supported by the previously mentioned experiments of Englebrecht [93]. Otherwise, there was considerable scattering in the measured contact angles and the fit to the ideal electrowetting equation (23) was not very good. All the measured curves showed hysteresis, so that with increasing voltage the cosine curve was wider and with decreasing voltage the shape was narrower than the ideal curve. From the measured data of PET [97] it can be found using fitting of equations (59) and (60) that $U_0 \approx -130$ V, and $k \approx 0.5$ for the increasing voltage. For PTFE samples [73] it was difficult to obtain values for k and U_0 due to scattering.

B. Janocha et al. [82] have measured the competitive electrowetting behaviour of water and decane with nine samples of different materials: paraffin, PET, PTFE, PP (polypropylene), PVDF (polyvinylidene fluoride), PFA (perfluoroalkoxy) and PE (polyethylene), as standard and as oxidised with two different methods. They found that with all samples, the contact angle behaviour was more or less degraded from the ideal functional relationship given in equation (23). All curves showed offset and saturation or bending at high voltages. Only the advancing angle of paraffin showed ideal parabolic behaviour, all other curves were broadened. Janocha et al. proposed charge trapping as the mechanism for the observed contact angle saturation and the hysteresis as well, and suggested that precharge of the polymer is responsible for the shift. Degradation of electrowetting with lower voltages was suggested to be due to some additional mechanisms, like water intrusion into surface pores, which makes part of the induced charges ineffective. Janocha et al. summarise the effects as a modified electrowetting equation:

$$\cos\theta_e = \cos\theta_0 + \frac{\varepsilon_0\varepsilon_r}{2d\gamma_l} f\left(U, \frac{dU}{dt}\right)(U - U_0)^2, \quad (61)$$

where γ_l is the interfacial tension between water and decane, U_0 is the offset caused by the precharge, and f is the function of applied voltage and time which describes the charge trapping. The equation of Janocha et al. is essentially the same as the modified electrowetting equation derived in this work, except that

there is a function f instead of $(1-k)^2$. In the measurements of Janocha et al., the function f showed values between 1 and 0.02 with different polymers. This equals transfer factor k values between 0 and 0.9, respectively. The largest k value was found in PET, which is not surprising as the same material also showed strong charging in the experiments of Englebrect [93] and Vallet, Berge and Vovelle [97]. Measured contact angle curves showed quite small hysteresis, except with paraffin. Where it was measurable, saturation of the contact angle proved to be more dependent on the polymer thickness than on the polymer material. Paraffin with a thickness of 50 μm showed saturation with voltages of approximately $U_0 \pm 500$ V, while PE, PP and PTFE with thickness around 100 μm showed saturation with voltages of approximately $U_0 \pm 1000$ V.

Verheijen and Prins [83] have measured capacitively the contact angle of a water droplet using a 10 μm thick parylene insulator with an oil impregnated Teflon[®] AF surface. They found that up to the applied potential of ± 240 V, the contact angle obeys the electrowetting theory with excellent fit to equation (23) and with negligible hysteresis. According to Verheijen and Prins, at higher voltages, charge gets trapped in a threshold-like behaviour, limiting the charge density that can be induced in the liquid. Afterwards, discharging of the surface was possible with a zero-voltage droplet. The polarisation-independent nature of the charging suggests that the phenomenon is electrostatic adsorption of counterions. Verheijen and Prins have also derived a modified electrowetting equation, which takes into account the charge trapping:

$$\cos \theta_e = \cos \theta_0 + \frac{\epsilon_0 \epsilon_r}{2d\gamma_{lv}} (U - U_T)^2. \quad (62)$$

We notice that the equation is the same as equation (59) derived in this work. From the measurement results, Verheijen and Prins have derived a functional relationship for U_T which is essentially the same as the one presented in this work in equation (57) with $k = 0$ and $U_0 = 0$. This is also equal to the ideal charging curve of Chudleigh [94], shown in Figure 23 a, with $U_0 = 0$. A very interesting observation made by Verheijen and Prins [83] is that at the threshold field of charge adsorption, the electric-field induced surface tension is nearly equal to the surface tension of water. Based on this, they suggest that charge adsorption may be originating from instabilities in the solid-liquid interface,

leading to small charged droplet or molecular clusters being ejected and trapped in the surface. On the other hand, Janocha et al. [82] consider that charge adsorption is facilitated as the electric field reduces the solid-liquid interfacial tension. Both of these above considerations may be on the right track, because interfacial tensions are related to intermolecular forces, which determine the threshold of electrostatic adsorption according to Chudleigh [94].

It seems clear that the threshold type charging characteristics presented by Chudleigh [94] can be observed in the electrowetting effect as saturation and degradation and the saturation voltage is equal to the threshold voltage of electrostatic charge adsorption. In Figure 25 we have plotted the measured saturation voltage of electrowetting in the experiments of Berge et al. [73, 97], Janocha et al. [82], and Verheijen and Prins [83]. Their absolute values are plotted as a function of d/ϵ_r together with the threshold voltage value of electrostatic charge adsorption in the experiment of Chudleigh [94]. The solid line represents a condition where the electric-field induced surface tension is equal to the surface tension of water:

$$\frac{1}{2} \frac{\epsilon_0 \epsilon_r}{d} U^2 = \gamma_{lv} \Leftrightarrow U = \sqrt{\frac{2\gamma_{lv}d}{\epsilon_0 \epsilon_r}}. \quad (63)$$

As shown in Figure 25, equation (63) fits quite well with all of the previously mentioned experiments and it predicts the relation between threshold voltage and the square root of the insulator thickness, originally observed by Berge [73]. The results of Janocha et al. [82] show more scattering, but it must be remembered that it differs from the others in that water is not in contact with air but with decane, which results in smaller interfacial tension.

Recently, Moon et al. [98] reported electrowetting experiments with a very thin (70 nm) and high permittivity ($\epsilon_r = 180$) barium strontium titanate insulator covered with a thin (20 nm) layer of Teflon AF[®]. The contact angle change began to decrease around 12 V. This data, plotted in Figure 25, also show a very good fit with equation (63). In the same figure we have also plotted the measured surface potentials due to preferential adsorption of ions in the experiments of Chudleigh [94] and Yatsuzuka et al. [60]. Although the experiments of Chudleigh and Yatsuzuka et al. are quite different, the water

conductivity, which influences the charge adsorption, is nearly the same (around $50 \mu\text{S/m}$). The polymer materials are different, but according to literature data [53] they have equal advancing water contact angles (108°).

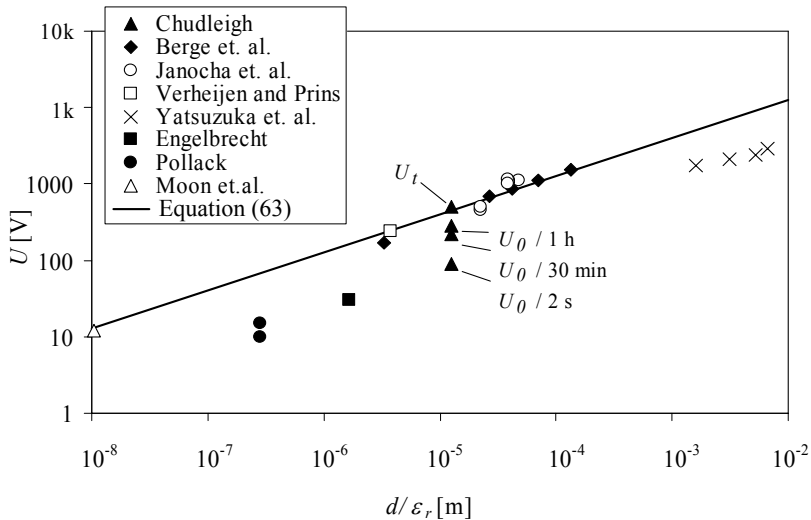


Figure 25. Surface potential due to adsorbed charge, as extracted from various water droplet experiments and plotted as a function of insulator thickness per permittivity. The voltage value is equal to the saturation voltage of electrowetting in the experiments of Berge et al. [73, 97], Verheijen and Prins [83], Janocha et al. [82] and Moon et al. [98], the measured surface potential in the experiments of Yatsuzuka et al. [60], and the threshold voltage to cancel the charge induced droplet motion in the experiments of Englebrecht [93] and Pollack [24]. From the experiment of Chudleigh [94], both the measured surface potential as a function of time (U_0) and the threshold voltage of charge trapping (U_t) are plotted. The solid line represents equation (63).

Between the experiments of Chudleigh [94] and Yatsuzuka et al. [60] the insulator thickness changes by three orders of magnitude, but it can be still seen that the charge induced potential is approximately proportional to the square root of the polymer thickness. It should be noted that in the case of preferential adsorption, the electrode beneath the surface is grounded and there is no applied field. However, the image charge effect generates electrostatic force between a charge and a conducting plane. B. E. Conway [64] states in his article on

electrical aspects of liquid interfaces that the image energy should provide an important contribution to the specific adsorption of ions. The electrostatic energy associated with a charge Q and its image is proportional to Q^2/d , which shows the same functional relationship as the charge density on a parallel-plate capacitor. Respectively, the previously mentioned experiments of Englebrecht [93] and Pollack [24] are nearly similar to each other. The insulator materials are different, but both had oil coating on them, so that it is possible that the charging surface is essentially oil, where charge adsorption is also possible. It has been reported elsewhere that OH⁻ ions adsorb spontaneously at the oil-water interface [99]. We will later show that the voltage needed to cancel the droplet motion is proportional to the surface potential due to the adsorbed charge. If we perform a very crude operation, and plot the reported voltage values in the same Figure 25, we notice that they obey with some factor the same relation between the square root of the insulator thickness versus the charge induced potential. The values are 860 nm and 10–15 V for Pollack [24], and 5 μm and 30 V for Englebrecht [93], respectively.

We can conclude that the physical mechanisms and basic formulations of the charge adsorption phenomena between water and polymer surfaces are not known yet, but the threshold type charging behaviour, presented by Chudleigh [94], is confirmed in the recent electrowetting experiments. Thus when the applied potential is large enough, adsorption of counter-charges occurs with all polymer materials. The threshold voltage U_t seems to be proportional to the square root of the polymer thickness, regardless of the material. This may be somehow related to the condition of electric-field induced surface tension being approximately equal to the surface tension of water. Below the threshold, there are large differences between different materials, and a charge transfer factor k is proposed to be used to describe the charging properties between liquid and polymer. The electrowetting experiment serves a simple way to determine these properties. The charging properties of different materials, extracted from various literature experiments, are summarised in Table 1. It should be noted that the preparation and condition of the surface probably has a significant contribution in the charging properties. Thus the values presented in Table 1 should not be considered as pure, universal material constants. Reversibility and hysteresis of the charge adsorption are also very important characteristics, and they seem to vary greatly between different materials. Because numerical data are difficult to obtain, reversibility is presented only qualitatively in Table 1.

Table 1. Charging properties of some polymers with respect to electrified water contact.

	d [μm]	θ_0 [$^\circ$] ¹	U_0 [V]	U_i [V]	k	Reversibility	ref.
Teflon [®] AF on parylene	10	119	0	± 240	0	Reversible, no hysteresis	[83]
PET	12	66	-130	≈ 170 ²	≈ 0.5	Irreversible	[97]
PET	100	79 (102)	200	?	0.9	?	[82]
FEP	25	105	-90 ... -280 ⁴	$\approx \pm 500$	$\approx 0.6 \dots$ 0.9 ³	?	[94]
Paraffin	50	110 (177)	30	-505 / +450	0	Reversible with hysteresis	[82]
PP	89.3	108 (168)	-120	-1100 / +1040	0.31	Reversible with small hysteresis	[82]
PE	100	103 (166)	-130	-1020 / +1160	0.37	Reversible with small hysteresis	[82]
PTFE	100	108 (148)	-3500	- ? / +1100	0.47	Reversible with small hysteresis	[82]

¹ Advancing or equilibrium angle measured with zero applied voltage. The value in parentheses is from the experiment performed in decane instead of air, and in that case advancing angle values from ref. [53] are given.

² AC measurement

³ Increased as a function of contact time

3.4 Model for droplet actuation

In this section we derive a model for droplet actuation, which can be used to calculate the actuation forces. In order to simplify the calculations, the droplet is approximated with a spherical cap conductor and the electrodes are presented with two semi-infinite planes with infinitely small spacing as shown in Figure 26. It was stated earlier that it is reasonable to assume the droplet as a conductor

instead of a lossy dielectric sphere, because of the large relative permittivity of water. Conductor approximation makes capacitance calculation much simpler. The electrode approximation is also reasonable, because according to 2-dimensional FE simulations, the gap between the electrodes should be as small as possible. In practice it can be of the order of micrometers, while the droplet diameter is in millimetres. The whole actuation process is composed of repeated steps of a droplet. A single step can be separated into four phases as shown in Figure 27.

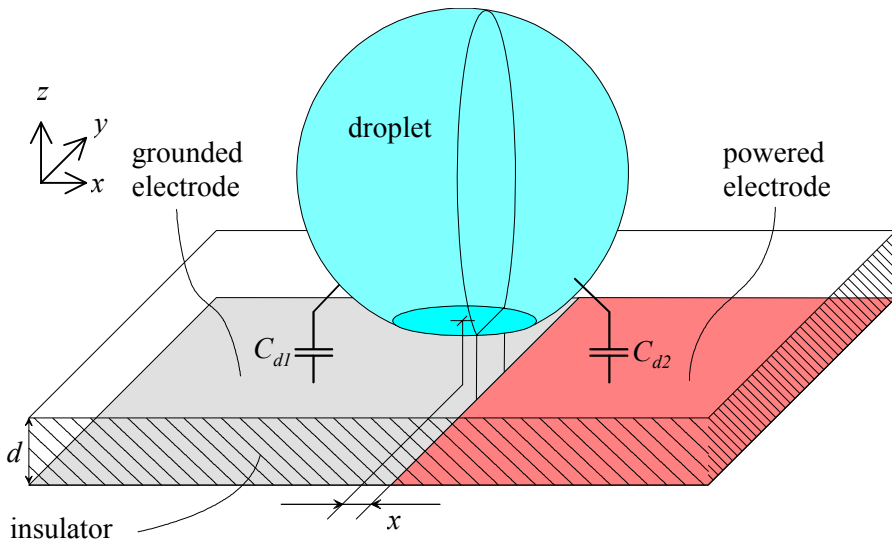


Figure 26. Simplified model for electrostatic droplet actuation.

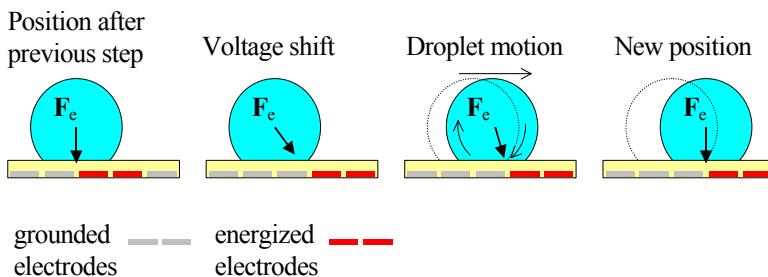


Figure 27. Phases of a single droplet actuation step.

3.4.1 Electrostatic energy and force

The electrical energy stored in the capacitance between the electrodes is

$$W_e = \frac{1}{2} C_e U^2, \quad (64)$$

where U is the voltage and C_e is the capacitance between the electrodes. The capacitance between the powered and grounded electrode outside the droplet is assumed to be constant, i.e. its value does not depend on the presence, position or shape of the droplet; thus it can be ignored in the analysis. If we divide the droplet into two segments along the projection of the electrode borderline we can distinguish two capacitances between the droplet and the electrodes C_{d1} and C_{d2} , as shown in Figure 26. C_e is the serial combination of C_{d1} and C_{d2} :

$$C_e = \frac{C_{d1} C_{d2}}{C_{d1} + C_{d2}}. \quad (65)$$

In order to solve the capacitances C_{d1} and C_{d2} , we first approximate the capacitance between droplet and plane using equivalent a circular parallel-plate capacitor so that the thickness remains unchanged. Then the capacitances C_{d1} and C_{d2} can be approximated as slices of the equivalent plate as shown in Figure 28. The radius of the equivalent plate is a function of droplet volume, contact angle, insulator thickness and permittivity. Using FE modelling (Appendix B) an approximate formula for the radius of the equivalent plate was derived:

$$R_{eq}^2 \approx R_c^2 + \frac{3.7}{\varepsilon_r^{0.57}} R_b^2 \left(\frac{d}{R_b} \right)^{0.734 \varepsilon_r^{0.085}}, \quad (66)$$

where R_c is the radius of the droplet bottom, R_b is the radius of a ball which has the same volume as the droplet, and ε_r and d are the relative permittivity and thickness of the insulator.

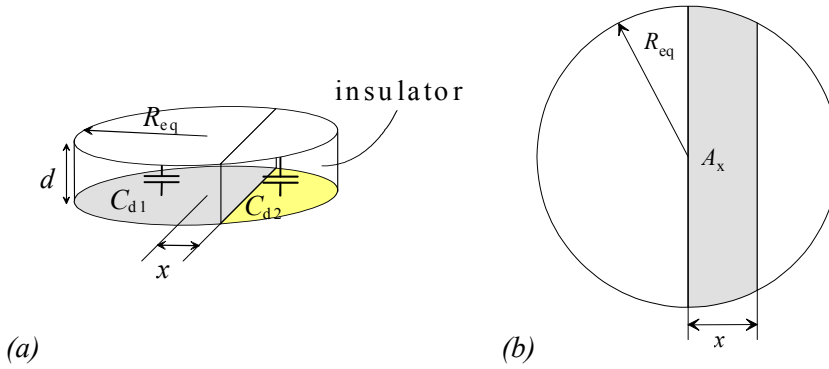


Figure 28. Droplet-electrode capacitances approximated as segments of the equivalent circular parallel plate capacitor. a) side view, b) top view; A_x is the shaded segment area.

From Figure 28 we get:

$$C_{d1} = \frac{\varepsilon}{d} \left(\frac{A_{eq}}{2} + A_x \right) \quad (67)$$

$$C_{d2} = \frac{\varepsilon}{d} \left(\frac{A_{eq}}{2} - A_x \right), \quad (68)$$

where $A_{eq} = \pi R_{eq}^2$ and A_x is the shaded segment in Figure 28b. ε is the absolute permittivity of the insulator ($= \varepsilon_0 \varepsilon_r$). A_x is calculated in Appendix C and equals

$$A_x = x \sqrt{R_{eq}^2 - x^2} + R_{eq}^2 \arcsin \left(\frac{x}{R_{eq}} \right). \quad (69)$$

Substituting C_{d1} and C_{d2} into equation (65) we get:

$$C_e = \frac{\frac{\varepsilon}{d} \left(\frac{A_{eq}}{2} + A_x \right) \cdot \frac{\varepsilon}{d} \left(\frac{A_{eq}}{2} - A_x \right)}{\frac{\varepsilon}{d} \left(\frac{A_{eq}}{2} + A_x \right) + \frac{\varepsilon}{d} \left(\frac{A_{eq}}{2} - A_x \right)} \quad (70)$$

$$= \frac{\frac{A_{eq}^2}{4} - A_x^2}{\frac{A_{eq}}{2}} = \frac{\varepsilon}{d} \left(\frac{A_{eq}}{4} - \frac{A_x^2}{A_{eq}} \right)$$

The electrostatic energy can now be written as

$$W_e = \frac{\varepsilon U^2}{2d} \left(\frac{A_{eq}}{4} - \frac{A_x^2}{A_{eq}} \right). \quad (71)$$

Figure 29 shows a plot of electrostatic energy as a function of x with the parameters shown below. It can be seen that the system reaches maximum energy when the droplet is located symmetrically above the electrodes. Thus the droplet feels a force towards that position. The electrostatic force can now be solved as the negative gradient of the electrostatic energy. Because only the horizontal x -component of the electrostatic force is capable of moving the droplet on the surface, we need only differentiate W_e with respect to x .

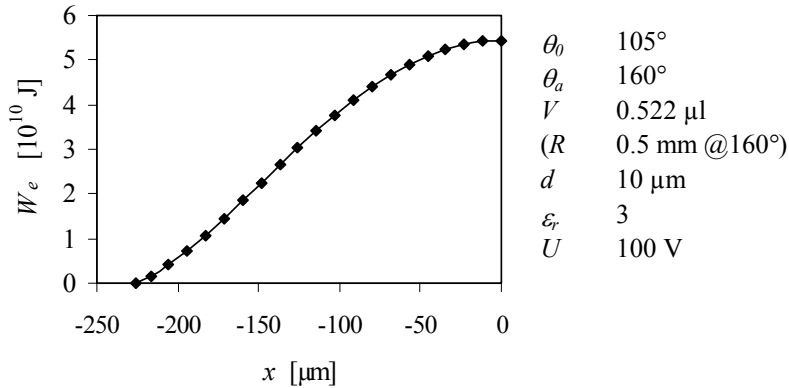


Figure 29. Plot of electrostatic energy as a function of droplet starting position.

When doing this, it is important to note that the only term in the equation of W_e which depends on x is A_x . Thus $dA_{eq}/dx = 0$, and the magnitude of the electrostatic force can be solved as:

$$F_e = \left| \frac{U^2}{2} \frac{d}{dx} \left[\frac{\varepsilon}{d} \left(\frac{A_{eq}}{4} - \frac{A_x^2}{A_{eq}} \right) \right] \right| = \frac{\varepsilon U^2}{d} \frac{A_x}{A_{eq}} \frac{d}{dx} A_x \quad (72)$$

The calculations for dA_x/dx are presented in detail in Appendix C. We get:

$$\frac{d}{dx} A_x = 2\sqrt{R_{eq}^2 - x^2} . \quad (73)$$

After substituting equation (73) and inserting $\varepsilon = \varepsilon_0 \varepsilon_r$ and $A_{eq} = \pi R_{eq}^2$ into equation (72) we can complete the equation for the horizontal electrostatic force:

$$F_e = 2 \frac{\varepsilon_0 \varepsilon_r U^2}{d} \frac{A_x}{\pi R_{eq}^2} \sqrt{R_{eq}^2 - x^2} , \quad (74)$$

where A_x is given in equation (69) and R_{eq} in equation (66). It can be seen in equation (74) that the electrostatic force is proportional to the voltage squared and inversely proportional to the insulator thickness. As R_{eq} is directly proportional to the droplet radius R and A_x is proportional to R squared, F_e is proportional to R .

Figure 30 shows an example of F_e plotted as a function of x . The parameters used in the calculation are also shown. The plot of Figure 30 actually represents a static case, calculated for a droplet with a static electric-field induced contact angle θ_e . As discussed in section 3.4.2, θ_e is the value which the droplet has at the stopping point of the previous step. θ_e can be calculated using equation (82) from the initial advancing contact angle θ_a of the droplet. In order to calculate electrostatic force during droplet motion, the droplet shape should be known. However, as discussed in section 3.4.2, it is not simple to solve. On the other hand, the surface tension of water is so high that the droplet shape cannot change very radically during actuation. Thus the plot can be considered as an approximation of the dynamic case. It can be seen in Figure 30 that when x becomes zero, so does F_e . This means that the droplet stops at the position where

it is symmetrically located on top of the borderline between the electrodes, as shown in Figure 27. It can be also seen that the actuation force reaches a maximum at a certain distance x . It appears that this distance is approximately equal to $2/3 R_{eq}$ irrespective of the other parameters.

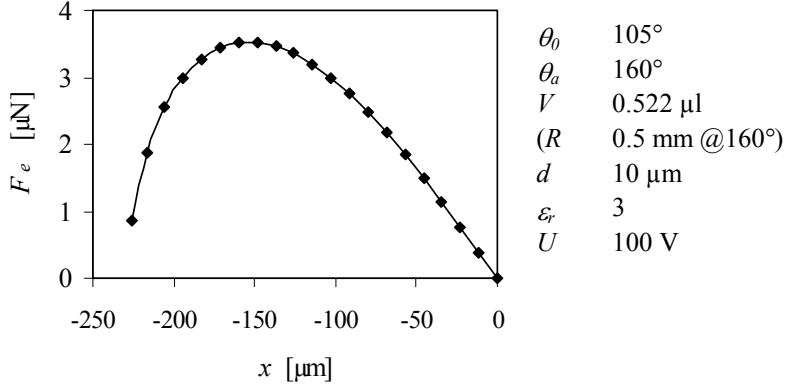


Figure 30. Plot of electrostatic force as a function of droplet starting position.

3.4.2 Contact angle and electrowetting force

Next we consider the electrowetting effect in the model geometry. Because the electric field induced surface tension is proportional to the local electric-field intensity at the solid-liquid interface, we have to calculate the electric-field induced surface tension separately for both electrodes. For simplicity, it is assumed that the electric-field induced surface tension is distributed along the droplet contact line as shown in Figure 31b. The electrostatic energy is stored in two capacitors C_{d1} and C_{d2} , which have voltages U_1 and U_2 . The electric-field induced surface tensions on different sides of the droplet can be calculated according to equation (34) as:

$$\gamma_{e1} = \frac{1}{2} \frac{\epsilon_0 \epsilon_r U_1^2}{d} \quad (75)$$

$$\gamma_{e2} = \frac{1}{2} \frac{\epsilon_0 \epsilon_r U_2^2}{d}. \quad (76)$$

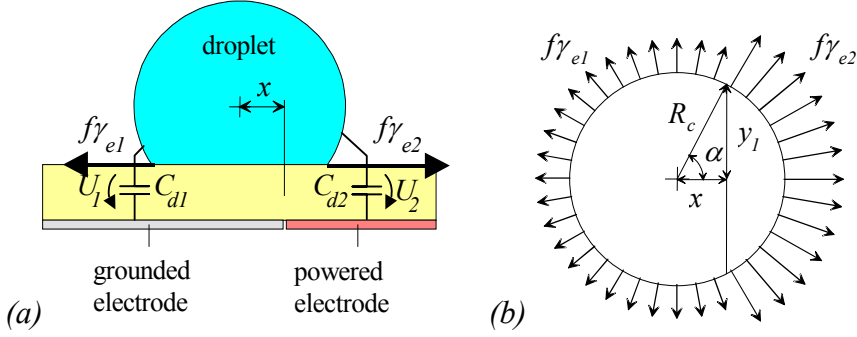


Figure 31. a) Cross-section of the model geometry. b) Top view of the electric-field induced surface tension at the droplet-surface contact line.

Because C_{d1} and C_{d2} are in serial connection, U_1 and U_2 are

$$U_1 = \frac{C_{d2}}{C_{d1} + C_{d2}} U \quad (77)$$

$$U_2 = \frac{C_{d1}}{C_{d1} + C_{d2}} U, \quad (78)$$

where U is the voltage between the electrodes. Substituting (77) into (75) and (78) into (76), and using the definitions of C_{d1} and C_{d2} in equations (67) and (68), we get:

$$\gamma_{e1} = \frac{1}{2} \frac{\epsilon_0 \epsilon_r U^2}{d} \left(\frac{1}{4} - \frac{A_x}{A_{eq}} + \frac{A_x^2}{A_{eq}^2} \right) \quad (79)$$

$$\gamma_{e2} = \frac{1}{2} \frac{\epsilon_0 \epsilon_r U^2}{d} \left(\frac{1}{4} + \frac{A_x}{A_{eq}} + \frac{A_x^2}{A_{eq}^2} \right). \quad (80)$$

In principle, the contact angle in droplet actuation is determined by the electric field induced surface tensions, which we have just calculated. However, it is very difficult to know what really happens in the droplet contact line during the droplet motion. As soon as the voltages are applied and the contact line begins to move towards the new equilibrium position, simultaneously the whole droplet

moves due to electrostatic force, which changes the equilibrium position. This again changes the electrostatic force and so on. Basically, the difficulties result from the fact that the contact angle represents the equilibrium of molecular forces, while the droplet motion is governed by the dynamics of the molecular forces. Thus, the contact angle may not be well defined during droplet motion, and it is pointless trying to calculate it. On the other hand, we are mostly interested in forces that initiate droplet motion. As shown in Figure 27, the stopping position of a single step is the starting position of the next. In the stopping position, the droplet is in equilibrium, and it is possible to calculate the contact angle. We notice from equations (79) and (80) that at the stopping point, where $A_x = 0$, the two components of the electric-field induced surface tensions are equal, and have value:

$$\gamma_{e1} = \gamma_{e2} = \frac{1}{8} \frac{\varepsilon_0 \varepsilon_r U^2}{d}. \quad (81)$$

Referring to section 3.3.3, we can write the electric-field induced contact angle at the stopping point of the droplet actuation step as

$$\cos \theta_e = \cos \theta_c + \frac{1}{8} f \frac{\varepsilon_0 \varepsilon_r U^2}{d \gamma_{lv}}. \quad (82)$$

Figure 32 shows the plot of equation (82) with $\theta_0 = 105^\circ$, $\theta_c = 160^\circ$ ($f \approx 0.08$) and with the insulator having $\varepsilon_r = 3$ and variable thickness. As discussed in section 3.4.5 the cosine of the contact angle saturates to a value $\cos \theta_c + f$ due to charging effects.

As shown in equations (79) and (80), the electric-field induced surface tension is different on different sides of the droplet. This asymmetry causes a net force, which displaces the contact line of the droplet. We term this force *the electrowetting force*. It can be calculated by integrating the effective electric-field induced surface tension along the droplet-surface contact line, shown in Figure 31b. We get:

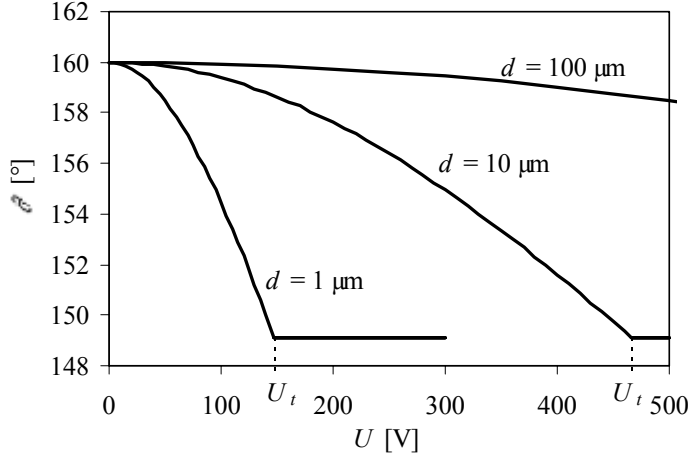


Figure 32. Contact angle at the droplet stopping position.

$$\begin{aligned}
 F_{EW} &= 2fR_c \left(\int_0^\alpha \gamma_{e2} \cos \alpha d\alpha + \int_\alpha^\pi \gamma_{e1} \cos \alpha d\alpha \right) \quad (83) \\
 &= 2fR_c [\gamma_{e2} \sin \alpha - \gamma_{e2} \sin 0 + \gamma_{e1} \sin \pi - \gamma_{e1} \sin \alpha] \\
 &= 2fR_c (\gamma_{e2} - \gamma_{e1}) \sin \alpha
 \end{aligned}$$

where α is the angle shown in Figure 31b. From the same figure we can calculate

$$\sin \alpha = \frac{y_1}{R_c} = \frac{\sqrt{R_c^2 - x^2}}{R_c}, \quad (84)$$

and we get

$$F_{EW} = 2fR_c (\gamma_{e2} - \gamma_{e1}) \frac{\sqrt{R_c^2 - x^2}}{R_c} = 2f (\gamma_{e2} - \gamma_{e1}) \sqrt{R_c^2 - x^2} \quad (85)$$

Using equations (79) and (80) for γ_{e1} and γ_{e2} , and inserting $A_{eq} = \pi R_{eq}^2$, we get:

$$F_{EW} = 2f \frac{\varepsilon_0 \varepsilon_r U^2}{d} \frac{A_x}{\pi R_{eq}^2} \sqrt{R_c^2 - x^2} \quad (86)$$

When comparing equations (74) and (86) for the electrostatic and electrowetting forces, they are seen to be nearly equal. The only differences are that there is the fractional area f in the electrowetting force and in the square root term the electrowetting force has R_c but the electrostatic force has R_{eq} . This is not surprising, as electrowetting can be considered an electrostatic force acting on the solid-liquid interface (section 3.3.4), and R_c is the radius of that interface. On the other hand, when the radius of the equivalent capacitor R_{eq} is used instead of R_c , both solid-liquid and liquid-vapour interfaces of the droplet are taken into account. We can conclude that the actuation force of the droplet is contributed entirely by the electrostatic force, while the electrowetting force represents only the contribution of the solid-liquid interface.

3.4.3 Actuation criterion

In order to utilise the droplet actuation model, we must determine the criterion for successful droplet actuation. There are two possibilities, both shown in Figure 33. The first criterion, shown in Figure 33a, is that the electrostatic force equals the sliding force:

$$F_e = F_s, \quad (87)$$

where F_e and F_s are given in equations (74) and (4), respectively. This criterion can be used if the sliding force behaves like friction, so that it diminishes once the droplet starts to move. Unfortunately we do not know whether this is true. On the other hand, some extra force is needed to accelerate the droplet mass from the resting position. However, we can use this criterion as a lower limit estimation of the actuation threshold voltage. Another, physically more correct actuation criterion is to equate electrostatic and sliding forces integrated along the droplet's sliding path as shown in Figure 33b. The problem with this approach is that our model considers a stationary droplet just before the step, and the forces acting on a moving droplet are not really known. If both electrostatic and sliding forces are expressed in terms of the contact angle, as we would like

to do, problems are encountered because there is no simple method to solve the contact angle during droplet motion, as discussed in section 3.4.2. The only simple possibility to use the integral criterion with our model is to assume that the droplet has the same constant contact angle during sliding as it does at the stopping position, and that the sliding force stays constant. On the other hand, the electrostatic energy reaches its maximum at the droplet stopping position, which means that the contact angle reaches its minimum. We can consider that the real contact angle may be higher and the sliding force lower than what we assume in our model. Thus the integral criterion, used in this way, overestimates the actuation threshold voltage. In conclusion, we can assume that the true actuation criteria is somewhere between the values given by the two methods, described below.

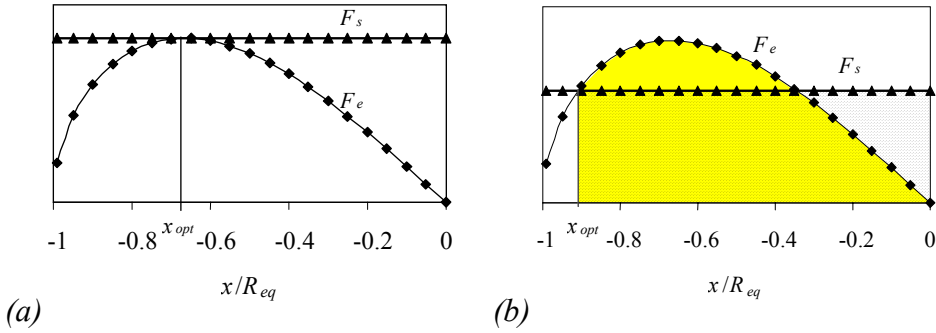


Figure 33. Two possible actuation threshold criteria (a) F_e and F_s are equal, (b) integrals of F_e and F_s are equal.

The integral criterion of Figure 33b equals:

$$\int_x^0 F_e dx = \int_x^0 F_s dx . \quad (88)$$

Because force is the negative gradient of energy, we can write the equation as:

$$\Delta W_e = \Delta W_s . \quad (89)$$

where ΔW_e and ΔW_s are changes in electrostatic and sliding energies between x and the zero position. ΔW_e can be solved from equation (71)

$$\Delta W_e = \frac{\varepsilon U^2}{2d} \frac{A_x^2}{A_{eq}}, \quad (90)$$

and ΔW_s is

$$\Delta W_s = xF_s. \quad (91)$$

The theoretical optimal value of $|x|$ is also dependent on the actuation criterion. With the force criterion, the theoretical optimal distance is at the maximum of the electrostatic force, which is approximately $2/3 R_{eq}$, but with the energy criterion the theoretical optimal distance is around $0.9 R_{eq}$, as shown in Figure 33. On the other hand, there are two practical limitations that must be taken into account: charge trapping and the critical pressure of the superhydrophobic surface.

3.4.4 Electrostatic pressure

As shown in section 2.3.3, the critical pressure of a composite surface can easily be exceeded in electrostatic droplet actuation; therefore we must consider the electrostatic pressure acting on the droplet in our model. The electrostatic pressure is given in equation (12), and for that we must calculate the voltages between the droplet and electrodes from the capacitances C_{d1} and C_{d2} . As $C_{d2} \leq C_{d1}$, the voltage across C_{d2} is larger than or equal to that across C_{d1} , and the electrostatic pressure above the energised electrode is larger than or equal to that above the grounded electrode. Thus we need only calculate the electrostatic pressure above the energised electrode. The voltage across C_{d2} is

$$U_2 = \frac{C_{d1}}{C_{d1} + C_{d2}} U, \quad (92)$$

After substitution of C_{d1} and C_{d2} from equations (67) and (68) we get:

$$U_2 = \frac{\frac{\varepsilon}{d} \left(\frac{A_{eq}}{2} + A_x \right)}{\frac{\varepsilon}{d} \left(\frac{A_{eq}}{2} + A_x + \frac{A_{eq}}{2} - A_x \right)} U = \left(\frac{1}{2} + \frac{A_x}{A_{eq}} \right) U. \quad (93)$$

Substituting equation (93) and $\varepsilon = \varepsilon_0 \varepsilon_r$ into equation (12), gives:

$$P_e = \frac{\varepsilon_0 \varepsilon_r U^2}{2d^2} \left(\frac{1}{2} + \frac{A_x}{A_{eq}} \right)^2. \quad (94)$$

Figure 34 shows a plot of electrostatic pressure as a function of x , and the parameters used in the calculation. The electrostatic pressure is seen to increase with distance from the electrode.

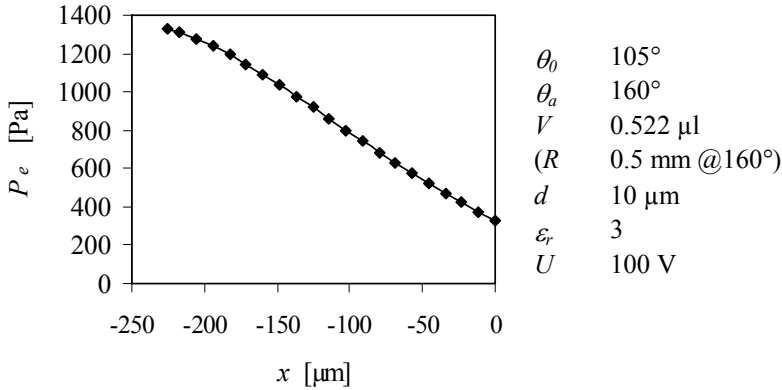


Figure 34. Electrostatic pressure as a function of the droplet starting position.

Remembering that the electrostatic force must not overcome the critical pressure of the superhydrophobic surface, in Figure 35 we have calculated the actuation and sliding forces when the voltage at the starting point is such that the electrostatic pressure equals the critical pressure of the surface, i.e. 1000 Pa in this example. It appears that droplet actuation is not possible if the electrode step is too low or too high. The ratio of actuation and sliding forces reaches its maximum at lower values of $|x|$ than in the ideal case, because the usable voltage decreases as a function of $|x|$. The optimal value for $|x|$ is around 0.5 R_{eq} in terms of force and around 0.6 R_{eq} in terms of energy.

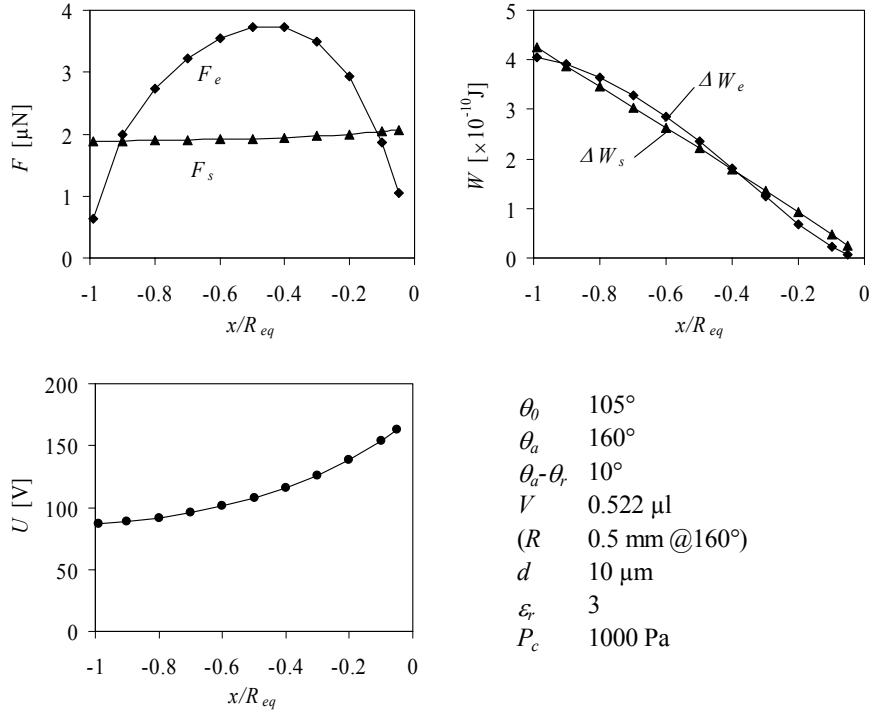


Figure 35. Effect of critical pressure limitation in droplet actuation.

3.4.5 Charging effects

Charging is a potential risk with both normal and superhydrophobic surfaces. This limitation is met if the sliding force is so large that voltages close to the threshold of charge trapping must be used. The charging effects in droplet actuation can be considered using a similar approach to that used with the electrowetting effect in section 3.3.6. If part of the charges in the solid-liquid interface become trapped, they are no longer electrically effective on the liquid side of the interface. Then the electrostatic energy stored in the capacitor C_e between the electrodes is reduced to the value

$$W_e = \frac{1}{2} C_e (U - U_c)^2, \quad (95)$$

where U_c is the voltage shift caused by the trapped charge. As discussed concerning the electrowetting effect in the above-mentioned section, U_c can be presented using the partially linear approximation given in equation (57). Thus we can write the horizontal electrostatic force as:

$$F_e = \begin{cases} F_{e,0}(1-k)^2(U-U_0)^2 & \text{when } U_0 - U_t \leq U \leq U_0 + U_t \\ F_{e,0}(1-k)^2 U_t^2 & \text{elsewhere} \end{cases}, \quad (96)$$

where $F_{e,0}$ is the electrostatic force without charge adsorption, given in equation (74). We notice that if the magnitude of the voltage is between $U_0 - U_t$ and $U_0 + U_t$ the actuation force is reduced by a factor $(1-k)^2$ due to charge trapping and if $k = 1$ the force is zero. There is also a voltage shift equal to U_0 which means that the adsorbed charge induces a force with zero applied voltage, as observed by Pollack [24] and Englebrect [93].

Equation (96) shows also that the actuation force can be increased only up to a certain limit. When the actuation voltage reaches the value $U_0 - U_t$ or $U_0 + U_t$, the force is saturated and the increase of voltage above that value does not introduce any more force. As noted in section 3.3.6, it seems that the threshold is reached when the electric-field induced surface tension is equal to the surface tension of water. In our model geometry, the electric-field induced surface tension $\gamma_{e2} \geq \gamma_{e1}$, so that possible charge trapping occurs first at the advancing edge of the droplet. Setting $\gamma_{e2} = \gamma_{lv}$, and substituting γ_{e2} from equation (80), we can write the threshold voltage of the charge adsorption in electrostatic droplet actuation as:

$$U_t = \sqrt{\frac{2d\gamma_{lv}}{\epsilon_0\epsilon_r \left(\frac{1}{4} + \frac{A_x}{A_{eq}} + \frac{A_x^2}{A_{eq}^2} \right)}}. \quad (97)$$

Figure 36 shows a plot of U_t as a function of x , and the parameters U used in calculation. U_t is seen to increase as the distance from the electrode decreases.

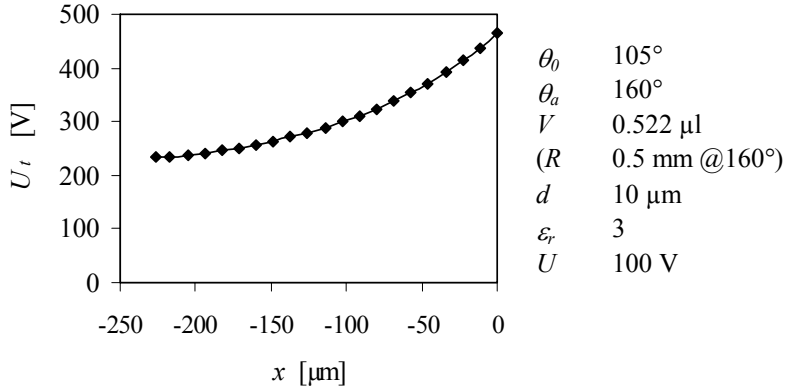


Figure 36. Threshold voltage of charge trapping as a function of droplet position.

As the electrostatic force is proportional to the voltage squared, we can plot the actuation force as a function of voltage and charge transfer factor k as in Figure 37. It can be seen that even a small degree of charge adsorption considerably reduces the available actuation force.

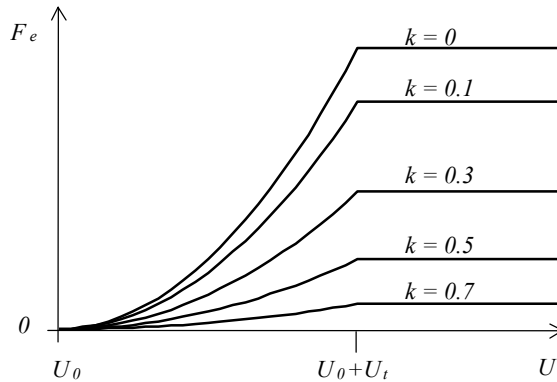


Figure 37. Effect of charge adsorption on the droplet actuation force.

As discussed in section 3.3.5, charge trapping occurs equally with DC and AC voltages at least up to a few kilohertz frequency. On the other hand, there are major differences in the charging properties between different materials. For example, if we consider the materials listed in Table 1 on page 81, we can conclude that only Teflon®AF [83] and paraffin [82] with $k = 0$ would be

acceptable choices for droplet actuation. With the second best material in Table 1, PP [82] with $k = 0.31$, it is possible to reach only half of the maximum force. Because charge adsorption may not be fully reversible, it is not wise to use voltages above the threshold, even if a material with $k = 0$ is used. As shown in Table 1, the reversibility of Teflon[®]AF is better, which suggests that it is a better choice than paraffin. Although charging effects have not been thoroughly considered in any previous droplet actuator publications, it is interesting to note that all of the groups who recently reported on work with droplet actuation have been working with Teflon[®] [20, 23, 25, 35].

Charging also causes saturation of the electrowetting effect, as discussed in section 3.3.6. Inserting equation (97) with $x = 0$ in equation (82), we can write the minimum possible contact angle at the droplet stopping position as

$$\cos\theta_e = \cos\theta_c + f. \quad (98)$$

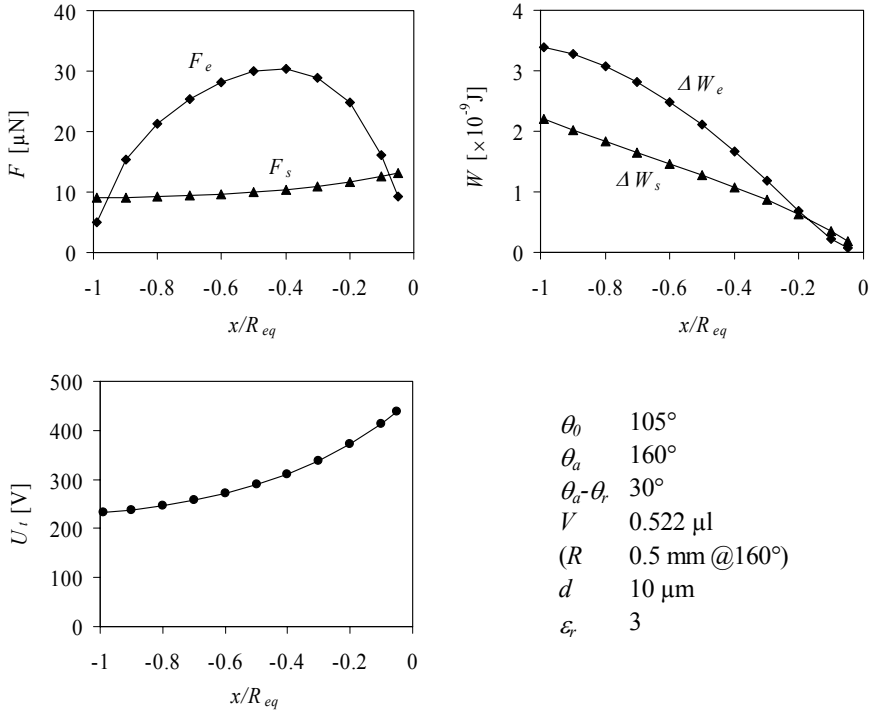


Figure 38. Effect of the charge adsorption threshold in droplet actuation.

Charging also influences the optimal electrode step. As shown in Figure 36, the threshold voltage U_t decreases as a function of $|x|$. In Figure 38 we have set the voltage at the starting point equal to U_t , given in equation (97). The contact angle hysteresis is larger than in the previous example in Figure 35. It can be seen that actuation is not possible if the electrode step is too low. The maximum usable voltage decreases as a function of $|x|$ and the optimal value for $|x|$ is around $0.5 R_{eq}$ in terms of force and around $0.7 R_{eq}$ in terms of energy.

3.4.6 Summary and limitations of the model

Like all models, the droplet actuation model of this work gives an idealised picture of the reality, and there are some limitations and edge conditions that need to be considered. First of all, the droplet shape is assumed to be a spherical cap. Actually the droplet is more or less distorted from the spherical shape due to external forces like gravity or electrostatic pressure. Some solutions for the droplet shape under gravity can be found from the literature [100, 101], but the shape cannot be given with a single formula. Thus the model of this work would have been too complicated to handle if true droplet shape had been used. Figure 39 shows schematically how the droplet shape is flattened due to gravity. The larger the droplet volume, the less it resembles a spherical cap. This means that the radius of the equivalent capacitor increases as a function of droplet volume at a higher rate than predicted by our model. Thus the model is more accurate with smaller droplets than with larger ones. This inaccuracy prevents us from getting any reliable results on droplet actuation as a function of droplet volume. The electrostatic pressure may also change the droplet shape, if very large electric fields are introduced, but the effects are only local and unstable, as discussed in section 3.2.1.

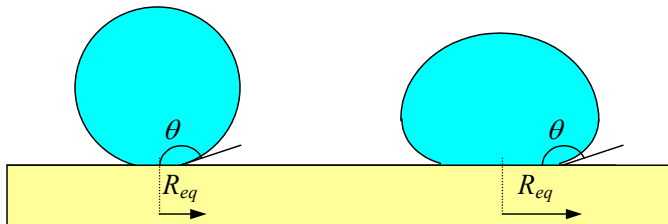


Figure 39. Effect of gravity on the shape of a droplet on a superhydrophobic surface.

Another significant approximation is the use of a segmented equivalent plate capacitor, as shown in Figure 28. With this approximation the electrostatic force becomes zero when $|x| > R_{eq}$. In practice, the force becomes asymptotically zero when $|x| \rightarrow \infty$. Thus the accuracy of the model is best with small values of x .

One practical phenomenon that may have a significant contribution in droplet actuation is dielectric breakdown, either in the insulator or in air. In our model, dielectric breakdown is neglected because it destroys the whole mechanism, and thus actuation must always be conducted under conditions where breakdown will not occur. On the other hand, dielectric breakdown has to be considered because of charge trapping. If the thickness and dielectric strength of the insulator are low enough, breakdown occurs below U_t , and charge trapping (in the sense we are interested in) does not occur at all. Inserting $U_t = E_b d$, where E_b is the breakdown field intensity, into equation (63), we can calculate the critical thickness as

$$d = \frac{2\gamma_{lv}}{\varepsilon_0 \varepsilon_r E_b^2}. \quad (99)$$

If the thickness of the insulator is below the value given in equation (99), dielectric breakdown may occur before charge trapping. This condition is strongly dependent on the insulator material used. Typical values of E_b for polymer materials are of the order of several hundred kV/cm [58], which gives a critical thickness of the order several tens of μm . On the other hand, with a good quality silicon dioxide, E_b is of the order of 9 MV/cm and further increases as the thickness falls below 100 nm [102], so that breakdown cannot be reached before U_t . In practice, it is possible to use good insulators such as silicon dioxide in combination with a hydrophobic polymer so that breakdown does not occur below U_t . If we limit the voltages in our model calculations to U_t , the dielectric breakdown can be neglected.

One of the major uncertainties in the model is the sliding force. It is determined by contact angle hysteresis, which is assumed to be constant. As discussed in section 3.3.3, liquid penetrates deeper into the surface pores of a superhydrophobic surface when the voltage is increased. Intuitively thinking, this increases the sliding force. Unfortunately, at present there is no good theory

on the subject, and it is impossible to estimate beforehand the strength of the effect. If this effect is large, the optimal electrode distance is smaller than analysed. Another parameter that is underestimated is the threshold voltage of actuation. Because the electrostatic pressure is a function of insulator thickness, the inaccuracy due to the sliding force is smaller with a larger insulator thickness. Despite all the limitations and inaccuracy in our model, it can be used to calculate various quantities from simple initial parameters. The initial parameters, auxiliary variables, and calculated quantities are summarised in Table 2.

Table 2. Parameters of the droplet actuation model.

Initial parameters	Auxiliary variables	Eq.	Calculated quantities	Eq.
Contact angle hysteresis	$\theta_a - \theta_r$	Contact angle at starting position	θ_e (82)	Electrostatic force F_e (74)
Droplet volume	V	Droplet radius	R (C10)	Electrowetting force F_{EW} (86)
Water surface tension	γ_v	Droplet contact radius	R_c (C3)	Electrostatic pressure P_e (94)
Insulator thickness	d	Area / radius of equivalent capacitor	A_{eq} (B2) R_{eq}	Sliding force F_s (4)
Insulator permittivity	ϵ_r	Segment area	A_x (C15)	Threshold voltage U_t of charge trapping (97)
Voltage	U			Minimum actuation voltage U
Droplet starting position	x			
Two of three:				
- Advancing contact angle	θ_a			
- Fractional area	f			
- Young angle	θ_0			

3.5 FE simulations

3.5.1 3-dimensional simulation

The purpose of FE simulations was to visualise the electric field around the droplet, and to get information about the influence of different parameters on the electrostatic force. One 3-dimensional simulation was carried out at Helsinki University of Technology using the ANSYS[®] tool. Figure 40 shows the model, and the parameters are given in Table 3. In this case the droplet was treated as a dielectric sphere. Otherwise the values of the parameters are close to those used in the experiments. Figure 41 shows the calculated electric field intensity in three cross-sections of the model. The maximum electric field intensity is 4.5×10^6 V/m, while the threshold field for electrostatic pressure effects, calculated in section 3.2.1, is 8.1×10^6 V/m. Thus the shape of the liquid-vapour interface is not modified in this case. Another effect, electrowetting, may have a contribution to the overall shape of the droplet, but it cannot be taken into account in the FE simulation.

The electrostatic force acting on the droplet was calculated with the Maxwell stress method (section 3.1.3), by summing the integrand of equation (16) over the elements of the droplet surface. As a result, the horizontal component of the force was 3.5 μ N. The result is of the same order of magnitude as that obtained in the model calculations. It should be noted that the electrode geometry was not exactly the same due to some idealisations applied to the model.

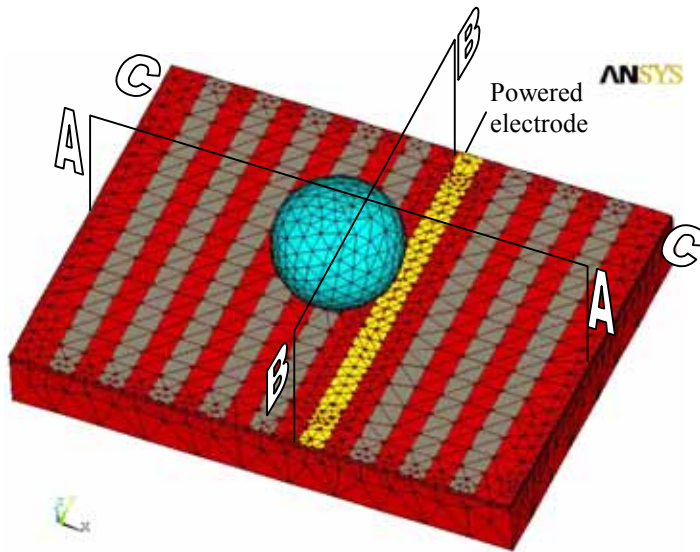


Figure 40. Model for 3-dimensional FE simulation. Air is not shown for clarity.

Table 3. Parameters of the 3-dimensional FE simulation.

R	0.5 mm
θ	160°
d	50 μm
x	400 μm
ϵ_r	80 (droplet) / 3 (insulator)
Electrode step / width	400 μm / 200 μm
U	500 V

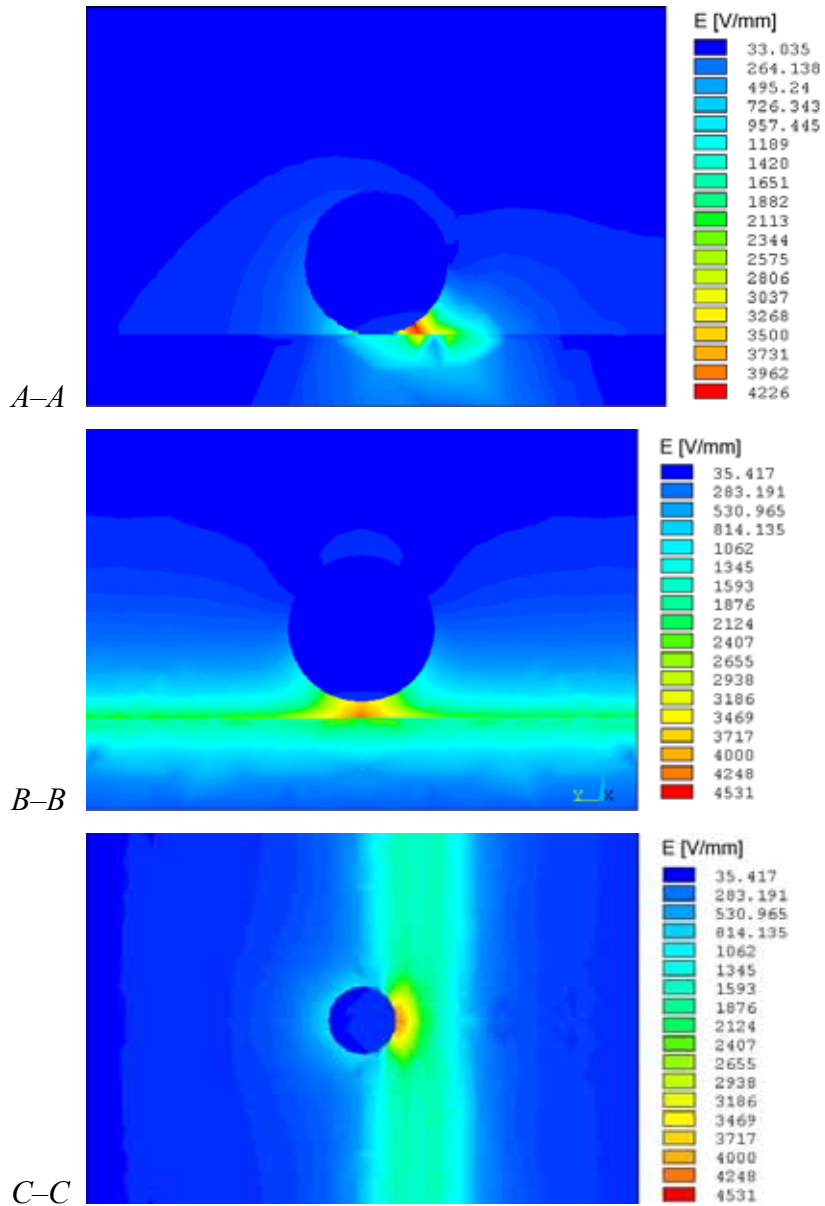


Figure 41. Simulated electric field around the droplet. The location of the cross-sectional planes is marked in Figure 40. C-C is the upper surface of the insulator.

3.5.2 2-dimensional simulations

Since the 3-dimensional simulation tool was not in house, more detailed simulations with variable geometries and electrode configurations were made using QuickField™, which is a 2-dimensional FE tool. The simulated plane was equal to A–A in Figure 40. Although some error was caused by the reduced dimensions, the use of this method was found reasonable, since it appears in 3-dimensional simulation that the maximum electric field is located within quite a narrow area near the centre axis of the droplet (Figure 41). Another advantage of Quickfield™ is that it is very fast and simple to use and the electrostatic force is calculated automatically with the Maxwell stress method. Generally, the droplet was treated as a dielectric body, and the parameters were the same as in the 3-dimensional simulation (Table 3), except that d , x and the electrode configuration were varied. An example is shown in Figure 42, with a meshed geometry and the calculated field in the form of equipotential lines.

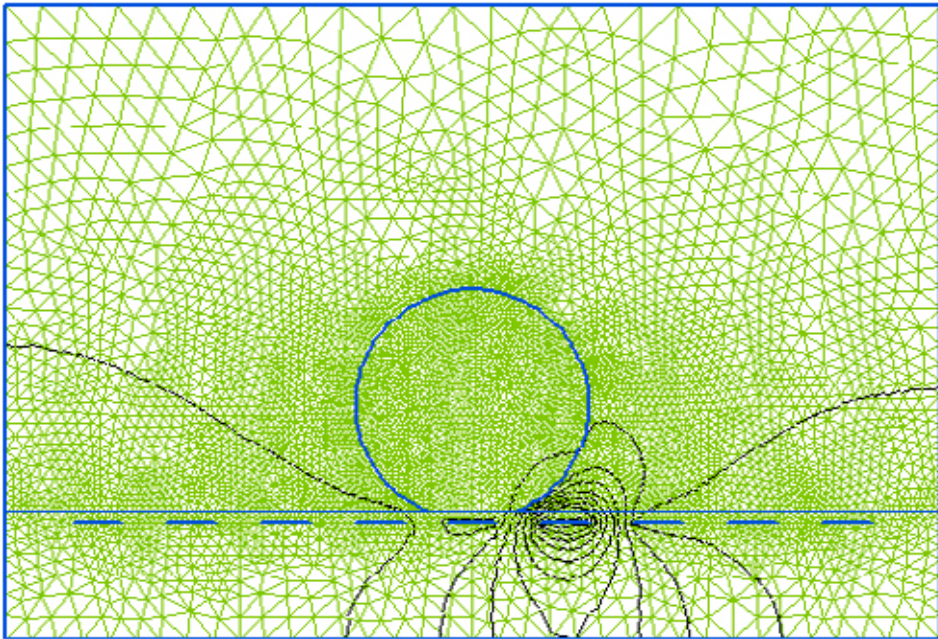


Figure 42. Example of a 2-dimensional FE simulation. The simulation parameters are the same as in Table 3. The lines represent equipotential lines with 50 V division.

It can be seen from Figure 42 that the droplet is a nearly equipotential body. This means that the droplet is quite close to a conducting shell. It was found that when the droplet is treated as a conductor the resulting force is roughly 10–20% larger than if it is treated as a dielectric sphere.

The main results of the 2-dimensional simulations were clarification of how the electrode configuration should be optimised to increase the electrostatic force. The effect of electrode width on the spacing ratio is shown in Figure 43. It can be seen that the electrode spacing should be minimised in order to maximise the force. When multiple electrodes are powered the force can be further increased, as shown in Figure 44.

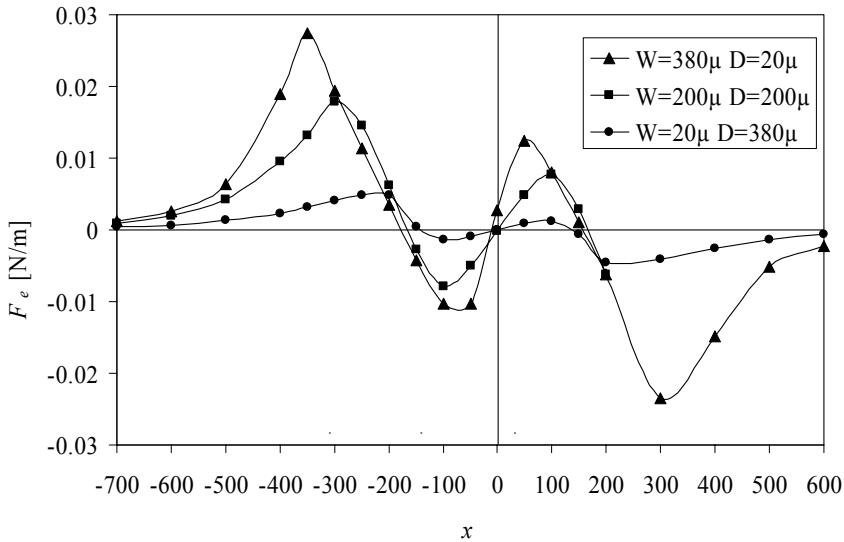


Figure 43. Electrostatic force as a function of droplet position. The parameters are the same as in Table 3, except that the electrode width (W) and spacing (D) are varied.

It can be seen that the electrostatic force shows a maximum at a certain x value. A similar feature was also found in the force calculated by the theoretical model (Figure 30 in section 3.4.1). Another interesting feature is that when a single powered electrode is used, the electrostatic force becomes zero in three values of x . It is not clear if this is a real effect or caused by the reduced dimensions in simulation, but it is a potential problem, since it means that there are three points

at which the droplet can stop. However, the point at $x = 0$ is unstable due to the direction of the force around that point. With positive values of F_e the force is directed towards increasing x , and with negative values the opposite happens. At any rate, multiple electrodes control does not show a similar feature, which is another advantage of the method. The best experimental results were achieved using multiple powered electrodes.

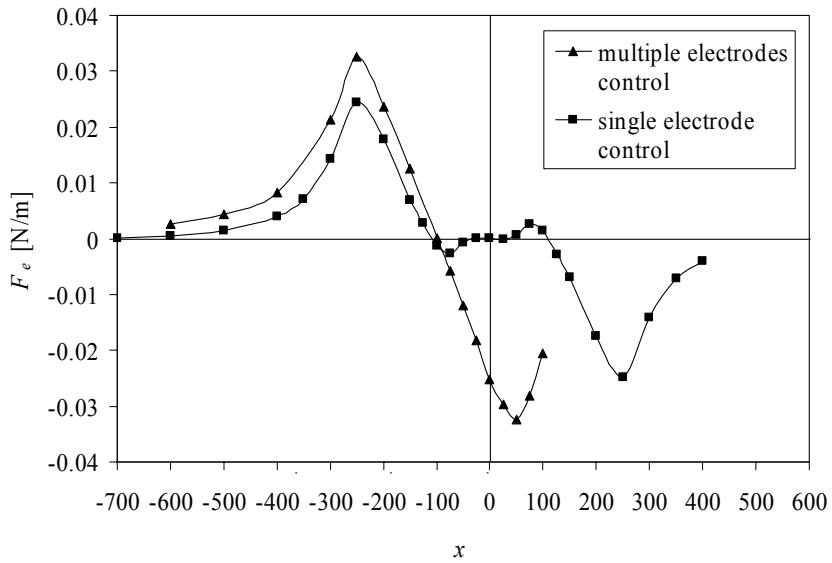


Figure 44. Electrostatic force as a function of droplet position. The parameters are the same as in Table 3, except that the electrode width is $380 \mu\text{m}$ and electrode spacing $20 \mu\text{m}$. With multiple electrodes control, 5 electrodes out of 10 are powered and the others grounded.

4. Experimental results and discussion

4.1 Setup and methods

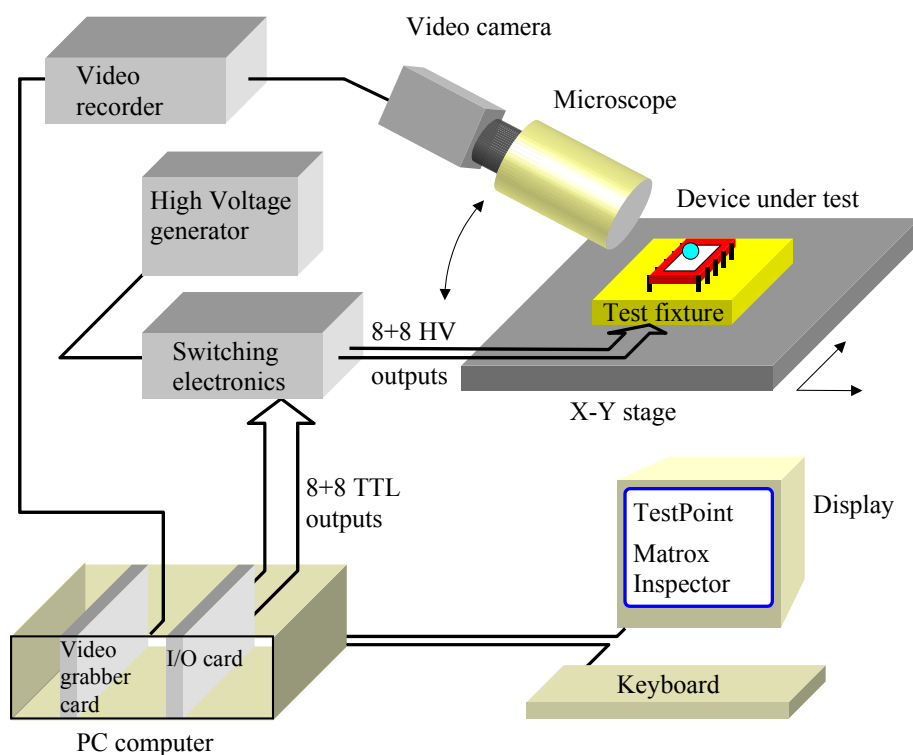


Figure 45. Test setup.

The experimental setup is shown schematically in Figure 45. To monitor the droplet motion, a tiltable zoom stereo Microscope was used and equipped with a video camera, which was connected to a video recorder and a PC with a digitizer card. The same PC was running measurement software (TestPoint) used for sequentially switching the actuation voltages through home-made switch electronics. Both relay and TRIAC based switching electronics with up to 8 + 8 output channels were used. The actuation voltages were generated using AC or DC high voltage sources. The whole equipment was placed in a cabinet with HEPA filtered laminar air flow to prevent pollution from dust.

The basic test liquid was deionised (DI) water, with resistivity $> 18 \text{ M}\Omega\text{cm}$. Tap water was also tested and worked equally well, but DI water was used because it is essentially free from impurities and does not form drying residues. Some buffer solutions of biochemical assay were also tested, and the results are reported further. Dosing the droplets on the surface was made either with a pipette, or a syringe connected with a flexible tube to a capillary needle made of glass, plastic or metal. With superhydrophobic surfaces, accurate dosing was found to be very difficult, because water does not adhere to the surface. In order to improve the dosing, coating of the needles with a hydrophobic material like AKD was used in some cases. If a syringe and needle was used, the droplet volume was calculated from the measured diameter and contact angle of the droplet. We also tested a commercial piezo-driven nanolitre pump (GeSiM), but this was not useful. Small droplets with a diameter of about $100 \mu\text{m}$ were emitted with such high speed that they were bouncing off the surface.

Contact angle measurements were made from the side view of a sessile droplet on a surface. In most cases the ratio between the contact radius and droplet radius was measured with image analysis software (Matrox Inspector) from the image captured on a PC. If the contact line was clearly visible, the angle was also measured directly by aligning the measurement cursors to match the contact angle. With tilted surfaces this was the only method used. The accuracy of the contact angle measurement is estimated as $\pm 2^\circ$ for angles of $< 160^\circ$. With larger values gravity widens the droplet contact area, which leads to underestimation of the contact angle.

Direct measurement of the contact angle hysteresis of superhydrophobic surfaces was difficult due to the inaccuracy of our method. Especially with rough surfaces, the contact line was not visible clearly enough. Therefore a sliding angle measurement was used instead. This gives the sliding force directly, which is of primary interest. A droplet of known volume was placed on a planar surface and the surface was continuously tilted until the droplet started to move. The accuracy of the sliding angle measurement was estimated to be $\pm 0.5^\circ$. If possible, the measurement of a sample was repeated several (3–5) times, and the average was calculated. On the other hand, contact angle hysteresis is a more convenient parameter than the sliding angle, since it can be given independently of the droplet volume. Thus the contact angle hysteresis was calculated from the measured droplet sliding angle and the droplet volume from equation (4).

4.2 Hydrophobic surfaces

In this section, the most important experiments with hydrophobic surfaces are reported. Development of the surfaces was carried out parallel to droplet actuation work and therefore all combinations of surfaces and actuator devices were not tested. Smooth surfaces are introduced first and they were used only with 1st generation droplet transport devices. Next the irregular superhydrophobic surfaces are discussed. The best of them were used in droplet actuation. The results of lithographically patterned surfaces are also presented although they were not applied for droplet actuation. The goal was to investigate their fabrication and study their behaviour. Finally, the compatibility of the best superhydrophobic surfaces with biological buffer solutions is reported.

4.2.1 Spin-coated Teflon[®] AF

Teflon[®] AF 1600 is an amorphous fluoropolymer product made by DuPont. Due to its good hydrophobic properties and relatively simple coating from solution, it is a very popular hydrophobic material for use with various droplet-based systems. The advancing contact angle reported by the manufacturer is 104° [103]. We used spin coated Teflon[®] AF with 1st generation transport devices. Teflon[®] AF, supplied as an 18% solution in Fluorinert[®] FC-75 (3M), was first diluted at a ratio of 1:4 with Fluorinert FC-75, then spin coated using 1000 rpm for 30 sec. Next the film was baked using the procedure recommended by the manufacturer. This resulted in a layer with thickness of around 1 µm. The surface was smooth at the microscopic scale, but had large-scale thickness variations of around 300 nm, giving the film a wavy appearance to the naked eye. Later it was found that the problem was probably too rapid drying, and smoother surfaces were obtained using a less volatile solvent (FC 70). These surfaces were not applied for droplet actuation. Dicing of the chips with Teflon[®] AF was also found difficult, as it appeared that the film was peeling off due to water spray during wafer sawing. Poor adhesion of Teflon[®] AF with silica has also been reported in the presence of water, despite pre-treating the silica surface with a fluorosilane compound [104]. This property of Teflon[®] AF is a potential problem for water droplet actuation. As there were no simple solutions in sight, cleaving was used instead.

Figure 46 shows a water droplet on spin-coated Teflon[®] AF. The advancing contact angle was measured around 110°. The average sliding angle of a 12 μ l droplet was 16°, which corresponds to contact angle hysteresis of 9°. Thus the average contact angle is close to the contact angle value given by the material supplier. The contact angle hysteresis is not given by the manufacturer, apparently because it depends on the surface condition and preparation method. Verheijen and Prins [83] report a hysteresis value of 7° for as-deposited spin coated Teflon[®] AF, and after impregnation with silicone oil the hysteresis was reduced down to 2°, which is the smallest value reported for this material. They propose that the effect is related to penetration of oil into nanopores of the layer.



Figure 46. Water droplet (diameter 2 mm) on spin coated Teflon[®] AF surface.

4.2.2 ICP fluoropolymer

The material referred to in this work as ICP fluoropolymer was deposited in an ICP (Inductively Coupled Plasma) type deep reactive ion etcher, by decomposing C_4F_8 (gas) in plasma. Blank ICP polymer is another hydrophobic material used with 1st generation devices and is discussed here separately to the patterned case. The polymer is originally used as a passivation layer to prevent sidewall etching of silicon. The resulting film is “Teflon-type” in terms of chemical resistance and hydrophobic properties. The thickness of the film deposited on the actuator wafers was 150 nm. Figure 47 shows a water droplet (diameter \sim 2 mm) on an ICP fluoropolymer surface. The surface is tilted to visualise the contact angle hysteresis. The advancing and receding contact angles of ICP fluoropolymer surfaces were measured instead of sliding angles. The average advancing contact angle of ICP fluoropolymer was 114° and contact angle hysteresis 23°. Thus Teflon[®] AF is a much better surface than the ICP fluoropolymer.



Figure 47. Water droplet (diameter 3.7 mm) on a tilted ICP fluoropolymer surface.

In order to study the origins of the large contact angle hysteresis, we studied the composition of the polymer with XPS (X-ray Photoelectron Spectroscopy) analysis. In Figure 48 we can see that the measured spectrum fits very well with four different type C-F bond energies. The peaks are slightly shifted, which suggests that the sample is charged. Even with the thinnest measured sample (50 nm) no signal was recorded from the underlying silicon surface, which proves that the film was uniform. The results indicate that the material is pure fluoropolymer, with no other substances. By comparison, the XPS spectrum of spin coated Teflon[®] AF shows only CF₃ and CF₂ peaks [105]. Thus, qualitatively speaking, ICP fluoropolymer is less fluorinated than Teflon[®] AF. However, the XPS analysis gave no information as to the origins of the hysteresis.

Later we tested the effect of various plasma treatments (Ar, O₂, SF₆), which could be performed in the same ICP reactor after deposition. The samples were characterised by measuring the advancing and receding water contact angles, but within the angle measurement accuracy no change in hysteresis with respect to the untreated film was observed.

ESCA CURVE FIT 12/29/87 ANGLE= 45 deg ACO TIME=12.69 min
FILE: Curve_Fit Si, 150 nm, 0
SCALE FACTOR= 0.047 k c/s, OFFSET= 0.000 k c/s PASS ENERGY= 35.750 eV Al 300 W

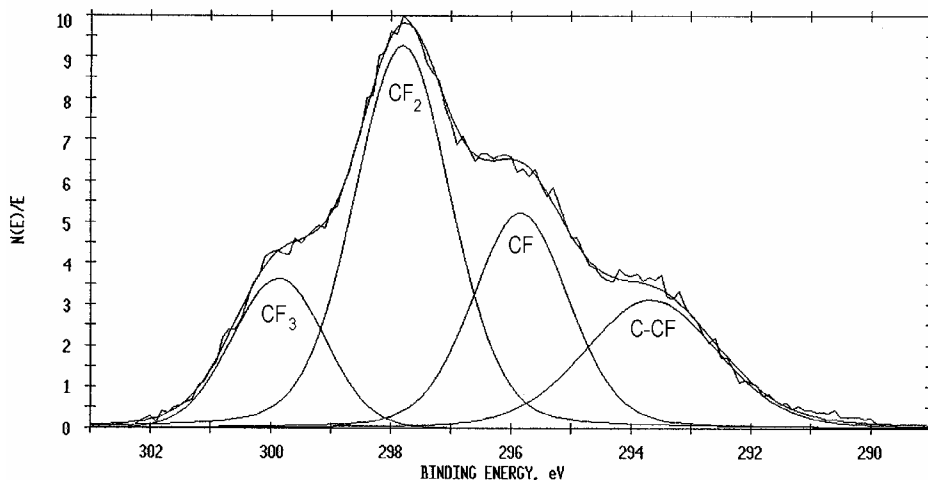


Figure 48. XPS analysis results with ICP plasmapolymer.

4.2.3 Sprayed AKD

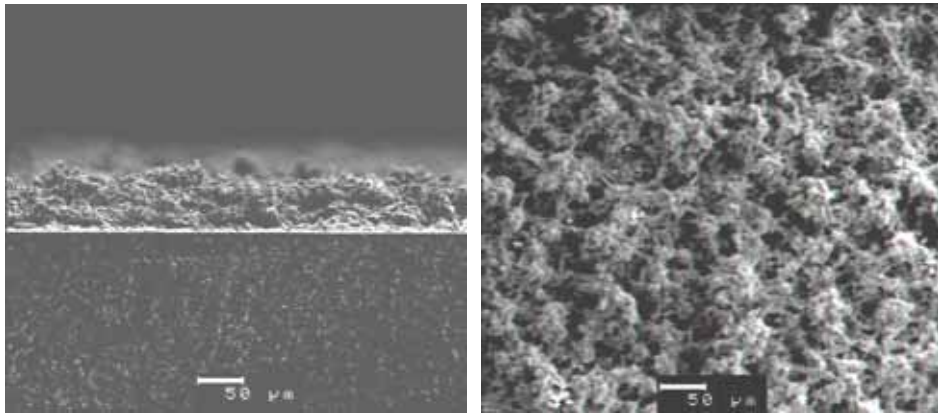
AKD is a wax-type material used as a paper-sizing agent to make paper more hydrophobic. We used a hydrolysed AKD powder (RAISARES A, Raisio Chemicals) as a starting material to achieve a rough superhydrophobic AKD surface. Shibuichi et al. [106] have reported that AKD forms a fractal rough surface when solidified from the melt. A contact angle of 174° and very small tilting angle were achieved, which indicate superhydrophobic properties. Shibuichi et al. [106] measured a Young contact angle of 109° for the AKD, which was synthesised by the authors. We measured advancing and receding water contact angles of 107° and 93° for our AKD, as a smooth layer molten and poured on a clean silicon wafer. After cooling, the solidified AKD layer was carefully detached from the wafer, so that the surface in contact with the silicon wafer during cooling could be measured.

In order to form superhydrophobic layers, we first tried spin-coating the melted AKD, but this was not successful. The layer was not uniform and showed improved wetting characteristics only in a narrow radial area. Two other

methods, spraying and evaporating, appeared to be more useful instead. Sprayed AKD was used successfully with 2nd generation actuator devices. The sprayed AKD surfaces were fabricated by melting AKD and dissolving it in warm chloroform to a ratio of 1 : 6 and spraying the warm solution with an airbrush (Badger 200G). The control and reproducibility of this method is not very good, as the structure and thickness of the resulting layer depends on many parameters such as adjustments to the airbrush, spraying time, spraying distance, hand motion, and temperature of the solution. On the other hand, AKD layer formation is easily visible to the naked eye due to its mat white appearance. The hydrophobic properties can also easily be tested during surface fabrication, and spraying can be continued until the water repellence is good enough. Generally, it was found that the best surfaces were obtained when large amounts of thin layers were deposited using a scanning motion of the brush at a distance of 20–30 cm from the sample.

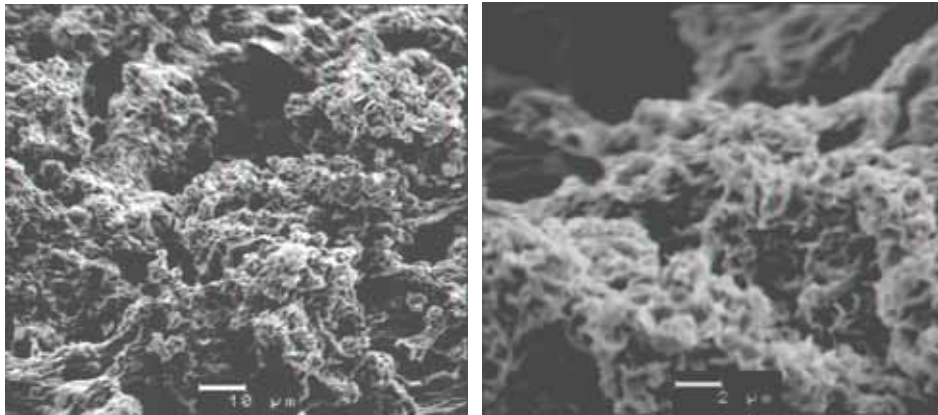
The sprayed AKD resulted in a very rough surface, as shown in the SEM photographs of Figure 49. The surface is actually porous, with the effective pore size varying in μm up to tens of micrometres. This kind of surface can be also considered as a fractal surface. Due to the high degree of roughness it is not easy to determine the thickness of the coating. It is possible to consider an effective thickness, which is determined by the average level of water membranes, when a droplet is placed on the surface. From the SEM micrographs it was estimated that the effective thickness is of the order of 60 μm . In addition to the normal roughness there were some larger surface bumps about 100 μm high, presumably as artefacts of the spraying process. Deposition of AKD also occurs on the inside surfaces of the spray nozzle, and particles may detach and fly onto the surface.

Advancing contact angles between 150–160° were measured for sprayed AKD surfaces. The average sliding angles of 1 μl and 5 μl water droplets were measured as 14° and 4.7°. Calculated from equation (4) with $\theta_a = 155^\circ$, the sliding angle values correspond to contact angle hysteresis of around 7°. Figure 50 shows a water droplet on a sprayed AKD surface.



(a)

(b)



(c)

(d)

Figure 49. SEM photographs of sprayed AKD surface. a) side view, b) top view, b) and c) tilted views.



Figure 50. Water droplet (diameter 2 mm) on sprayed AKD surface.

4.2.4 Evaporated AKD

The best hydrophobic surface in terms of droplet motion was evaporated AKD, and it was used with 2nd and 3rd generation actuator devices. It was fabricated using a resistive-heating vacuum evaporator (Balzers). A droplet actuator device was placed about 50 mm from the crucible, where approximately 2 cm³ of hydrolysed AKD powder was loaded. The chamber was pumped down to $< 10^{-5}$ Torr, and the heating power was increased until the AKD started to evaporate. The evaporated AKD surface was much thinner and showed much smaller scale roughness than the sprayed one, as shown in Figure 51. The large-scale roughness in Figure 51a originates from the substrate of the sample (cellulose acetate tape). The largest magnifications reveal that the surface consists of thin hexagonal crystals with a diameter of 1–2 μm and thickness of about 0.1 μm . The crystals are partially merged, but preferentially located so that the thin side is perpendicular to the surface. Thus the surface is close to a pillar configuration with a characteristic surface dimension of about 0.1 μm . The effective thickness of the layer was estimated to be about 3 μm .

The advancing contact angle of the evaporated AKD was roughly the same as with the sprayed AKD (150–160°). If the surface is approximated as a pillar configuration with $D_s = 0.1 \mu\text{m}$ and $\theta_0 = 107^\circ$, it can be calculated from the Cassie and Baxter equation (7) that $f = 0.09$ – 0.19 , and from equation (11) that $P_c = 20$ – 80 kPa. The sliding angles of 1 μl and 5 μl water droplets were measured as 11° and 2.7°. Calculated from equation (4) with $\theta_a = 155^\circ$, the sliding angles correspond to a contact angle hysteresis of 5° and 4°, respectively. The difference between hysteresis values for 1 μl and 5 μl droplets indicates a droplet size effect, discussed in section 4.3.11, but it can also be explained in terms of measurement uncertainty. The main difficulty was to dispense small droplets on superhydrophobic surfaces. Because water adhesion to the pipette head is much stronger than adhesion to the surface, some liquid may remain in the pipette, making the actual droplet size smaller than that set by the pipette. Furthermore, the surface properties are not uniform and droplets are likely to be deposited in places that are less hydrophobic than the surroundings. Because smaller droplets are more difficult to dose than larger ones, both mechanisms lead to overestimation of sliding angles of small droplets. In conclusion, the evaporated AKD was somewhat more water-repellent than the sprayed one. Figure 52 shows a water droplet on an evaporated AKD surface.

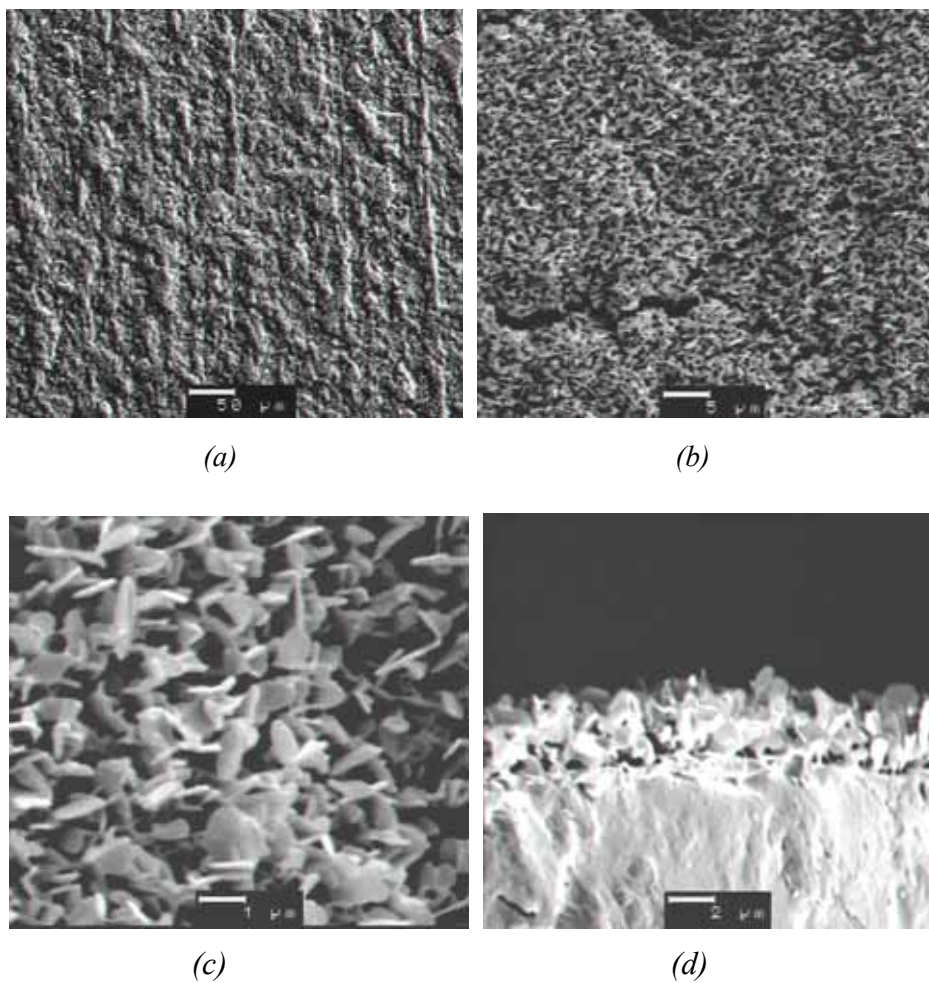


Figure 51. SEM photographs of evaporated AKD surface. a) b) and c) top views, d) side view.



Figure 52. Water droplet (diameter 2 mm) on evaporated AKD surface.

4.2.5 Sprayed Teflon[®] AF

Sprayed Teflon[®] AF was used as a surface only with 4th generation devices. Teflon[®] AF 1600 provided by DuPont was diluted with Fluorinert FC 77 (3M) to give a final concentration of solids in the sprayed solution of roughly 3%. FC 77 is more volatile than FC 75, and gave somewhat better results. The solution was sprayed using the same equipment and setup as for AKD spraying (section 4.2.3).

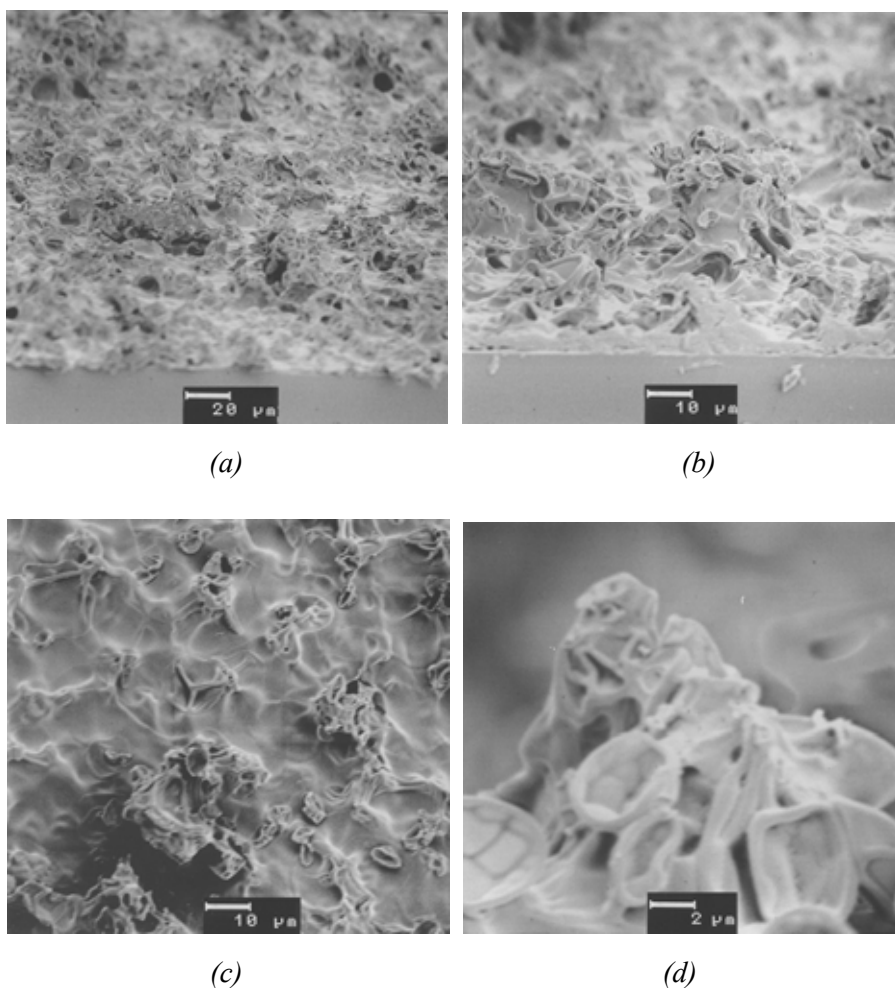


Figure 53. SEM photographs of sprayed Teflon[®] AF. a), b), d) side views, c) top view.

Figure 53 shows SEM photographs of sprayed Teflon[®] AF. The large scale roughness is comparable to that of AKD deposited using the same method, but the minimum pore size is larger, as shown at the highest magnification. Figure 53c also reveals some fairly smooth areas.

The advancing contact angles of sprayed Teflon[®] AF were approximately the same as with the sprayed and evaporated AKD (150–160°). The sliding angles of 1 μ l and 5 μ l water droplets were measured as 7.7° and 3.2°. Calculated from equation (4) with $\theta_a = 155^\circ$, the sliding angles correspond to a contact angle hysteresis of 4° and 5°, respectively. Thus the sprayed Teflon[®] AF was roughly as good as the evaporated AKD. Figure 54 shows a water droplet on sprayed Teflon[®] AF.



Figure 54. Water droplet (diameter 2 mm) on a sprayed Teflon[®] AF surface.

4.2.6 Plasma-etched Teflon[®] AF

Plasma treatment is a well-known method for modifying the wetting properties of polymer surfaces [50]. M. Morra, E. Occhiello and F. Garbassi have reported that a long enough O₂ plasma treatment of PTFE results in a composite surface with superhydrophobic properties [107]. We tried the same method for Teflon[®] AF. First a thick layer of Teflon[®] AF (18% solution in Fluorinert[®] FC-75) was poured on a silicon wafer and cured. The thickness of the layer was approximately 50 μ m. Next the wafer was etched for 12 min in a parallel-plate plasma reactor (Electrotech) with pressure 15 mTorr, O₂ flow 8 sccm, and power 100 W. The parameters and time were the same as used by Morra, Occhiello and Garbassi [107]. Before processing the sample wafer, the etch rate of Teflon[®] AF was tested using a thinner film, and a value of about 1 μ m / min was obtained.

The resulting film consisted of needle-like structures with diameters in the sub-micrometer range, as shown in Figure 55. The result is completely different from that of Morra, Occhiello and Garbassi [107], who obtained a swamp-like porous structure. Unfortunately, the thickness of the original surface or local etch rate of the material varied so much that in some portions the surface was etched away.

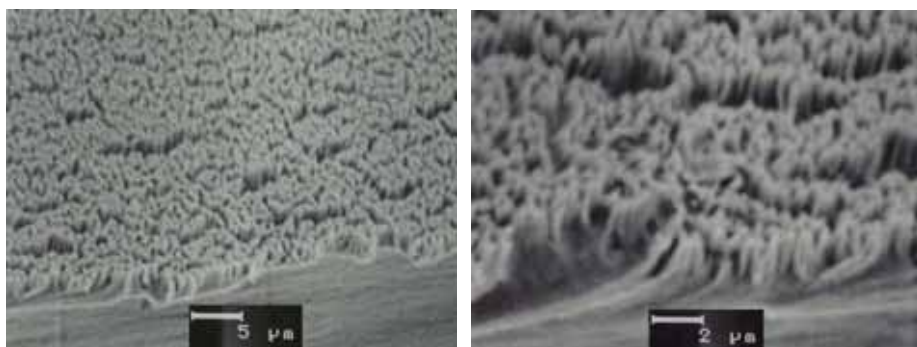


Figure 55. SEM photographs of O₂ plasma-etched Teflon[®] AF.



Figure 56. Water droplet (diameter ~1.6 mm) on vertically tilted O₂ plasma-etched Teflon[®] AF.

The resulting film did not show superhydrophobic properties due to large contact angle hysteresis. Advancing contact angles were between 150 and 160°, and the contact angle hysteresis was about 30°. In sliding tests, droplets with volume less than 2.5 μl did not slide at any tilting angle, as is shown in Figure 56. The large hysteresis is probably related to the geometrical microstructure of the surface. It was noticed in the SEM investigations that the tips of the needle-like surface structures were cone-shaped. Apparently, the slope angle of the tips is

too small to achieve a composite surface condition. Since the results were not encouraging, this method was not developed further.

4.2.7 Lithographic patterning of Teflon[®] AF

With lithographic patterning, it is possible to fabricate superhydrophobic surfaces that are more uniform than irregularly rough surfaces. This is a great advantage in droplet actuation, since the weak surface points can more easily be avoided, but there are some challenges, too. The fundamental requirement is that the pattern must have nearly vertical side walls. Another requirement, which is especially critical in electrostatic droplet actuation, is that the surface dimensions should be as small as possible in order to maximise the critical pressure.

The most straightforward approach is direct patterning of a hydrophobic material. This was tested with Teflon[®] AF using the process shown in Figure 57. Since spin coating of smooth and thick Teflon[®] AF layers was found to be difficult, the layer was formed on silicon wafers either by dip coating or by spraying followed by smoothing at 330°C. The resulting film thickness was about 5 µm. The adhesion of photoresist to Teflon[®] AF was so weak that full coverage could not be achieved. This problem is also known in the literature, and Cho, Wallace, and Files-Sesler have reported two methods – short etch in O₂ plasma and addition of fluorosurfactant into photoresist – to improve the adhesion between Teflon[®] AF and photoresist, but both had serious drawbacks. [105]. O₂ plasma also increased the surface roughness, and the (equilibrium) water contact angle decreased from 105° to 93°. Contact angle hysteresis was not reported, but it most probably increased due to the increased roughness. Addition of surfactant resulted in a rough photoresist surface, which may be a problem if very small features are to be patterned. Since both of the above methods were problematic, we decided to use a 50 nm thick layer of sputtered aluminium as a mask layer. The Al mask was pattern etched and stripped using a commercial phosphoric acid-based wet etch. Teflon[®] AF etching was performed using the same equipment and recipe as that used in the O₂ plasma treatment discussed in section 4.2.6.

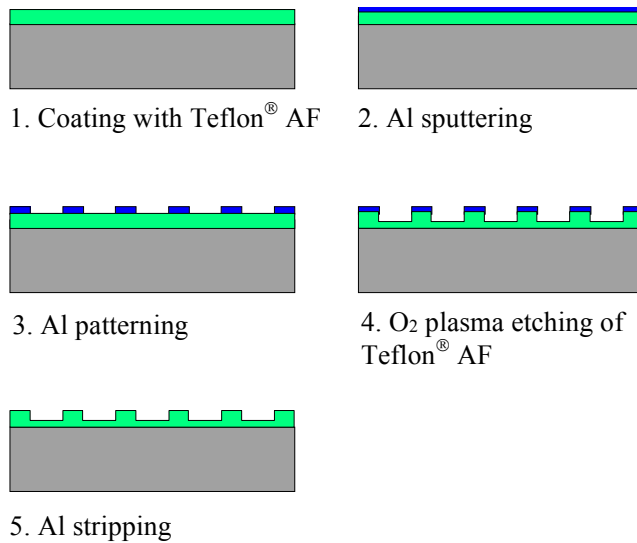


Figure 57. Lithographic patterning of Teflon[®] AF.

Figure 58 shows an SEM photograph of the sample before stripping off the aluminium. The quality of the photograph is not very good due to sample charging, but it can be seen that the etched areas are covered by a very fine grass-like residue. This is a well-known side-effect in plasma etching, called micromasking. It is caused by the deposition of small particles which locally prevent etching of the surface. The structure resembles that obtained with a longer blanket O₂ plasma treatment, discussed in section 4.2.6, but on a smaller scale. In fact, the grass-like structure in a hydrophobic material is a nano-scale pillar structure that should act as a superhydrophobic structure. Superhydrophobic properties of a surface fabricated using this kind of micromasking method have been reported by Kim and Kim [108].

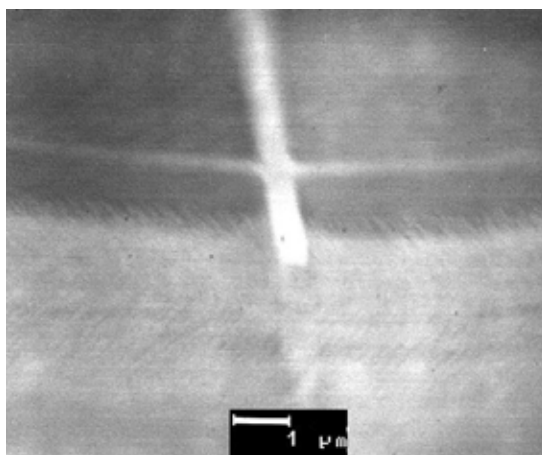


Figure 58. SEM photograph of patterned Teflon[®] AF.

To our surprise, the sample was not superhydrophobic but showed increased adhesion compared to the untreated Teflon[®] AF. Later it was found from the literature that aluminium reacts with Teflon[®] AF to form AlF_3 [109]. Similar reactions were also observed between Al and some other fluoropolymers [110]. The chemical nature of AlF_3 is not clear to us, but it could possibly be the reason for increased surface energy.

In conclusion, lithographic patterning of low energy fluoropolymers is not a straightforward task. One possibility might to use some other masking material than aluminium. For example, Wu et al. [109] have reported that silver, copper and gold do not react with Teflon[®] AF. Since deposition and etching of these materials was not possible using our standard processes, further experiments with patterning of Teflon[®] AF were not carried out.

4.2.8 Structured silicon surfaces with ICP fluoropolymer

Another approach to fabricate lithographically defined superhydrophobic surfaces is to form the surface profile from a suitable material and coat the surface with a low energy material. With this method, the problems of patterning of low energy material are avoided. This was tested using single-crystal silicon as a starting material. The basic process used is shown in Figure 59. Both grid and pillar type patterns were used, the dimensions of which are given in Table 4.

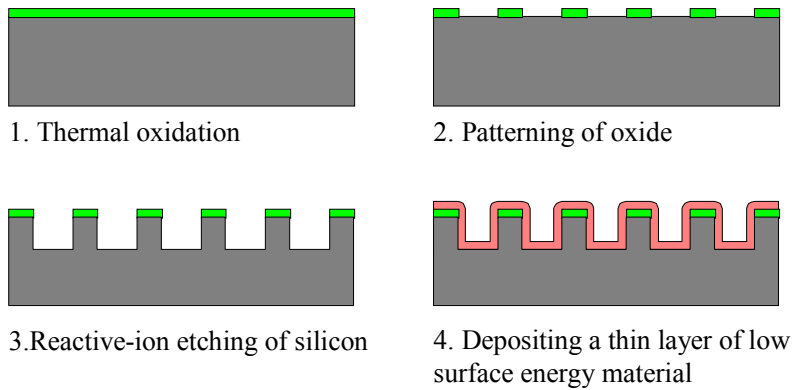


Figure 59. Fabrication of structured silicon surfaces.

The benefit of silicon is that wafers can easily be patterned lithographically, and various etch methods to form well-defined side wall profiles are available. One drawback is that silicon is conductive and does not therefore work with underlying electrodes. In the final application, the silicon should be replaced with a thick non-conductive material, which could be deposited on the electrodes. The simplest way would be to use of a photosensitive polymer like photoresist as a structuring material. Unfortunately, photoresist patterns usually have more or less sloped side walls. On the other hand, with a negative resist the side walls are sloped inwards, which could make it suitable for the purpose. Unfortunately, only positive photoresist was available in our standard process, and the side walls were too strongly sloped.

Table 4. Dimensions of lithographically patterned surfaces.

Pattern	D_s [μm]	W_s [μm]	F
Grid	1	1.5	0.44
	1	4	0.36
	1	9	0.19
	1	19	0.098
Pillars	1	9	0.01

Two low-energy materials were tested with the silicon structures. The first material was ICP fluoropolymer. The grid surfaces were etched with an ICP type deep-reactive ion etcher (STS), and the fluoropolymer deposition was done with the same equipment. With the pillar samples the process was otherwise the same, but they were etched with a parallel-plate reactor (Plasmatherm), and the mask oxide was stripped and a thin thermal oxide (~50nm) was grown before coating with the hydrophobic material. SEM photographs of the fabricated surfaces are shown in Figure 60.

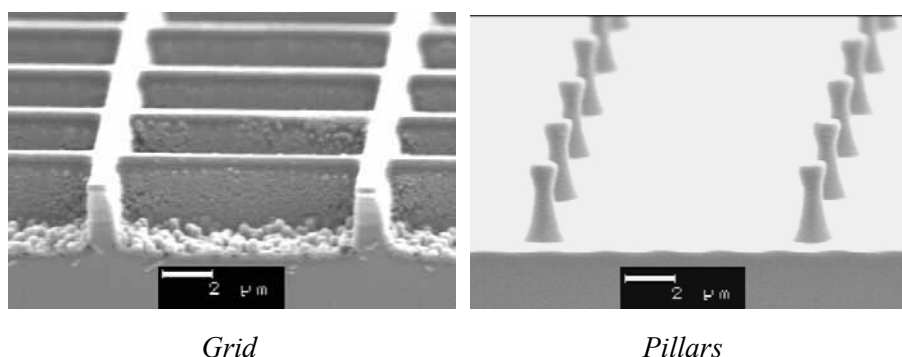


Figure 60. SEM photographs of structured silicon surfaces with ICP fluoropolymer coating.

The overall side-wall profile is straighter with the ICP etched surface. Actually, this should not be important since the microscopic radius of curvature in the corners of the structure determines the position of the liquid membranes. The critical condition for a composite surface is that the maximum slope angle is high enough, and with both surfaces the maximum slope is above 90° near the corner of the structures. The etch depth was about $3 \mu\text{m}$, and the ICP fluoropolymer thickness was 100 nm with grid patterns and 75 nm with the pillar pattern.

The measured contact angles are presented in Figure 61 and photographs of water droplets on the surfaces are shown in Figure 62. Values for a smooth (planar) ICP fluoropolymer surface are shown for comparison. It can be seen that the advancing contact angle of the grid surfaces obeys quite well the Cassie and Baxter equation (7), while the pillar surface has a lower contact angle than expected. As explained in section 4.1, our method underestimates large ($>160^\circ$)

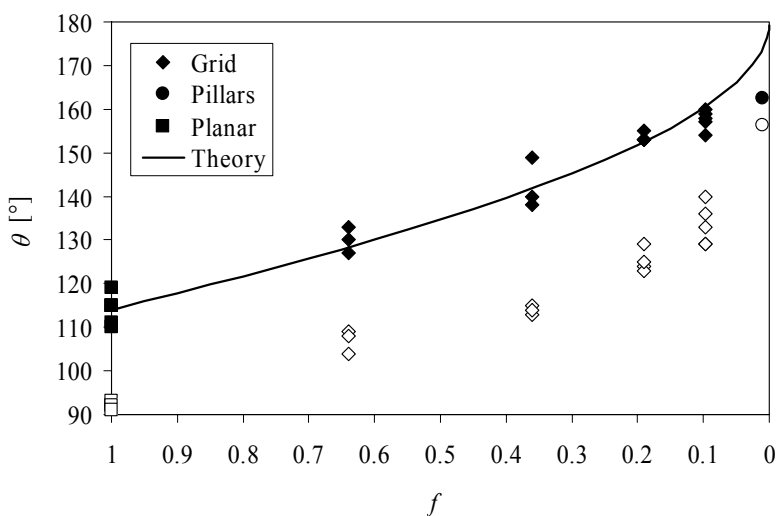


Figure 61. Measured contact angles of structured silicon surfaces with ICP fluoropolymer coating. Solid markers are advancing angles, open markers receding angles, and the line represents the Cassie and Baxter equation (7) with initial contact angle 114° .

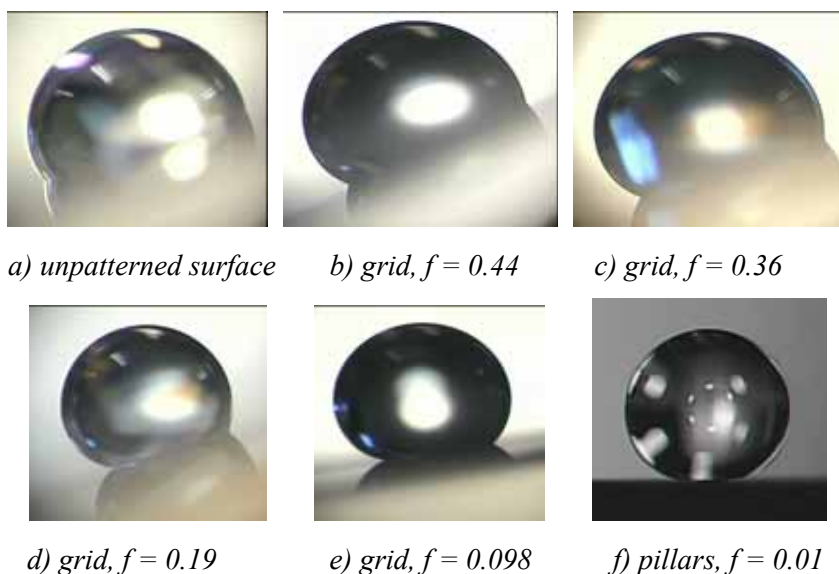


Figure 62. Water droplets on structured silicon surfaces with ICP fluoropolymer coating. The diameters of the droplets are a) 3.6 mm, b) 3.6 mm, c) 3.6 mm, d) 2.9 mm, e) 2.8 mm and f) 1.5 mm.

contact angles. It should be noted that only one value was obtained from the pillar surface. The measurement was very difficult due to low critical pressure of the surface. Usually the droplets collapsed when trying to dispense them on the surface. Using a specially fabricated thin capillary needle and very careful dispensing, one droplet could be obtained. Theoretically, the contact angle of the surface is 174° and critical pressure of the order of 1200 Pa, so that droplets with diameter <2 mm should be supported by the surface. In practice it is very difficult to apply droplets so that no extra force is directed towards the surface. Thus the low critical pressure of the pillar surface makes it practically useless. In order to apply the surface in droplet actuation the surface dimensions must be changed.

4.2.9 Structured silicon surfaces with FAS coating

Another hydrophobic material that was combined with the structured silicon was fluoroalkylsilane (FAS). The silicon substrates were fabricated similarly to the pillar-type silicon surfaces with ICP fluoropolymer. The FAS material was fabricated using the so-called Sol-Gel method. One molar part of triethoxy-1H,1H,2H,2H-perfluorodecyl)silane and 23.6 molar parts of IPA (isopropyl alcohol) were mixed and stirred at room temperature for 2 h. Then 3 molar parts of 0.1M HCl was added and the mixture was left to react for one day. The solution was filtered with a Whatman \varnothing 0.2 μm PTFE membrane filter and sprayed onto the silicon surfaces and sintered using a 20 min thermal cycle with maximum temperature of 360°C . The coating was repeated twice on the samples to remove possible pinholes. SEM photographs of the structures are shown in Figure 63.

The measured contact angles of the FAS coated silicon surfaces are shown in Figure 64. The non-structured surface is termed “planar” and shows an advancing contact angle of 106° , which is smaller than with ICP fluoropolymer (114°), but the average hysteresis (23°) is the same. The contact angle values of the FAS grid surfaces are close to those of the ICP fluoropolymer grid surfaces, but the FAS pillar surface is somewhat better than the ICP fluoropolymer pillar surface. First of all, it was easier to apply droplets to the surface, which indicates that the critical pressure is higher. Droplet collapse was still quite often observed. An example is shown in Figure 65, where a droplet is pushed towards the surface.

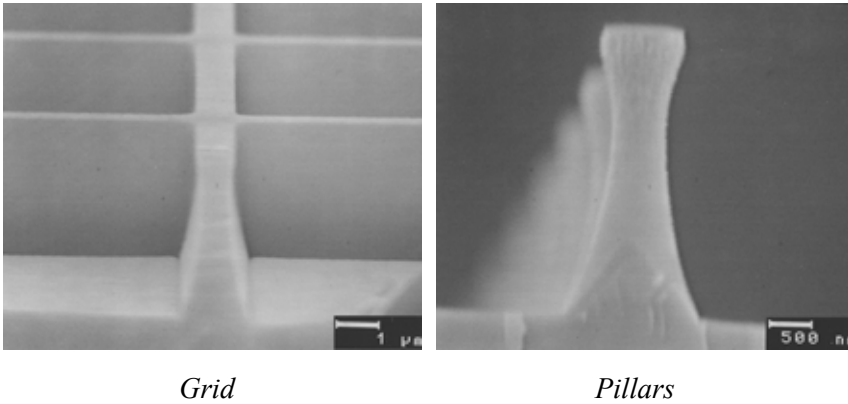


Figure 63. SEM photographs of FAS-coated silicon structures.

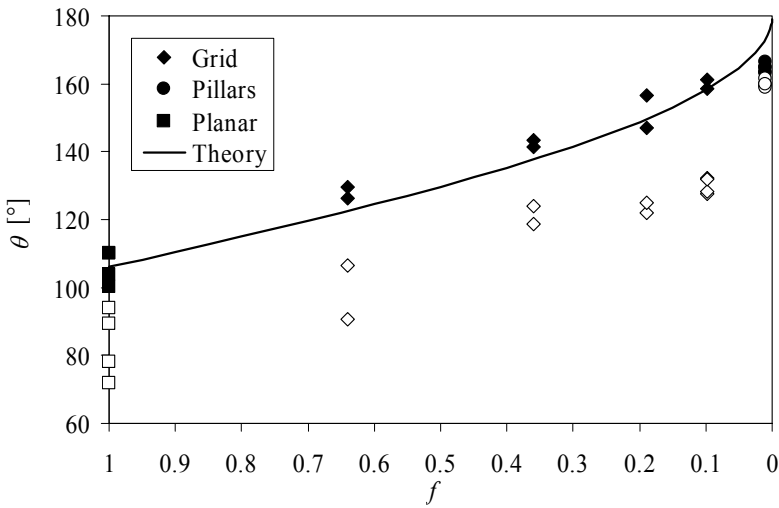


Figure 64. Measured contact angles of structured silicon surfaces with FAS coating. Solid markers are advancing angles, open markers receding angles, and the line represents the Cassie and Baxter equation (7) with initial contact angle 106° .

In theory, the smaller advancing angle should lead to a lower critical pressure. It was speculated that the FAS coating was thicker than the ICP fluoropolymer coating, which leading to larger D_s . However, FAS pillar surfaces should have 20% larger D_s than with ICP fluoropolymer surfaces to compensate for the difference in advancing angles, but such a difference was not observed in the

SEM photographs. Thus it can be only concluded that the Sol-Gel FAS is somehow a better surface than the ICP fluoropolymer, but the reason is not clear.

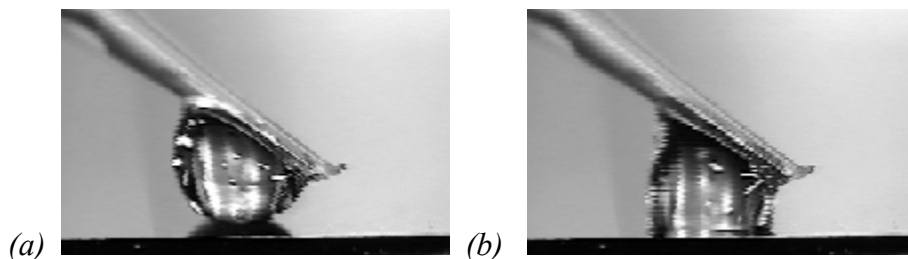


Figure 65. Exceeding of the critical pressure during droplet dispensing on a pillar FAS surface¹. a) Droplet touches the surface. b) Droplet collapses.

The average advancing angle was 165° , and the calculated contact angle hysteresis of the FAS pillar surface was 5° (with average droplet volume of $1.6 \mu\text{l}$), which means that the sliding force is comparable to the best irregularly rough superhydrophobic surfaces (evaporated AKD and sprayed Teflon[®] AF). Figure 66 shows a tilting test of a pillar/FAS surface. It does not show the lowest observed sliding angle, but does show very clearly the advancing and receding contact angles. These values can be compared with the contact angle hysteresis calculated from the sliding force using equation (4). Direct estimation gives contact angle hysteresis between 4 and 11° and the calculated value for this particular droplet is 5° . Thus both methods give quite similar results.



Figure 66. Droplet (diameter 1.4 mm) sliding on a tilted pillar FAS surface¹.

¹ The experiment is available as a movie file. See the table of contents.

A feature that is quite similar to the ICP fluoropolymer and FAS coated silicon structures is the behaviour of the contact angle hysteresis. It seems that the hysteresis is roughly constant with the non-patterned and grid surfaces, but much smaller with the pillar surface. The difference between hysteresis of pillar and grid surfaces has also been discussed by Chen et al. [44], who claim that the receding angle of the grid pattern is equal to that of a smooth surface. Our results show that the hysteresis is not that high, but still too large to show superhydrophobic behaviour. The pillar surface is clearly superhydrophobic, but the low critical pressure is too low for droplet actuation. Fortunately the critical pressure can be significantly increased by making f larger. As discussed in section 4.2.4, it was estimated that the evaporated AKD had f of the order of 0.1. It can be concluded that lithographic patterning with resolution of the order of 1 μm could possibly be used to make superhydrophobic surfaces for droplet actuation, and further experiments with new pillar patterns should be made.

4.2.10 Structured silicon with nanoporous Al_2O_3 and FAS

A combination of irregular and regular surface roughness was tested by applying a porous Al_2O_3 layer on structured silicon surfaces before FAS coating. Al_2O_3 can be formed using a Sol-Gel process, and made porous by boiling in water. Such a surface has been reported by Tadanaga, Katata, and Minami [111], and with FAS coating super water-repellent properties with advancing and receding contact angles of 168° and 150° were obtained. The porous Al_2O_3 was fabricated from aluminium tri-sec-butoxide [$\text{Al}(\text{OBu}^s)_3$], ethyl acetoacetate (EtAcAc), 0.1M HCl and isopropyl alcohol (IPA) in molar ratios of 1 : 1 : 4.1 : 25.5. $\text{Al}(\text{OBu}^s)_3$ and half of the IPA were mixed and stirred at room temperature for 1 h. Then EtAcAc was added and the mixture was stirred for 3 h. Finally HCl, diluted with the remaining IPA, was added and the solution was left to react for 24 h. The solution was filtered with a Whatman \varnothing 0.2 μm PTFE membrane filter and spin coated on the silicon surface samples using 4000 rpm for 30 s. Next the samples were sintered using a 20 min thermal cycle with maximum temperature of 360°C . The samples were then boiled in distilled water for 5 to 30 min to introduce roughness, and sintered again. Following this step the Sol-Gel FAS coating was applied. SEM photographs of the fabricated samples are shown in Figure 67; the porous layer is seen to cover the side walls of the structure very well.

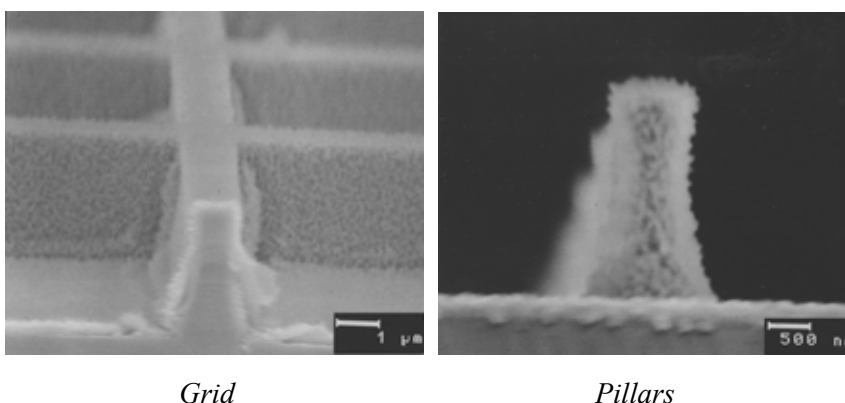


Figure 67. SEM photographs of porous Al_2O_3 + FAS coated silicon surfaces.

Figure 68 shows the measured contact angles of the surfaces. The porous Al_2O_3 layer increased the advancing contact angle of unpatterned FAS surfaces to 125° , but the contact angle hysteresis did not seem to change. Compared to the values obtained by Tadanaga, Katata, and Minami [111] the surface is not very good, and definitely not superhydrophobic. Actually, the droplet sliding resistance was increased due to incorporation of the porous layer. This is shown clearly in Figure 69. A droplet on a plain non-structured FAS surface slides with a tilt angle of about 45° , but a droplet with equal volume, placed on an FAS surface with porous Al_2O_3 underneath, is stuck even with a tilt angle of 90° . This suggests that the true hysteresis of an Al_2O_3 coated surface is greater than the value obtained in the measurement. The explanation is that even vertical tilting does not induce large enough droplet displacement to reveal the receding angle.

With the grid surfaces, the results were more scattered than without Al_2O_3 and no improvement in contact angles was observed. The pillar surface appeared as non-composite, so that all droplets collapsed, and showed contact angles similar to a non-structured surface. In theory, the increase in advancing angle should increase the critical pressure. Apparently the porosity of Al_2O_3 is not steep enough to achieve a composite solid-liquid interface. It is also possible that the FAS layer does not perfectly cover the porous Al_2O_3 surface, leaving some high energy areas visible. This problem has been observed in SEM/EDX studies of other non-structured samples. It can be concluded that fabrication of superhydrophobic surfaces from porous Al_2O_3 is not yet controlled well enough, and future work is needed to improve the process.

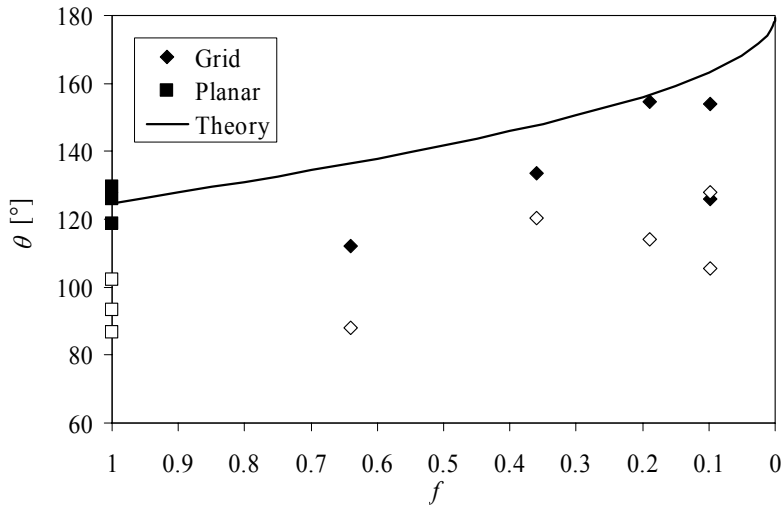


Figure 68. Measured contact angles of structured silicon surfaces with porous Al_2O_3 and FAS coating. Solid markers are advancing angles, open markers receding angles, and the line represents the Cassie and Baxter equation (7) with initial contact angle 125° .

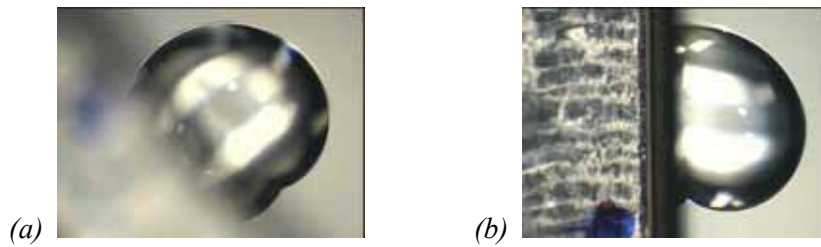


Figure 69. a) A water droplet sliding on a tilted Sol-Gel FAS on an unpatterned silicon surface. b) A droplet stuck on a Sol-Gel FAS on porous Al_2O_3 on an unpatterned silicon surface. The diameter of both droplets is around 3 mm.

4.2.11 Surfaces with sloped side walls

In order to verify the theory of superhydrophobic surfaces, we also fabricated surfaces with sloped side walls using the process shown in Figure 70. In this case, the silicon substrate was used only as a negative master for the final surface, and instead of deep reactive ion etching, silicon substrate was etched using anisotropic wet etching in 25% tetramethyl ammonium hydroxide (TMAH) solution. This resulted in pyramid-shaped cones with a side wall slope angle of 55° , defined by the $\langle 100 \rangle$ and $\langle 111 \rangle$ crystal planes of silicon. Next a hydrophobic material was cast on the surface, and after curing and detaching, a surface with pyramid-shaped cones was achieved. The same masks were used as for the vertically patterned surfaces, so that the pitch of the cones varied between 2.5 and 20 μm .

According to equation (5), the slope angle of 55° requires a material with a Young angle $> 125^\circ$ to produce a composite surface. As mentioned earlier, such materials do not exist. Thus a large contact angle hysteresis is expected. We used three hydrophobic materials: AKD, Teflon[®] AF and polydimethyl siloxane (PDMS). PDMS was tested because it is known for good pattern replication properties and is used in a similar manner in microcontact printing to produce structures with dimensions down to nanometer scale [112].

The surfaces were tested by dispensing and removing water droplets. Photographs of the droplets are shown in Figure 71 – Figure 73. The apparent (advancing) contact angle of the dispensed droplets was around 130° – 140° . When the droplets were removed a residue remained on the surface, which reveals a large contact angle hysteresis. There were no significant differences between different surface dimensions, but PDMS showed a smaller receding angle than AKD or Teflon[®] AF. Thus of these materials PDMS seems to be the least promising choice for a superhydrophobic surface. The results of this experiment are in good accordance with the theoretical considerations of superhydrophobic surfaces. Thus it is shown experimentally that the slope of the surface structures is very critical, and if the slope criterion in equation (5) is not fulfilled, the contact angle hysteresis is increased and the surface is less water-repellent than the original smooth surface.

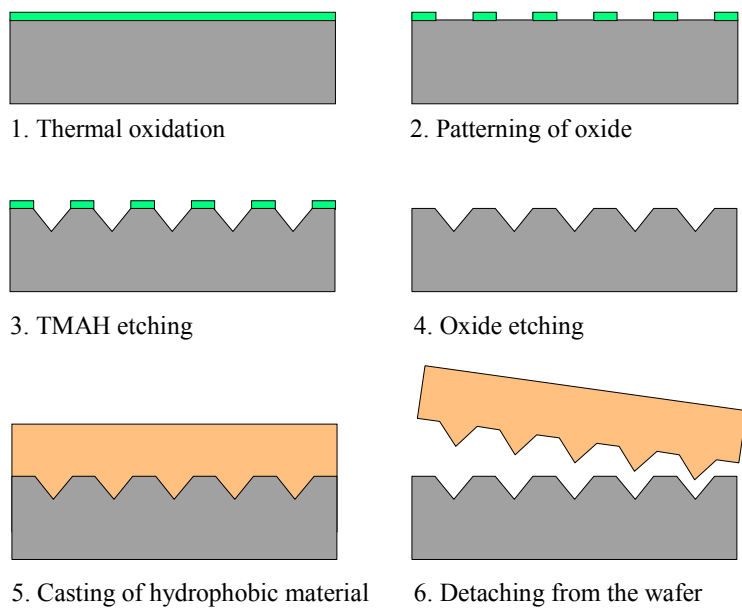


Figure 70. Fabrication of surfaces with sloped side walls.

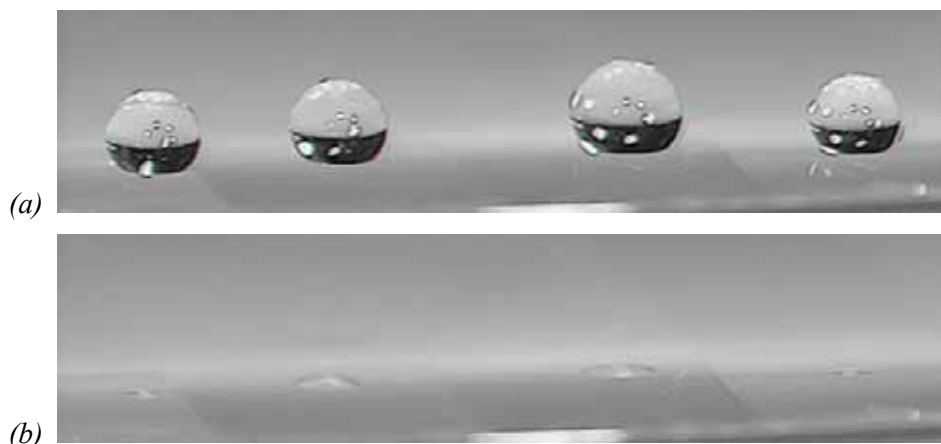


Figure 71. a) As deposited water droplets on a PDMS surface with pyramid-shaped cones. b) Droplet residues. The pitch of the cones varies from left to right as 2.5, 5, 10 and 20 μm .

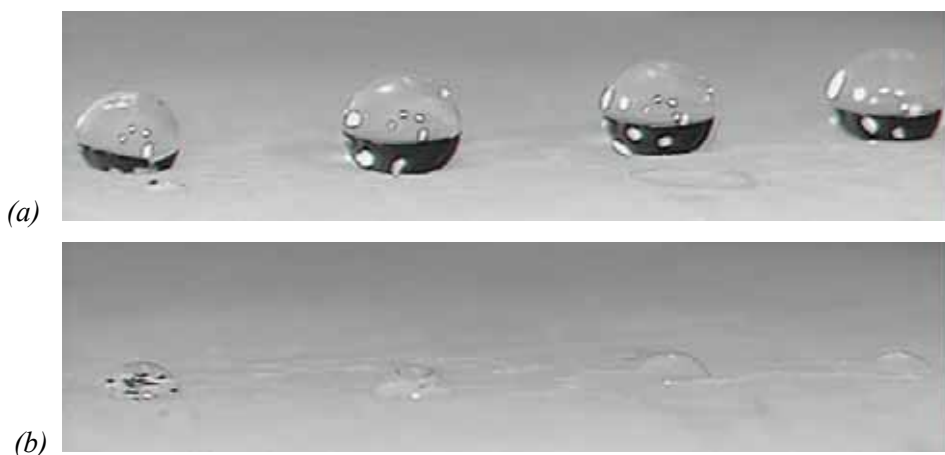


Figure 72. a) As deposited water droplets on an AKD surface with pyramid-shaped cones. b) Droplet residues. The pitch of the cones varies from left to right as 2.5, 5, 10 and 20 μm .

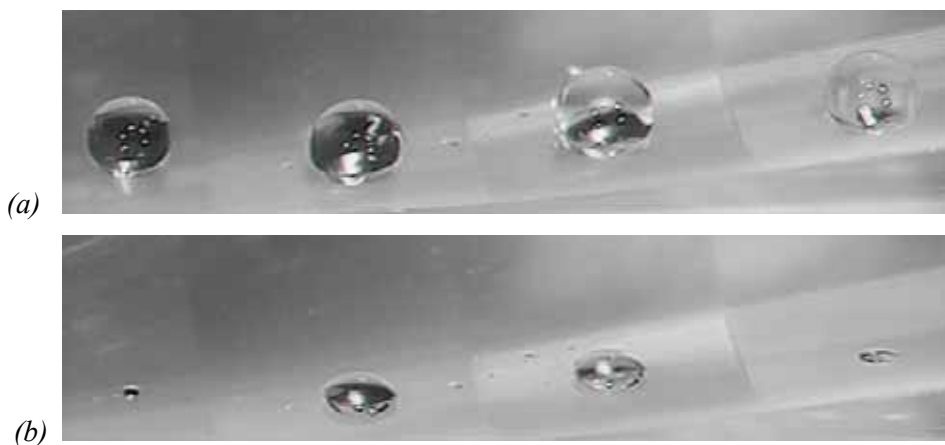


Figure 73. a) As deposited water droplets on a Teflon[®] AF surface with pyramid-shaped cones. b) Droplet residues. The pitch of the cones varies from left to right as 2.5, 5, 10 and 20 μm .

4.2.12 Compatibility of superhydrophobic surfaces with biological solutions

If the droplet reactor concept is to be applied in biochemistry, the surface must be hydrophobic for various water solutions. Usually the specific substances analysed in biochemistry are present in very small concentrations; most of the liquid is a buffer used to stabilise the environment for the desired molecular interactions. We tested the compatibility of the best superhydrophobic surfaces with some buffer solutions and their modifications. The solutions and the results are shown in Table 6. Each value is an average of five measured points, and the variation between them was usually of the order of $\pm 1^\circ$ or 20%. Solution B, TSA buffer, has a pH of 8.0 and contains 50 mM Tris(hydroxymethyl)-aminomethane-hydrochloric acid (Tris-HCl), 150 mM NaCl, and 0.05% NaN₃. Solution C is a modification of B with more salt and without NaN₃, which is used to prevent bacterial growth. Solution D is a modification of B with 20% added PEG (polyethylene glycol), which is used to reduce unwanted interactions between proteins and surfaces. Solution E is a modification of B with 0.01% added detergent (Tween-20). Solution F is a modification of B with added proteins (7.5% bovine serum albumin, BSA). Solution G is a commercial assay buffer produced by Wallac (currently PerkinElmer Life Sciences), comprising Tris-HCl buffered NaCl solution (pH 7.8) containing 0.05% sodium azide, bovine serum albumin (BSA), bovine gamma globulins, Tween 40, diethylenetriaminepentaacetic acid (DTPA) and an inert red dye. Solution H is a modification of B with added 100 μ M estradiol hormone.

Noticeably, the sliding resistance of TSA buffer (B) modified and added with extra salt (B) or a small amount of hormones (H) is close to that of pure water (A). With these solutions, the evaporated AKD is best with the lowest tilting angles. The measured sliding angles are generally better with solutions A and B than with pure water. The reason for this is not clear, but one possibility is that droplets of deionised water become charged during dispensing, which leads to increased adhesion due to electrostatic force. Salt makes solutions more conductive, which reduces charging, as discussed in section 3.3.5. Addition of PEG (D), detergent (E) and proteins (F) increases the sliding resistance clearly. Comparing their concentrations, it can be concluded that the detergent has the largest effect, proteins the second largest, and PEG the smallest. With these solutions and with the commercial buffer (G), sprayed Teflon[®] AF is the best

surface. Especially the effect of dissolved proteins is lowest with Teflon[®] AF. Evaporated AKD seems to lose its hydrophobic properties upon addition of detergent (solutions E and F), but this does not occur with sprayed AKD.

Table 5. Measured sliding angles [°] of droplets of various solutions on superhydrophobic surfaces. X indicates that the droplet did not slide even at a tilt angle of 90°.

Surface	Droplet Volume	Solution							
		A	B	C	D	E	F	G	H
AKD evaporated	5 µl	2.7	1.5	1.3	12	X	16	X	3.5
	1 µl	11	2.8	3.3	18	X	37	X	6.7
AKD sprayed	5 µl	3.2	2.2	2.3	6.2	11	13	12	4.5
	1 µl	15	9.8	6.7	20	41	37	26	13
Teflon [®] AF sprayed	5 µl	3.2	2.5	3.0	5.3	17	4.7	5.5	4.3
	1 µl	7.7	5.5	5.7	14	45	11	12	11

- A Deionised water
- B TSA buffer (50 mM Tris-HCl, 150 mM NaCl, 0.05% NaN₃), pH 8
- C 1 M NaCl, 50 mM Tris-HCl, pH 8
- D 20% PEG-8000 in TSA buffer
- E 0.01% Tween-20 in TSA buffer
- F 7.5% BSA in TSA buffer
- G Assay Buffer (Wallac)
- H 100 uM estradiol in TSA buffer

The negative effect of detergents and proteins are both related to their molecular structure. They have hydrophobic parts that are preferably located in the solid side of the solid-liquid interface, thus reducing the solid-liquid interfacial tension. This has a very negative effect on the superhydrophobic surfaces. It reduces the critical pressure or even leads to wetting of the surface structures. This is seen presumably with evaporated AKD. The difference from sprayed

AKD may be related to a morphological difference of the surfaces. Evaporated AKD consists of a thin layer of small hydrophobic grains (Figure 51), and if lowering the surface tension leads to wetting of the capillaries between the grains, all air is lost from the surface. Sprayed AKD has a fractal-type morphology (Figure 49), and apparently some air can remain in the surface even if some of the capillaries are wetted. The same may hold true for sprayed Teflon[®] AF. In conclusion, superhydrophobic surfaces are very critical to detergents and to proteins in water. Sprayed Teflon[®] AF seems to be the best of the tested superhydrophobic surfaces for biochemical applications.

4.3 Droplet transport experiments

4.3.1 1st generation transport devices

Several different droplet actuation devices were fabricated during the course of the work. The first transport devices were designed without any calculations, by using the principle of sequential parallel line electrodes and scaling the dimensions according to the droplet volumes of the order of nanolitres. A cross-section of the device perpendicular to the direction of droplet motion is shown in Figure 74. The device consists of three metal and four insulator layers, which were deposited on a silicon substrate and patterned using standard UV lithography. The first insulator layer was thermally grown silicon dioxide with a thickness of 1 μm , while the others were made using PECVD (Plasma Enhanced Chemical Vapour Deposition), and had a thickness of 2 μm . The metal layers were made with sputtering. After processing, a hydrophobic layer was applied. Next the silicon wafer was diced into chips and bonded into ceramic DIL cases. The control electronics with the 1st generation devices were based on relays, and the control sequence was operated so that one of the eight outputs was energised at one time while the others were grounded.

The electrodes are made from the topmost metal layer and are connected in groups of eight into the supply lines via holes in the insulator. The voltage supply lines are connected to contact pads at both ends of the chip. The centre metal is a shield layer, which prevents the droplet from sensing the electric field of the supply lines. Figure 75 shows the top views of some electrode configurations. The shape of the electrodes was varied between straight and

folded. The electrode width, defined as the dimension parallel to the direction of motion, was 20 μm . The electrode path width, defined as the dimension perpendicular to the direction of motion, was 500 μm . The electrode step was varied between 40 and 240 μm with straight electrodes and between 100 and 440 with folded electrodes. The idea behind the design was to keep the electrodes narrow in order to increase the electric field gradient and the dielectrophoretic force. Later it was found that this kind of design was completely wrong; the electrodes should be wide and have narrow spacings instead. As discussed in section 3.1.2, this mistake was caused by the mistaken understanding of droplet actuation as a manifestation of dielectrophoresis. The idea of the gradient electrode shown in Figure 75c was to generate a lateral electric field gradient in the direction of motion. When voltage is applied between electrodes located on both sides of the droplet, the droplet should move towards the smaller spacing of the electrodes. The complete layout of the 1st generation droplet transport devices is shown in Figure 75d. It consists of eight chips with different designs, such as straight and crossing paths. The dimensions of a single chip are 10 \times 5 mm^2 . The hydrophobic layer of the 1st generation transport devices was either a spin coated Teflon[®] AF 1600 or an ICP fluoropolymer. The fabrication and properties of the surfaces are reported in sections 4.2.1 and 4.2.2.

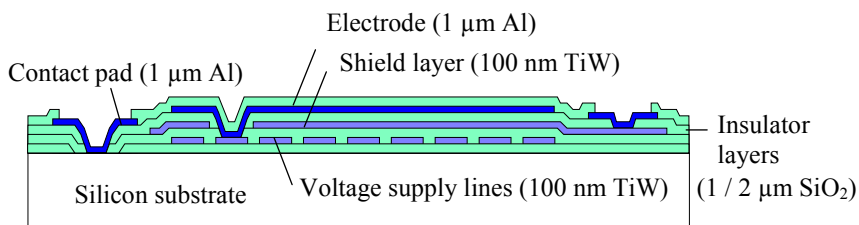


Figure 74. Cross-section of 1st generation droplet actuation device perpendicular to the direction of droplet motion. The hydrophobic layer is not shown.

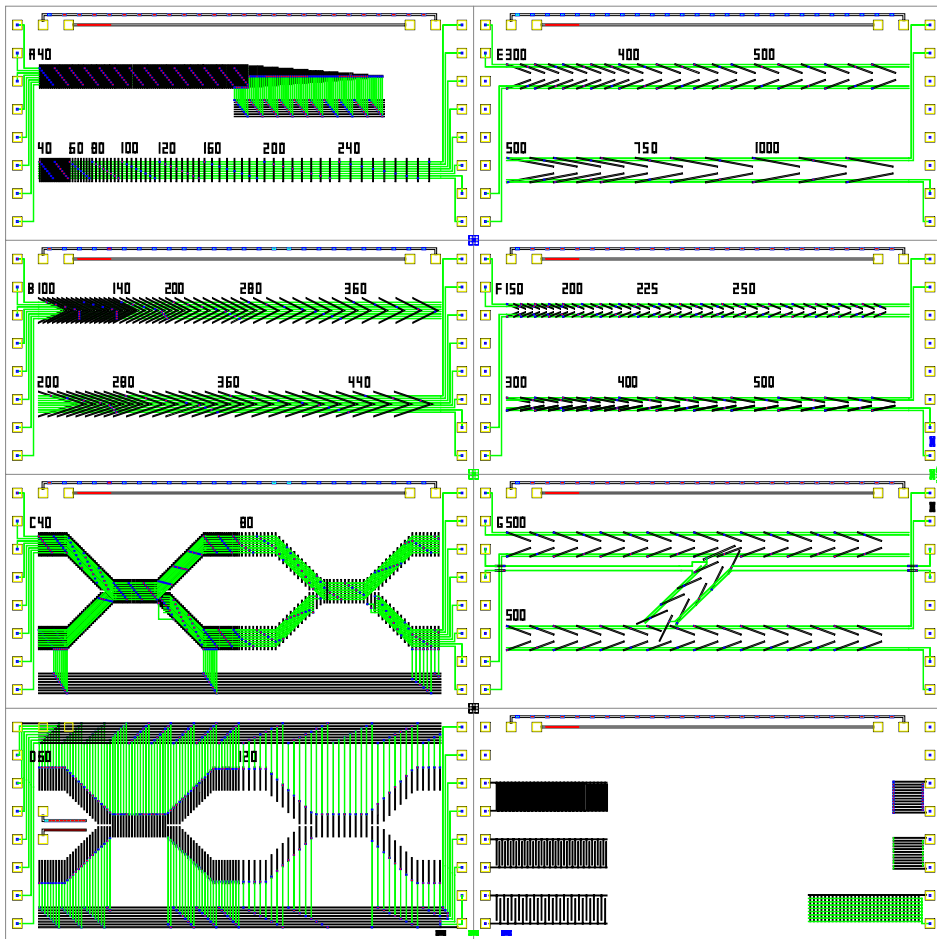
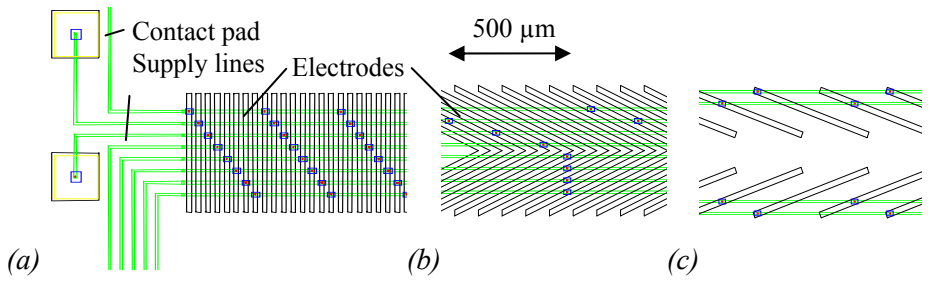


Figure 75. Top view of the electrode configuration of the 1st generation droplet actuation device. a) Straight line electrodes, b) Folded line electrodes, c) "gradient" electrodes. d) The complete layout of the 1st generation droplet transport devices. Total area is $20 \times 20 \text{ mm}^2$.

Droplet transport with the 1st generation devices was unsuccessful, both with Teflon[®] AF and ICP fluoropolymer surfaces. The maximum usable DC voltage was around 400V; with higher values dielectric breakdown occurred in the oxide layers. The only visible effects were some occasional modifications of the contact angle, which can be considered as the electrowetting effect. The basic problem with the 1st generation devices was wrong design. The devices were designed for nanolitre droplets with a diameter of a few hundred μm , which are very difficult to work with. In our equipment we were only able to place accurately droplets with a diameter down to 0.5 mm, (volume 30 nl), and they were so large that they overlapped the electrodes of two groups. There were electrodes with a larger step, but as already mentioned they were designed so as to vary the electrode spacing and keep the electrode width constant. This resulted in a very small actuation force. It was estimated using 2-dimensional FE analysis that the usable electrostatic force with the 1st generation electrode design was about 10% of the value which could be achieved with the idealised model geometry, shown in section 3.4. It was calculated that if the model geometry were used, the threshold voltage of droplet actuation would be around 80V with Teflon[®] AF and around 100 V with ICP fluoropolymer surfaces. The values used in the calculations were $\epsilon_r = 2$ and $d = 1 \mu\text{m}$ for Teflon[®] AF, $\epsilon_r = 2$ and $d = 150 \text{ nm}$ for ICP fluoropolymer, and $\epsilon_r = 3.9$ and $d = 2 \mu\text{m}$ for silicon dioxide. As the electrostatic force is proportional to the voltage squared, it can be estimated that the 10% electrode efficiency (with respect to ideal design) could be compensated by using an approximately three times higher actuation voltage. Thus actuation should have been possible around 300 V with both surface materials.

Due to the approximations and possible errors in the sliding force estimations, FE analysis and model calculations, it is possible that the minimum actuation voltage is actually above 400 V. However, it is also possible that the electrostatic force was saturated due to charge trapping before it was high enough for droplet actuation. The threshold voltage for charge trapping is given in equation (97). Since the electrode area is very small compared to grounded areas, we can approximate that $A_x \approx A_{eq}/2$. Using the values given above we can calculate that charge trapping occurs when the voltage is 130 V with Teflon[®] AF, and 100 V with ICP fluoropolymer. Thus it can be estimated that charge trapping occurred with the 1st generation devices at electrode voltages far below what would be needed for droplet actuation.

It should be remembered that this discussion is only theoretical and needs to be verified experimentally. At the time of experimental testing of the 1st generation devices, the liquid charging effects were not considered, because we were not aware that such effects may occur. On the other hand, we noticed in all other experiments as well that if the droplet did not move at expected voltages, they did not move at any voltage (up to 1000 V). Charge trapping predicts this kind of behaviour. With superhydrophobic surfaces, overcoming the critical pressure may lead to the same behaviour.

4.3.2 Polymer ball actuation

Instead of droplets we were able to transport spherical polystyrene particles with a diameter of 80 μm using the 1st generation actuator devices with Teflon[®] AF coating. This experiment has two functions: First, it verifies that the devices were functional in the sense that they generate electrostatic forces. It should be noted, however, that the particle transport voltages cannot be compared directly to droplet transport, because the restoring forces are different. Second, particles have a very important role in biochemistry, as they are used for immobilising specific molecules on their surface [28]. Thus electrostatic actuation of particles is a function which could be utilised in bioMEMS. Figure 76 shows a photograph of the actuation.

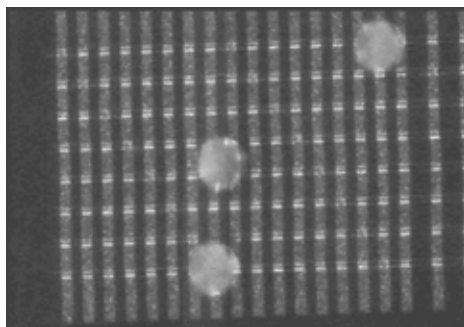


Figure 76. Electrostatic actuation of polymer balls on 1st generation actuator devices¹.

¹ The experiment is available as a movie file. See the table of contents.

Particle transport was not very well controlled. It appeared that the particles followed the electrostatic control, but frequently made longer arbitrary jumps in other directions or stuck to one position. Some response to the actuation was observed with voltages down to a few tens of volts, but better control was achieved using voltages around 100 V. Long jumps indicate the presence of repulsive forces between particles and energised electrodes, which is thought to be caused by charging of the particles. It is not clear if the charge originated from storage in plastic containers, or arose during actuation. Electrostatic particle transportation has also been reported by A. Desai et al. [113]. They too experienced poor control, with a best achieved transport efficiency of 90%. Thus there is plenty of work to do with particle transport as well.

4.3.3 2nd generation transport devices

The 2nd generation actuator devices were made from a single metal layer printed wiring board (PWB). This technology was selected instead of silicon processing for several reasons. First, the time from design to completed device was reduced radically. Second, higher actuation voltages could be used, because the dielectric strength of PWBs is better than what can be achieved with silicon devices. Third, it was learnt from the 1st generation devices that the scale of the electrodes should be larger. Thus the lower resolution of PWB process was not considered a problem.

Three design sets were fabricated with the 2nd generation devices. The spacing between the electrodes was a constant 200 μm , which was the minimum line width of the PWB process. The electrodes were arranged as wide arrays, or straight or branched baths, with a path width of 2 mm. Layout A, shown in Figure 77, consists of straight, folded and rounded electrodes of different widths. Layout B, shown in Figure 78, consists of the best-working design from layout A with some extra designs to increase the electric field gradient, like spike and saw electrodes and curved gradient electrodes. At the time of design it was still believed that droplet actuation could best be treated with dielectrophoresis. Figure 79 shows the last PWB layout version, C, which consists of different junctions of electrode paths. The electrode width and spacing were 0.4 and 0.2 mm in all versions, but the shape of the electrodes was varied. In this version other types of connectors were used.

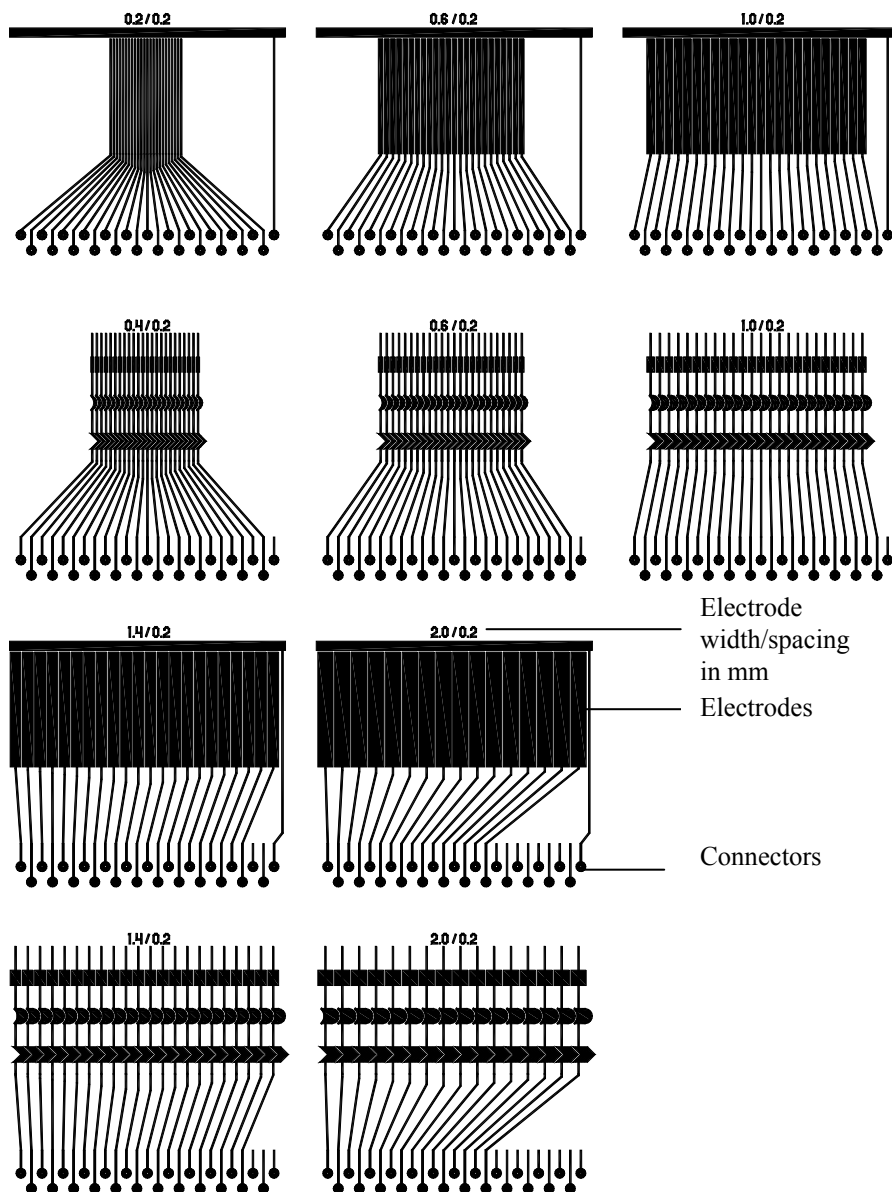


Figure 77. Layout A for 2nd generation transport devices (actual scale).

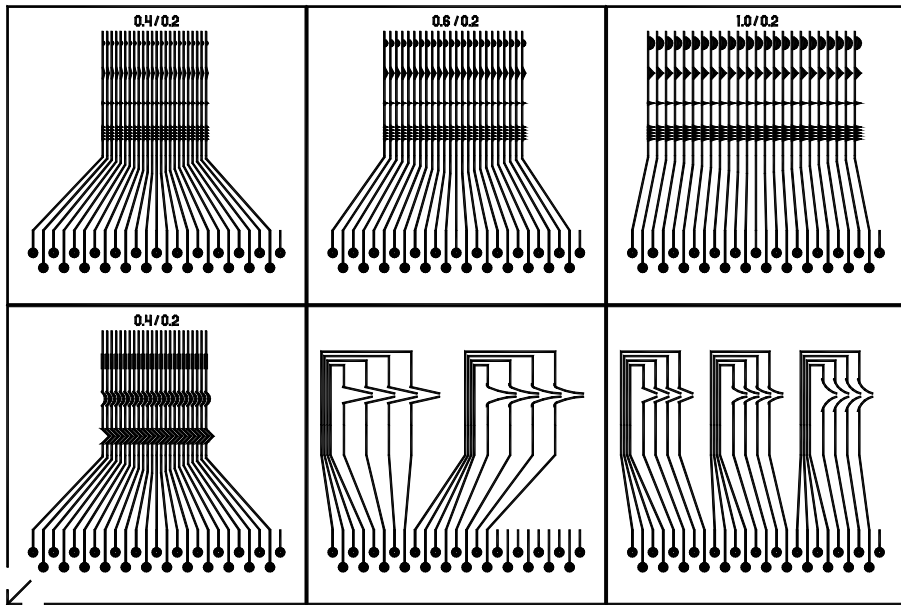


Figure 78. Layout B for 2nd generation transport devices (actual scale).

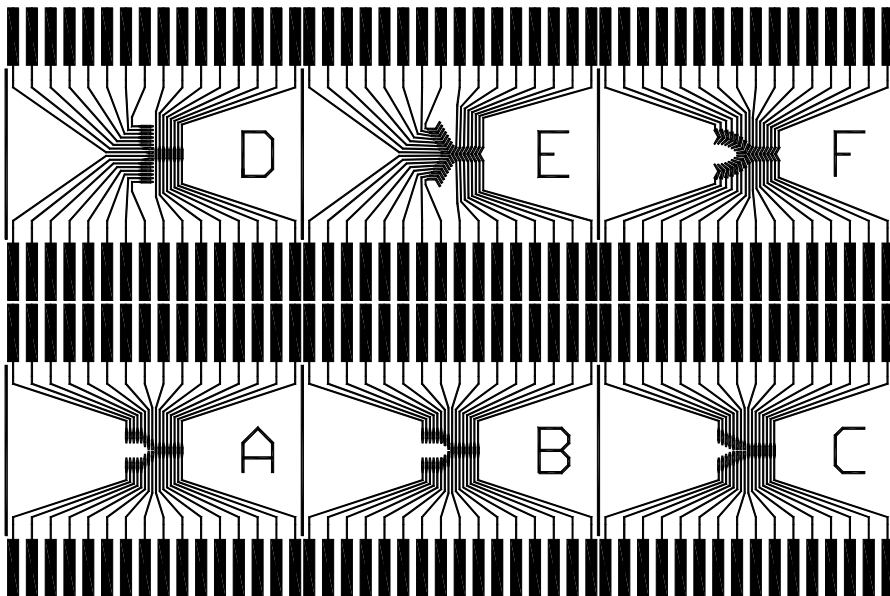


Figure 79. Layout C for 2nd generation transport devices (actual scale).

The electrode metal in all PWB devices was copper of thickness 30 μm . The insulator was a cellulose acetate adhesive film of thickness 65 μm (Scotch™ 810 Magic Transparent Tape, 3M). The advantage of using tape insulator is that it planarises the high steps formed by the copper metal, and provides a thick enough layer to reduce the electrostatic pressure and charge trapping. The hydrophobic layer used with the 2nd generation devices was AKD, either sprayed or evaporated.

With the 2nd generation actuator devices, droplet actuation was successful. The voltage was varied between 300 and 750 V DC during the experiments. Photographs of moving droplets are shown in Figure 80. The droplet motion was clearly stepwise and a single droplet step occurred quite rapidly. The maximum droplet transportation speed was not limited by the droplet motion during a step, but by the switching time of the control electronics. Because of the high voltages we used relays, which limited the maximum transportation speed to around 1 cm/s. It was noticed frequently that the distance between individual steps varies markedly. One reason is probably the non-uniformity of the sprayed AKD surface properties. Another possible reason, as explained in the section on FE analysis, is that the droplet has two possible places to stop when only one electrode at a time is energised.

An important result is that the droplets usually stayed on track, so that no side walls or guiding grooves were needed. Thus it is possible to actuate droplets on a planar surface. A planar surface makes the droplet system much more versatile, and the design and fabrication are easier. The effect appeared stronger with folded than with straight electrodes, but the difference was not quantified.

The actuator device in Figure 80 is version 0.4/0.2, shown in Figure 77 and Figure 78, which with either folded or straight electrodes appeared to be the best. Short-term transportation was also achieved with version 0.2/0.2, and at least one single step with version 0.6/0.2, but other dimension variations were not functional. The average droplet diameter in the experiments was about 2 mm, and according to model calculations the optimal electrode step for such a droplet is 300–500 μm . Thus the model predicts correctly that versions 0.2/0.2 and 0.4/0.2 with electrode steps of 400 and 600 μm , respectively, are the best versions.

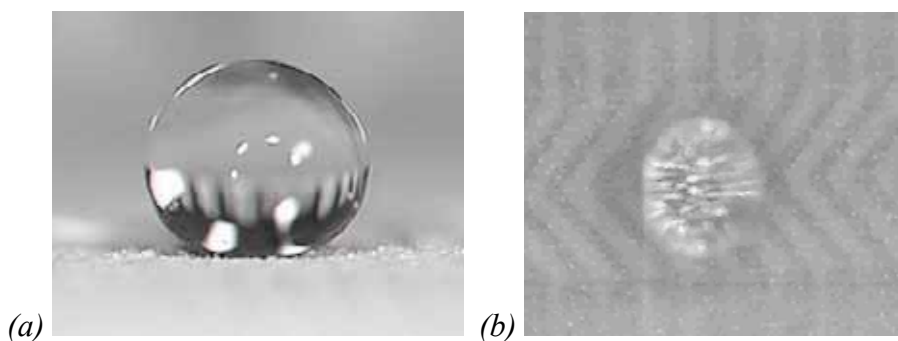


Figure 80. Photographs of droplets moving on a sprayed AKD surface. a) Side view¹. b) Top view of the maximum speed actuation¹. The diameters of the droplets are 2.4 and 1.7 mm, respectively.

An interesting parameter to compare between model calculations and the experimental results is the minimum actuation voltage. Some extra uncertainty of the calculated voltages is expected, because the effective insulator thickness and permittivity are not known accurately due to the very rough profile of the sprayed AKD. The permittivity of the cellulose acetate tape was measured to be around 4, but the effective value between the droplet and electrodes is lower because there is also a thick non-uniform composite layer consisting of air and AKD. Nevertheless, using values 120 μm and 3 for the insulator thickness and permittivity, respectively, and 155° and 7° for the advancing contact angle and hysteresis, the threshold voltage of actuation with a 500 μm electrode step is 240 V in terms of energy and 270 V in terms of force. The experimentally observed minimum actuation voltage also has uncertainty. Single jumps occurred at around 300 V DC, but several jumps usually required higher values, and for two-directional transport across the whole path the voltage had to be increased still further. Maximum voltages used were 750 V DC. Nevertheless, the model predicts smaller voltages than what is required in practice. However this is reasonable, as the electrode geometry of the 2nd generation devices was not optimal, the electrode spacing being quite large compared to the electrode width and only one electrode at a time being energised. Another explanation is that the resistance to sliding in electrostatic actuation may be higher than expected from the tilting tests. A single jump with a lower voltage was usually observed right after a fresh droplet was placed on the surface. Thus it is assumed that when the

¹ The experiment is available as a movie file. See the table of contents.

electric field is applied for the first time the droplet moves, but simultaneously penetrates slightly deeper into the surface due to electrostatic pressure, and the resistance to sliding increases for the next jump. Because in model calculations the sliding force was extracted from tilting tests performed without any electric field, the voltage predicted by the model calculations should correspond to the voltage needed for the first jump. Taking into account the non-optimal electrode geometry, we can estimate that this is the case. The reason for even higher voltages for full-path transport is assumed to be non-uniformity of the surface. Usually, at some point on the path there was a step that required higher voltages than the others. It was assumed that there was some kind of microscopic defect or higher point in the coating. Because the net electrostatic force was directed downwards, it was difficult for the droplet to overcome any vertical steps on the surface.

The model can be also used to calculate the contact angle of a droplet during actuation. For example, with a voltage of 500 V, the contact angle is expected to be reduced only by 2–3°, if the initial value is between 150 and 160°. Because the actual geometry is less optimal, the changes should be smaller. Comparing the droplet shape in Figure 80 with that in Figure 50, one can see that the contact angle is not significantly reduced when the droplet is actuated. It should be remembered that this comparison is only indicative, because the surface quality is not necessarily the same.

A quick test was also made with the gradient electrodes shown in Figure 78. Lateral movement of a droplet towards the throat of the leftmost electrode pair was observed in the version shown in the middle of the bottom row in Figure 78, but the step to the next electrode pair was not successful. It was speculated that either the movement was too short or the next electrodes were “shadowed” by the previous ones, making transfer impossible. Unfortunately, no video grab was obtained from the experiment. The other layout versions were not functional. The voltages were of the same order of magnitude as used with the traditional, ladder-type electrode paths. Thus the gradient electrodes seem not to offer any advantage in actuation voltages. On the other hand, it is estimated that gradient electrodes generate less electrostatic pressure towards the surface than traditional electrodes, which reduces the electrowetting effects. However, a major disadvantage is that they can be only used for one-way transportation. Because

the results with ladder-type electrode paths were better, gradient electrodes were rejected for future designs.

Exceeding of the critical pressure of the sprayed AKD surface was observed when attempts were made to actuate a droplet with a bakelite particle (diameter $\sim 400 \mu\text{m}$) inside. The particle was non-wetting, so that it stayed on the surface of the droplet, which made actuation much more difficult than without the particle. Therefore unusually high voltages of up to 1000 V DC were used to achieve some motion. The experiment was observed from the top, and exceeding of the critical pressure did not cause any visible changes in the appearance of the droplet, but when the droplet was removed a wet residue remained on the surface. Figure 81 shows the residue with a bakelite particle (left) and a fresh droplet (right).

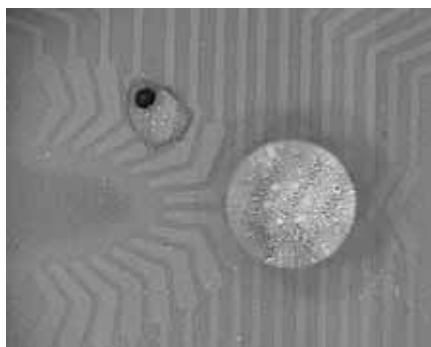


Figure 81. Wetted area on a sprayed AKD surface as a result of exceeding of the critical pressure.

4.3.4 Droplet branching and fusion

Layout C of the 2nd generation transport devices shown in Figure 79 consisted of different junctions designed for droplet branching and fusion experiments. Both functions could be demonstrated successfully. The actuation voltages were typically between 300 and 400 V. An example of droplet branching is shown in Figure 82. Because the electrodes are not very clearly visible through the AKD coating, the paths are marked with arrows. The actuation speed is low because the electrode voltages were switched using manual timing. Manual switching was found to be more flexible in these experiments.

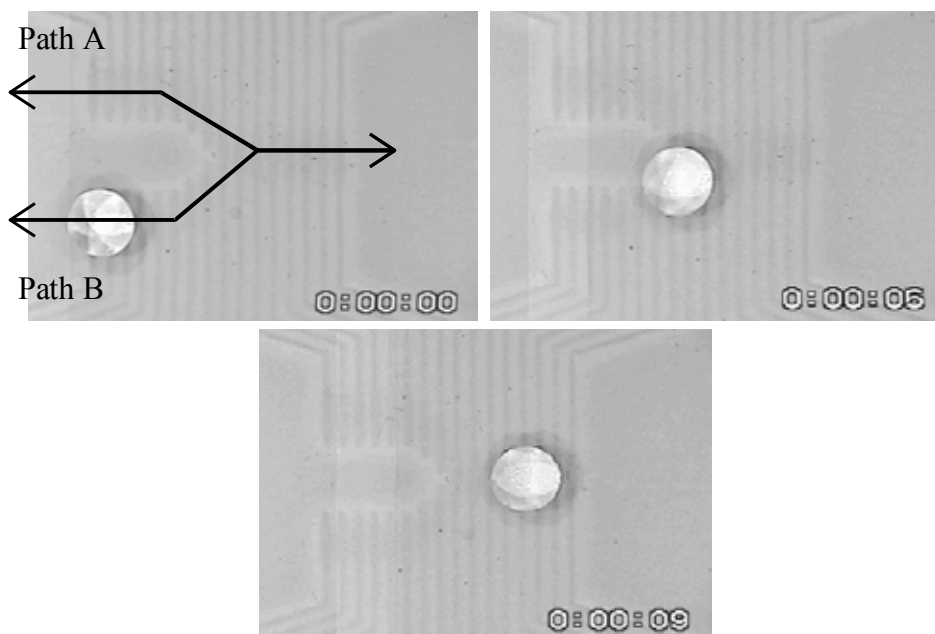


Figure 82. Sequential photographs showing droplet transportation across a junction¹.

Branching was successful with devices B, E and F. It is not clear whether the other devices were non-functional due to poor layout or due to poor quality of the surface. Differences in the surface properties between different devices arose because the AKD coating was made individually for each device. Droplet fusion is shown in Figure 83. The device is the same as in Figure 82. The AKD coating in these experiments was made by evaporation, but sprayed AKD also worked.

¹ The experiment is available as a movie file. See the table of contents.

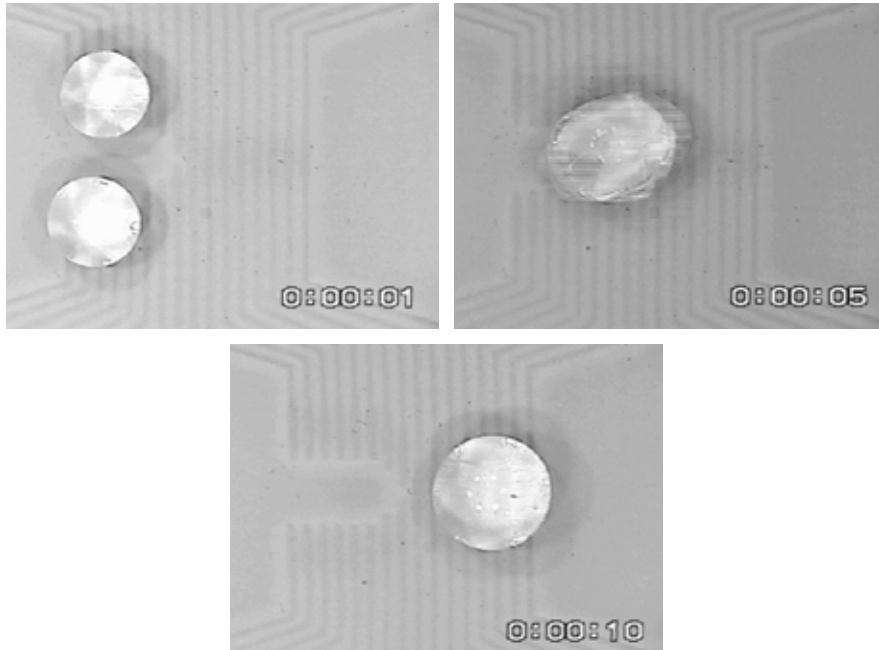


Figure 83. Sequential photographs showing droplet fusion in a junction¹.

4.3.5 Double-sided control

Double-sided actuation of droplets was tested using two similar 2nd generation PWB devices with sprayed AKD surface. The second actuator device was flipped and aligned on top of the other device using a micromanipulator and the overlapping electrodes were connected together. A droplet was placed on the bottom device and the gap between the devices was adjusted until the droplet contacted both surfaces. The actuation voltage was then increased until the droplet started to move. Figure 84 shows a photograph of the experiment. The actuation required around 400 V, which was the same as using only one of the devices. It is assumed that the actuation force is doubled, but the sliding force is also doubled because of the two contact areas. Thus double-sided control seems to offer no advantages over single-sided. However, a system with double-sided

¹ The experiment is available as a movie file. See the table of contents.

electrode plates is much more complicated and less versatile. Thus the experiments gave no reason to depart from the original single-layer design.

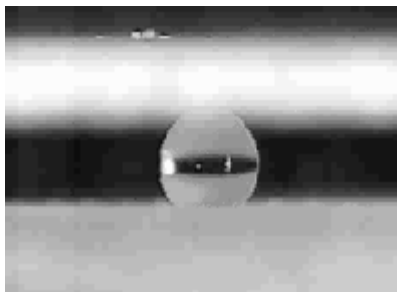


Figure 84. Two-sided actuation experiment¹.

4.3.6 3rd generation transport devices

3rd generation droplet transport devices were made using silicon processing. The goal was to find optimal electrode dimensions in order to minimise the actuation voltage, therefore different electrode dimension variations were fabricated. All device variations are shown in Figure 85. In order to maximise the dielectric strength of the devices, overlapping metal layers were avoided, and all electrodes were made from a single metal layer of 70 nm-thick sputtered molybdenum. The metal thickness was kept low in order to minimise step heights. The electrode metal was capped between two low pressure chemical vapour deposited (LPCVD) silicon nitride layers with a thickness of 50 nm. Silicon nitride capping was used to prevent any reactions between molybdenum and silicon dioxide. The bottom insulator was a combination of thermally grown and deposited silicon dioxide (tetraethyl orthosilicate, TEOS) with a thickness of 2 μm , and the top insulator was 2 μm thick phosphorous doped silicon dioxide (PSG, phosphosilicate glass) deposited with LPCVD. The reason for using PSG was that it could be densified and smoothed by annealing at 1100°C, where PSG softens.

¹ The experiment is available as a movie file. See the table of contents.

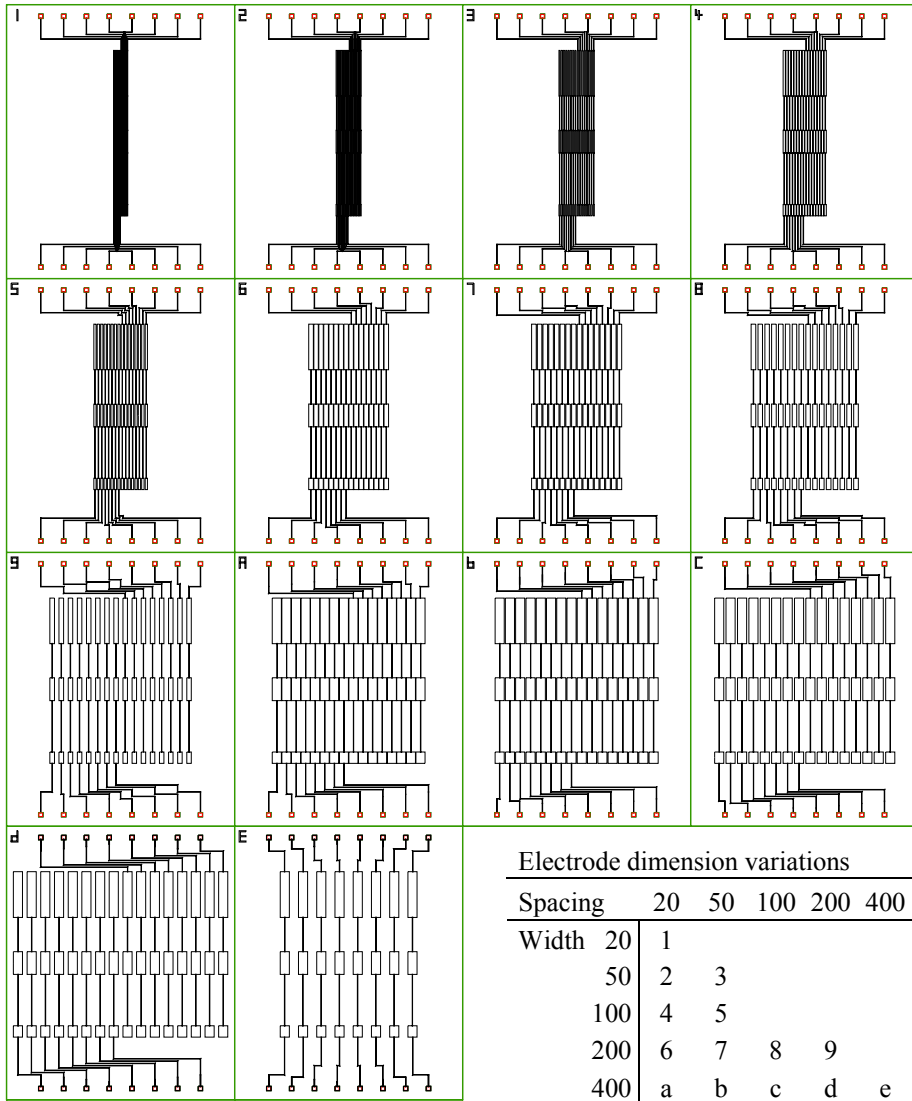


Figure 85. Layout and dimensions of different versions of the 3rd generation actuator devices. The dimensions of one chip are 10 x 12 mm², and electrode path widths are 2, 1 and 0.5 mm.

After depositing all insulator layers, contact areas were opened using plasma etching and contact metal (aluminium) was sputtered and patterned. The devices were diced using a protective photoresist layer, which was subsequently removed in acetone. The diced chips were glued into ceramic DIL cases. The

insulator thickness was varied by applying cellulose acetate tape of thickness 65 μm on some devices before coating of the hydrophobic layer, which was evaporated AKD. The cross-section of the device is shown in Figure 86.

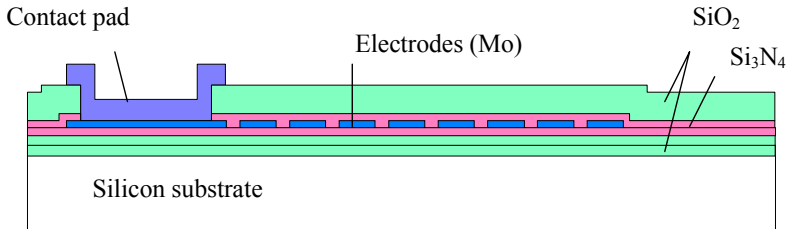


Figure 86. Cross-section of the 3rd generation actuator device.

With the 3rd generation transport devices we used AC voltage and a new kind of switching sequence, where multiple electrodes were energised at one time. It was noticed in the FE analysis that this leads to a larger electrostatic force. Actually, this electrode geometry is closer to the model geometry than a single energised electrode.

Table 6. Minimum actuation voltages of the functional 3rd generation devices.

Device version	Insulator thickness [μm] ¹	Electrode width [μm]	Electrode spacing [μm]	Electrode step [μm]	Droplet diameter [mm]	Apparent contact angle [$^\circ$] ²	Actuation voltage [V]
4	70	100	20	120	1.5	154	124
6	70	200	20	220	2.5	-	150
7	70	200	50	250	2	-	270
8	5	200	100	300	1.8	-	250
B	70	400	50	450	2	160	180
C	5	400	100	500	2.8	-	178
					2.3	140	250
D	70	400	200	600	2	-	300

¹ Effective thickness of the hydrophobic layer is included.

² Measured during actuation from the droplet and contact area diameters. If no value is given the droplet was observed from the top, which prevented measurement.

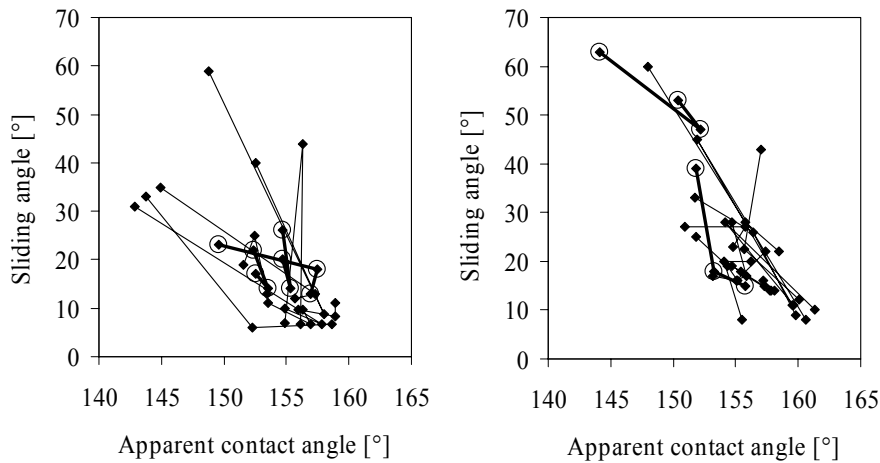
The results of the operational testing of the 3rd generation devices are shown in Table 6. A DI water droplet with a diameter of approximately 2 mm was dispensed manually onto the device, and the voltage was increased until the droplet was transported throughout the whole track in both directions. Before that, one or two steps were often observed with lower voltages, as with the 2nd generation devices. The lowest actuation voltage was achieved with device version 4, but device version 6 was nearly as good. Figure 87 shows a photograph of droplet actuation with 124 V on device version 4.



Figure 87. Droplet moving with the lowest achieved actuation voltage (124 V)¹.

As shown in Table 6, only part of the devices were functional. The most probable reason is related to the hydrophobic surface. Afterwards, the apparent contact and sliding angles of the devices were measured, with the exception of devices 1, 4 and 6 with 70 μm insulator, which were no longer available. The surface in each component was measured in three places; the results are shown in Figure 88. It can be seen in Figure 88 that there is some correlation between a high apparent contact angle and a small sliding angle, especially with FAS on tape surfaces. However, the operational devices do not show any better sliding angles than the non-operational devices. Furthermore, variations nearly as large appear in the values of the same devices as between different devices. There was deviation in droplet volumes, but each droplet diameter was measured, and the slide angle did not show any clear correlation with droplet size. The results indicate that the non-functionality of some devices may be caused by poor surface quality.

¹ The experiment is available as a movie file. See the table of contents.



a) FAS on SiO₂ ($d \approx 5 \mu\text{m}$)

b) FAS on tape ($d \approx 70 \mu\text{m}$)

Figure 88. Measured contact and sliding angles of the 3rd generation transport devices. Values measured from the same device are connected by a line and the operational devices are marked with a circle and a thicker line. Average droplet volume was 1.8 μl .

With some non-functional devices it is also possible that the electrode geometry is too far from optimal. It can be seen, for example, that the versions with the shortest and longest step, 1, 2, 3 and E, were not functional. Furthermore, as shown in Table 6, most of the functional devices were equipped with the thicker insulator. According to measured sliding angles, the AKD surface is slightly more water-repellent on tape than on silicon, because the tape increases the roughness, but this should not make a significant difference. A more important difference is that with a lower insulator, the electrostatic pressure is almost 200 times greater than with the thicker insulator. Thus the critical pressure is much more easily exceeded with the thinner insulator. Since the hydrophobic properties are varied on the surface, the critical pressure is also varied. This was also observed, and one example is shown in Figure 89. The droplet is transported until it sticks at a certain point of the path. This can be seen as small decrease in the contact angle. When the droplet is removed from the track, and it can be seen that the adhesion is very strong. The droplet elongates before it detaches leaving a residue on the surface.

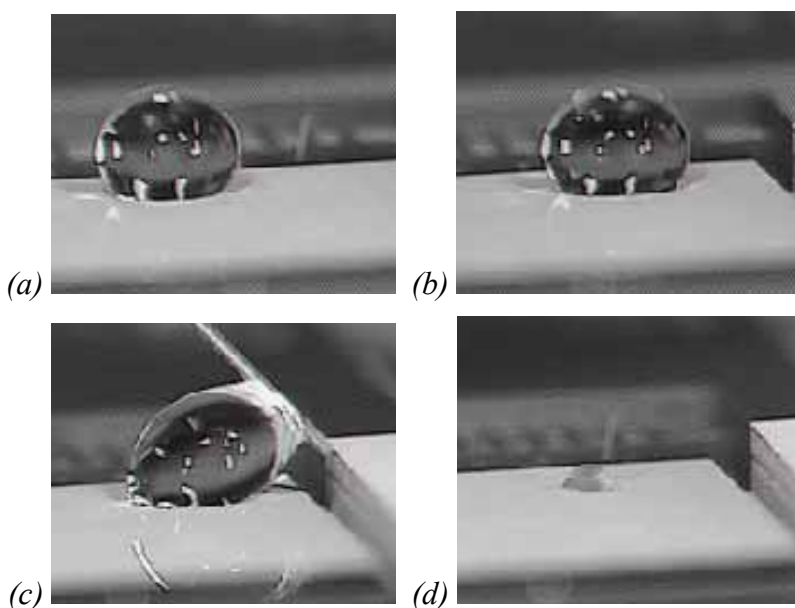


Figure 89. Sequential photographs of droplet sticking due to exceeding of the critical pressure on an evaporated AKD surface¹. a) Droplet is moving from left to right. b) Droplet sticks. c) Stuck droplet is being removed. c) Droplet residue.

It is surprising that the minimum actuation voltages with thin and thick insulators are of the same order of magnitude, although the insulator thickness, as well as the electrostatic force, varies over tenfold in magnitude. Using model calculations with $\theta_0 = 107^\circ$ and $\varepsilon_r = 3$, and neglecting the critical pressure and charging effects, we find that the measured hydrophobic properties of evaporated AKD ($\theta_a = 150^\circ\text{--}160^\circ$, $\theta_a - \theta_r = 4\text{--}5^\circ$) should correspond to minimum actuation voltages between 100 and 180 V with the 70 μm insulator, and between 33 and 55 V with the 5 μm insulator, depending on the actuation criteria (force or energy). It can be seen that the measured values for the 70 μm insulator are at the expected level, whereas the 5 μm values are not. Apparently, the sliding resistance is significantly higher with the thinner insulator. In tilting tests no such differences were observed, as shown in Figure 88.

¹ The experiment is available as two movie files. See the table of contents.

With the devices with the thinner insulator, the apparent contact angle of the moving droplet was observed to be lower. This is assumed to result from the electrowetting effect, and is evidenced in Figure 90. A droplet is dispensed on a device with a thin insulator, and right after dispensing the contact angle is approximately 150° . When the electrodes are energised to 250V and droplet starts to move, the contact angle decreases to about 140° . This can also be seen as a small change in the droplet height. Using equation (82) with initial parameters $f = 0.19$ (from the Cassie and Baxter equation (7) with values $\theta_c = 150^\circ$ and $\theta_0 = 107^\circ$), $d = 5 \mu\text{m}$, $\varepsilon_r = 3$ and $U = 250\text{V}$, we find that the contact angle should change from 150° to 139° . The result is in good agreement with the observations.

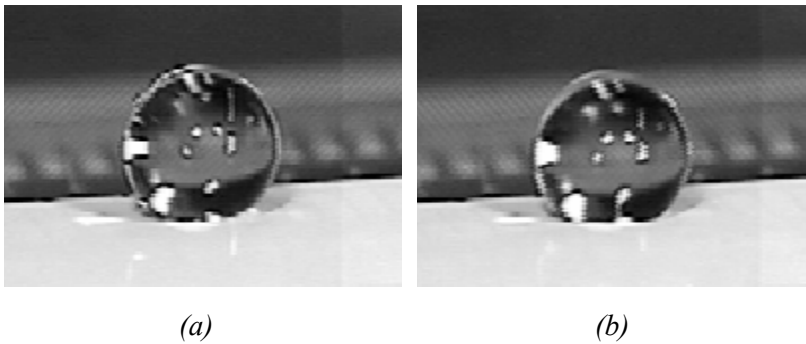


Figure 90. A droplet on a device with a thin ($5 \mu\text{m}$) insulator¹. (a) As dispensed, no voltage. (b) Electrodes are energised to 250 V and droplet starts to move.

However, the increase of droplet contact radius due to decreased contact angle does not explain the increase in sliding resistance. The most probable explanation is related to the vertical motion of liquid membranes as a result of electrostatic pressure, as discussed in section 3.3.3. The critical pressure of the surface is not completely exceeded because the droplet can move. As discussed in section 4.2.4, the surface can be approximated as a pillar configuration with $D_s = 0.1 \mu\text{m}$, and the contact angle of 150° corresponds to a critical pressure of the order of 20 kPa. The electrostatic pressure cannot be calculated directly from equation (94) since the droplet position with respect to the electrodes is not known exactly. On the other hand, the maximum possible value for P_e is given

¹ The experiment is available as a movie file.

in equation (12), and using the values above, it can be calculated that at least 600 V is needed to overcome the critical pressure with this device. It should be noted, however, that with irregularly rough surfaces the critical pressure is not an abrupt limit, and it is possible that some larger pores which have a lower critical pressure become wetted at smaller voltages.

Although the differences between electrode geometry variations of the 3rd generation devices were partially covered by the surface quality variations, some conclusions can be drawn concerning the optimal electrode step. Figure 91 shows the minimum actuation voltages of the devices in Table 1 plotted as a function of electrode step $|x|$ normalised to the radius of the equivalent capacitor plate R_{eq} . R_{eq} is a function of the droplet radius, contact angle and insulator thickness and permittivity, given by equation B2 in Appendix B. All the values needed for calculation of R_{eq} are given in Table 1, except ϵ_r , which is assumed to be equal to 3. Although the data points in Figure 91 are scattered, there is a trend that lower actuation voltages are achieved with lower $|x|/R_{eq}$ values. According to theory, when decreasing with $|x|/R_{eq}$, the actuation voltage should show a minimum somewhere, but this is not seen. It should be noted that some tested devices had lower $|x|/R_{eq}$ values, but they were not functional. It is possible that actuation was not possible because of too low an $|x|/R_{eq}$ value. This suggests that there may be a minimum between $0 < |x|/R_{eq} < 0.3$. According to the model calculations, the optimal electrode step is between $|x|/R_{eq} = 0.5$ and 0.9 , depending on whether the sliding force or sliding energy is considered, and if the critical pressure and charging effects are taken into account. The lower observed value for optimal $|x|/R_{eq}$ suggests that the proper actuation criterion is the sliding force instead of energy. This means that droplet sliding is governed by a friction type of force so that it is largest just before the droplet moves, and is significantly lowered when the droplet moves. Furthermore, the sliding force per surface area was a constant in the model calculations, but as already discussed in the previous section, there is evidence that the sliding force increases as a function of electrostatic pressure. Because the electrostatic pressure increases as a function of $|x|$, this leads to a smaller optimal electrode step than was predicted by the model calculations.

With device C in Table 6 two values for the minimum actuation voltage were obtained, so that a larger droplet moved with a smaller voltage than a smaller droplet. Unfortunately, there is not enough data to draw sound conclusions as to

the droplet size effect, as it was not one of the parameters studied in our experiments. One difficulty is that it is not known which of the droplets was actuated first. As explained later in this work, the reproducibility of the transport was poor and the devices somehow degraded during the course of testing.

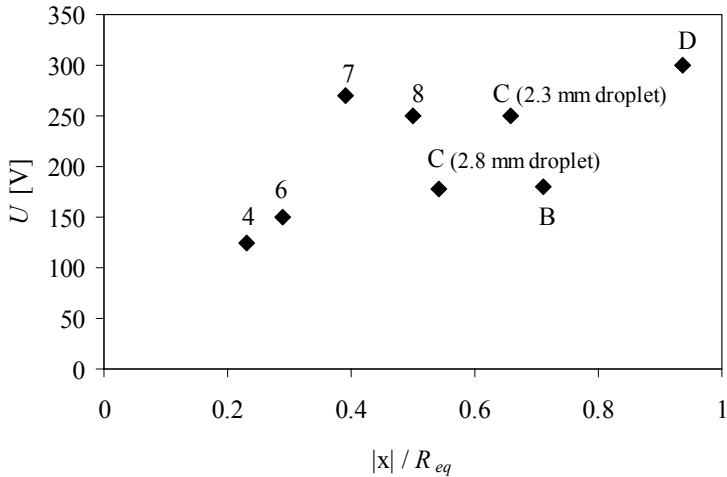


Figure 91. Threshold voltage of actuation versus normalised electrode step in the functional 3rd generation transport devices.

4.3.7 Droplet vibrations with AC voltage

Both 50 Hz AC and DC voltages were used in the experiments, and usually no differences were observed. Within the accuracy of the observations, the AC (rms) voltage level needed for actuation was the same as the DC voltage. However, the AC voltage was sometimes seen to generate instability in the droplet motion. Figure 92a shows a droplet being transported on the 2nd generation transport device version E (Figure 79); the surface is evaporated AKD. The droplet is seen to vibrate so strongly that it does not stay on track. The vibrations were observed to be dependent on the droplet size. When a larger droplet was actuated on the same track using AC control, no vibrations were noticed. Another example of droplet vibrations is shown in side view in Figure 92b. In this case, the device is a 3rd generation actuation device, and the surface is evaporated AKD. Unfortunately, the accurate droplet size is not known in this case. Here the droplet is seen to lift as it starts to vibrate, thus vibrating

periodically out-of-plane, although some in-plane motion is visible. Sometimes the droplets appeared oval. A very clear example of this is Figure 92c, where a large droplet (diameter 3.6 mm) is formed as a result of droplet fusion. The electrode geometry varies due to the curved shape of the path, and the droplet shape is seen to become a rotating oval at a certain position. It is assumed that the rotational motion in the 12 frames/sec video capture is the result of a stroboscopic effect.

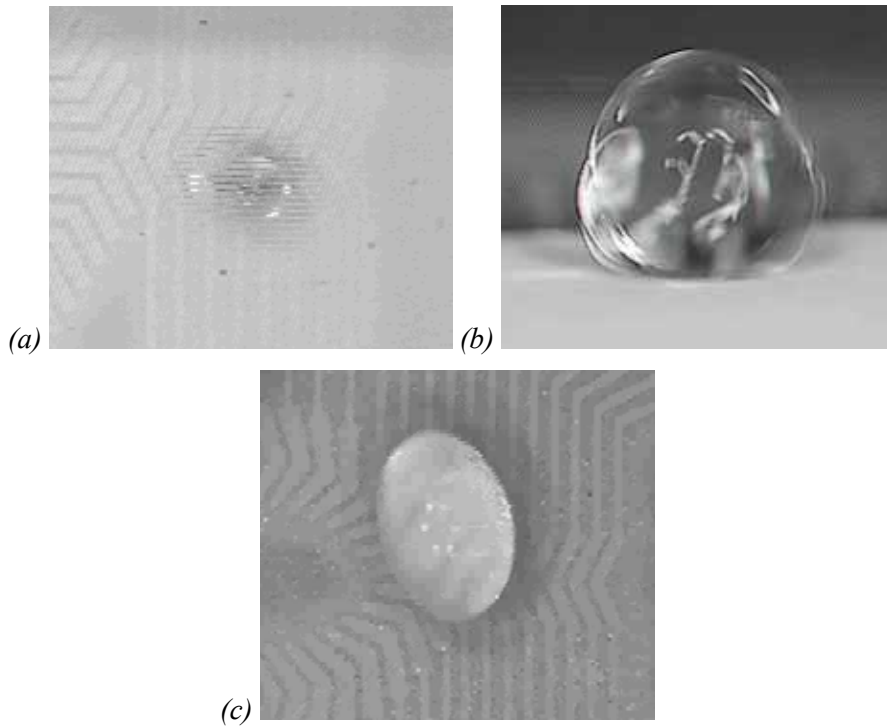


Figure 92. Droplet vibrations (a) top view, droplet diameter 1.45 mm¹. (b) side view, droplet diameter about 2 mm¹ (c) oval droplet (diameter 3.6 mm), top view¹.

Some theory and experiments of droplet vibrations can be found in the literature. Strani and Sabetta [114] have mathematically analysed free vibrations of a

¹ The experiment is available as a movie file. See the table of contents.

sessile droplet. They found that the resonance frequencies of axisymmetric out-of-plane vibrations (Figure 93a) are given by

$$f_r = \frac{1}{2\pi} \sqrt{\frac{\gamma_{lv}}{\rho R^3 \Lambda_M}}, \quad (100)$$

where ρ is the liquid density, R is the droplet radius and Λ_M is the eigenvalue for a given resonance mode. The eigenvalues for a given resonance mode depend on the contact angle and on the density of liquid and the surrounding media. Equation (100) was found to be in good agreement with the previous work of others, especially with contact angles above 140° . Thus equation (100) works well with droplets on superhydrophobic surfaces. More recently, Yamakita, Matsui and Shiokawa [115] have analysed vibrations of a sessile water droplet and found that the theory is in good agreement with the experiments, regardless of the excitation method. The methods used were surface acoustic waves, pulling up the droplet with a needle, blowing air onto the droplet and dropping the droplet from a height of 1–2 cm. Thus we can assume that also electrostatic force can induce droplet vibrations, and the theory of Strani and Sabetta [114] can be used at least for order of magnitude calculations. Figure 93 shows droplet shape modification in the first order out-of-plane resonance mode discussed by Strani and Sabetta [114]. It can be seen that the vibration resembles the observed mode in Figure 92b quite closely.

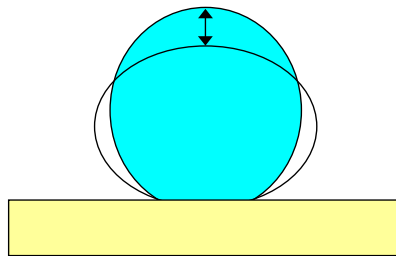


Figure 93. Droplet shape modification in the first order out-of-plane resonance mode discussed by Strani and Sabetta [114].

Calculation of the eigenvalues involves rather complex mathematics and the authors do not tabulate the eigenvalues in numerical form. However, they can be extracted from the resonance frequencies calculated by Yamakita, Matsui and

Shiokawa [115] by using equation (100). For a 10 μl droplet with contact angle of 150° , the first mode resonance was calculated around 40 Hz, which corresponds to an eigenvalue of around 0.47. The droplet in Figure 92a is approximately 1.45 mm in diameter, and calculated from equation (100) with the value $A_M = 0.47$, we get $f_r \approx 100$ Hz. In conclusion, the wild behaviour observed in Figure 92a can be explained as follows: the electrostatic force alternating at the double frequency of the applied voltage excites the first out-of-plane resonance mode of the droplet, and the droplet gains so much mechanical energy that it can make arbitrary long jumps. With larger droplets, jumps were not observed that could be explained by the resonance frequency of the first mode being at lower frequencies, and similar energy transfer could not occur.

The non-circular (oval) shapes of larger droplets are apparently caused by in-plane vibrations. There is no theory available for the in-plane vibrations of sessile droplets, but because the droplets on superhydrophobic surfaces are nearly spherical, we can use the theory on free oscillations of spherical droplets presented by H. Lamb [116] for order of magnitude calculations. The first mode of vibration produces the oval shape, and its frequency is given by

$$f_r = \frac{1}{2\pi} \sqrt{\frac{8\gamma_{lv}}{\rho R^3}}. \quad (101)$$

The droplet in Figure 92c has a diameter of 3.6 mm, and the first resonance frequency for such a droplet, calculated using equation (101), is 50 Hz. This equals the frequency of the applied voltage, which is surprising, because the electric field alternates at 100 Hz. Thus it seems that the polarity of the field has influence on the droplet vibrations, which suggests the presence of some charging phenomena.

In conclusion, AC voltage has been observed to induce droplet vibrations, which can be explained qualitatively using existing theories, but further experiments and analysis are needed to get a deeper understanding of the phenomenon. Droplet vibrations could be possibly utilised for reaction incubation, but at present are only an unwanted side-effect of droplet actuation, which makes further investigations less interesting.

4.3.8 Droplet motion analysis

As discussed in section 2.3.5, there is a question of whether a droplet moves on a superhydrophobic surface by sliding or rolling. Droplet motion during electrostatic actuation was studied by following the position of a particle with the droplet. Figure 94 shows a photograph of the studied droplet and trajectory of a particle, which is marked with an arrow. The particle is presumably AKD that has been detaching from the surface, and since AKD is hydrophobic, the particle is located on the surface of the droplet. The particle moves due to internal flows on the surface of the droplet, but the motion is so steady that the position change during the droplet step can be easily detected. If the droplet rolls like a solid sphere along the surface, the particle makes an angular rotation around the centre point of the droplet, which has an angle of

$$\alpha_r = \frac{180\Delta x}{\pi R}, \quad (102)$$

where R is the droplet radius, and Δx is the step length. With the droplet in Figure 94 $\alpha_r \approx 18^\circ$. However, it can be estimated that the particle moves only $\sim 4^\circ$ around the centre point of the droplet during the step. Thus the internal flows inside the droplet do not induce a motion that could be considered perfect rolling of the droplet during electrostatic actuation.

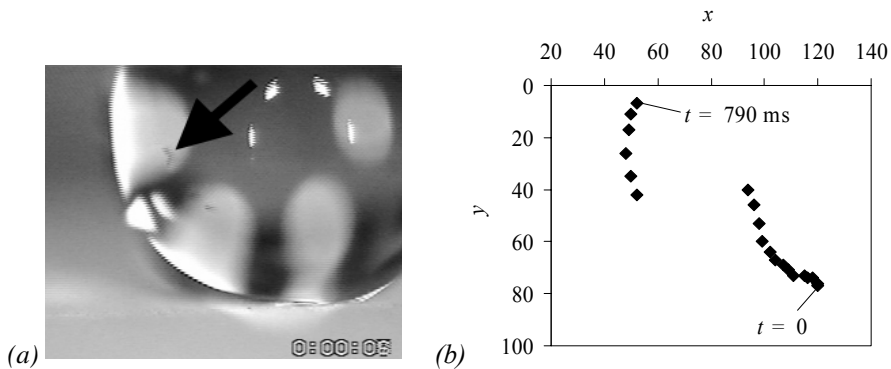


Figure 94. a) Particle inside a droplet (arrow) and b) its co-ordinates on the screen as the droplet is actuated one step. The period between markers is around 40 ms.

4.3.9 Long term stability problems

A serious problem with all droplet actuation experiments was that the transportation could not be continued for infinitely long periods. The ultimate limitation is droplet evaporation, of course, but well before that, after several minutes or half an hour at the most, the droplets started to stick to the surface. In some cases increasing the voltage got the droplets running again, but even this no longer helped after a while. Usually, replacement of the droplet with a new one did not help and the track was irreversibly non-functional.

At present there is no firm explanation for the phenomenon. Wearing of the surface is one hypothesis. Especially AKD is a very soft material, and it was observed that small particles were detaching from the surface and accumulating to the moving droplet. AKD particles in the droplet were seen in many experiments, for example in Figure 80. As actuation is highly critical to the surface properties, even detachment of a single particle from the surface may lead to formation of a weak point, where critical pressure is lower, and which may become wetted due to electrostatic pressure.

Another possibility is that the surface becomes gradually charged. This has also been proposed by J. Lee et al. [25], who reported similar long term stability problems in a closed cavity droplet actuation on Teflon[®] AF. Treatment with silicone oil was found to decrease the effect. Using the model calculations, we can estimate that the threshold voltage of charge adsorption is between 600 and 1200 V with the thicker 70 μm insulator, and between 170 and 330 V with the thinner 5 μm insulator, depending on the droplet position on the track. Thus the charging could have occurred due to exceeding the critical voltage with the 2nd generation devices and with the 3rd generation devices with a 5 μm insulator. However, with 3rd generation devices having a 70 μm insulator, and with the 4th generation devices the threshold voltage should not have been exceeded, but the stability was no better. On the other hand, due to the surface roughness, the maximum electric field at microscopic level is higher than the average value, so that charging on sharp tips of the surface may occur at lower voltages. Another possibility is that charge trapping occurs gradually below the threshold. As discussed in section 3.3.6. there are materials that trap charges on the surface to some extent with all voltages. It is not known whether AKD is such a material. On the other hand, Teflon AF[®] was not significantly better for long term

stability. It is also possible that both of the mechanisms contribute, so that the surface wears gradually and more and more voltage is needed to transport the droplets, until the charge trapping threshold is reached and the surface becomes permanently charged.

During the experiments charging was considered, but in a different way than discussed in the theory section of this work. It was assumed that the surface becomes charged due to frictional charging by droplets running back and forth along the same track. The charge trapping mechanisms were not yet understood. Nevertheless, we tried to neutralise the charge by using an air ioniser above the track. Sometimes this did get the stuck droplet moving again, but not always. Sometimes, if the ioniser tip was too close to the track, the droplet started to vibrate or even bounced off the track.

As the problem is apparently related to the solid-liquid interface between droplet and surface, some visual investigations were performed on that. Figure 95 shows an enlarged side view of the contact line of a droplet being actuated on a 3rd generation actuator device with evaporated AKD surface. The droplet is just about to stick, and actuation is very difficult. As can be seen, the contact line is not smooth but has spike-like liquid bridges between the surface and the liquid.

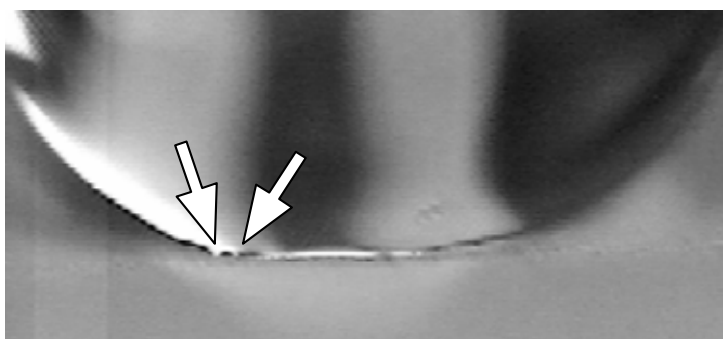


Figure 95. Spikes (arrows) in the droplet contact line during actuation on a 3rd generation device and evaporated AKD surface¹. Droplet radius is around 1 mm.

¹ The experiment is available as a movie file. See the table of contents.

Similar spikes were also seen on a sprayed AKD surface, and are therefore not caused by the surface structure. Such bridges may be originally created by the electrohydrodynamic instabilities in the liquid-vapour interface, which are discussed in section 3.2.1. It was found using FE simulations that the electric field close to the contact line of the droplet can, in some cases, exceed the threshold voltage of the electrostatic pressure effects. On the other hand, EHD instabilities cannot usually be maintained for long periods, so that the presence of nearly stable spikes suggests areas of strong local adhesion between surface and liquid. Thus the originally water-repellent AKD surface is either chemically modified or locally charged. Because the test liquid is DI water, the chemical modification is unlikely. It is possible that the spikes are manifestations of trapped charges. Charges that are not trapped should not generate such stable effects, since the applied electric field is alternating at 50Hz. The droplet in Figure 95 started to move after a while, but similar spikes were still seen during actuation. Furthermore, the spikes were not wholly stable but some disappeared as new ones formed, even when the droplet was immobile. Unfortunately, during the experimental phase we did not have enough theoretical knowledge of liquid charging phenomena. Thus further investigations on the charging phenomenon are required to ascertain its contribution to the long-term stability problems of droplet transport.

4.3.10 Actuation of biological solutions

The possibility to actuate biological solutions is very important for useful operation of the droplet reactor concept. We tested three different buffers, which contain among other things detergents and proteins. They are listed in Table 7. The commercial Assay Buffer of Wallac (currently PerkinElmer Life Sciences) was also used with the sliding tests discussed in section 4.2.12. The components of the modified buffers I and II were also tested in the sliding tests with the exception of EDTA (ethylenediamine tetra-acetic acid), an amino acid used to control unwanted side reactions with metal ions.

None of the solutions could be actuated electrostatically with any of the devices that were operational with water droplets. When comparing this result with the sliding tests, discussed in section 4.2.12, it is seen that with evaporated AKD the reason for the poor result is clearly the detergent (Tween), which destroys the

hydrophobic properties. With sprayed AKD or Teflon[®] AF the detergent had a smaller effect, but the sliding force increased by an average factor of 3. Thus 70% more voltage is needed to increase the electrostatic force by the same amount. Since detergent reduces the surface tension of the liquid, the critical pressure of the surface decreases. Taking these effects into account, it is possible that the electrostatic pressure exceeds the critical pressure of the surface before droplets can move. Droplet residues were seen on the surface after actuation tests, which indicates wetting of the surface. The proteins were also observed to reduce hydrophobicity in the sliding tests, but the effect was smaller than with the detergent, especially with the sprayed Teflon[®] AF. The protein concentration in the tested solutions is also much lower than that used in the sliding test. EDTA may also have some influence, but its concentration is so small that it can be neglected.

Table 7. Buffer solutions tested with electrostatic droplet actuation.

Solution	Description
Assay Buffer (Wallac)	Tris-HCl buffered NaCl solution (pH 7.8) containing 0.05% sodium azide, bovine serum albumin (BSA), bovine gamma globulins, Tween-40, diethylenetriaminepentaacetic acid (DTPA) and an inert red dye.
Modified assay buffer I	50 mM Tris-HCl (pH 8), 150 mM NaCl, 0.1% Tween-20, 100 μ M EDTA, 0.1% BSA, 0.05% NaN ₃
Modified assay buffer II	50 mM Tris-HCl (pH 8), 150 mM NaCl, 0.01% Tween-20, 100 μ M EDTA, 0.1% BSA, 0.05% NaN ₃

The poor result with buffer solutions is a very serious problem. It is possible that in some applications the detergent is not needed, but this does not wholly solve the problem since the proteins have a similar effect. Anyway, if the transported liquid has to be tailored according to the actuation compatibility, the usability of the droplet reactor concept is severely limited. It is worth noting that Washizu [20] was able to actuate ionic biological buffer solutions and protein solution on

a smooth hydrophobic surface. Thus the origin of the problem is not in the electrostatic actuation but in the superhydrophobic surfaces.

4.3.11 Downscaling of droplet volumes

This work demonstrates the actuation of droplets having volumes ranging from 1.6 to 50 μl . The smallest volumes are of the same order of magnitude as reported by Washizu [21] and Pollack, Fair and Shenderov [23], who report actuation of droplets down to 0.5 and 0.7 μl , respectively. On the other hand, Lee et al. [27] claim that their electrowetting-based system deals with droplets down to 5 nl, and Chiou et al. have been able to actuate droplets as small as 10 pl using a novel laser-driven opto-electrowetting method [35]. It should be noted that the systems of Pollack, Fair and Shenderov, Lee et al. and Chiou et al. are closed chambers where droplet volumes can be reduced by making the gap smaller so that the droplet shape is actually like a pancake. At any rate there seem to be no fundamental limitations to the downscaling of droplet-based microsystems. Droplet evaporation may be a problem but is easily solved, as discussed later.

Originally, our goal was also to go down to nanolitre level, where droplet diameters are of the order of few hundred micrometers, but this was not successful. Problems with such small droplets were partially related to the lack of suitable dosing instruments, but it was also found that very small droplets “stick” to superhydrophobic surfaces and do not move as easily as larger droplets. This has also been observed by Richard and Quéré [54], who tested running velocities of glycerol droplets on a tilted superhydrophobic surface. On the other hand, the actuation and sliding forces given in equations (74) and (4), respectively, are both proportional to the droplet radius and no droplet size effects are expected. Apparently the sliding equation (4) is not adequate and the contact angle hysteresis depends on the droplet size. This can be explained qualitatively, so that with small droplets the mechanical vibrational energy is so low that they cannot overcome the energy barriers associated with the surface structures. Intuitively speaking, the minimum droplet size could be reduced by making the surface structures smaller. This would be an interesting issue for future studies, but good methods for producing nanometre scale surfaces in a controlled manner should be developed first. Another method to actuate smaller

droplets is to increase the vibrational energy. This is actually done when droplets are being actuated using ultrasound. Although this aspect is not discussed in existing papers, the smallest droplet volumes actuated on open surfaces have been reported using this method. Strobl et al. [32] demonstrated transportation of droplets down to 1 nl on a planar SAW device.

4.4 Droplet reactor functions

4.4.1 Droplet import

One step towards complete droplet reactor is to develop methods for droplet import and export. It was found that dispensing droplets on superhydrophobic surfaces with conventional methods is difficult due to weak adhesion of the surface. The water repellence can, however, be put to use by making a small hole in the surface and pumping liquid through the hole, as shown in Figure 96. Due to the high contact angles of the surface an almost spherical droplet forms on the superhydrophobic surface, and the droplet remains connected to the rest of the liquid by a thin liquid bridge that can be broken by applying tangential force to the droplet. We used gravitational force (tilting) to break the bridge.

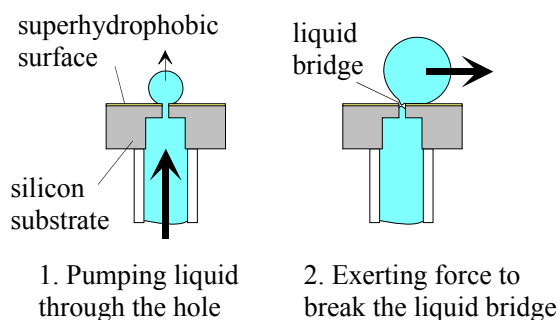


Figure 96. Principle of importing a droplet on a superhydrophobic surface.

The same devices were used for droplet import, export and filtering experiments. They were fabricated using a simple two-mask process and deep reactive ion etching of silicon with an ICP reactor. First, the back holes were etched to a depth of 350 μm ; next the front side was etched until the holes were through. In the final step of wafer processing, the holes were rendered hydrophilic by

chemical oxidation in hydrogen peroxide for 15 min. Figure 97 shows the layout of the devices. The back hole is a square $200 \times 200 \mu\text{m}^2$ and the top hole is either a single hole or an array. Both circular and rectangular top holes were used, and the hole diameter was varied between 5, 10, 20 and $40 \mu\text{m}$. After processing, the wafers were cleaved into smaller chips and small metal tubes were glued on the bottom of the device. Finally a layer of AKD was sprayed on the top side. Figure 98 shows an SEM photograph of a cleaved droplet import / export hole.

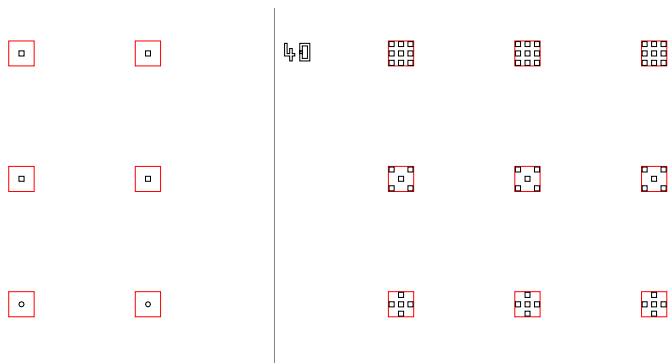


Figure 97. Example layout of droplet import / export devices. The side length of the large squares is $200 \mu\text{m}$.

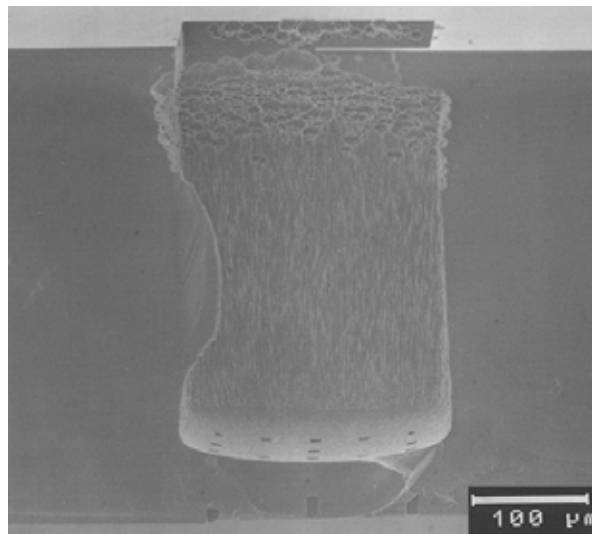


Figure 98. SEM photograph of a cleaved droplet import / export hole fabricated in a silicon wafer. The device is upside down.

It was found that only the devices with 40 μm holes were functional; apparently the spraying resulted in such a thick layer that smaller holes smaller were blocked. Thus the effective hole diameter was less than 20 μm . An example of a droplet generation experiment is shown in Figure 99. The droplet grows in size when water is pushed through the hole, and when the gravity force exceeds the breaking force of the liquid bridge, the droplet detaches and slides away. An enlarged view of the droplet neck just before breaking is shown in Figure 100. The droplet diameter just before sliding is approximately 2.75 mm and the tilt angle of the device about 18°, giving an in-plane force to break the neck of the droplet of about 30 μN . According to model calculations, such forces can be achieved in droplet actuation with less than 200 V, if the insulator thickness is around 10 μm or less. Thus it should be possible to integrate the demonstrated droplet import method with droplet actuation.

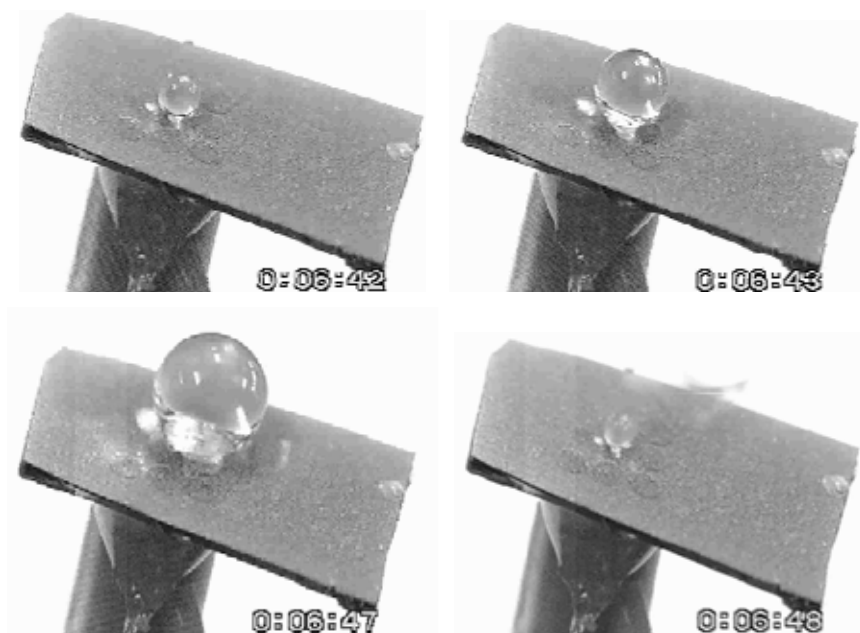


Figure 99. Sequential photographs of a droplet import experiment¹. The diameter of the droplet before sliding is 2.75 mm.

¹ The experiment is available as a movie file. See the table of contents.



Figure 100. Enlarged view of the neck of the droplet just before breaking.

4.4.2 Droplet export and filtering

Droplet export was demonstrated using a small hole similar to that in the import device. The hydrophilic side wall condition is actually not necessary for droplet generation, but in droplet export it was essential. When a droplet is placed on a hole, the capillary force of the side walls absorbs the droplet as shown in Figure 101. A piece of paper was placed underneath the chip to increase the absorbing volume. In a complete system, an external pipeline could be used as well.

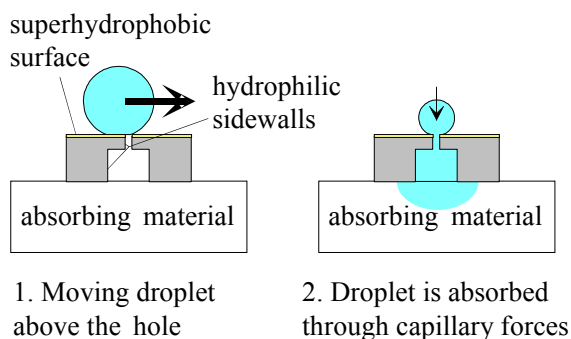


Figure 101. Principle of exporting droplets from a superhydrophobic surface.

An example of droplet export is shown in Figure 102. A droplet was placed on top of a hole, and it was absorbed away due to capillary force. A closer look at the device revealed a damaged point in the AKD surface close to the export hole, and it is possible that the capillary action was initiated from this point. On the other hand, with some other functional devices such clear spots were not visible. In those cases it is assumed that absorption was initiated so that the dispensed

droplet was pushed towards the surface with such high force that the critical pressure was exceeded. Thus in the complete system, droplet export could be initiated by applying a high enough voltage when the droplet is on the export hole, so that the critical pressure of the surface is exceeded.

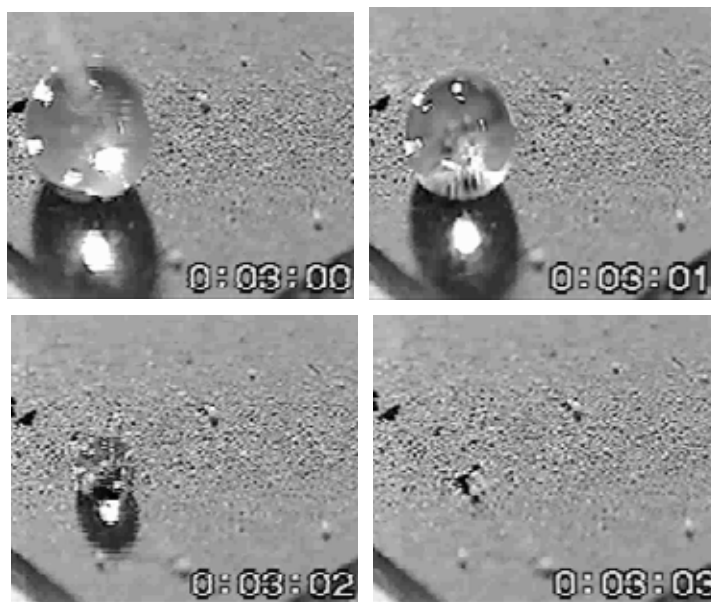


Figure 102. Sequential photographs of a droplet export experiment¹.

The export hole was also shown to be suitable for filtering polymer particles from droplets. If the particles are used as a solid phase in biochemistry, this function can be used for washing out the molecules that have not reacted with the surface of the particle. This effect is demonstrated in Figure 103. A couple of polystyrene particles with diameter 80 μm were deposited on the surface. A droplet was wiped across the surface, so that the particles were collected by the droplet. The droplet was then placed on top of the export hole and after droplet absorption the particles remained on top of the surface.

¹ The experiment is available as a movie file. See the table of contents.

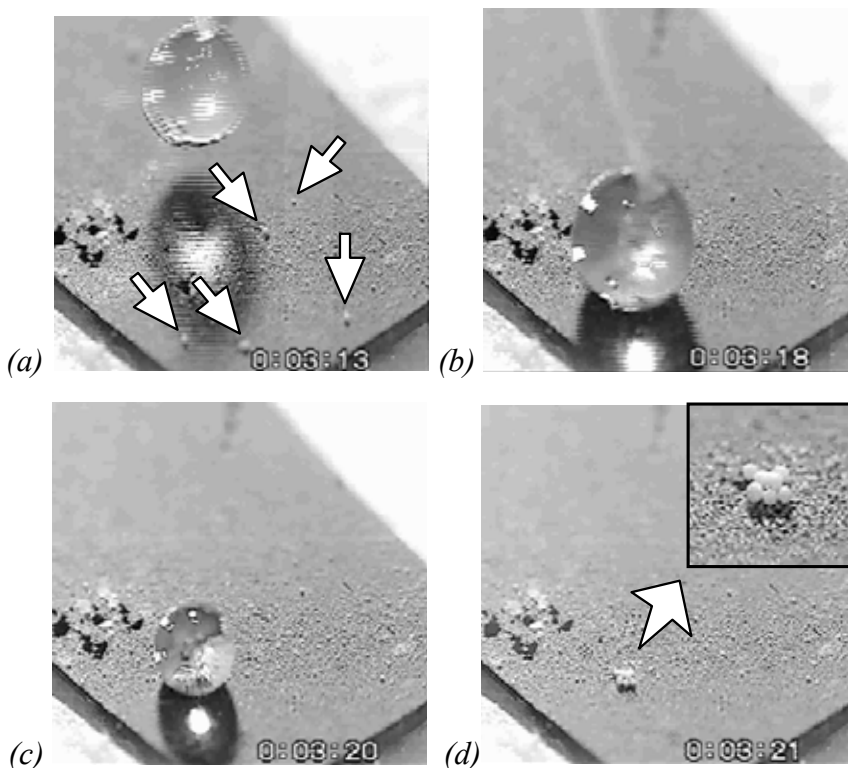


Figure 103. Sequential photographs of droplet filtering¹. a) Particles (arrows) are collected by the droplet. b) Droplet is placed on top of the export hole. c) Droplet is absorbed. d) Particles remain on top of the surface.

4.4.3 Evaporation control

In our experiments, evaporation was not a problem because the droplet volumes were large and the experiments were relatively short. However, in a fully operational droplet reactor the evaporation must be controlled. A simple method to prevent evaporation is to arrange a saturated water vapour atmosphere around the droplet. This idea was tested simply by placing a lid over the cavity of a DIL case in which an actuator device was mounted. The volume of the cavity was of the order of 300 mm³. It was found that droplets could be maintained over one night. Apparently the air humidity inside the closed volume was saturated due to

¹ The experiment is available as a movie file. See the table of contents.

the small volume evaporated from the droplet. The volume change of the droplet is given by Lee et al. [27] as follows:

$$\Delta V = \frac{PV - n_M}{\rho_l \frac{R_M T}{M} - P} \quad (103)$$

where P is the pressure, V the initial volume of the gas phase in the cavity, n_M the initial mole number of vapour molecules in the gas phase, ρ_l the density of the liquid, R_M the molar gas constant ($8.3143 \text{ Jmol}^{-1}\text{K}^{-1}$), M the molecular weight of the liquid, and T the absolute temperature. Assuming that initially there is no water vapour in the cavity ($n_M = 0$), and using the values $\rho_l = 1000 \text{ kg/m}^3$, and $M = 18 \text{ g/mol}$, we get a cavity of $V = 300 \text{ mm}^3$ becoming saturated when $0.22 \text{ }\mu\text{l}$ has evaporated. A droplet with initial diameter of 2 mm (volume $4.2 \text{ }\mu\text{l}$) then loses about 5% of its volume and about $36 \text{ }\mu\text{m}$ from its diameter. If the cavity and cover were optimised to reduce useless space, the volume loss would have been smaller. In a real system the volume loss of critical samples and reagents can be totally eliminated by first running a couple of buffer droplets so that the atmosphere becomes saturated. It can be concluded that droplet evaporation is solved rather easily, although at first sight it may appear problematic. The use of a cover over the droplet reactor is not a serious complication since it must be protected against dirt and dust anyway.

4.4.4 Integration of droplet functions

With the 4th generation devices the goal was to combine all demonstrated droplet functions onto a single device. Figure 104 shows the planned functions and their location on the device surface. The different functions are designed to be performed in the numbered sequence. The electrode dimensions were based on the previous devices, with an electrode step of either 100 or $200 \text{ }\mu\text{m}$ and electrode spacing of either 10 or $20 \text{ }\mu\text{m}$. Both straight and folded electrode shapes were used. The electrodes were arranged in groups of 16 and part of the path was scaled down for polymer ball transport. For droplet import and export, the devices were provided with small through holes. The hole diameter on the electrode side was varied in different device versions between 10 , 20 and $40 \text{ }\mu\text{m}$,

while the back side diameter was always 300 μm . On the export site, the top side of the hole consisted of seven holes in a circular matrix.

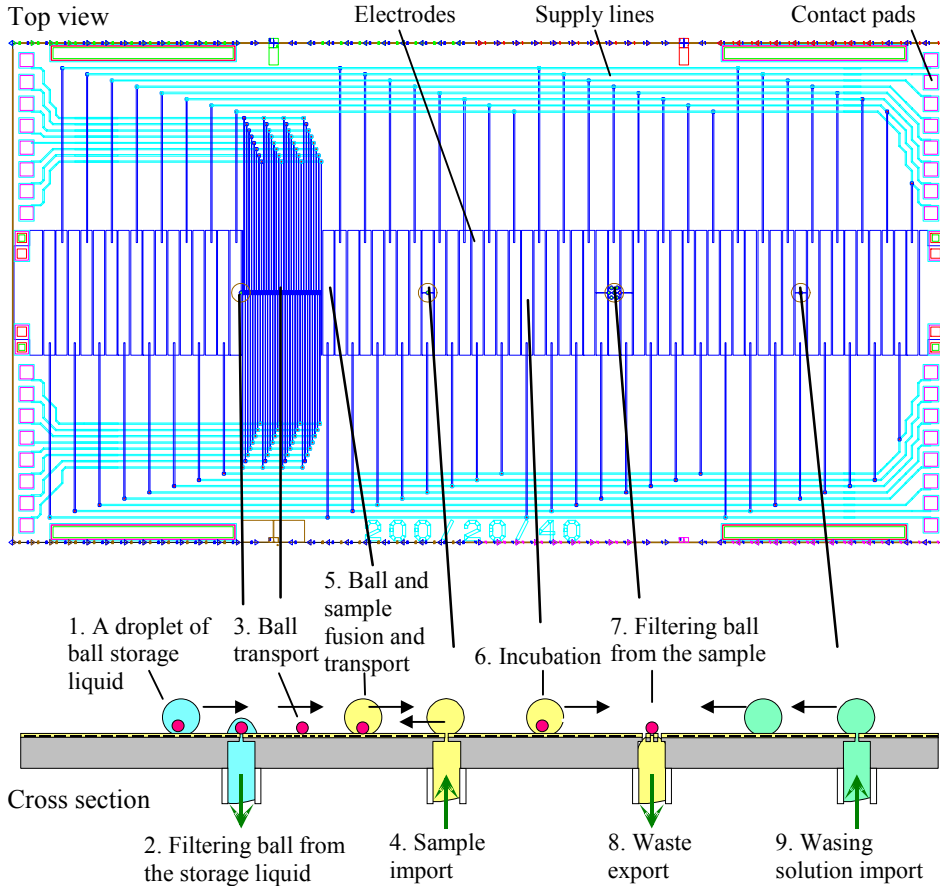


Figure 104. Layout and schematic presentation of planned droplet functions of the 4th generation droplet transport devices. Dimensions of a single chip are 15 x 8 mm².

Figure 105 shows a schematic cross-section of the 4th generation actuator device. The bottom insulator was a combination of thermal and LPCVD silicon dioxide with a total thickness of 2 μm . The electrodes were made of 300 nm thick sputtered titanium-tungsten, and the supply lines and contact pads were sputtered aluminium with a thickness of 1 μm . The intermediate and top insulators were LPCVD silicon dioxide layers with a thickness of 2 μm . After electrode fabrication, ICP etching was used to etch through the silicon substrate from both

sides. The top insulator was deposited after top side ICP etch to provide hydrophilic side walls on the neck of the holes.

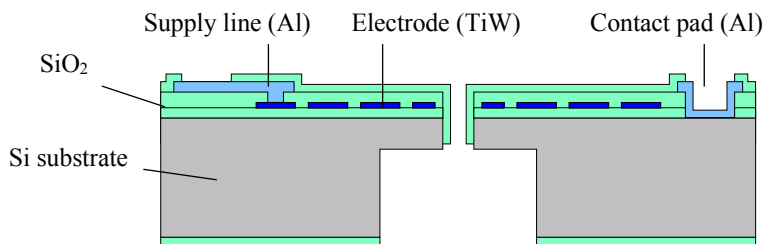


Figure 105. Cross-section of a 4th generation actuator device.

The diced chips were bonded into ceramic DIL cases, which were opened from the bottom. Small metal tubes were glued into the bottom of the chip as tube connectors. Before hydrophobic coating a cellulose acetate adhesive film with thickness 65 μm (ScotchTM 810 Magic Transparent Tape, 3M) was applied on the top side of the device. This was used because the best results so far have been achieved using this insulator. For droplet import and export, the tape had to be provided also with small through holes, which appeared to be a very challenging task. Hole formation beforehand was not possible, because attachment of the tape was not accurate enough to align the holes in the tape with the device. Thus the holes had to be made after tape attachment. First it was tried with a YAG laser, but the tape absorption was too low and the power required to burn a hole in the tape damaged the underlying silicon. We then tried making a hole with a hot needle actuated using a micromanipulator, but the method was hard to control. Finally, the holes were made successfully with an XeCl excimer laser. Finally a layer of Teflon[®] AF was sprayed on the device, having been chosen because it showed the best compatibility with buffer solutions.

With the 4th generation transport devices we used AC voltage and a new kind of switching electronics, in which relays are replaced by TRIACs and allow for greater actuation speeds. Continuous droplet transportation was successful with voltages down to 250 V, but the droplet motion was not steady, and droplets did not always completely follow the electrode voltage sequence. Furthermore, not all devices were functional. These actuation problems are thought to be related to quality and variations of the sprayed surface. As shown in Figure 53, sprayed

Teflon[®] AF consists of large bumps, and the droplet may even have to move vertically to overcome them.



Figure 106. Top view of a droplet being transported on a 4th generation device¹. The electrodes are straight with step 200 μm and spacing 20 μm .

Problems were also encountered in droplet import. The major problem was poor adhesion of Teflon[®] AF. When pushing water through the hole, it penetrated between tape and the Teflon[®] AF layer. Due to the hydrophobic layer and tape insulator there is a hydrophobic capillary, and quite large pressure is required to push liquid through it. Some droplets were formed, but since both droplet generation and actuation suffered from severe problems, the targeted function to form a droplet which could be transported further in a controlled manner using electrostatic force could not be demonstrated.

Droplet export was completely unsuccessful. As shown Figure 106, the droplet passed the export holes without being absorbed. Apparently, there was no capillary action in the neck of the hole due to the tape and hydrophobic layer. The advancing contact angle of the tape surface was measured as $> 90^\circ$, and if this is also the case with the tape hole side walls, the capillary pressure in the hole would be negative. The holes without tape and hydrophobic layer were operational, so that water was drained through the device when a piece of paper was placed on the bottom side of the chip. There was an idea to initiate droplet export by pushing a small droplet to the surface to capture the moving droplet, but due to problems with droplet import this was not possible.

¹ The experiment is available as a movie file. See the table of contents.

In brief, the presented attempt to demonstrate a complete droplet reactor system was unsuccessful, since we tried to move too fast towards the system before the individual droplet functions were fully analysed and optimised. Also the need was recognised for further improvement of the fabrication technology. In light of these problems the technical development of the system was not carried further. The work continued with theoretical analysis of droplet actuation and physical mechanisms as reported in the theoretical part of this thesis.

5. Conclusions

This work reports on the theoretical analysis and experimental results of electrostatic droplet actuation, which can be used as a method to manipulate small liquid volumes on a planar hydrophobic surface. Two-directional transportation of water droplets along a straight electrode path and across a junction, fusion of two droplets and methods for importing, exporting and filtering of droplets were demonstrated. The combination of functions on the same device is considered to be possible, but it requires improvements in fabrication and better control of individual operations. There is only one previous study on electrostatic droplet actuation on an open surface [21], and the most important new system-level features demonstrated in this work are the guiding of droplets by electrode shaping instead of grooves and the methods for importing, exporting and filtering.

The main original feature of this work is the use of so-called superhydrophobic surfaces. This was motivated by the experience that droplet motion is highly critical to the sliding resistance of the surface, which is given in terms of contact angle hysteresis. It was found, however, that equally important are the charging properties, and in the case of superhydrophobic surfaces the critical pressure, which is defined as the negative capillary pressure of the surface structures.

The superhydrophobic surfaces developed in this thesis include evaporated AKD, sprayed AKD, sprayed Teflon[®] AF and lithographically structured silicon coated with ICP fluoropolymer or Sol-Gel FAS. These are all new combinations of methods and materials. The first three were used successfully in droplet actuation, and the best surface (evaporated AKD) showed the minimum droplet actuation voltage of 124 VAC and the maximum actuation speed in the order of cm/s. The characteristics are better than in the previous study [21], which shows that superhydrophobic surfaces can be used to improve droplet actuation, at least when the liquid is water.

One of the contributions of the thesis is a deeper understanding of the droplet actuation mechanism. A model is presented which can be used to calculate actuation forces and voltages, and it correlates with the experiments, although the variations in surface properties made precise judgement difficult. A major limitation of the model is related to the sliding force of the droplet. There was

evidence that the force increases as a function of the contact pressure, and also the contact angle hysteresis may depend on the droplet size, but inclusion of the effects would require a better theory of contact line dynamics on superhydrophobic surfaces.

The force that moves the droplet is an electrostatic force. This force, acting on the solid-liquid interface, also modifies the contact angle, which is known as the electrowetting effect. The electrowetting effect in the case of superhydrophobic surfaces is analysed and formulated for the first time in this thesis. It was found that the effect of an electric field on the apparent contact angle of the droplet is very small, but there is a much stronger change in the contact angle between the water membranes and the surface structures. This phenomenon, termed the vertical electrowetting effect, can lead to penetration of water into the surface structures, which destroys the superhydrophobic properties. This can be treated equally as the electrostatic pressure exceeding the critical pressure of the surface.

It follows that the actuation mechanism should not be considered a consequence of the electrowetting effect, as has been done in recent papers on droplet actuation [23, 27]. In that case only the solid-liquid interface of the droplet is taken into account and the liquid-air interface is neglected. With smooth hydrophobic surfaces and with thin insulators this simplification may be acceptable, but with superhydrophobic surfaces this is incorrect. With superhydrophobic surfaces, droplet actuation occurs without observable modification of the apparent contact angle. Thus it is proposed that the droplet actuation mechanism should be termed generally as electrostatic instead of electrowetting-based.

Vertical electrowetting causes severe problems in droplet actuation, since it may cause droplet sticking. Furthermore, the driving voltages cannot be reduced by dropping with the insulator thickness, since the electrostatic pressure increases more rapidly than the useful electrostatic force. The insulator permittivity does not have the same effect and can be increased to reduce the voltages. As the critical pressure is inversely proportional to the characteristic dimensions of the surface structures, the resistance of the surface to the wetting can be reduced by surface design. Evaporation and spraying produced roughness with surface dimensions down to around 0.1 μm , but the surface properties varied quite a lot.

Lithographic patterning gives better control of the surface dimensions. The fabricated lithographic surfaces with dimensions of about 1 μm showed low sliding resistance, but all too low critical pressures. However, the design can be significantly improved and further experiments should be made to verify their usability in droplet actuation.

Charging effects in the solid-liquid interface have received little attention in the literature, and despite its importance in this context it is not discussed in detail in any other droplet actuation work. Threshold-type charge trapping, originally discovered by Chudleigh [94], was confirmed by reviewing later studies of the electrowetting phenomenon. There seems to be a square root dependence with the threshold voltage and the insulator layer thickness. This can be related to the electrowetting effect, and based on this assumption the charge trapping was included in model calculations. It was also found that there are large differences in the charging properties of different hydrophobic materials. Charge trapping limits the useful electrostatic force, and if it is very strong, droplet actuation is not possible at all. The long term stability problems observed with droplet actuation were thought, but not confirmed, to originate from gradual charging of the surface.

The experiments also revealed further effects related to superhydrophobic surfaces. The droplets may vibrate harmfully when AC voltages are used, but this can be suppressed with DC voltages. A serious problem is the sensitivity of the superhydrophobic surfaces to the properties of the liquid, especially to additives, which alter the interfacial tension. For this reason, actuating of biological buffer solutions was not successful, which is a severe problem for practical applications of the droplet reactor concept. Actuation of similar solutions has been reported on a smooth surface [21], leading to the conclusion that a smooth surface with low hysteresis is a better choice for droplet actuation than a superhydrophobic surface. Such surfaces exist; for example Chen et al. [44] have reported several surface treatments of silicon wafers which result in only 1° hysteresis. It follows that the future of the droplet reactor concept is strongly dependent on how the charge trapping problems are solved. This requires basic research on the subject, and possibly new materials and surface treatments will have to be developed. It should be noted, however, that charge trapping problems were encountered also in early MOS transistors, but after extensive research the problems were solved.

References

1. L. J. Kricka, Microchips, microarrays, biochips and nanochips: personal laboratories for the 21st century, *Clinica Chimica Acta* 307, 2001, 219–223.
2. F. Vinet, P. Chaton and Y. Fouillet, Microarrays and microfluidic devices: miniaturized systems for biological analysis, *Microelectronic Engineering* 61-62, 2002, 41–47.
3. P. Gwynne and G. Heebner, Laboratory technology trends: DNA and Biochips: 3, *Science* 298 (5593), 2002, 629–641.
4. E. Mounier and M. Provence, Technologies and market trends in biocips and microfluidic chips, *MST News* 5, Nov 2002, 4–6.
5. R. Linnemann, P. Woias, C.-D. Senfft and J. A. Ditterich, A self-priming and bubble-tolerant piezoelectric silicon micropump for liquids and gases, *Proc. 11th IEEE Int. Conf. Micro Electro Mechanical Systems, MEMS 98*. Jan 25–29 1998, Heidelberg, Germany, 532–537.
6. W. van der Wijngaart, H. Andersson, P. Enoksson, K. Noren and G. Stemme, The first self-priming and bi-directional valve-less diffuser micropump for both liquid and gas, *Proc. 13th IEEE Int. Conf. Micro Electro Mechanical Systems, MEMS 2000*. Jan 23–27 2000, Miyazaki, Japan, 674–679.
7. D. Maillefer, S. Gamper, B. Frehner, P. Balmer, H. van Lintel and P. Renaud, High performance silicon micropump for disposable drug delivery systems, *Proc. 14th IEEE Int. Conf. Micro Electro Mechanical Systems, MEMS 2001*. Jan 21–25 2001, Interlaken, Switzerland, 413–417.
8. S. Santra, P. Holloway and C. D. Batich, Fabrication and testing of a magnetically actuated micropump, *Sensors and Actuators B* 87, 2002, 358–364.
9. G. Urban, G. Jobst and I. Moser, A hybrid modular microsystem (HYMOS) for a Laboratory on chip, *Proc. 13th European conf. Solid-State Transducers, EUROSENSORS XIII*, Sept 12–15 1999, The Hague, Netherlands, 171–172.

10. Advice for setting up robust DELFIA® binding assays, PerkinElmer Life Sciences, Application Notes, 2001, <http://lifesciences.perkinelmer.com/Notes/1234979.pdf>
11. A. Manz, D. J. Harrison, J. C. Fettinger, E. Veerporte, H. Lüdi and H. M. Widmer, Integrated electroosmotic pumps and flow manifolds for total chemical analysis systems, Proc. Int. Conf Solid-State Sensors and Actuators, TRANSUDCERS '91, Montreux, Swizerland – Tokyo, Japan – San Fransisco, USA, 24–27 June 1991, 939–941.
12. S. Zeng, C.-H. Chen, J. C. Mikkelsen Jr. and J. G. Santiago, Fabrication and characterization of electroosmotic micropumps, Sensors and Actuators B 79, 2001, 107–114.
13. P. Selvaganapathy, Y. L. Ki, P. Renaud and C. H. Mastrangelo, Bubble-free electrokinetic pumping, J. Microelectromech. Syst. 11 (5), 2002, 448–453.
14. P. A. Greenwood and G. M. Greenway, Sample manipulation in micro total analytical systems, Trends in Anal. Chem. 21 (11), 2002, 726–740.
15. T. D. Boone, Z. H. Fan, I. Gibbons, A. J. Ricco, A. Sassi, S. Singh, D. Slomski, H. Tan, S. J. Williams, V. Xiao and Q. Xue, Disposable plastic microfluidic arrays for applications in biotechnology, Proc. 11th Int. Conf Solid-State Sensors and Actuators, TRANSUDCERS '01 – EUROSENSORS XV, 10–14 June 2001, Munich, Germany, 1146–1149.
16. S. H. Ahn and Y.-K. Kim, Fabrication and experiment of a planar micro ion drag pump, Sensors and Actuators A 70, 1998, 1–5.
17. J. Jang and S. S. Lee, Theoretical and experimental study of MHD (magnetohydrodynamic) micropump, Sensors and Actuators A 80, 2000, 84–89.
18. D. C. Duffy, H. L. Gillis, J. Lin, N. F. Sheppard Jr. and G. J. Kellogg, Microfabricated centrifugal microfluidic systems: characterization and multiple enzymatic assays, Anal. Chem. 71, 1999, 4669–4678.
19. T. K. Jun and C.-J. Kim, Valveless pumping using traversing vapor bubbles in microchannels, J. Appl. Phys., 83 (11), 1998, 5658–5664.

20. M. Washizu, Electrostatic Actuation of Liquid Droplets for Microreactor Applications, Proc. IEEE Industry Applications Society, Annual Meeting, Oct 5–9, New Orleans, Louisiana, US, 1997.
21. M. Washizu, Electrostatic Actuation of Liquid Droplets for Microreactor Applications, IEEE Trans. Industry App. 34 (4), 1998, 732–737.
22. J. S. Batchelder, Dielectrophoretic manipulator, Rev. Sci. Instrum. 54 (3), 1983, 300–302.
23. M. G. Pollack, R. B. Fair and A. D. Shenderov, Electrowetting-based actuation of liquid droplets for microfluidic applications, App. Phys. Lett. 77 (11), 2000, 1725–1726.
24. M. G. Pollack, Electrowetting-based microactuation of droplets for digital microfluidics, Ph.D. Thesis, Duke University, US, 2001.
25. J. Lee, H. Moon, J. Fowler, C.-J. Kim and T. Schoellerhammer, Addressable micro liquid handling by electric control of surface tension, Proc. 14th IEEE Int. Conf. Micro Electro Mechanical Systems, MEMS 2001, Jan 21–25 2001, Interlaken, Switzerland, 499–502.
26. S. K. Cho, S.-K. Fan, H. Moon and C.-J. Kim, Towards digital microfluidic circuits: creating, transporting, cutting and merging liquid droplets by electrowetting-based actuation, Proc. 15th IEEE Int. Conf. Micro Electro Mechanical Systems, MEMS 2002, Jan 20–24 2002, Las Vegas, US, 32–35.
27. J. Lee, H. Moon, J. Fowler, T. Schoellerhammer and C.-J. Kim, Electrowetting and electrowetting-on-dielectric for microscale liquid handling, Sensors and Actuators A 95, 2002, 259–268.
28. H. Härmä, Particle-based bioaffinity assay systems – sensitive miniature single-particle immunoassay, Ph.D. dissertation, University of Turku, Finland, Turun Yliopiston Julkaisuja – Annales Universitatis Turkuensis, Ser. A1, 273, 2001.
29. T. B. Jones, M. Gunji, M. Washizu and M. J. Feldman, Dielectrophoretic liquid actuation and nanodroplet formation, J. App. Phys, 89 (2), 2001, 1441–1448.

30. O. Sandre, L. Gorre-Talini, A. Ajdari, J. Prost and P. Silberzan, Moving droplets on asymmetrically structured surfaces, *Phys. Rev. E* 60 (3), 1999, 2964–2972.
31. S. Nilsson, S. Santesson, E. Degerman, E. Cedergren, T. Johansson, T. Laurell and J. Nilsson, Airborne chemistry: Micro-analysis, Proc. 13th European conf. Solid-State Transducers, EUROSENSORS XIII, Sept 12–15 1999, The Hague, Netherlands, 7–8.
32. C. J. Strobl, A. Rathgeber, A. Wixforth, C. Gauer and J. Scriba, Planar microfluidic processors, proc. IEEE Int. Ultrasonic Symposium, Oct 8–11, 2002, Munich, Germany, in press.
33. A. Wixforth, J. Scriba and C. Gauer, Flatland fluidics, *MST News* 5, Nov 2002, 42–43.
34. Y.-T. Tseng, F.-G. Tseng and C.-C. Chieng, Experimental and Numerical Studies on Micro-Droplet Movement Driven by Marangoni Effect, Proc. 12th Int. Conf Solid-State Sensors, Actuators and Microsystems, TRANSUDCERS '03, 8–12 June 2003, Boston, USA, 1879–1882.
35. P. Chiou, Z. Chang and M. Wu, Pico liter droplet manipulation based on a novel continuous opto-electrowetting mechanism, Proc. 12th Int. Conf Solid-State Sensors, Actuators and Microsystems, TRANSUDCERS '03, 8–12 June 2003, Boston, USA, 468–471.
36. H. Ren, R. B. Fair, M. G. Pollack and E. J. Shaughnessy, Dynamics of electro-wetting droplet transport, *Sensors and Actuators B* 87, 2002, 201–206.
37. A. Torkkeli, A. Häärä, J. Saarilahti, H. Härmä, T. Soukka and P. Tolonen, Electrostatic transportation of water droplets on superhydrophobic surfaces, Proc. 14th IEEE Int. Conf. Micro Electro Mechanical Systems, MEMS 2001. Jan 21–25 2001, Interlaken, Switzerland, s. 475–478.
38. A. Torkkeli, A. Häärä, J. Saarilahti, H. Härmä, T. Soukka and P. Tolonen, Pertti. Droplet manipulation on a superhydrophobic surface for microchemical analysis. Proc. 11th Int. Conf. Solid-State Sensors and Actuators, TRANSDUCERS '01 – EUROSENSORS XV, 10–14 June 2001, Munich, Germany, 1150–1153.

39. A. Torkkeli, Oral presentation in 3rd Electrowetting Workshop, Grenoble, France, 24–25 Jan, 2002.
40. T. Nishino, M. Meguro, K. Nakamae, M. Matsushita and Y. Ueda, The Lowest Surface Free Energy Based on $-CF_3$ Alignment, *Langmuir* 15, 1999, 4321–4323.
41. C. G. L. Furnidge, Studies at phase interfaces I. The sliding of liquid drops on solid surfaces and a theory for spray retention. *J. Colloid Sci.* 17, 1962, 309–324.
42. E. B. Dussan and R. T.-P. Chow, On the ability of drops or bobbles to stick to non-horizontal surfaces, *J. Fluid Mech.* 137, 1983, 1–29.
43. A. Nakajima, K. Hashimoto and T. Watanabe, Recent Studies on Super-Hydrophobic Films, *Monatshefte für Chemie* 132, 2001, 31–41.
44. W. Chen, A. Y. Fadeev, M. C. Hsieh, D. Öner, J. Youngblood and T. McCarthy, Ultrahydrophobic and Ultralyophobic Surfaces: Some Comments and Examples, *Langmuir* 15, 1999, 3395–3399.
45. D. Öner and T. Mc Carthy, Ultrahydrophobic surfaces. Effects of topography length scales on wettability, *Langmuir* 16, 2000, 7777–7782.
46. M. Miwa, A. Nakajima, A. Fujisima, K. Hashimoto and T. Watanabe, Effects of the surface roughness on sliding angles of water droplets on superhydrophobic surfaces, *Langmuir*, 16, 2000, 5754–5760.
47. R. E. Johnson and R. H. Dettre, Contact angle hysteresis I. Study of and Idealized Rough Surface. *Advances in Chemistry series* 43, 1964, 112–135.
48. R. E. Johnson and R. H. Dettre, Contact angle hysteresis II. Contact Angle Measurements on Rough Surfaces. *Advances in Chemistry series* 43, 1964, 136–144.
49. C. Neinhuis and W. Barthlott, Characterization and distribution of water-repellent, self-cleaning plant surfaces, *Ann. Botany* 79, 1997, 667–677.
50. S. Wu, *Polymer interface and adhesion*, Marcel Dekker, New York, 1982, ISBN 0-8247-1533-0.
51. J. Bico, C. Marzolin and D. Quéré, Pearl drops, *Europhys. Lett.* 47 (2), 1999, 220–226.

52. R. H. Dettre, H. L. Jackson and R. E. Johnson, Water-Repellant surface, U.S. Patent 3,354,022, 1967.
53. A. W. Adamson and A. P. Gast, *Physical Chemistry of Surfaces*, 6th ed, Wiley, New York, 1997, ISBN 0-471-14873-3.
54. D. Richard and D. Quere, Viscous droplet rolling on a tilted non-wettable solid, *Europhys. Lett*, 48 (3), 1999, 286–291.
55. L. Mahadevan and Y. Pomeau, Rolling droplets, *Phys. Fluids* 11 (9), 1999, 2449–2453.
56. R. C. Anderson, G. J. Bogdan, A. Puski and X. Su, Genetic analysis systems: improvements and methods, *Proc. Solid-State Sensor and Actuator Workshop*, Hilton Head, June 8–11, 1998, 7–10.
57. W. Shen, J. Kim and C.-J. Kim, Controlling the adhesion force for electrostatic actuation of microscale mercury drop by physical surface modification, *Proc. 15th IEEE Int. Conf. Micro Electro Mechanical Systems, MEMS 2002*, Jan 20–24 2002, Las Vegas, US, 52–55.
58. David R. Lide, editor-in-chief, *CRC Handbook of Chemistry and Physics*, 80th ed., CRC Press, Boca Raton, 1999, ISBN 0-471-09804-3.
59. D. K. Cheng, *Field and Wave Electromagnetics*, 2nd ed., 4th printing, Addison–Wesley, Reading, Massachusetts, 1991, ISBN 0-201-52820-7.
60. K. Yatsuzuka, Y. Mizuno and K. Asano, Electrification of pure water droplets dripping and sliding on a polymer surface, *J. Electrostatics* 32, 1994, 157–171.
61. H. A. Pohl, *Dielectrophoresis*, Cambridge University Press, Cambridge, 1978, ISBN 0-521-21657-5.
62. D. T. Paris and F. K. Hurd, *Basic electromagnetic theory*, McGraw–Hill, New York, 1969.
63. S. Marguiles, Force on a dielectric slab inserted into a parallel-plate capacitor, *Am. J. Phys.* 52 (6), 1984, 515–518.

64. B. E. Conway, Electrical aspects of liquid/vapour, liquid/liquid and liquid/metal interfaces, In: E. E. Kunhardt, L. G. Christophorou and L H. Luessen (eds.), *The liquid state and its electrical properties*, NATO ASI Series B: Physics, Vol 193, Plenum Press, New York, 1988, ISBN 0-306-43145-9.
65. R. Tobazéon, Electrical phenomena of dielectric materials, in: J-S Chang, A. J. Kelly and J. M. Crowley, (eds.) *Handbook of electrostatic processes*, Marcel Dekker Inc., New York, 1995, ISBN 0-8247-9254-8.
66. A. G. Bailey, *Electrostatic spraying of liquids*, Research Studies Press, Taunton, Somerset, England, 1988, ISBN 0-471-92100-9.
67. R. Cade, The electrohydrodynamics of a quasi-conical sessile meniscus developing into the Taylor cone, *J. Electrostatics* 35, 1995, 279–293.
68. D. J. Shaw, *Introduction to Colloid and surface chemistry*, 4th ed., Butterworths, London, 1992, ISBN 0-7506-1182-0
69. J. N. Israelachvili, *Intermolecular and surface forces*, 3rd printing, Academic Press, London, 1989, ISBN 0-12-375180-2.
70. L. Minnema, H. A. Barneveld and P. D. Rinkel, An investigation into the mechanism of water treeing in the polyethylene high voltage cables, *IEEE Transactions on Electrical Insulation EI-15*, (6) 1980, 461–472.
71. G. Beni and S. Hackwood, Electro-wetting displays, *App. Phys. Lett.* 38 (4), 1981, 207–209.
72. G. Beni and S. Hackwood, Dynamics of electrowetting displays, *J. Appl. Phys.* 52 (10), 1981, 6011–6015.
73. B. Berge, Electrocapillarity and wetting of insulator films by water. (Abridged english version of: *Électrocapillarité et mouillage de films isolants par l'eau*), *C. R. Acad. Sci Paris*, t.317, Série II. 1993, 157–163.
74. C. Quillet and B. Berge, Electrowetting: a recent outbreak, *Current Opinion in Colloid & Interface Science* 6, 2001, 34–39.
75. B. Berge and J. Peseux, Variable focal lens controlled by an external voltage: An application of electrowetting, *Eur. Phys. J. E*, 3, 2000, 159–163.

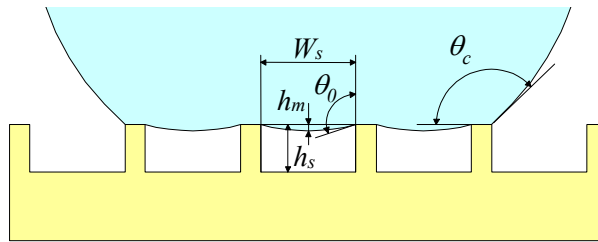
76. S. Kwon and L. P. Lee, Focal length control by microfabricated planar electrodes-based liquid lens (μ PELL), Proc. 11th Int. Conf Solid-State Sensors and Actuators, TRANSUDCERS '01 – EUROSENSORS XV, Munich, Germany, June 10–14, 2001, 1348–1351.
77. J. Lee and C.-J. Kim, Surface-Tension-Driven Microactuation Based on Continuous Electrowetting, *J. Microelectromech. Syst.* 9 (2), 2000, 171–180.
78. H. Matsumoto and J. E. Colgate, Preliminary investigation of micropump based on electrical control of interfacial tension, Proc. IEEE conf. Micro Electro Mechanical Systems, Napa Valley, CA, USA, 11–14 Feb, 1990, 105–110.
79. E. Colgate and H. Matsumoto, Investigation of electrowetting-based microactuation, *J. Vac. Sci. Technol. A* 8 (4), 1990, 3625–3633.
80. K.-S. Yun, I.-J. Cho, J.-U. Bu, C.-J. Kim and E. Yoon, A surface tension driven micropump for low-voltage and low-power operations, *J. Microelectromech. Syst.* 11 (5), 2002, 454–461.
81. M. Vallet, M. Vallade and B. Berge, Limiting phenomena for the spreading of water on polymer films by electrowetting, *Eur. Phys. J. B* 11, 1999, 583–591.
82. B. Janocha, H. Bauser, O. Oehr, H. Brunner and W. Göpel, Competitive electrowetting of polymer surfaces by water and decane, *Langmuir*, 16, 2000, 3349–3354.
83. H. J. J. Verheijen and M. W. J. Prins, Reversible Electrowetting and Trapping of Charge: Model and Experiments, *Langmuir*, 15, 1999, 6616–6620.
84. T. D. Blake, A. Clarke and E. H. Strattersfield, An investigation of electrostatic assist in dynamic wetting, *Langmuir*, 16, 2000, 2928–2935.
85. R. Digilov, Charge-Induced Modification of Contact Angle: The Secondary Electrocapillary effect, *Langmuir* 16 (16), 2000, 6719–6723.
86. M. W. J. Prins, W. J. J. Welters and J. W. Weekamp, Fluid Control in Multichannel Structures by Electrocapillary Pressure, *Science* 291 (12 Jan), 2001, 277–280.

87. R. Digilov, personal communication, 2000.
88. T. D. Blake, Oral presentation in 3rd Electrowetting Workshop, Grenoble, France, 24–25 Jan, 2002.
89. B. Saphiro, H. Moon, R. Garrell and C.-J. Kim. Equilibrium behaviour of sessile drops under surface tension, applied external fields and material variations, submitted for Journal of Applied physics.
90. H. J. J. Verheijen and M. W. J. Prins, Contact angles and wetting velocity measured electrically, *Rev. Sci. Instr.* 70 (9), 1999, 3668–3673.
91. G. M. Sessler, *Electrets*, Springer, Berlin, 1980, ISBN 3-540-09570-5.
92. P. W. Chudleigh, Charging of polymer foils using liquid contacts, *App. Phys. Lett.* 21 (11), 1972, 547–548.
93. R. S. Engelbrecht, Electrostatic recording on insulators by nonwetting conducting liquids, *J. App. Phys.* 45 (8), 1974, 3421–3423.
94. P. W. Chudleigh, Mechanism of charge transfer to a polymer surface by a conducting liquid contact, *J. App. Phys.* 47 (10), 1976, 4475–4483.
95. A. G. Bailey, Electrostatic hazards during liquid transport and spraying, in: J.-S. Chang, A. J. Kelly and J. M. Crowley, (eds.) *Handbook of electrostatic processes*, Marcel Dekker Inc., New York, 1995.
96. M. Matsui, N. Murasaki, K. Fujibayashi, P. Y. Bao and Y. Kishimoto, Electrification of pure water flowing down a trough set up with a resin sheet, *J. Electrostatics*, 31, 1993, 1–10.
97. M. Vallet and B. Berge, Electrowetting of water and aqueous solutions on poly(ethylene terephthalate) insulating films, *Polymer* 37 (12), 1996, 2465–2470.
98. H. Moon, S. K. Cho, R. L. Garrell and C. J. Kim, Low voltage electrowetting-on-dielectric (EWOD), *J. Appl. Phys.*, 92 (7), 2002, pp. 4080–4087.
99. K. G. Marinova et al. Charging of oil-water interfaces due to spontaneous adsorption of hydroxyl ions, *Langmuir* 12, 1996, 2045–2051.
100. M. E. R. Shanahan, Profile and contact angle of small sessile drops, *J. Chem. Soc. Faraday Trans.* 80, 1984, 37–45.

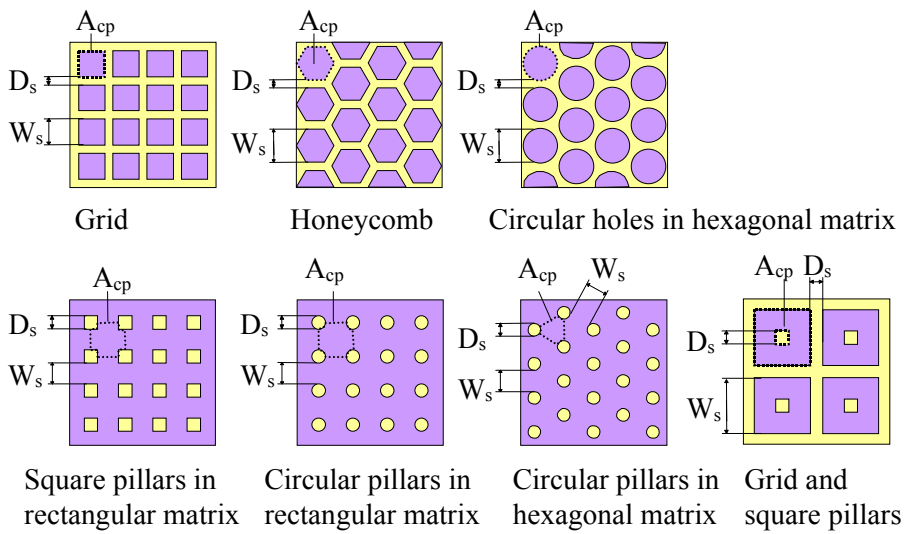
101. S. B. G. M. O'Brien and B. H. A. A. van den Brule, Shape of a small sessile drop and the determination of contact angle, *J. Chem. Soc. Faraday Trans.* 87 (10), 1991, 1579–1583.
102. C. M. Osburn and D. W. Ormond, Dielectric breakdown in silicon dioxide films on silicon, *J. Electrochem. Soc., Solid-State Sci. Technol.* 119 (5), 1972, 591–603.
103. Teflon® AF Amorphous Fluoropolymers, DuPont Data Sheet.
104. S. J. Mackenzie, M. Johnson and J. P. Dakin, A Novel Waveguide Configuration for Convenient and Sensitive Fluorescence and Raman Measurements of Liquids Over Optical Fibers, *Proc. Europto EnviroSense '97*, Munich, 16–20 Jun, 1997.
105. C.-C. Cho, R. M. Wallace and L. A. Files-Sesler, Patterning and etching of amorphous Teflon films, *J. Electronics Materials* 23 (8), 1994, 827–830.
106. S. Shibuichi, T. Onda, N. Satoh and K. Tsujii, Super water-repellent surfaces resulting from fractal structure, *J. Phys. Chem* 100, 1996, 19512–19517.
107. M. Morra, E. Occhiello and F. Garbassi, Contact angle hysteresis in oxygen plasma treated poly(tetrafluoroethylene), *Langmuir* 5, 1989, 872–876.
108. J. Kim and C.-J. Kim, Nanostructured surfaces for dramatic reduction of flow resistance in droplet-based microfluidics, *Proc. 15th IEEE Int. Conf. Micro Electro Mechanical Systems, MEMS 2002*, 20–24. Jan, Las Vegas, 479–482.
109. P. K. Wu, G.-R. Yang and T.-M. Lu, Interaction of amorphous fluoropolymer with metal, *Appl. Phys. Lett.* 65 (4), 1994, 508–510.
110. Y. Du and J. S. Gardella, Jr., A study of the interaction between thermally deposited aluminium films and fluoropolymer substrates, *J. Vac. Sci. Technol. A*, 13 (4), 1995, 1907–1912.
111. K. Tadanaka, N. Katata and T. Minami, Super-water-repellent Al₂O₃ coating films with high transparency, *J. Am. Ceram. Soc.* 80 (4), 1997, 1040–1042.

112. H. A. Biebuyck, N. B. Larsen, E. Delamarche and B. Michel, Lithography beyond light: Microcontact printing with monolayer resists, *IBM J. Res. Develop.* 41 (1/2) Jan/March 1997, 159–170.
113. A. Desai, S. W. Lee and Y.-C. Tai, A MEMS electrostatic particle transportation system, *Sensors and Actuators A* 73, 1999, 37–44.
114. M. Strani and F. Sabetta, Free vibrations of a drop in partial contact with a solid support, *J. Fluid Mech.* 141, 1984, 233–247.
115. S. Yamakita, Y. Matsui and S. Shiokawa, New method for measurement of contact angle (droplet free vibration frequency method), *Proc. 10th Int. Conf Solid-State Sensors and Actuators, TRANSUDCERS '99*, June 7–10, 1999, Sendai, Japan, 462–465.
116. H. Lamb, *Hydrodynamics*, 6th Ed. 1975, Cambridge University Press, New York, ISBN 0-521-05515-6

Appendix A: Analysis of model surfaces with different patterns



(a)



(b)

Figure A1. Analysed vertical surface structures a) cross-section, b) top views.

Grid

Let us consider a grid, which consists of square holes with side length W_s and spacing D_s . The elementary capillary has a square cross-section, denoted A_{cp} in Figure A1. The area and perimeter of the elementary capillary are then:

$$A_{cp} = W_s^2 \quad (\text{A1})$$

$$L_{cp} = 4W_s. \quad (\text{A2})$$

The critical pressure is then according to equation (9)

$$P_c = -\lambda_{lv} \cos \theta \frac{L_{cp}}{A_{cp}} = -\lambda_{lv} \cos \theta \frac{4W_s}{W_s^2} = -\lambda_{lv} \cos \theta \frac{4}{W_s}. \quad (\text{A3})$$

The proportional area is the proportional amount of original material in the surface plane:

$$f = 1 - \frac{W_s^2}{(W_s + D_s)^2}. \quad (\text{A4})$$

Next, we eliminate W_s from the critical pressure by solving $1/W_s$ from the proportional area:

$$\frac{1}{W_s} = \frac{1}{D_s} \left(\frac{1}{\sqrt{1-f}} - 1 \right), \quad (\text{A5})$$

and substituting it into the equation for the critical pressure:

$$P_c = \lambda_{lv} \cos \theta \frac{4}{D_s} \left(1 - \frac{1}{\sqrt{1-f}} \right). \quad (\text{A6})$$

Honeycomb

The honeycomb surface consists of hydrophobic capillaries with a hexagonal cross-section, diameter W_s and spacing D_s . The area and perimeter of the elementary capillary are then:

$$A_{cp} = \frac{\sqrt{3}}{2} W_s^2, \quad (\text{A7})$$

$$L_{cp} = \frac{6}{\sqrt{3}} W_s. \quad (\text{A8})$$

The critical pressure is

$$P_c = -\lambda_{lv} \cos \theta \frac{L_{cp}}{A_{cp}} = -\lambda_{lv} \cos \theta \frac{\frac{6}{\sqrt{3}} W_s}{\frac{\sqrt{3}}{2} W_s^2} = -\lambda_{lv} \cos \theta \frac{4}{W_s}, \quad (\text{A9})$$

which is same as with the grid surface. The proportional area is

$$f = 1 - \frac{\frac{\sqrt{3}}{2} W_s^2}{\frac{\sqrt{3}}{2} (W_s + D_s)^2} = 1 - \frac{W_s^2}{(W_s + D_s)^2}. \quad (\text{A10})$$

Also the proportional area is identical to the grid pattern. Without further calculation we can conclude that the grid and honeycomb have equal critical pressure.

Circular holes in a hexagonal matrix

If we replace the hexagonal holes with circular ones, the area and perimeter of the elementary capillary are:

$$A_{cp} = \frac{\pi}{4} W_s^2, \quad (\text{A11})$$

$$L_{cp} = \pi W_s. \quad (\text{A12})$$

The critical pressure is

$$P_c = -\lambda_{lv} \cos \theta \frac{L_{cp}}{A_{cp}} = -\lambda_{lv} \cos \theta \frac{\pi W_s}{\frac{\pi}{4} W_s^2} = -\lambda_{lv} \cos \theta \frac{4}{W_s}, \quad (\text{A13})$$

which is the same formula as with the square holes. However, the proportional area is

$$f = 1 - \frac{\frac{\pi}{4} W_s^2}{\frac{\sqrt{3}}{2} (W_s + D_s)^2} = 1 - \frac{\pi}{2\sqrt{3}} \frac{W_s^2}{(W_s + D_s)^2}, \quad (\text{A14})$$

which is larger than with the grid or honeycomb surfaces. Thus this surface pattern is not as good as the grid and honeycomb.

Square pillars in a rectangular matrix

With pillar type surfaces, the elementary capillary is not as easy to determine as with grid type surfaces. However, we can distinguish the elementary meniscus supported by four adjacent pillars. This is defined as the cross-section of the elementary capillary as shown in Figure A1. The area of the elementary capillary is the area of a square less the area cut off by four pillar quarters,

$$A_{cp} = (W_s + D_s)^2 - D_s^2. \quad (\text{A15})$$

The perimeter of the elementary capillary is the total length of the contact lines between the elementary meniscus and the supporting pillars.

$$L_{cp} = 4D_s. \quad (\text{A16})$$

The critical pressure is then

$$P_c = -\lambda_{lv} \cos \theta \frac{L_{cp}}{A_{cp}} = -\lambda_{lv} \cos \theta \frac{4D_s}{(W_s + D_s)^2 - D_s^2}. \quad (\text{A17})$$

The proportional area equals

$$f = \frac{D_s^2}{(W_s + D_s)^2}. \quad (\text{A18})$$

W_s can be eliminated from the equation of critical pressure by solving $(W_s + D_s)^2$ from the proportional area and substituting it into the equation of the critical pressure. We get

$$P_c = -\lambda_{lv} \cos \theta \frac{4D_s}{\frac{D_s^2}{f} - D_s^2} = \lambda_{lv} \cos \theta \frac{4}{D_s \left(1 - \frac{1}{f}\right)}. \quad (\text{A19})$$

Circular pillars in a rectangular matrix

With circular pillars the area and the perimeter of the elementary capillary are defined respectively as with rectangular pillars, as shown in Figure A1. The area of the elementary capillary is the area of a square less the area cut off by four pillar quarters.

$$A_{cp} = (W_s + D_s)^2 - \frac{\pi}{4} D_s^2. \quad (\text{A20})$$

The perimeter of the elementary capillary is the total length of the contact lines between the elementary meniscus and the supporting pillars.

$$L_{cp} = \pi D_s. \quad (\text{A21})$$

The critical pressure is then

$$P_c = -\lambda_{lv} \cos \theta \frac{L_{cp}}{A_{cp}} = -\lambda_{lv} \cos \theta \frac{\pi D_s}{(W_s + D_s)^2 - \frac{\pi}{4} D_s^2}. \quad (\text{A22})$$

The proportional area equals

$$f = \frac{\frac{\pi}{4} D_s^2}{(W_s + D_s)^2}. \quad (\text{A23})$$

Elimination of W_s from the equation of critical pressure by solving $(W_s + D_s)^2$ from the proportional area and substituting it into the equation of the critical pressure yields:

$$P_c = -\lambda_{lv} \cos \theta \frac{\pi D_s}{\frac{\pi}{4} \frac{D_s^2}{f} - \frac{\pi}{4} D_s^2} = \lambda_{lv} \cos \theta \frac{4}{D_s \left(1 - \frac{1}{f}\right)}. \quad (\text{A24})$$

The result is the same as with the square pillars.

Circular pillars in a hexagonal matrix

With circular pillars in a hexagonal matrix, the area of the elementary capillary is the area of a rectangle less the area cut off by three pillars.

$$A_{cp} = \frac{\sqrt{3}}{4} (W_s + D_s)^2 - \frac{\pi}{8} D_s^2. \quad (\text{A25})$$

The perimeter of the elementary capillary is the total length of the contact lines between the elementary meniscus and the supporting pillars:

$$L_{cp} = \frac{\pi}{2} D_s . \quad (\text{A26})$$

The critical pressure is then

$$P_c = -\lambda_{lv} \cos \theta \frac{L_{cp}}{A_{cp}} = -\lambda_{lv} \cos \theta \frac{\frac{\pi}{2} D_s}{\frac{\sqrt{3}}{4} (W_s + D_s)^2 - \frac{\pi}{8} D_s^2} . \quad (\text{A27})$$

The proportional area equals

$$f = \frac{\frac{\pi}{8} D_s^2}{\frac{\sqrt{3}}{4} (W_s + D_s)^2} = \frac{\pi D_s^2}{2\sqrt{3} (W_s + D_s)^2} . \quad (\text{A28})$$

Elimination of W_s from the equation of critical pressure by solving $(W_s + D_s)^2$ from the proportional area and substituting it into the equation for the critical pressure yields:

$$P_c = -\lambda_{lv} \cos \theta \frac{\frac{\pi}{2} D_s}{\frac{\sqrt{3}}{4} \frac{\pi}{2\sqrt{3}} \frac{D_s^2}{f} - \frac{\pi}{8} D_s^2} = \lambda_{lv} \cos \theta \frac{4}{D_s \left(1 - \frac{1}{f} \right)} . \quad (\text{A29})$$

The result is the same as with the square and circular pillars in a rectangular matrix.

Combination of grid and square pillars

The cross-sectional area of the elementary capillary is the area of a rectangle less the area of the central pillar:

$$A_{cp} = W_s^2 - D_s^2 . \quad (\text{A30})$$

The perimeter of the elementary capillary is the total length of the contact lines between the elementary meniscus and the supporting pillars:

$$L_{cp} = 4W_s + 4D_s . \quad (\text{A31})$$

The critical pressure is then

$$P_c = -\lambda_{lv} \cos \theta \frac{L_{cp}}{A_{cp}} = -\lambda_{lv} \cos \theta \frac{4W_s + 4D_s}{W_s^2 - D_s^2} = -\lambda_{lv} \cos \theta \frac{4}{W_s - D_s} . \quad (\text{A32})$$

The proportional area equals

$$f = \frac{(W_s + D_s)^2 - W_s^2 + D_s^2}{(W_s + D_s)^2} = \frac{2W_s D_s + 2D_s^2}{(W_s + D_s)^2} = \frac{2D_s}{W_s + D_s} . \quad (\text{A33})$$

Solving W_s from the proportional area gives:

$$W_s = \left(\frac{2}{f} - 1 \right) D_s . \quad (\text{A34})$$

Substituting this into the equation of critical pressure yields:

$$P_c = -\lambda_{lv} \cos \theta \frac{4}{\left(\frac{2}{f} - 1 \right) D_s - D_s} = \lambda_{lv} \cos \theta \frac{2}{D_s \left(1 - \frac{1}{f} \right)} . \quad (\text{A35})$$

The result shows that with the given proportional area, the critical pressure of this surface is half of the value for the pillar surface.

Appendix B: Capacitance between a spherical droplet and a conducting plane

A conducting spherical droplet with volume V , radius R and contact angle θ is separated by an insulator from a conducting plane (Figure B1). The insulator has thickness d and relative permittivity ϵ_r . The droplet and the plane form a capacitor with capacitance C_d .

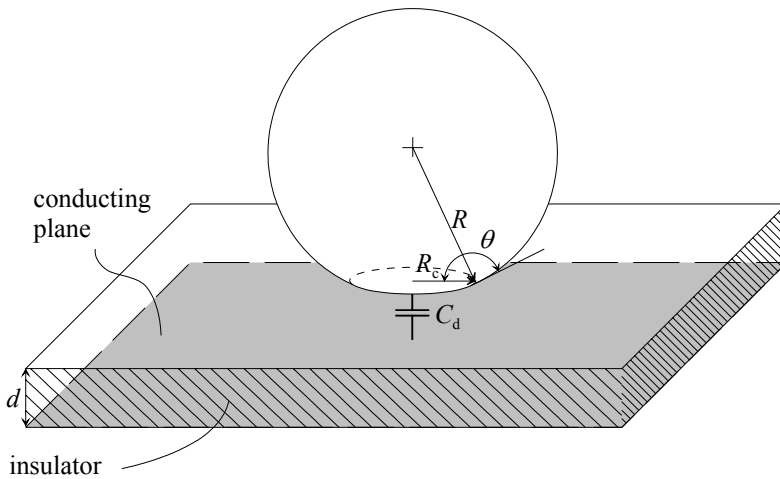


Figure B1. Droplet separated by an insulator from a conducting plane.

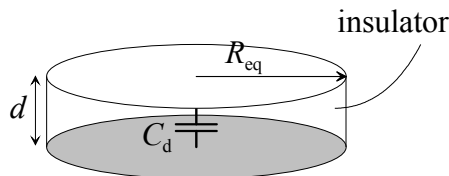


Figure B2. Equivalent circular parallel plate capacitor for the droplet and plane.

The droplet and the plane can be replaced with an equivalent circular parallel plate capacitor, which has the same capacitance and the same insulator in between (Figure B2). The parallel plate capacitor is assumed to be ideal, so that there is no fringe field at the plate edges. The capacitance between the plates is:

$$C_d = \frac{\varepsilon_0 \varepsilon_r}{d} \pi R_{eq}^2, \quad (B1)$$

where ε_0 is the permittivity of the vacuum and R_{eq} is the radius of the plate.

An approximating equation for R_{eq} was determined using FE calculation with QuickField™ as follows: First an axially symmetric model geometry was built. The initial parameters were the same as in ANSYS® and 2-dimensional QuickField™ simulations (Droplet radius 500 μm , contact angle 160°, insulator thickness 50 μm and relative permittivity 3). The conducting plate was circular with a radius of 1500 μm and the height of the modelling space was 1500 μm . Next the capacitance between the plane and the droplet was calculated by solving the electric field and using the capacitance wizard of QuickField™. Figure B3 shows an example of the FE model geometry and Figure B4 shows the same geometry after solving the electric field. For clarity, only the equipotential lines are shown. The calculation was then iterated while varying the contact angle, insulator thickness and insulator permittivity. While changing the contact angle, the droplet volume was kept constant and the radius was changed according to equation (C10) in Appendix C. The values of the variables are listed in Table B1. After a large number of simulations with different geometries, the calculated capacitance values were plotted as a function of the contact angle for different insulator thickness and permittivity values. Trial functions of variables were then fitted into the plots until the best fitting functions were found.

The plate area was not varied in order to reduce the number of simulations. The area was selected to be a nearly infinite plate but still close to the size of the droplet actuator electrodes. The error caused by the non-infinity can be estimated from the capacitance values calculated with contact angle 180 and $\varepsilon_r = 1$, since an accurate solution for the capacitance between the ball and an infinite conducting plane can be found in the literature [59]. Compared to those, the simulated capacitance values were 30% smaller with an insulator thickness of 500 μm and 8% smaller with an insulator thickness of 5 μm .

Only one droplet volume was simulated with QuickField™, because scaling of the droplet radius, insulator thickness and simulation space while simultaneously keeping the shape of the geometry unchanged does not change the shape of the

electric field. Only the absolute values of the electric field are changed; as a result, the capacitance values change respectively. For example, the capacitance between a 0.5 mm diameter droplet and a plane separated by a 25 μm insulator is half the capacitance between a 1 mm diameter droplet and a plane separated by a 50 μm insulator.

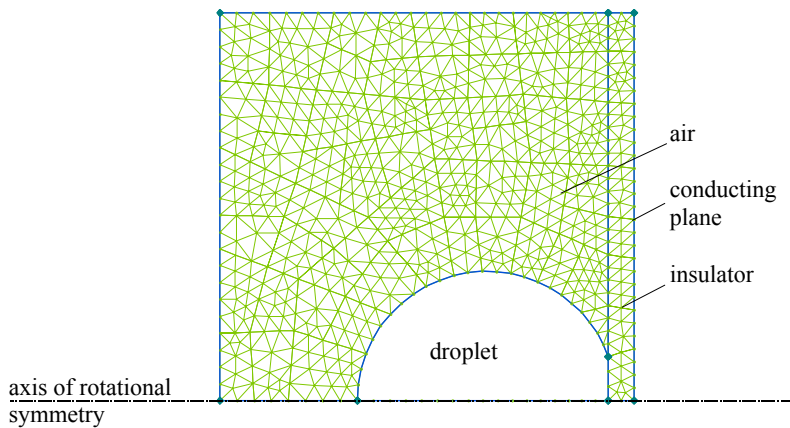


Figure B3. Example of the FE model used for droplet capacitance calculation. Droplet radius is 0.5 mm, contact angle 160° , insulator thickness $50\mu\text{m}$ and relative permittivity 3.

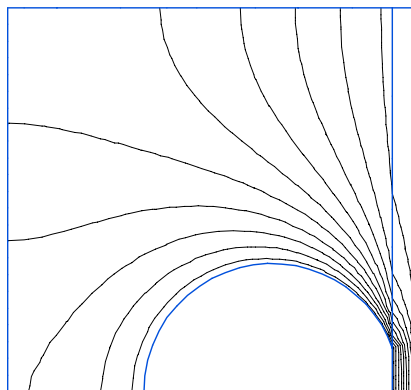


Figure B4. Example of the FE model after electric field calculation. Solid lines represent cross-sections of the equipotential surfaces.

Table B1. Variable parameters and their values used in QuickField™ calculations.

Parameter	Simulated values
Contact angle θ	with $\varepsilon_r = 3$: 90°, 105°, 120°, 145°, 150°, 160°, 170°, 175°, 180° with $\varepsilon_r = 1, 2, 6, 10$: 90°, 120°, 160°, 175°, 180°
Insulator thickness d	with $\varepsilon_r = 3$: 5 μm , 10 μm , 50 μm , 100 μm , 500 μm with $\varepsilon_r = 1, 2, 6, 10$: 5 μm , 10 μm , 50 μm , 100 μm , 500 μm
Insulator permittivity ε_r	1, 2, 3, 6, 10

The goal was to find a differentiable function that gives the capacitance accurately enough. As a result of function fitting the following equation was found, which gives approximately the equivalent plate radius.

$$R_{eq}^2 \approx R_c^2 + \frac{3.7}{\varepsilon_r^{0.57}} R_b^2 \left(\frac{d}{R_b} \right)^{0.734\varepsilon_r^{0.085}}. \quad (\text{B2})$$

R_b is the radius of a ball, which has the same volume V as the droplet:

$$R_b = \sqrt[3]{\frac{3V}{4\pi}}. \quad (\text{B3})$$

R_c is the radius of the droplet-insulator contact surface (Figure B1), which according to Appendix C equals:

$$R_c = R \sin \theta. \quad (\text{B4})$$

Combining all the equations, which give the capacitance between the droplet and the plane as a function of droplet volume, radius, contact angle and insulator thickness and permittivity, we get:

$$C_d \approx \frac{\varepsilon_0 \varepsilon_r \pi}{d} \left[R_c^2 + \frac{3.7}{\varepsilon_r^{0.57}} R_b^2 \left(\frac{d}{R_b} \right)^{0.734 \varepsilon_r^{0.085}} \right]. \quad (\text{B5})$$

$$\text{where } R_c = R \sin \theta \quad \text{and} \quad R_b = \sqrt[3]{\frac{3V}{4\pi}}$$

Either the droplet volume or the droplet radius can be eliminated using the equation (C9) or equation (C10) in Appendix C.

The approximate model of droplet capacitance fits quite well the FE calculated capacitance values, as can be seen in Figure B5.

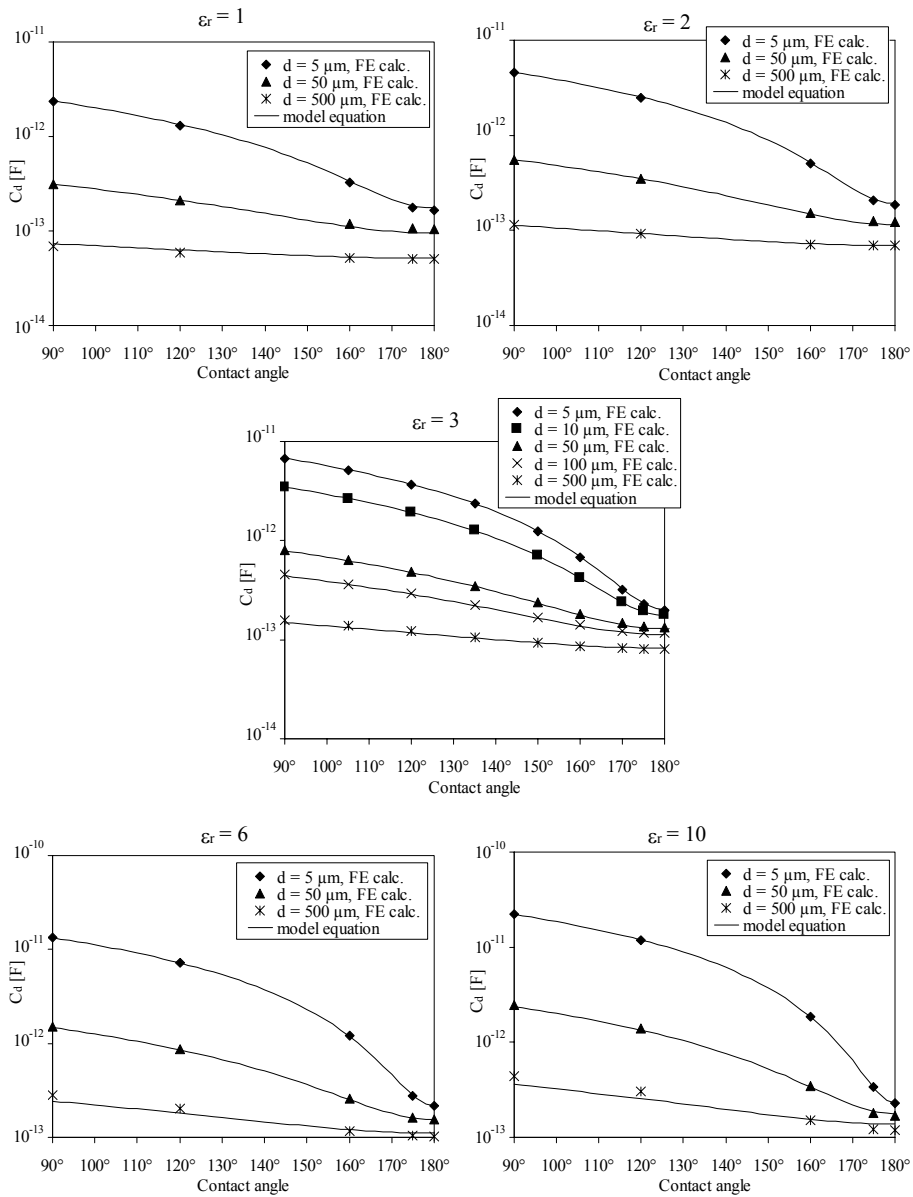


Figure B5. Calculated capacitance between a $0.522 \mu\text{l}$ droplet and a plane with radius 1.5 mm , separated by an insulator with variable thickness d and relative permittivity ϵ_r . FE calculated values are marked with dots and approximate equation with solid lines. Droplet diameter is 1 mm at a contact angle of 160° .

Appendix C: Auxiliary equations for a spherical droplet and an equivalent capacitor

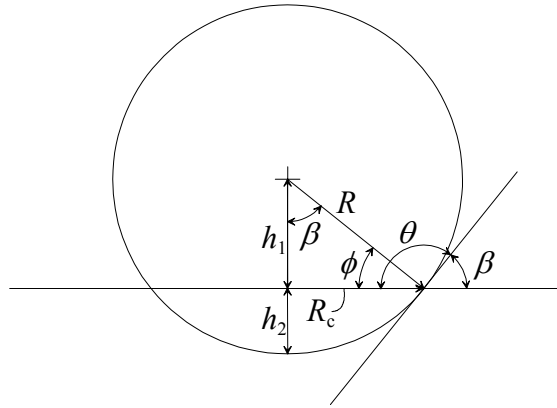


Figure C1. Cross-section of a spherical droplet.

Radius of the contact area

Let us consider a droplet which is a cap of a ball with radius R . The radius of the contact area is, according to Figure C1:

$$R_c = R \sin \beta. \quad (C1)$$

The angle β can be solved from the droplet contact angle θ as

$$\beta = \pi - \theta. \quad (C2)$$

We get:

$$R_c = R \sin(\pi - \theta) = R \sin \theta, \quad (C3)$$

Droplet volume

The volume of a spherical droplet equals the volume of a ball less the volume of the missing ball segment:

$$V = \frac{4}{3}\pi R^3 - \pi h_2^2 \left(R - \frac{1}{3}h_2 \right), \quad (\text{C4})$$

where R is the radius of the droplet and h_2 is the height of the missing segment. However, h_2 is not a very convenient distance to measure. In the following calculations, the volume is calculated as a function of droplet radius and contact angle θ , which is the characteristic parameter of the solid-liquid interface. From Figure C1 we get:

$$h_2 = R - h_1 \quad (\text{C5})$$

$$h_1 = R \sin \phi \quad (\text{C6})$$

$$\phi = \theta - \frac{\pi}{2} \quad (\text{C7})$$

which can be combined to solve h_2 :

$$\begin{aligned} h_2 &= R - R \sin \left(\theta - \frac{\pi}{2} \right) = R + R \sin \left(\frac{\pi}{2} - \theta \right) \\ &= R + R \cos \theta = R(1 + \cos \theta) \end{aligned} \quad (\text{C8})$$

Substituting h_2 into equation (C4) gives:

$$\begin{aligned}
V &= \frac{4}{3}\pi R^3 - \pi R^2(1 - \cos\theta)^2 \left[R - \frac{1}{3}R(1 - \cos\theta) \right] & (C9) \\
&= \frac{4}{3}\pi R^3 - \left(\pi R^2 + 2\pi R^2 \cos\theta + \pi R^2 \cos^2\theta \right) \left(\frac{2}{3}R - \frac{1}{3}R \cos\theta \right) \\
&= \frac{4}{3}\pi R^3 - \left(\frac{2}{3}\pi R^3 + \frac{4}{3}\pi R^3 \cos\theta + \frac{2}{3}\pi R^3 \cos^2\theta - \right. \\
&\quad \left. \frac{1}{3}\pi R^3 \cos\theta - \frac{2}{3}\pi R^3 \cos^2\theta - \frac{1}{3}\pi R^3 \cos^3\theta \right) \\
&= \frac{4}{3}\pi R^3 - \frac{2}{3}\pi R^3 - \pi R^3 \cos\theta + \frac{1}{3}\pi R^3 \cos^3\theta \\
&= \frac{1}{3}\pi R^3 (\cos^3\theta - 3\cos\theta + 2).
\end{aligned}$$

If the droplet volume is known, the radius can be solved from the equation:

$$R = \sqrt[3]{\frac{3V}{\pi(\cos^3\theta - 3\cos\theta + 2)}}. \quad (C10)$$

Area A_x

Area A_x is the fraction of the equivalent capacitor area, shown as the shaded area in Figure C2. It can be calculated geometrically by splitting the area into smaller fractions A_{x1} and A_{x2} :

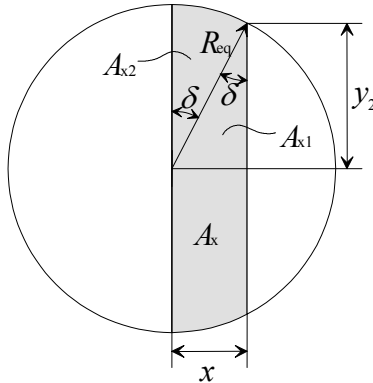


Figure C2. Definition of A_x (shaded area).

$$A_{x1} = \frac{xy_2}{2}, \quad (\text{C11})$$

where

$$y_2 = \sqrt{R_{eq}^2 - x^2}. \quad (\text{C12})$$

And

$$A_{x2} = \pi R_{eq}^2 \frac{\delta}{2\pi} = R_{eq}^2 \frac{\delta}{2}, \quad (\text{C13})$$

where

$$\delta = \arcsin\left(\frac{x}{R_{eq}}\right). \quad (\text{C14})$$

A_x can now be solved by combining the equations C11–C14:

$$A_x = 2A_{x1} + 2A_{x2} = x\sqrt{R_{eq}^2 - x^2} + R_{eq}^2 \arcsin\left(\frac{x}{R_{eq}}\right) \quad (\text{C15})$$

Calculating dA_x/dx

The derivative of A_x with respect to x can be calculated as follows:

$$\begin{aligned}
\frac{dA_x}{dx} &= \frac{d}{dx} \left[x\sqrt{R_{eq}^2 - x^2} + R_{eq}^2 \arcsin\left(\frac{x}{R_{eq}}\right) \right] = & (C16) \\
&= \sqrt{R_{eq}^2 - x^2} + x \frac{d}{dx} \sqrt{R_{eq}^2 - x^2} + R_{eq}^2 \frac{d}{dx} \arcsin\left(\frac{x}{R_{eq}}\right) \\
&= \sqrt{R_{eq}^2 - x^2} + x \frac{-2x}{2\sqrt{R_{eq}^2 - x^2}} + R_{eq}^2 \frac{1}{R_{eq}} \frac{1}{\sqrt{1 - \left(\frac{x}{R_{eq}}\right)^2}} \\
&= \frac{R_{eq}^2 - x^2}{\sqrt{R_{eq}^2 - x^2}} + \frac{-x^2}{\sqrt{R_{eq}^2 - x^2}} + \frac{R_{eq}^2}{\sqrt{R_{eq}^2 - x^2}} \\
&= \frac{2R_{eq}^2 - 2x^2}{\sqrt{R_{eq}^2 - x^2}} = 2\sqrt{R_{eq}^2 - x^2}
\end{aligned}$$

Author(s) Altti Torkkeli			
Title Droplet microfluidics on a planar surface			
Abstract This work reports on the modelling of, and experiments on, a method in which liquid is transported as droplets on a planar hydrophobic surface with no moving parts, merely through electrostatic forces generated by the underlying electrodes. Two-directional transportation along a straight electrode path and across a junction, fusion of two droplets and methods for importing, exporting and filtering of water droplets were demonstrated, and can be used as basic functions of a lab-on-a-chip type microfluidic system. In this work, the electrostatic droplet actuation is for the first time demonstrated on superhydrophobic surfaces. Such surfaces are composed of air-filled pores and exhibit a very low droplet sliding resistance due to reduced contact angle hysteresis and a high water contact angle (usually $> 150^\circ$). This work shows that superhydrophobic surfaces can be used to reduce the minimum voltage and to increase the maximum speed under certain conditions, but there are some harmful side-effects. First of all, the electrostatic pressure can push water into the surface pores, which hinders actuation. The phenomenon can also be treated as a vertical electrowetting effect. Another drawback is that the use of superhydrophobic surfaces makes actuation more critical to the properties of the liquid. For example, actuation of biological buffer solutions was not successful. For these reasons, it is concluded that it is more beneficial to use a smooth surface with low hysteresis than a superhydrophobic surface in droplet actuation. Electrostatic droplet actuation is a potential method for manipulating liquid on a microscopic scale, but there is still work to do. This work contains a detailed examination of the droplet actuation mechanism, and trapping of charges in the solid-liquid interface is found to be the most severe problem that needs to be solved.			
Keywords Microfluidics, lab-on-a-chip, electrostatic droplet actuation, electrowetting, superhydrophobic surface, MEMS			
Activity unit VTT Information Technology, Tietotie 3, P.O.Box 1208, FIN-02044 VTT, Finland			
ISBN 951-38-6237-2 (soft back ed.) 951-38-6238-0 (URL: http://www.vtt.fi/inf/pdf/)		Project number E7SU00393	
Date September 2003	Language English	Pages 194 p. + app. 19 p.	Price D
Name of project Wallac 97, Tutkijakoulu (Graduate School of Electronics Manufacturing)		Commissioned by Wallac (currently PerkinElmer Life Sciences), Tekes (The National Technology Agency), Academy of Finland, VTT	
Series title and ISSN VTT Publications 1235-0621 (soft back ed.) 1455-0849 (URL: http://www.vtt.fi/inf/pdf/)		Sold by VTT Information Service P.O.Box 2000, FIN-02044 VTT, Finland Phone internat. +358 9 456 4404 Fax +358 9 456 4374	

This work deals with a method in which liquid is transported as droplets on a planar hydrophobic surface with no moving parts, merely through electrostatic forces generated by the underlying electrodes. The work contains a thorough examination of the droplet actuation mechanism and related physical phenomena especially on superhydrophobic surfaces and gives a model for actuation. In the experimental part, various droplet manipulations are demonstrated which can be used as basic functions of a lab-on-a-chip type microfluidic system.

Tätä julkaisua myy
VTT TIETOPALVELU
PL 2000
02044 VTT
Puh. (09) 456 4404
Faksi (09) 456 4374

Denna publikation säljs av
VTT INFORMATIONSTJÄNST
PB 2000
02044 VTT
Tel. (09) 456 4404
Fax (09) 456 4374

This publication is available from
VTT INFORMATION SERVICE
P.O.Box 2000
FIN-02044 VTT, Finland
Phone internat. +358 9 456 4404
Fax +358 9 456 4374

ISBN 951-38-6237-2 (soft back ed.)
ISSN 1235-0621 (soft back ed.)

ISBN 951-38-6238-0 (URL: <http://www.vtt.fi/inf/pdf/>)
ISSN 1455-0849 (URL: <http://www.vtt.fi/inf/pdf/>)